

## Technologies for integrated millimeter-wave antennas

**Citation for published version (APA):**

Johannsen, U. (2013). *Technologies for integrated millimeter-wave antennas*. [Phd Thesis 1 (Research TU/e / Graduation TU/e), Electrical Engineering]. Technische Universiteit Eindhoven. <https://doi.org/10.6100/IR754833>

**DOI:**

[10.6100/IR754833](https://doi.org/10.6100/IR754833)

**Document status and date:**

Published: 01/01/2013

**Document Version:**

Publisher's PDF, also known as Version of Record (includes final page, issue and volume numbers)

**Please check the document version of this publication:**

- A submitted manuscript is the version of the article upon submission and before peer-review. There can be important differences between the submitted version and the official published version of record. People interested in the research are advised to contact the author for the final version of the publication, or visit the DOI to the publisher's website.
- The final author version and the galley proof are versions of the publication after peer review.
- The final published version features the final layout of the paper including the volume, issue and page numbers.

[Link to publication](#)

**General rights**

Copyright and moral rights for the publications made accessible in the public portal are retained by the authors and/or other copyright owners and it is a condition of accessing publications that users recognise and abide by the legal requirements associated with these rights.

- Users may download and print one copy of any publication from the public portal for the purpose of private study or research.
- You may not further distribute the material or use it for any profit-making activity or commercial gain
- You may freely distribute the URL identifying the publication in the public portal.

If the publication is distributed under the terms of Article 25fa of the Dutch Copyright Act, indicated by the "Taverne" license above, please follow below link for the End User Agreement:

[www.tue.nl/taverne](http://www.tue.nl/taverne)

**Take down policy**

If you believe that this document breaches copyright please contact us at:

[openaccess@tue.nl](mailto:openaccess@tue.nl)

providing details and we will investigate your claim.

# **Technologies for integrated millimeter-wave antennas**

This research was financially supported by the European Catrene project PANAMA as well as the FP7-project Par4CR.

Technologies for integrated millimeter-wave antennas / by U. Johannsen –  
Eindhoven : Technische Universiteit Eindhoven, 2013 – Proefschrift

A catalogue record is available from the Eindhoven University of Technology  
Library

ISBN: 978-90-386-3394-7

NUR: 959

This thesis was prepared with the  $\text{\LaTeX}2_{\epsilon}$  documentation system

Reproduction: TU/e print-service, Eindhoven, The Netherlands

Cover design: "Single-Chip-Radar" (courtesy of Omniradar: [www.omniradar.eu](http://www.omniradar.eu))

Copyright ©2013 by U. Johannsen. All rights reserved.

# **Technologies for integrated millimeter-wave antennas**

PROEFSCHRIFT

ter verkrijging van de graad van doctor aan de  
Technische Universiteit Eindhoven, op gezag van de  
rector magnificus, prof.dr.ir. C.J. van Duijn, voor een  
commissie aangewezen door het College voor  
Promoties in het openbaar te verdedigen  
op woensdag 3 juli 2013 om 14.00 uur

door

Ulf Johannsen

geboren te Flensburg, Duitsland



Dit proefschrift is goedgekeurd door de promotoren:

prof.dr.ir. A.B. Smolders

en

prof.dr.ir. G. Gerini

“So eine Arbeit wird eigentlich nie fertig,  
man muss sie für fertig erklären,  
wenn man nach Zeit und Umständen  
das Möglichste getan hat.”

Johann Wolfgang von Goethe (1749-1832)



Meinen Eltern



# Contents

---

<b>Summary</b>	<b>xiii</b>
<b>Samenvatting</b>	<b>xv</b>
<b>List of abbreviations</b>	<b>xvii</b>
<b>1 Introduction</b>	<b>1</b>
1.1 Context and general background of the thesis . . . . .	1
1.1.1 Societal context . . . . .	1
1.1.2 Brief review of 60 GHz wireless communication . . . . .	1
1.1.3 Motivation . . . . .	3
1.2 Objectives, research approach and outline . . . . .	4
1.3 Original contribution of the thesis . . . . .	6
<b>2 Electromagnetic theory and antenna modeling</b>	<b>9</b>
2.1 Electromagnetic fields in dielectric media . . . . .	10
2.1.1 The Maxwell equations . . . . .	10
2.1.2 Effect of finite electric resistivity . . . . .	11
2.1.3 Vector potentials . . . . .	12
2.1.4 Confined substrate modes . . . . .	14
2.2 Numerical computation . . . . .	15
2.2.1 The method of moments . . . . .	15
2.2.2 Finite-difference time-domain . . . . .	17
2.3 Antenna parameters . . . . .	18
2.3.1 Field regions . . . . .	18
2.3.2 Input impedance and radiation efficiency . . . . .	18
2.3.3 Gain, polarization, and radiation pattern . . . . .	19
2.3.4 Friis transmission equation . . . . .	22
2.4 Thin-wire circular loop antenna model . . . . .	23
2.4.1 Derivation of the integral equation . . . . .	24

2.4.2	Moment method solution for the electric current distribution . . . . .	27
2.4.3	Magnetostatic frill source . . . . .	28
2.4.4	Comparison with a FDTD solver . . . . .	31
<b>3</b>	<b>Integrated millimeter-wave antennas: State-of-the-art</b>	<b>33</b>
3.1	Antenna requirements for 60 GHz communications . . . . .	33
3.2	Antenna-in-Package . . . . .	37
3.2.1	Definition . . . . .	37
3.2.2	Review of typical IC packaging technologies . . . . .	37
3.2.3	State-of-the-art . . . . .	38
3.3	Antenna-on-Chip . . . . .	41
3.3.1	Definition . . . . .	41
3.3.2	Review of typical silicon IC technologies . . . . .	41
3.3.3	State-of-the-art . . . . .	42
3.4	Hybrid integrated mm-wave antenna . . . . .	46
3.4.1	Definition . . . . .	46
3.4.2	State-of-the-art . . . . .	46
3.5	Discussion . . . . .	49
<b>4</b>	<b>Antenna-in-Package concept</b>	<b>51</b>
4.1	Technology choice . . . . .	51
4.2	Design . . . . .	52
4.2.1	General module concept . . . . .	52
4.2.2	Antenna design . . . . .	53
4.3	Measurement setups . . . . .	56
4.3.1	Input impedance . . . . .	57
4.3.2	Radiation pattern . . . . .	58
4.4	Measurement results . . . . .	61
4.5	Summary and conclusions . . . . .	64
<b>5</b>	<b>Antenna-on-Chip concept</b>	<b>67</b>
5.1	Technology choice . . . . .	67
5.2	Design . . . . .	68
5.2.1	Mode suppression in the silicon substrate . . . . .	68
5.2.2	Antenna design . . . . .	72
5.3	Basic package concept . . . . .	75
5.4	Measurement results . . . . .	78
5.4.1	Input impedance . . . . .	78
5.4.2	Radiation pattern . . . . .	80
5.5	Application example: Single-chip radar module . . . . .	83
5.6	Summary and conclusions . . . . .	87

---

<b>6</b>	<b>Hybrid concept</b>	<b>89</b>
6.1	Technology choice . . . . .	89
6.2	Design and modeling approach . . . . .	90
6.2.1	General module concept . . . . .	90
6.2.2	Antenna design and modeling approach . . . . .	91
6.3	Fabrication and measurement results . . . . .	96
6.3.1	Bond-wire shape . . . . .	96
6.3.2	Prototype . . . . .	97
6.4	Yield analysis . . . . .	101
6.4.1	Analysis . . . . .	101
6.4.2	Result discussion . . . . .	102
6.5	Summary and conclusions . . . . .	103
<b>7</b>	<b>Antenna array considerations</b>	<b>105</b>
7.1	Modular array concept . . . . .	105
7.1.1	Linearly polarized array . . . . .	107
7.1.2	Circularly polarized array . . . . .	112
7.2	Axial ratio enhancement for modular array concept . . . . .	114
7.2.1	Sequential rotation technique for beam-steering . . . . .	114
7.2.2	Experiment . . . . .	116
7.3	Mutual coupling between bond-wire-antennas . . . . .	119
7.3.1	Model extension . . . . .	119
7.3.2	Verification . . . . .	121
7.3.3	60 GHz example . . . . .	123
7.4	Conclusions . . . . .	125
<b>8</b>	<b>Conclusions and recommendations</b>	<b>127</b>
8.1	Conclusions . . . . .	127
8.1.1	Technology choice . . . . .	127
8.1.2	Antenna modeling . . . . .	130
8.1.3	Millimeter-wave measurements . . . . .	130
8.2	Recommendations . . . . .	131
8.2.1	Technology choice . . . . .	131
8.2.2	Antenna modeling . . . . .	132
8.2.3	Millimeter-wave measurements . . . . .	132
<b>A</b>	<b>Derivation of the magnetostatic frill source model</b>	<b>133</b>
A.1	The electric vector potential . . . . .	133
A.2	Generated electric fields . . . . .	135
<b>B</b>	<b>Measured radiation patterns of all antenna concepts at a glance</b>	<b>139</b>



<b>C Phase angles of the S-parameters shown in Figure 7.17</b>	<b>143</b>
<b>List of publications</b>	<b>145</b>
<b>Bibliography</b>	<b>147</b>
<b>Acknowledgements</b>	<b>153</b>
<b>Curriculum Vitae</b>	<b>155</b>

# Summary

## Technologies for integrated millimeter-wave antennas

---

The recent release of the unlicensed 60 GHz band tackles the increasing demand for more bandwidth in the wireless consumer electronics market. In order to meet the cost requirements of this market, many research groups have worked towards 60 GHz front-end electronics in mainstream silicon technologies, i.e., CMOS and BiCMOS. However, the technology choice for suitable antennas has not been as unitary and is controversially discussed. While there is a wide consensus that the antenna should be integrated in the same package with the front-end integrated circuit (IC), there are three main approaches on the realization. First, there is the Antenna-in-Package approach, in which the antenna is implemented in the IC's packaging technology. Second, there is the Antenna-on-Chip approach, in which the antenna is directly implemented in the back-end of the IC. Finally, the third approach can be considered as a hybrid of Antenna-on-Chip and Antenna-in-Package, in which the feed-point of the antenna is implemented on-chip while the radiating element itself is realized off-chip.

This thesis focuses on the clash between those three main integration strategies. Its goal is to explore the challenges and potentials of each technology with respect to millimeter-wave antenna integration. For this, integrated antenna concepts for the 60 GHz band are developed using mainstream technologies. This restriction is necessary in order to achieve cost-effective solutions for the highly price-competitive wireless consumer electronics market. The following technology choices are made:

1. Printed-circuit-board technology for the Antenna-in-Package concept.
2. NXP's "Qubic4" BiCMOS technology family for the Antenna-on-Chip concept.
3. Generic wire-bond technology for the hybrid solution.

The Antenna-in-Package and Antenna-on-Chip concepts are designed using commercially available electromagnetic simulation software. For the hybrid solution a computationally efficient modeling approach is developed that supplements standard IC design tools towards the co-integration of such Bond-Wire-Antennas with the IC. The simulation results of all three antenna concepts are verified by experiments. Finally, the concepts are compared with respect to their cost, bandwidth, radiation efficiency, directivity, yield, and possible application area. Based on this assessment, it can be concluded that the major challenge for an in-package solution lies in the design of a broad-band low-loss interconnect between the IC and the antenna in order not to jeopardize the good overall performance. On-chip antennas on the other hand suffer from severe dielectric loss unless advanced post-processing steps are added or advanced packaging technologies are used. The Bond-Wire-Antenna as a hybrid solution merges both advantages of the in-package and on-chip antennas and achieves high radiation efficiency without the need for a low-loss chip-to-package interconnect design. Moreover, standard IC packaging technologies can be used, which makes this approach highly cost-effective. On the contrary, this concept does not offer a high design flexibility and exhibits a radiation null in the broad-side direction, which prohibits this antenna for certain applications.

Beside the main focus on integration technologies, a steerable antenna-array concept based on the developed integrated millimeter-wave antenna concepts was developed that exhibits a high flexibility with respect to array size and polarization. For the latter, special attention is paid to the axial ratio enhancement of circularly polarized arrays that are steered off broad-side. Due to its flexibility, the proposed array concept covers the full spectrum of mm-wave applications in the consumer electronics sector.

# Samenvatting

---

De recente vrijgave van de licentievrije 60 GHz-band pakt de toenemende vraag naar meer bandbreedte in de draadloze consumentenelektronicamarkt aan. Om eisen met betrekking tot kosten op deze markt te vervullen, hebben vele onderzoeksgroepen gewerkt aan elektronica voor 60 GHz front-ends in heersende silicium technologieën, dat wil zeggen, CMOS en BiCMOS. De technologiekeuze voor geschikte antennes is echter niet zo eenduidig en wordt controversieel bediscussieerd. Hoewel er een brede consensus is dat de antenne moet worden geïntegreerd in hetzelfde package als het front-end integrated circuit (IC), zijn er drie aanpakken voor de uitvoering. Allereerst is er het Antenna-in-Package concept, waarbij de antenne is uitgevoerd in de package-technologie van het IC. Bij het tweede concept, de Antenna-on-Chip, wordt de antenne direct geïntegreerd in het back-end van het IC. De derde aanpak kan worden beschouwd als een hybride van Antenna-on-Chip en Antenna-in-Package, waarbij de voedingspunt van de antenne is uitgevoerd op de chip, terwijl het stralende element zelf off-chip is uitgevoerd.

Dit proefschrift richt zich op de botsing tussen deze drie belangrijke integratiestrategieën. Het doel is om de uitdagingen en mogelijkheden van elke technologie te verkennen met betrekking tot millimeter-wave antenne-integratie. Hiervoor zijn geïntegreerde antenneconcepten voor de 60 GHz-band in heersende technologieën ontwikkeld. Deze beperking is noodzakelijk om kosteneffectieve oplossingen voor de zeer prijsgevoelige draadloze consumentenelektronicamarkt te realiseren. De volgende technologiekeuzes zijn gemaakt:

1. Printed-circuit-board technologie voor het Antenna-in-Package concept.
2. De "Qubic4" BiCMOS technologiestroom van NXP voor het Antenna-on-Chip concept.
3. Generieke wire-bond technologie voor de hybride oplossing.

De Antenna-in-Package en Antenna-on-Chip concepten worden ontworpen met

behulp van commerciële elektromagnetische simulatiesoftware. Voor de hybride oplossing is een efficiënt model ontwikkeld, dat als aanvulling op standaard IC-ontwerpsgereedschap kan dienen om deze Bond-Wire-Antenne's met het IC samen te integreren. De simulatieresultaten van alle drie de antennes zijn geverifieerd door middel van experimenten. Tenslotte worden de concepten met elkaar vergeleken met betrekking tot hun kosten, bandbreedte, stralingsefficiëntie, richtkarakteristiek, productierendement en mogelijk toepassingsgebied. Op basis van deze evaluatie kan worden geconcludeerd, dat de grootste uitdaging voor een in-package oplossing het ontwerp van een breedbandige en verliesarme interconnect tussen het IC en de antenne is. Aan de andere kant hebben on-chip antennes grote diëlektrische verliezen, tenzij geavanceerde nabewerkingsstappen worden toegevoegd of geavanceerde verpakkingstechnologieën worden gebruikt. De Bond-Wire-Antenna als hybride oplossing voegt de voordelen van de in-package en on-chip antennes samen en bereikt een hoog stralingsrendement zonder grote verliezen tussen de chip en het IC. Bovendien kunnen standaard IC-verpakkingstechnologieën worden gebruikt, hetgeen deze aanpak zeer kosteneffectief maakt. Dit concept biedt echter geen grote ontwerpflexibiliteit, waardoor deze antenne niet toegepast kan worden voor bepaalde applicaties.

Naast de focus op integratietechnologieën, is er een stuurbaar concept voor een antenne array uitgewerkt op basis van de ontwikkelde geïntegreerde millimeter-wave antenneconcepten. Dit array-concept beschikt over een grote flexibiliteit met betrekking tot de grootte van het array en de polarisatie. Voor circulair gepolariseerde arrays wordt in het bijzonder aandacht besteed aan de verbetering van de ellipticiteit voor gestuurde antennebundels. Door zijn flexibiliteit dekt dit array-concept het volledige spectrum van mm-wave toepassingen in de consumentenelektronicasector af.

# Abbreviations

---

AiP	Antenna-in-Package
AMC	artificial magnetic conductor
AoC	Antenna-on-Chip
AR	axial ratio
AUT	antenna-under-test
balun	balanced-to-unbalanced converter
BEOL	back-end-of-line
BWA	bond-wire-antenna
CDF	cumulative distribution function
CMOS/BiCMOS	complementary metal-oxide-semiconductor
CPW	coplanar waveguide
EBG	electromagnetic band-gap
EFIE	electric field integral equation
EIRP	equivalent isotropic radiated power
ETSI	European Telecommunications Standards Institute
FDTD	finite-difference time-domain
FMCW	frequency-modulated continuous-wave
GPS	global positioning system
GS	ground-signal
GSG	ground-signal-ground
GSSG	ground-signal-signal-ground
HD	high definition
HDMI	high-definition multimedia interface
HDTV	high-definition television
IC	integrated circuit
IF	intermediate frequency

LO	local oscillator
LTCC	low-temperature co-fired ceramic
MEMS	micro-electro-mechanical-system
mm-wave	millimeter-wave
MoM	method of moments
OMP-package	overmolded plastic-package
PC	personal computer
PDA	personal data assistant
PDF	probability density function
PEC	perfect electric conductor
PLL	phase-locked-loop
RCS	radar-cross-section
SG	signal-ground
SGH	standard gain horn
SNR	signal-to-noise ratio
TE	transverse-electric
TM	transverse-magnetic
UTD	uniform geometrical theory of diffraction
vias	vertical interconnect
VNA	vector network analyzer
WLAN	wireless local area network

## CHAPTER ONE

# Introduction

---

## 1.1 Context and general background of the thesis

### 1.1.1 Societal context

The trend in the consumer electronics sector towards wireless products has led to numerous advancements in our everyday lives. The existence of a wireless local area network (WLAN) in a café, public building, or private home, for example, is often taken for granted. Similarly, the use of satellite navigation using the global positioning system (GPS) to get to a destination has largely substituted the use of printed maps. If none of the two options are available, one may still browse the internet for an online-map on a smartphone, or call a friend using a hands-free headset that is connected to a mobile phone via *bluetooth*. All those advancements, however, have also led to a congested microwave frequency spectrum, i.e., below 30 GHz. Future applications that require wireless high-data-rate communication in the Gb/s-range can, therefore, not be accommodated for in this frequency range due to an insufficient amount of available bandwidth. Hence, the consumer electronics industry has laid an eye on the millimeter-wave (mm-wave) spectrum, i.e., 30 GHz to 300 GHz. Especially the unlicensed 60 GHz band with a large worldwide overlap seems an attractive option here, see, for example, [1, 2].

### 1.1.2 Brief review of 60 GHz wireless communication

The interest of the wireless consumer electronics industry in mm-wave frequencies is currently mainly focused on the 60 GHz band. Here, a large bandwidth of unlicensed spectrum is available worldwide, with a large frequency overlap between



different countries and regions<sup>1</sup>. In Europe, for example, the 60 GHz band covers all frequencies from 57 GHz up to 66 GHz, i.e., a bandwidth of 9 GHz, for which the European Telecommunications Standards Institute (ETSI) released a harmonized European standard in early 2012, see [3]. A nice overview of the regulations in other parts of the world can be found in [2].

Prior to those regulations, many researchers had already studied some possibilities and challenges for the development of wireless consumer products operating around 60 GHz, see, for example, [1, 2, 4, 5, 6, 7, 8]. Various application scenarios were mentioned in this respect. The three top applications according to [4] are high definition (HD) video streaming, file transfer, and wireless Gigabit Ethernet. Here, HD video streaming includes, for example, uncompressed video/audio streaming from a portable media player, laptop, or personal data assistant (PDA) to a HD television (HDTV) or projector. The file transfer scenario covers applications such as communication between a personal computer (PC) and a printer, a digital camera, or similar. A further possible application mentioned is a "kiosk in a store" that sells audio and video contents by directly uploading the product to a customer's portable device. In addition, the authors of [5] also envision a replacement of wired connections inside PCs by 60 GHz wireless interconnects.

In order for above stated applications to be successful, products have to be developed that can compete on the highly cost-driven consumer electronics market. Hence, from the technology perspective, standard low-cost fabrication processes are preferred. One of the early publications on the exploitation of the 60 GHz band for consumer applications, [1], already briefly discusses technologies for wireless front-ends in this respect. For the antenna in particular, an implementation into the semiconductor technology is suggested in order to avoid significant interconnection losses. For cost reasons, the author advises to use silicon-germanium based semiconductor technologies. Nowadays, there indeed seems to be a wide consensus among 60 GHz research groups that silicon- or silicon-germanium-based technologies, i.e., CMOS or BiCMOS, should be used for the electronics of the wireless front-end. This is, for example, also outlined by the authors of [6], published in 2009, who compare two different integration strategies for the antenna. They distinguish the Antenna-on-Chip (AoC) solutions, i.e., (Bi-)CMOS integrated antennas, from the Antenna-in-Package (AiP) solutions, i.e., antennas that are integrated in the package technology of the integrated circuit (IC). From this comparison, they conclude that on-chip antennas are less favorable than in-package antennas for 60 GHz applications. They support their conclusion with the argument that AoCs only achieve radiation efficiencies of

---

<sup>1</sup>The reason for allocations of worldwide almost identical unlicensed frequency bands around 60 GHz is due to an additional 10-15 dB/km attenuation at those frequencies caused by atmospheric oxygen. Therefore, 60 GHz communication is not suitable for communication distances larger than 2 km, see [1].

less than 12 % unless non-mainstream processing steps are added, which would increase the cost of the solution accordingly. In contrast, the authors of [5] claim only a year later that AoCs offer the cheapest solution and suggest that more research should be conducted in order to increase their gain values to meet those of their AiP counterparts.

### 1.1.3 Motivation

With respect to 60 GHz antennas it is commonly accepted that the antenna should be located as close as possible to the mm-wave front-end electronics in order to keep interconnect losses at a minimum. Here, 'close' refers to the electrical distance of the antenna to the front-end IC, i.e., measured in terms of the operating wavelength. The free space wavelength,  $\lambda_0$ , at 60 GHz is 5 mm and, hence, the antenna should preferably be inside the IC package. Such an antenna is called an *integrated antenna* throughout this thesis. Moreover, since the considerations are limited to antennas for the mm-wave range, such an antenna is more specifically called *integrated mm-wave antenna*, whereas both expressions are interchangeable.

Although there is a wide consensus regarding the integration of the antennas, the choice for the integration technology does not appear to be as unitary, as outlined in the previous section. On one hand, one of the main reasons for this controversy can be found in the vast variety of process technologies in the semiconductor industry. Many "classical" antenna engineers simply do not know or have no access to the full spectrum of semiconductor processes and, as a consequence, cannot exploit their full capabilities. Furthermore, IC processes have hardly ever been characterized with respect to antenna parameters, which poses difficulties for a proper antenna design. On the other hand, IC design engineers, who have good insights in various semiconductor process technologies, often do not have a very broad antenna-engineering background and, therefore, might not always come up with as well-designed integrated antenna solutions. An extreme example of such a questionable antenna design was published in [9], where an on-chip metallic patch over a ground plane is simultaneously used as a high-Q resonator, for which typically low losses are desired, and as an antenna, for which (radiation) loss and a low-Q behavior are key characteristics.

As a consequence of this technologically complex field of engineering, in which strict company confidentialities within the semiconductor industry pose additional difficulties in obtaining a thorough overview, two main opinions have emerged in the mm-wave society. First, there is the group of people that do not believe in a success of the AoC approach. Their opinion is largely motivated by the problems with the lossy silicon substrate and the associated low radiation efficiency. Furthermore,

it is often argued that possible processing steps that would enhance the radiation efficiency are non-standard and, therefore, too expensive. On the contrary, the second major group is mostly searching for cost-effective alternative ways to improve the radiation behavior of on-chip antennas rather than excluding this approach once and for all. Their efforts are strongly supported by successfully integrated on-chip antenna designs in the terahertz band (0.3 THz - 3 THz) at which the AoC approach can be considered largely superior to the AiP approach, see, for example, [10].

The obvious question that arises from the above sketched controversy is the following: "Which integration technology will ultimately be the best choice for mm-wave antennas in the consumer market?" For this, beside the two main integration approaches, a third concept can be distinguished and should also be taken into consideration. This third approach can be understood as a hybrid between AiP and AoC concept, which is further described in Chapter 3. Finally, another interesting question that needs to be answered is that of the frequency limits of the concepts, i.e., "at what frequency range is the AiP, AoC, or hybrid solution superior to the other two approaches?"

## 1.2 Objectives, research approach and outline

The objective of this thesis is to answer above raised questions based on mainstream technologies. This is done in a unified approach by investigating the AiP, AoC, and hybrid integration approach in an equal manner. The general outline of this thesis, shown in Figure 1.1, adopts the structure of this research approach. First, a brief review of the most important aspects of electromagnetic theory and antenna modeling is provided in Chapter 2. Antenna specifications for the 60 GHz band are then derived in Chapter 3, where also an overview of typical state-of-the-art antenna concepts for AiP, AoC, and hybrid solutions is given. Based on those studies, integrated mm-wave antenna concepts were developed for each approach, which are presented in Chapters 4 to 6. Here, since this study is focused on the effect of the integration technology, basic antenna topologies were chosen for the investigations, i.e., dipole and loop antennas. In Chapter 4, also the measurement setups that were used for the characterization of the antenna prototypes are described. Since, eventually, antenna arrays will be required for many mm-wave applications, respective considerations in this direction are summarized in Chapter 7. Finally, a comparison of all three antenna concepts with respect to their performance is provided in Chapter 8, where also general conclusions and recommendations are drawn. Here, special emphasis is also laid on the suitability of the concepts for the major application areas as identified in [4, 5], i.e.,

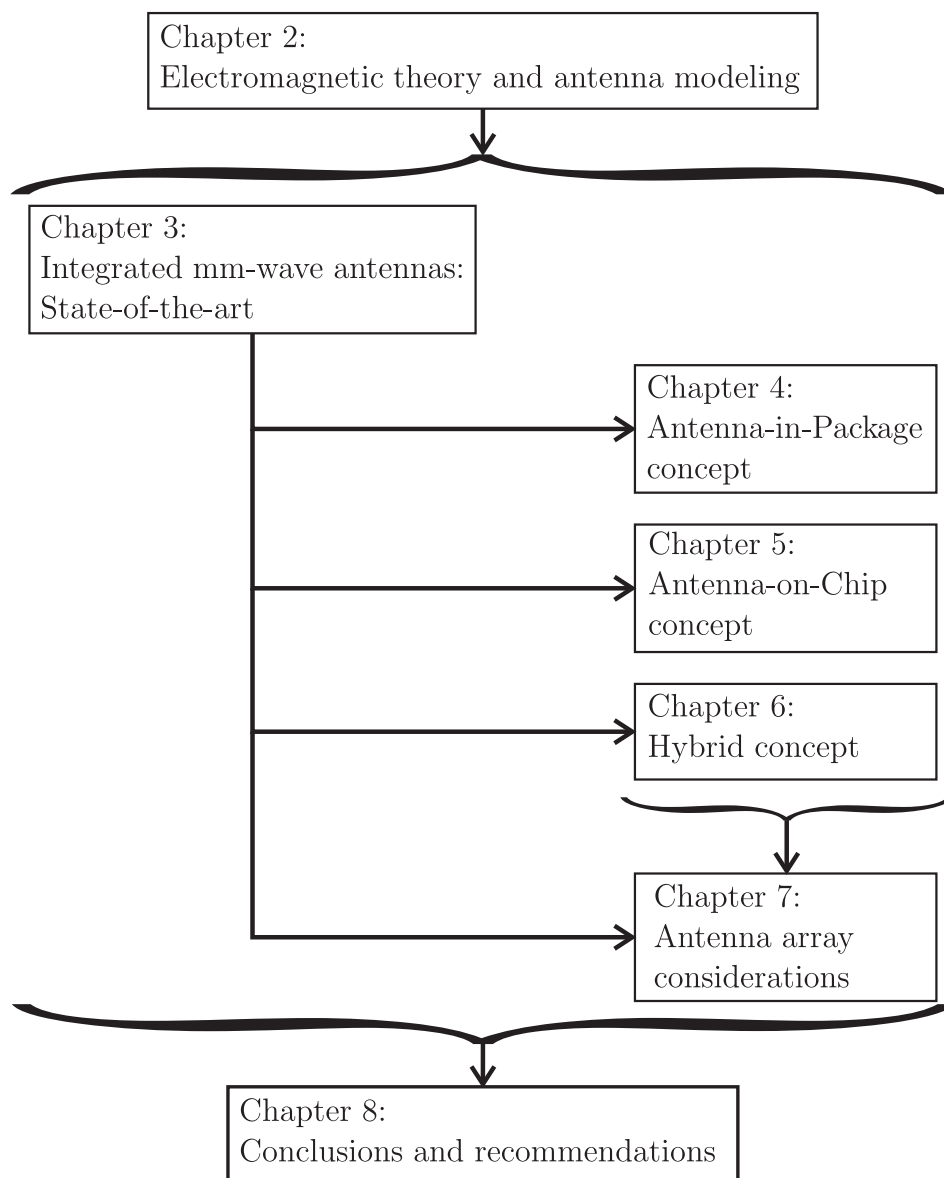


**Figure 1.1.** General outline of this thesis.

- a) HD video streaming and wireless Gigabit Ethernet,
- b) file transfer,
- c) wireless interconnects.

Note that the designated goal of this thesis is an assessment of those process technologies that are nowadays widely considered as standard for the consumer market. Therefore, the drawn conclusions reflect the general requirements of this market and exclude antenna designs in more advanced or more costly technologies. For example, the considerations are limited to silicon-based IC technologies. There are, however, also research groups that focus on, for example, gallium-arsenide based IC processes. Due to the typically much lower losses in those semiconductor substrates, on-chip antennas with significantly higher efficiencies could be accomplished. Gallium-arsenide is more expensive than silicon, however, and, therefore, those solutions are generally considered as less competitive on the consumer electronics market.

### 1.3 Original contribution of the thesis

The work that is presented in this thesis contains the following original contributions (listed by their order of appearance in the thesis):

- Correction of the formulas presented in [11] for the magnetostatic frill source, see Chapter 2.
- Quantification of antenna gain requirements for the European 60 GHz-band, see Chapter 3.
- Categorization of integrated mm-wave antenna concepts based on their integration technology, see Chapter 3.
- Review of typical state-of-the-art antenna concepts per category, see Chapter 3.
- Investigation of three integrated mm-wave antenna concepts in a unified approach, see Chapters 4 to 6.
- Contribution to mm-wave anechoic chamber design, see Chapter 4.
- Proposal of basic packaging concept for Antenna-on-chip concepts on thin silicon substrates, see Chapter 5.
- Antenna design for 60 GHz single-chip-radar in BiCMOS technology, see Chapter 5.

- 
- Formulation and verification of computationally efficient model for the hybrid antenna concept including mutual coupling, see Chapter 6 and 7.
  - Unified yield analysis of the hybrid antenna concept for the entire mm-wave band, see Chapter 6.
  - Proposal of modular array concept for achieving flexible mm-wave front-end solutions, see Chapter 7.
  - Contribution to axial ratio enhancement algorithm for sequentially rotated antenna arrays, see Chapter 7.



## CHAPTER TWO

# Electromagnetic theory and antenna modeling

---

The multidisciplinary field of integrated mm-wave antennas caught the attention of not only the antenna society but also, for example, of the solid-state circuits and electron devices societies. Since the latter two do not naturally deal directly with antenna problems, it is meaningful to summarize some basic principles of antenna theory that are essential for the understanding of the remainder of this thesis. For this, a brief review of basic electromagnetic theory is first of all given in Section 2.1. Here, a link is also made between a substrate's electric resistivity, which is a commonly used parameter in the semiconductor industry, and the material's loss tangent, which is used in general microwave engineering. Due to their importance for two of the three developed integrated mm-wave antenna concepts, some basic properties of confined substrate modes and their respective cut-off frequencies are also presented in this section. An overview of the numerical methods that were used for the solution of electromagnetic problems throughout this thesis is then given in Section 2.2, followed by a review of important antenna parameters in Section 2.3. Finally, the described theoretical foundations are put into practice by the derivation of a numerically efficient model for a circular loop antenna in Section 2.4, which also plays a major role for the modeling approach of the hybrid integrated antenna concept in Chapter 6.



## 2.1 Electromagnetic fields in dielectric media

### 2.1.1 The Maxwell equations

The relation between electromagnetic fields and their electric and magnetic sources is given by Maxwell's equations,

$$\nabla \times \mathcal{H}(\mathbf{r}) = \frac{\partial}{\partial t} \mathcal{D}(\mathbf{r}) + \mathcal{J}(\mathbf{r}), \quad (2.1)$$

$$\nabla \times \mathcal{E}(\mathbf{r}) = -\frac{\partial}{\partial t} \mathcal{B}(\mathbf{r}) - \mathcal{M}(\mathbf{r}), \quad (2.2)$$

$$\nabla \cdot \mathcal{D}(\mathbf{r}) = \rho_e(\mathbf{r}), \quad (2.3)$$

$$\nabla \cdot \mathcal{B}(\mathbf{r}) = 0, \quad (2.4)$$

with the magnetic field strength  $\mathcal{H}(\mathbf{r})$ , the electric field strength  $\mathcal{E}(\mathbf{r})$ , and the electric-flux density and magnetic-flux density  $\mathcal{D}(\mathbf{r})$  and  $\mathcal{B}(\mathbf{r})$ , respectively. Furthermore,  $\rho_e(\mathbf{r})$  describes the electric charge density,  $\mathcal{J}(\mathbf{r})$  the electric, and  $\mathcal{M}(\mathbf{r})$  the magnetic<sup>1</sup> current densities, see, for example, [12]. The coordinate vector to the observation point is denoted  $\mathbf{r}$ . Assuming harmonic time dependence, i.e., all field quantities are proportional to  $e^{j\omega t}$ , where  $t$  is the time and  $\omega$  the angular frequency, (2.1) to (2.4) can be written as

$$\nabla \times \mathbf{H}(\mathbf{r}) = j\omega \mathbf{D}(\mathbf{r}) + \mathbf{J}(\mathbf{r}), \quad (2.5)$$

$$\nabla \times \mathbf{E}(\mathbf{r}) = -j\omega \mathbf{B}(\mathbf{r}) - \mathbf{M}(\mathbf{r}), \quad (2.6)$$

$$\nabla \cdot \mathbf{D}(\mathbf{r}) = \rho_e(\mathbf{r}), \quad (2.7)$$

$$\nabla \cdot \mathbf{B}(\mathbf{r}) = 0. \quad (2.8)$$

For homogeneous and isotropic media, the relation between the electric-flux density and electric field strength as well as the relation between the magnetic-flux density and the magnetic field strength is given by the following constitutive relations:

$$\mathbf{D}(\mathbf{r}) = \epsilon \mathbf{E}(\mathbf{r}) = \epsilon_0 \epsilon_r \mathbf{E}(\mathbf{r}), \quad (2.9)$$

$$\mathbf{B}(\mathbf{r}) = \mu \mathbf{H}(\mathbf{r}) = \mu_0 \mu_r \mathbf{H}(\mathbf{r}), \quad (2.10)$$

with  $\epsilon_0 = 8.85 \cdot 10^{-12} \frac{\text{As}}{\text{Vm}}$  the permittivity and  $\mu_0 = 4\pi \cdot 10^{-7} \frac{\text{Vs}}{\text{Am}}$  the permeability of vacuum, respectively. The factors

$$\epsilon_r = \epsilon'_r - j\epsilon''_r, \quad (2.11)$$

$$\mu_r = \mu'_r - j\mu''_r \quad (2.12)$$

---

<sup>1</sup>The magnetic current density is not a physical quantity, but is often introduced to simplify calculations.

denote the relative permittivity and relative permeability of the medium with respect to vacuum. Both factors are, therefore, dimensionless. In particular, for dielectric media it holds that  $\mu_r = 1$ . In case of an infinite resistivity of the medium,  $\epsilon_r''$  accounts for polarization losses, i.e., damping of the vibrating dipole moments in the material, see [13]. Instead of stating the imaginary value, however, material suppliers usually characterize the losses of a dielectric by its loss tangent, defined as

$$\tan(\delta) = \frac{\epsilon_r''}{\epsilon_r'} . \quad (2.13)$$

### 2.1.2 Effect of finite electric resistivity

For a medium that exhibits an electric resistivity  $\rho$ , the electric-current density in Equation (2.5) can be decomposed in two parts, i.e.,

$$\mathbf{J}(\mathbf{r}) = \mathbf{J}_{\text{conduct.}}(\mathbf{r}) + \mathbf{J}_{\text{imposed}}(\mathbf{r}) , \quad (2.14)$$

see [12]. The first component is the conduction current density,

$$\mathbf{J}_{\text{conduct.}}(\mathbf{r}) = \frac{\mathbf{E}(\mathbf{r})}{\rho} \quad (2.15)$$

which describes the current due to an electric field strength acting on the conductive medium. The other term in Equation (2.14),  $\mathbf{J}_{\text{imposed}}(\mathbf{r})$ , is the imposed current density and represents a source term of the electromagnetic fields.

Equation (2.5) for homogeneous and isotropic media can be re-written with the aid of Equations (2.9), (2.11), (2.14), and (2.15) to

$$\nabla \times \mathbf{H}(\mathbf{r}) = j\omega\epsilon_0 \left( \epsilon_r' - j\epsilon_r'' - j\frac{1}{\rho\omega\epsilon_0} \right) \mathbf{E}(\mathbf{r}) + \mathbf{J}_{\text{imposed}} . \quad (2.16)$$

Hence, the electric resistivity contributes as ohmic losses to the imaginary part of the relative permittivity, i.e.,

$$\epsilon_r = \epsilon_r' - j \left( \epsilon_r'' + \frac{1}{\rho\omega\epsilon_0} \right) = \epsilon_r' - j\tilde{\epsilon}_r'' , \quad (2.17)$$

and has the same effect as polarization losses. Since both loss mechanisms are indistinguishable, see [13], the loss tangent (2.13) for materials with finite resistivity is given by

$$\tan(\delta) = \frac{\tilde{\epsilon}_r''}{\epsilon_r'} = \frac{\rho\omega\epsilon_0\epsilon_r'' + 1}{\rho\omega\epsilon_0\epsilon_r'} . \quad (2.18)$$

As an example, Figure 2.1 provides the relation between the resistivity of a doped silicon substrate with  $\epsilon_r' = 11.9$  and its resulting loss tangent at 60 GHz under the assumption of low polarization losses, i.e.,  $\epsilon_r'' \approx 0$ .

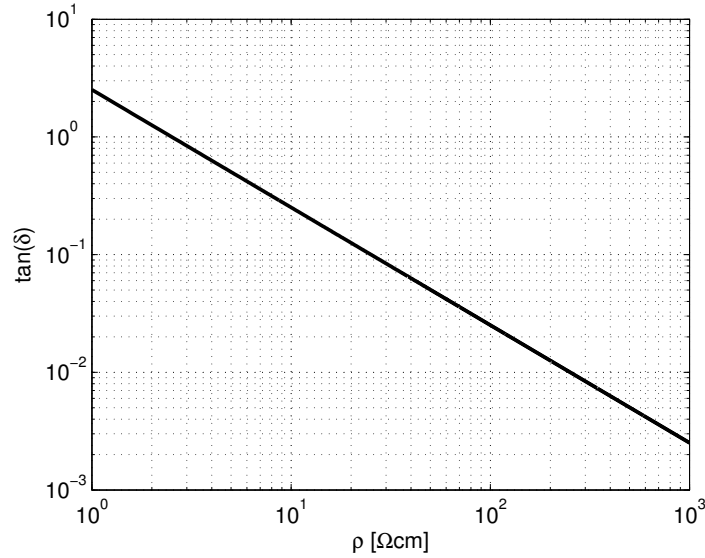


**Figure 2.1.** Relation between the resistivity,  $\rho$ , of a doped silicon substrate with  $\epsilon'_r = 11.9$  and its resulting loss tangent at 60 GHz (low polarization losses assumed, i.e.,  $\epsilon''_r \approx 0$ ).

Finally, since the resistivity can be considered as part of the relative permittivity of a medium, the term  $\mathbf{J}(\mathbf{r})$  implies the imposed current density  $\mathbf{J}_{\text{imposed}}(\mathbf{r})$  only throughout the remainder of this thesis.

### 2.1.3 Vector potentials

As mentioned in [14], it is possible to calculate the electromagnetic fields directly from the source term  $\mathbf{J}(\mathbf{r})$ , but it is often much simpler to calculate the fields from auxiliary functions, known as vector potentials<sup>2</sup>. The two most commonly used vector potentials are the magnetic vector potential,  $\mathbf{A}(\mathbf{r})$ , and the electric vector potential,  $\mathbf{F}(\mathbf{r})$ . The following paragraph summarizes the derivation of the magnetic vector potential under the assumption that only electric currents are present, i.e.,  $\mathbf{M}(\mathbf{r}) = \mathbf{0}$ , and that the medium is homogeneous and isotropic.

The magnetic field is solenoidal, i.e.,

$$\nabla \cdot \mathbf{H}(\mathbf{r}) = 0. \quad (2.19)$$

Therefore, the magnetic field can be represented as the curl of a vector field,

$$\mathbf{H}(\mathbf{r}) = \nabla \times \mathbf{A}(\mathbf{r}), \quad (2.20)$$

---

<sup>2</sup>The author adds that "although the electric and magnetic field intensities ( $\mathbf{E}$  and  $\mathbf{H}$ ) represent physically measurable quantities, among most engineers the potentials are strictly mathematical tools."

with  $\mathbf{A}(\mathbf{r})$  the magnetic vector potential. Using this result and Equation (2.10) in (2.6) yields

$$\nabla \times (\mathbf{E}(\mathbf{r}) + j\omega\mu\mathbf{A}(\mathbf{r})) = \mathbf{0}. \quad (2.21)$$

This implies that the vector field, given by  $(\mathbf{E}(\mathbf{r}) + j\omega\mu\mathbf{A}(\mathbf{r}))$ , is irrotational and can therefore be represented by the gradient of a scalar field  $\Phi(\mathbf{r})$ , i.e.,

$$\mathbf{E}(\mathbf{r}) + j\omega\mu\mathbf{A}(\mathbf{r}) = -\nabla\Phi(\mathbf{r}). \quad (2.22)$$

Using this result, Equation (2.20), and (2.9) in (2.5) results in

$$\nabla \times \nabla \times \mathbf{A}(\mathbf{r}) - k^2\mathbf{A}(\mathbf{r}) = -j\omega\epsilon\nabla\Phi(\mathbf{r}) + \mathbf{J}(\mathbf{r}), \quad (2.23)$$

where  $k = \omega\sqrt{\epsilon\mu}$  is the wave number of the medium. This equation can be re-written using the Laplace operator, defined as

$$\nabla^2\mathbf{A}(\mathbf{r}) = \nabla\nabla \cdot \mathbf{A}(\mathbf{r}) - \nabla \times \nabla \times \mathbf{A}(\mathbf{r}), \quad (2.24)$$

to arrive at

$$\nabla^2\mathbf{A}(\mathbf{r}) + k^2\mathbf{A}(\mathbf{r}) = \nabla(j\omega\epsilon\Phi(\mathbf{r}) + \nabla \cdot \mathbf{A}(\mathbf{r})) - \mathbf{J}(\mathbf{r}). \quad (2.25)$$

The scalar function  $\Phi(\mathbf{r})$  can be freely chosen and is set to satisfy

$$j\omega\epsilon\Phi(\mathbf{r}) = -\nabla \cdot \mathbf{A}(\mathbf{r}), \quad (2.26)$$

in order to simplify Equation (2.25) to the vectorial Helmholtz-equation

$$\nabla^2\mathbf{A}(\mathbf{r}) + k^2\mathbf{A}(\mathbf{r}) = -\mathbf{J}(\mathbf{r}). \quad (2.27)$$

Equation (2.26) is known as the Lorentz gauge. It can be shown that the solution of (2.27) is generally given by

$$\mathbf{A}(\mathbf{r}) = \frac{1}{4\pi} \int_{V'} \frac{\mathbf{J}(\mathbf{r}')}{R(\mathbf{r} - \mathbf{r}')} e^{-jkR(\mathbf{r} - \mathbf{r}')} dV', \quad (2.28)$$

in which  $\mathbf{r}'$  denotes the coordinate vector to a source point,  $V'$  the volume that contains the source points,  $\mathbf{r}$  the coordinate vector to an observation point, and  $R(\mathbf{r} - \mathbf{r}') = |\mathbf{r} - \mathbf{r}'|$  denotes the distance between source and observation point, see also [14]. Note that the kernel of (2.28) exhibits a singularity at  $\mathbf{r} = \mathbf{r}'$ , which poses a challenge for the exact evaluation of the integral. After the magnetic vector potential is calculated, the magnetic field strength in an observation point can be computed by Equation (2.20). The electric field strengths can be obtained from

$$\mathbf{E}(\mathbf{r}) = \frac{1}{j\omega\epsilon} (k^2\mathbf{A}(\mathbf{r}) + \nabla\nabla \cdot \mathbf{A}(\mathbf{r})), \quad (2.29)$$

where Equation (2.26) was used in conjunction with Equation (2.22).

Similarly, the electric vector potential can be derived from the magnetic current distribution  $\mathbf{M}(\mathbf{r})$ . For this, only magnetic current densities are considered, i.e.,  $\mathbf{J}(\mathbf{r}) = \mathbf{0}$ . The result for the electric vector potential is then given by

$$\mathbf{F}(\mathbf{r}) = \frac{1}{4\pi} \int_{V'} \frac{\mathbf{M}(\mathbf{r}')}{R(\mathbf{r} - \mathbf{r}')} e^{-jkR(\mathbf{r} - \mathbf{r}')} dV'. \quad (2.30)$$

From this, the electric and magnetic fields can be determined by equating

$$\mathbf{E}(\mathbf{r}) = -\nabla \times \mathbf{F}(\mathbf{r}) \quad (2.31)$$

and

$$\mathbf{H}(\mathbf{r}) = \frac{1}{j\omega\mu} (k^2\mathbf{F}(\mathbf{r}) + \nabla\nabla \cdot \mathbf{F}(\mathbf{r})), \quad (2.32)$$

respectively.

### 2.1.4 Confined substrate modes

Two of the three integrated mm-wave concepts that are presented in this thesis are directly located on top of dielectric substrates. As explained in [12, 15], a dielectric substrate can confine and guide electromagnetic energy. Since this mechanism is often unwanted and can pose additional challenges to an antenna design, it is important to understand under what circumstances this can occur. As explained in [12], the confinement of the electromagnetic energy inside an infinite substrate is due to total reflections at its top and bottom surface. Those reflections result in a standing wave pattern inside the substrate as shown in Figure 2.2(a). As known from basic electromagnetic theory, a total reflection at a dielectric interface results in an evanescent field on the opposite side of the interface, see, for example, [13]. Therefore, the shown electric field strength in Figure 2.2(a) decays exponentially for  $z < -h$  and  $z > 0$ . The amount of confined energy inside the slab depends on its thickness,  $h$ , its permittivity,  $\epsilon$ , as well as the permittivity of the surrounding medium, usually air. The fields inside the substrate can be subdivided into two fundamentally different field configurations, namely transverse-electric (TE) and transverse-magnetic (TM), with transverse referring to the orientation of the electric and magnetic field vectors with respect to the direction of propagation. For both cases, TE and TM propagation, several modes can exist in the substrate. The lower cut-off frequencies for those modes are given by [15] as

$$f_c = \frac{n c_0}{2h\sqrt{\epsilon_r' - 1}}, \quad n \in \mathbb{N}_0, \quad (2.33)$$

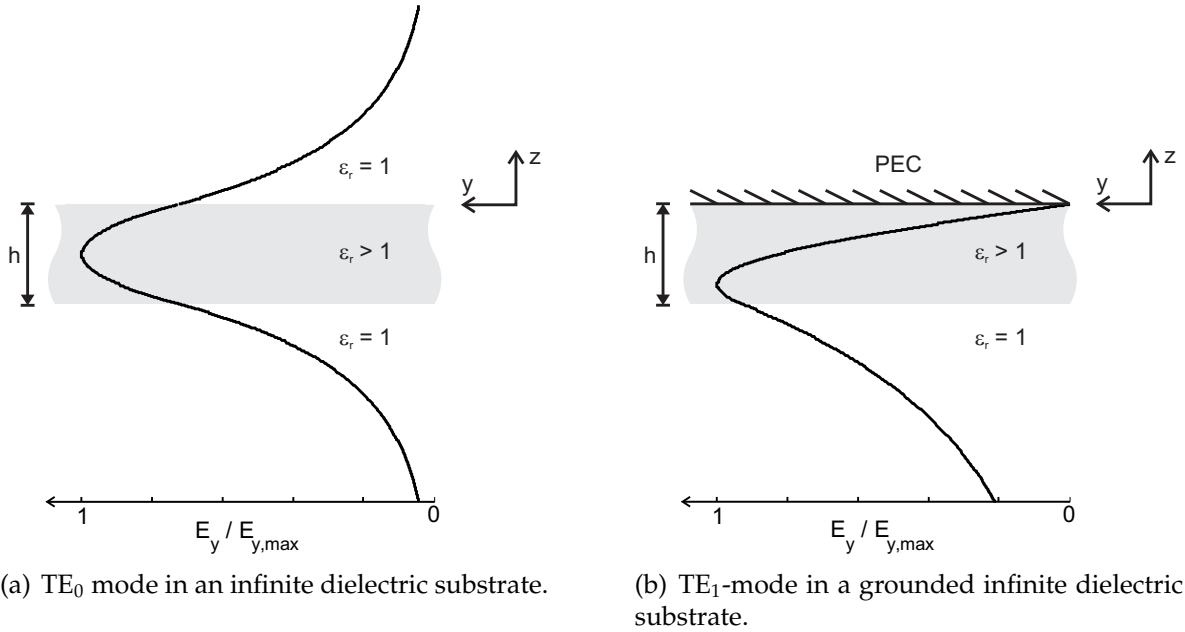


**Figure 2.2.** Examples of electric field distributions inside infinite silicon substrates of thickness  $h$ .

with  $n$  the mode number,  $c_0$  the speed of light in vacuum,  $h$  the thickness, and  $\epsilon_r$  the relative permittivity of the substrate. The modes are then named as  $\text{TM}_n$  and  $\text{TE}_n$ , respectively. A striking characteristic of the  $\text{TM}_0$  and  $\text{TE}_0$  mode is that their cut-off frequency is 0 Hz, i.e., they can always propagate.

Another important configuration that shall be considered here is the case in which the substrate is covered with a metallic plate as shown for the lowest order TE-mode in Figure 2.2(b). Here, the tangential electric field at the top surface has to be zero at all times. The cut-off frequencies of this configuration are given by [15] as

$$f_c = \frac{n c_0}{4h\sqrt{\epsilon_r' - 1}}, \quad (2.34)$$

with  $n = 0, 2, 4, \dots$  for the TM modes and  $n = 1, 3, 5, \dots$  for the TE modes. Hence, the lowest-order TE mode has a non-zero cut-off frequency for this configuration.

## 2.2 Numerical computation

### 2.2.1 The method of moments

According to the explanation in Section 2.1.3, all electromagnetic fields in space that originate from an electric or magnetic current distribution can be obtained from the

vector potentials (2.28) and (2.30). Usually, however, the current densities of a configuration are not known beforehand and have to be determined from the boundary conditions of the problem. For example, in case of a thin metallic wire with  $\mathbf{M}(\mathbf{r}) = \mathbf{0}$ , an electric-field integral-equation (EFIE) can be formulated that links the boundary condition on the wire's surface  $\mathcal{S}$  to the unknown current distribution. Obviously, for a perfectly conducting wire the sum of all tangential field components on the surface has to be zero, i.e.,

$$\mathbf{n} \times [\mathbf{E}_{\text{scat.}}(\mathbf{r}) + \mathbf{E}_{\text{inc.}}(\mathbf{r})] = \mathbf{0} \Big|_{\mathbf{r} \in \mathcal{S}}, \quad (2.35)$$

with  $\mathbf{n}$  the unit normal vector on  $\mathcal{S}$ ,  $\mathbf{E}_{\text{inc.}}(\mathbf{r})$  the incident electric field, and  $\mathbf{E}_{\text{scat.}}(\mathbf{r})$  the (scattered) electric field due to the electric current distribution on the wire, given by (2.29). After substituting (2.29) in (2.35) and some mathematical manipulations, the EFIE may be of the following form:

$$\mathbf{n} \times E_{\text{inc.}}(\mathbf{r}) = \int_{l'} K(\mathbf{r}, \mathbf{r}') I(\mathbf{r}') dl' \Big|_{\mathbf{r} \in \mathcal{S}}, \quad (2.36)$$

where  $K(\mathbf{r}, \mathbf{r}')$  denotes the kernel of the integral. A concrete derivation of a EFIE in the form of (2.36) is given in Section 2.4.1. Here, the focus is first of all laid on the mathematical solution of such an equation.

In (2.36), the unknown current distribution,  $I(\mathbf{r}')$ , is the argument of a linear operator rather than the inhomogeneity of the equation. Hence, the solution cannot be obtained directly. In order to find an approximate solution of (2.36), the method of moments (MoM) can be employed, see, for example, [16]. For this, the unknown current distribution is expanded in a finite series of  $N$  known basis functions  $I_1(\mathbf{r}')$  to  $I_N(\mathbf{r}')$  that approximate the exact current distribution according to

$$I(\mathbf{r}') \approx \sum_{n=1}^N \alpha_n I_n(\mathbf{r}'), \quad n = 1, 2, \dots, N, \quad (2.37)$$

in which the factors  $\alpha_n$  are now the unknowns. Using the approximation (2.37) in the EFIE (2.36) yields

$$\mathbf{n} \times E_{\text{inc.}}(\mathbf{r}) = \sum_{n=1}^N \alpha_n \int_{l'} K(\mathbf{r}, \mathbf{r}') I_n(\mathbf{r}') dl' \Big|_{\mathbf{r} \in \mathcal{S}}. \quad (2.38)$$

In order to solve (2.38), both sides are weighed with a set of  $M$  pre-defined testing functions,  $w_1(\mathbf{r})$  to  $w_M(\mathbf{r})$ , to arrive at a system of  $M$  linear equations of the form

$$\int_l w_m(\mathbf{r}) E_{\text{tangential}}(\mathbf{r}) dl = \sum_{n=1}^N \alpha_n \int_l w_m(\mathbf{r}) \int_{l'} K(\mathbf{r}, \mathbf{r}') I_n(\mathbf{r}') dl' dl \Big|_{\mathbf{r} \in \mathcal{S}}, \quad (2.39)$$

$$V_m = \sum_{n=1}^N \alpha_n Z_{m,n}, \quad m = 1, 2, \dots, M, \quad (2.40)$$

$$[V] = [Z] [\alpha], \quad (2.41)$$

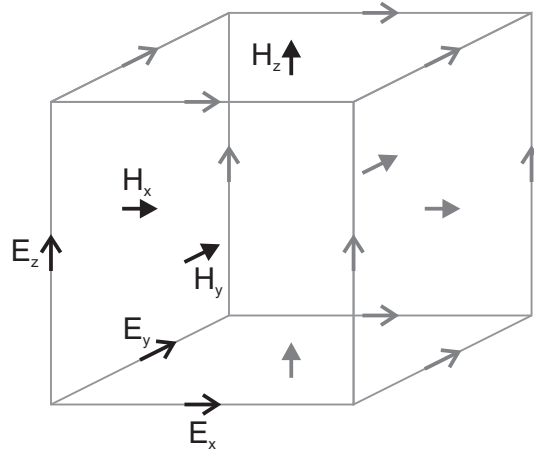


**Figure 2.3.** Sketch of a Yee-cell with its electromagnetic field arrangement.

which can be solved for the coefficients  $[\alpha]$ , if the MoM-matrix  $[Z]$  is nonsingular and, thus, invertible. The approximate solution for the electric current density is then given by (2.37), from which the electromagnetic fields can be calculated.

### 2.2.2 Finite-difference time-domain

An alternative to the MoM for obtaining the electromagnetic field distribution is the finite-difference time-domain (FDTD) method. In this method, the Maxwell Equations (2.1) to (2.4) are solved directly in the time-domain, with all time derivatives replaced by central differences, i.e.,

$$\frac{\partial \mathcal{F}(x, y, z, t)}{\partial t} \rightarrow \frac{\Delta \mathcal{F}(x, y, z, t)}{\Delta t} = \frac{\mathcal{F}(x, y, z, t + \frac{\Delta t}{2}) - \mathcal{F}(x, y, z, t - \frac{\Delta t}{2})}{\Delta t}, \quad (2.42)$$

with  $\mathcal{F}(x, y, z, t)$  an arbitrary time-dependent field quantity. Similarly, the spatial derivatives are also replaced by central differences according to

$$\frac{\partial \mathcal{F}(x, y, z, t)}{\partial x} \rightarrow \frac{\Delta \mathcal{F}(x, y, z, t)}{\Delta x} = \frac{\mathcal{F}(x + \frac{\Delta x}{2}, y, z, t) - \mathcal{F}(x - \frac{\Delta x}{2}, y, z, t)}{\Delta x}, \quad (2.43)$$

$$\frac{\partial \mathcal{F}(x, y, z, t)}{\partial y} \rightarrow \frac{\Delta \mathcal{F}(x, y, z, t)}{\Delta y} = \frac{\mathcal{F}(x, y + \frac{\Delta y}{2}, z, t) - \mathcal{F}(x, y - \frac{\Delta y}{2}, z, t)}{\Delta y}, \quad (2.44)$$

$$\frac{\partial \mathcal{F}(x, y, z, t)}{\partial z} \rightarrow \frac{\Delta \mathcal{F}(x, y, z, t)}{\Delta z} = \frac{\mathcal{F}(x, y, z + \frac{\Delta z}{2}, t) - \mathcal{F}(x, y, z - \frac{\Delta z}{2}, t)}{\Delta z}. \quad (2.45)$$

For this, the entire computation domain is subdivided into rectangular cells, known as Yee-cells. An example of such a cell is shown in Figure 2.3. The interaction between all field components is then determined for discrete time steps and involves



only neighboring nodes. Therefore, this method is also referred to as a local method, whereas the MoM is referred to as a global method since it directly takes into account interactions between all segments/cells. Another important difference between the two methods is that for FDTD an absorbing boundary condition is required at the boundary of the calculation domain to mimic radiation into free space. On the contrary, radiation is inherently included in the MoM approach.

From this brief description, the FDTD method may appear very straightforward. However, there are many criteria, for example, with respect to computational stability, that have to be met for a successful implementation. Therefore, for further reading about this method it shall be referred to, for example, [17].

A commercially available EM solver that uses the FDTD method is Empire XCell from IMST GmbH, see [18]. Most of the simulation results that are presented in this thesis were obtained with this program.

## 2.3 Antenna parameters

### 2.3.1 Field regions

The space around an antenna can be subdivided into three regions, see [14]. The direct vicinity of the antenna, called the reactive near-field region, is electromagnetically dominated by the reactive fields of the antenna. This region exists until approximately  $0.63\sqrt{D^3/\lambda_0}$  from the antenna surface, where  $\lambda_0$  is the considered wavelength and  $D$  is the largest dimension of the antenna. The region between this boundary and up to a distance of approximately  $2D^2/\lambda_0$  is called the radiating near-field or Fresnel region. Here, the radiating fields predominate, but the angular field distribution depends on the distance from the antenna. As stated in [14], this region may not exist for antennas whose largest dimension  $D$  is not large as compared to the wavelength. The region beyond the  $2D^2/\lambda_0$ -boundary is called the far-field or Fraunhofer region at which the angular field distribution is essentially independent of the distance from the antenna.

### 2.3.2 Input impedance and radiation efficiency

From a circuit point of view, an antenna can be described, just as any other load, by means of an impedance<sup>3</sup>

$$Z_{\text{ant}}(f) = R_{\text{ant}}(f) + jX_{\text{ant}}(f), \quad (2.46)$$

---

<sup>3</sup>Note, however, that the following treatment is only valid for a single mode excitation.

or, alternatively, as an admittance

$$Y_{\text{ant}}(f) = G_{\text{ant}}(f) + jB_{\text{ant}}(f), \quad (2.47)$$

where both the imaginary as well as the real part are a function of the frequency  $f$ . From an electromagnetic perspective, the imaginary part of the antenna impedance (or admittance) is determined by the reactive fields of the antenna and, thus, by its near-field. The resistive part of the impedance can be split into two different components,

$$R_{\text{ant}} = R_{\text{rad}} + R_{\text{loss}}, \quad (2.48)$$

with the radiation resistance  $R_{\text{rad}}$  and the loss resistance  $R_{\text{loss}}$  of the antenna. For a loss mechanism in parallel, the admittance model can more easily be used, with

$$G_{\text{ant}} = G_{\text{rad}} + G_{\text{loss}}. \quad (2.49)$$

Here,  $R_{\text{rad}}$  and  $G_{\text{rad}}$  are associated with the power loss due to radiation and can, therefore, be linked to the far-field of the antenna.  $R_{\text{loss}}$  and  $G_{\text{loss}}$  then describe the conductor and dielectric losses inside the antenna.

Since antennas obviously exhibit undesired losses, the radiation efficiency of an antenna, defined as the ratio of the radiated power to the input power, see [12], is a vital performance parameter. From the lumped antenna models (2.46) and (2.47) in combination with (2.48) and (2.49), respectively, the radiation efficiency of the antenna can be calculated according to

$$\eta_{\text{rad}} = \frac{P_{\text{rad}}}{P_{\text{in}}} = \begin{cases} \frac{R_{\text{rad}}}{R_{\text{rad}} + R_{\text{loss}}}, & \text{or} \\ \frac{G_{\text{rad}}}{G_{\text{rad}} + G_{\text{loss}}}, & \text{respectively.} \end{cases} \quad (2.50)$$

Note that Equations (2.50) exclude losses due to a mismatch between the source, for example an amplifier, and the antenna. Therefore, the radiation efficiency is a circuit independent parameter, which makes it an ideal figure of merit for the comparison of antenna concepts in different technologies and with different input impedance specifications. Hence, it plays an important role in the antenna concept chapters 4 to 6.

### 2.3.3 Gain, polarization, and radiation pattern

In most cases, a communication antenna is used to bridge larger distances. Therefore, the radiation properties of an antenna as seen from its far-field are of major importance. For example, it is crucial to know the directional properties of an antenna, like

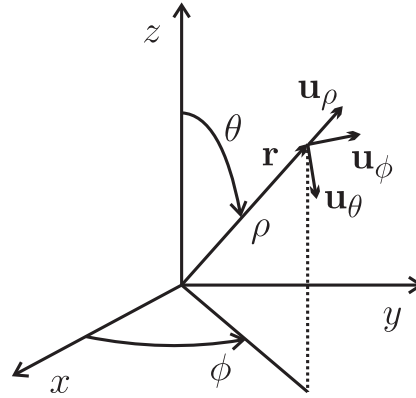


**Figure 2.4.** Definition of spherical coordinates.

the amount of power radiated into each direction, i.e., with respect to  $\theta$  and  $\phi$  of a spherical coordinate system as shown in Figure 2.4. For this, an isotropic radiator is considered as starting point here. Such a (hypothetical) antenna radiates the same amount of power in all directions. Thus, one can determine its radiation intensity  $U$ , defined as the radiated power per unit solid angle<sup>4</sup>, simply by

$$U_0 = \frac{P_{\text{rad}}}{4\pi}. \quad (2.51)$$

In the general case, however, the radiation intensity of an antenna is a function of direction, i.e.,  $U = f(\theta, \phi)$ , for which the following relation always holds:

$$\int_0^{2\pi} \int_0^\pi U(\theta, \phi) \sin(\theta) d\theta d\phi = P_{\text{rad}}. \quad (2.52)$$

Equation (2.52) simply states that the integration of the radiation intensity over all directions is equal to the total radiated power. Usually,  $U(\theta, \phi)$  of a considered antenna is described with respect to the isotropic radiator, i.e.,

$$D(\theta, \phi) = \frac{U(\theta, \phi)}{U_0} = \frac{4\pi U(\theta, \phi)}{P_{\text{rad}}}, \quad (2.53)$$

where  $D$  is known as the directivity of the antenna. This relation, however, excludes any antenna losses since only the radiated power is considered. In practice, one is usually more interested in the amount of power that is radiated in a certain direction with respect to the total input power. For this, the radiation efficiency, defined in (2.50), can be used to obtain the gain of the antenna,

$$G(\theta, \phi) = \eta_{\text{rad}} \frac{U(\theta, \phi)}{U_0} = \eta_{\text{rad}} D(\theta, \phi), \quad (2.54)$$

<sup>4</sup>Note that, in particular, the radiation intensity is independent of the distance from the antenna.

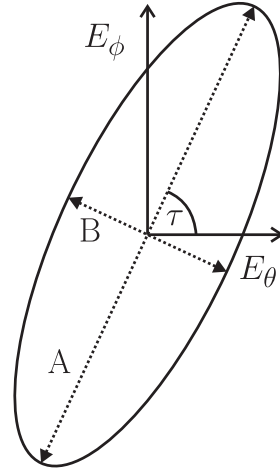


**Figure 2.5.** General polarization ellipse.

where it is assumed that the isotropic radiator does not exhibit any losses.

Another important far-field parameter is the polarization of an antenna, which is defined as the polarization of its radiated wave along its direction of propagation. Here, the polarization of an electromagnetic wave is further defined as the time-dependent direction and relative magnitude of the electric-field vector. Since the polarization of the radiated wave might vary with the observation direction, the polarization is usually taken to be in the direction of maximum gain, see [14]. Note, however, that although antennas are designed to radiate in a specified polarization, they always also radiate a certain amount of power in the orthogonal polarization. The component of the field that is radiated in the intended polarization is commonly referred to as co-polarization component and the orthogonal component is then referred to as cross-polarization component. A fundamental article on the possible different definitions of co- and cross-polarization was published by A.C. Ludwig in 1973, see [19]. In the outline of this thesis, however, both components coincide with either the  $\theta$  or  $\phi$  direction of the observation coordinate system, respectively. They are denoted accordingly, such that no further elaboration on this topic shall be undertaken here.

Moreover, in the far-field of an antenna, its radiated electromagnetic wave can be split into two orthogonal components, which superimpose to a general polarization ellipse as shown in Figure 2.5. For such an ellipse, the axial ratio (AR),

$$\text{AR} = \frac{A}{B} = \frac{|E_{\theta}\mathbf{u}_{\theta} + E_{\phi}\mathbf{u}_{\phi}|_{\max}}{|E_{\theta}\mathbf{u}_{\theta} + E_{\phi}\mathbf{u}_{\phi}|_{\min}}, \quad (2.55)$$

can be defined, which indicates whether the wave is mainly linearly, elliptically, or circularly polarized. For a perfectly linearly polarized antenna, for example, the axial ratio (2.55) is infinite. For a perfectly circularly polarized antenna, the axial ratio is

AR = 1. This case is of particular importance for the array considerations in Chapter 7.

Finally, the radiation characteristics of an antenna as a function of space coordinates are often represented in a plot, known as radiation pattern. If the gain of an antenna is shown, one also denotes it as power pattern since it describes the radiated power per unit solid angle. A power pattern could, however, also show the directivity or radiation intensity and is, therefore, not uniquely defined. Therefore, throughout this thesis the term gain pattern is used to indicate that the gain of the antenna is shown. Furthermore, radiation patterns are often normalized with respect to its maximum value, which is then denoted as normalized radiation pattern. In this thesis, these patterns are accordingly referred to as normalized gain patterns. Since the gain can be independently determined for co-polarization and cross-polarization components, the radiation patterns might show the results for one of the two polarizations only. If nothing is mentioned, however, the gain pattern is taken to be the absolute gain of the antenna in that direction. Furthermore, for linearly-polarized antennas it is common practice to limit the patterns to their two principle planes, i.e., E-plane and H-plane. In general, the E-plane is defined as the plane containing the electric field vector and the direction of maximum radiation. The H-plane is defined accordingly for the magnetic field vector and, since in the far-field the electric and magnetic field vectors are orthogonal to each other, the H-plane is orthogonal to the E-plane.

### 2.3.4 Friis transmission equation

Figure 2.6 shows a sketch of a general wireless communication scenario between a transmitter and a receiver. As known from Section 2.3.3, the transmitting antenna, in general, radiates power into all directions. Hence, not all the radiated power can be captured by the receiving antenna. The power density at the location of the receiving antenna can be calculated by

$$W_0 = \frac{P_{\text{in}} G_t(\theta_t, \phi_t)}{4\pi R^2}, \quad (2.56)$$

with  $G_t$  the gain of the transmitting antenna in the direction of the receiving antenna, specified by  $\theta_t$  and  $\phi_t$ , and with  $R$  the distance between both antennas. The receiving antenna captures the portion

$$P_r = A_r(\theta_r, \phi_r) W_0, \quad (2.57)$$

of the radiated power. In (2.57)  $A_r(\theta_r, \phi_r)$  denotes the effective aperture of the receiving antenna in the direction of the transmitting antenna, which is related to its gain

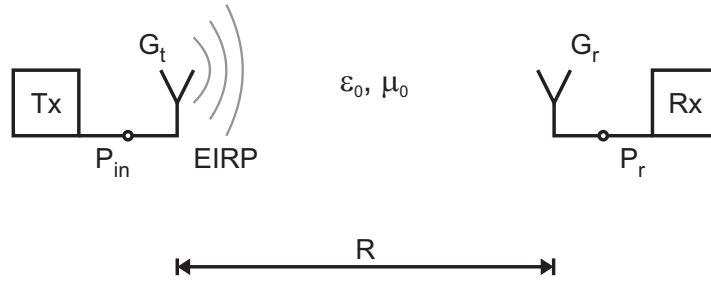


**Figure 2.6.** Free space wireless link between a transmitter (left) and a receiver (right) located at a distance  $R$ .

according to<sup>5</sup>

$$A_r(\theta_r, \phi_r) = G_r(\theta_r, \phi_r) \frac{\lambda_0^2}{4\pi}. \quad (2.58)$$

Using this relation and substituting (2.57) into (2.56) yields

$$\frac{P_r}{P_{in}} = \left( \frac{\lambda_0}{4\pi R} \right)^2 G_t(\theta_t, \phi_t) G_r(\theta_r, \phi_r), \quad (2.59)$$

which is known as the Friis transmission equation. The term  $\left( \frac{\lambda_0}{4\pi R} \right)^2$  in (2.59) is called the free-space path loss since it takes into account the losses in the wireless link due to the spherical spreading of the radiated power.

## 2.4 Thin-wire circular loop antenna model

In this final section of Chapter 2, the theoretical foundations from the preceding sections are put into practice by a derivation of a computationally efficient model for a circular loop antenna as shown in Figure 2.7. The modeling approach of the hybrid integrated mm-wave antenna from Chapter 6 is then based on this basic model.

In the first instance, the antenna is excited by a voltage generator that produces the voltage  $V_{in}$  at a frequency  $f$  across a small gap, see Figure 2.7. In order to determine the resulting current distribution on the wire by a MoM approach, an integral equation is needed as explained in Section 2.2.1. The derivation of the used EFIE for this antenna is, therefore, presented as the first step in Section 2.4.1. The MoM solution of this equation is then given in Section 2.4.2 followed by a description of an enhanced generator model in Section 2.4.3, which is used to reduce numerical instabilities and

<sup>5</sup>The derivation is presented in, e.g., [14].

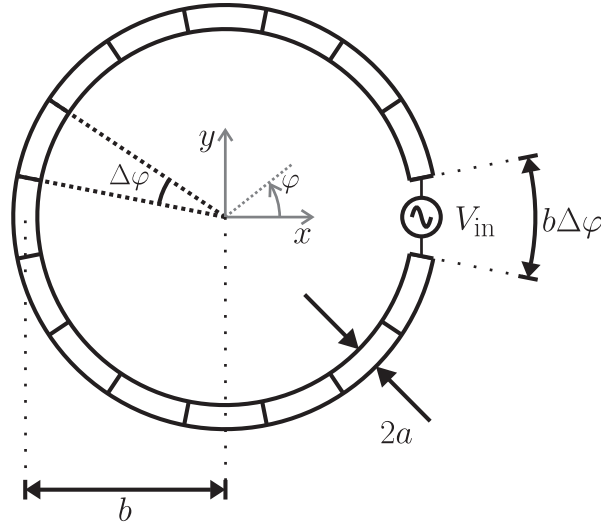


**Figure 2.7.** Definitions of full-loop antenna parameters according to [20].

achieve a convergent solution. Finally, a comparison of the antenna parameters obtained with this MoM solution and the results from the commercial FDTD solver Empire XCcel is given in Section 2.4.4 in order to prove the validity of the model.

### 2.4.1 Derivation of the integral equation

In order to arrive at an electromagnetic model for the thin-wire circular loop antenna, the electric current density on the wire has to be determined. From this, all generated electromagnetic fields can be computed with Equations (2.20) and (2.29), using the magnetic vector potential given by (2.28). First, however, an equation is needed that relates the current distribution on the wire to the impressed fields of the connected voltage generator. This equation is given by (2.29) in conjunction with the boundary condition that the tangential electric field has to be zero on the wire's surface  $\mathcal{S}$ , i.e.,

$$\mathbf{n} \times [\mathbf{E}_{\text{scat.}}(\mathbf{r}) + \mathbf{E}_{\text{inc.}}(\mathbf{r})] = \mathbf{0} \Big|_{\mathbf{r} \in \mathcal{S}}, \quad (2.60)$$

with  $\mathbf{n}$  the unit normal vector on the wire's surface,  $\mathbf{E}_{\text{inc.}}(\mathbf{r})$  the electric field produced by the voltage generator, and  $\mathbf{E}_{\text{scat.}}(\mathbf{r})$  the (scattered) electric field given by (2.29) due to the electric current distribution on the wire. Since the wire is electrically thin, i.e.,  $a \ll \lambda$ , it is sufficient to consider the tangential electric field in  $\varphi$ -direction only, such that (2.60) can be written as

$$-\mathbf{E}_{\text{inc.}}(\mathbf{r}) \cdot \mathbf{u}_\varphi = \frac{1}{j\omega\epsilon} [k^2 \mathbf{A}(\mathbf{r}) + \nabla \nabla \cdot \mathbf{A}(\mathbf{r})] \cdot \mathbf{u}_\varphi \Big|_{\mathbf{r} \in \mathcal{S}}. \quad (2.61)$$

Furthermore, due to the thin wire assumption, the current can be considered to flow on the central axis of the wire only. If the observation points remain on its surface,

the distance between source and observation point in cylindrical coordinates,

$$R(\mathbf{r} - \mathbf{r}') = \sqrt{r^2 + r'^2 - 2rr' \cos(\varphi - \varphi') + (z - z')^2}, \quad (2.62)$$

can then be approximated by

$$R(\mathbf{r} - \mathbf{r}') \approx R(\varphi - \varphi') = \sqrt{4b^2 \sin^2 \left( \frac{\varphi - \varphi'}{2} \right) + a^2}, \quad (2.63)$$

which is known as the thin-wire approximation. The inherent advantage of (2.63) is the fact that the singularity of the kernel of Equation (2.28) is avoided here. This simplification, however, comes at the price of obtaining an approximate solution of the integral only.

The final form of the EFIE for the electric current distribution can now be formulated by inserting the magnetic vector potential (2.28) together with the approximation (2.63) in Equation (2.61). The  $\varphi$ -component of the magnetic vector potential on the right-hand-side is then given by

$$\mathbf{A}(\mathbf{r}) \cdot \mathbf{u}_\varphi = \int_{\varphi'} I(\varphi') \mathbf{u}_{\varphi'} \cdot \mathbf{u}_\varphi \frac{e^{-jkR(\mathbf{r}-\mathbf{r}')}}{4\pi R(\mathbf{r}-\mathbf{r}')} b d\varphi'. \quad (2.64)$$

Due to the assumed confinement of the current to the center of the wire, the volume integral of (2.28) is reduced to a line integral here and the current density is replaced with the current  $I(\varphi')$ . Using the representation of  $\mathbf{u}_{\varphi'}$  in observation coordinates, i.e.,

$$\mathbf{u}_{\varphi'} = \mathbf{u}_\varphi \cos(\varphi - \varphi') + \mathbf{u}_r \sin(\varphi - \varphi'), \quad (2.65)$$

(2.64) can be re-written to

$$\mathbf{A}(\mathbf{r}) \cdot \mathbf{u}_\varphi = \int_{\varphi'} I(\varphi') \cos(\varphi - \varphi') \frac{e^{-jkR(\mathbf{r}-\mathbf{r}')}}{4\pi R(\mathbf{r}-\mathbf{r}')} b d\varphi'. \quad (2.66)$$

The second term in (2.61) can be developed in two steps. First, the divergence of the vector potential can be expressed as

$$\nabla \cdot \mathbf{A}(\mathbf{r}) = \int_{\varphi'} I(\varphi') \nabla \cdot \left[ \mathbf{u}_{\varphi'} \frac{e^{-jkR(\mathbf{r}-\mathbf{r}')}}{4\pi R(\mathbf{r}-\mathbf{r}')} \right] b d\varphi', \quad (2.67)$$

$$= \int_{\varphi'} I(\varphi') (-\nabla') \cdot \left[ \mathbf{u}_{\varphi'} \frac{e^{-jkR(\mathbf{r}-\mathbf{r}')}}{4\pi R(\mathbf{r}-\mathbf{r}')} \right] b d\varphi', \quad (2.68)$$

$$= \int_{\varphi'} I(\varphi') \left( -\frac{1}{b} \right) \frac{\partial}{\partial \varphi'} \frac{e^{-jkR(\mathbf{r}-\mathbf{r}')}}{4\pi R(\mathbf{r}-\mathbf{r}')} b d\varphi'. \quad (2.69)$$

Here, the fact that the argument of the divergence is a function of  $(\mathbf{r} - \mathbf{r}')$  is used to re-write the divergence in terms of the source coordinates. Using the thin-wire



approximation, however, the argument is actually a function of  $(\varphi - \varphi')$  only and, hence, (2.69) can be written as

$$\nabla \cdot \mathbf{A}(\mathbf{r}) = \int_{\varphi'} I(\varphi') \frac{1}{b} \frac{\partial}{\partial \varphi} \frac{e^{-jkR(\varphi - \varphi')}}{4\pi R(\varphi - \varphi')} b d\varphi', \quad (2.70)$$

where the relation  $\partial/\partial\varphi' = -\partial/\partial\varphi$  was used. As second step, the  $\varphi$ -component of the gradient of (2.70) has to be determined. The solution is straightforward and is given by

$$(\nabla \nabla \cdot \mathbf{A}(\mathbf{r})) \cdot \mathbf{u}_\varphi = \int_{\varphi'} I(\varphi') \frac{1}{b^2} \frac{\partial^2}{\partial \varphi^2} \frac{e^{-jkR(\varphi - \varphi')}}{4\pi R(\varphi - \varphi')} b d\varphi'. \quad (2.71)$$

Using (2.66) and (2.71) in (2.61), the EFIE is given by

$$-\mathbf{E}_{\text{inc.}}(\varphi) \cdot \mathbf{u}_\varphi = \frac{\eta}{jk} \int_{\varphi'} \left[ k^2 \cos(\varphi - \varphi') + \frac{1}{b^2} \frac{\partial^2}{\partial \varphi^2} \right] I(\varphi') \frac{e^{-jkR(\varphi - \varphi')}}{4\pi R(\varphi - \varphi')} b d\varphi', \quad (2.72)$$

with the free space impedance of the medium  $\eta = \sqrt{\mu/\epsilon}$ . Finally, all lengths parameters may be normalized with respect to the loop-radius<sup>6</sup>, i.e.,

$$b \rightarrow 1, \quad (2.73)$$

$$a \rightarrow a/b, \quad (2.74)$$

$$k \rightarrow kb, \quad (2.75)$$

resulting in the normalized EFIE

$$b \mathbf{E}_{\text{inc.}}(\varphi) \cdot \mathbf{u}_\varphi = \frac{j\eta}{4\pi} \int_{\varphi'} \left[ kb \cos(\varphi - \varphi') + \frac{1}{kb} \frac{\partial^2}{\partial \varphi^2} \right] \frac{e^{-jkbR_b(\varphi - \varphi')}}{R_b(\varphi - \varphi')} I(\varphi') d\varphi', \quad (2.76)$$

with the normalized  $\varphi$ -component of the incident electric field from the generator at the observation point on the left-hand side and

$$R_b(\varphi - \varphi') = \frac{R(\varphi - \varphi')}{b} = \sqrt{4 \sin^2 \left( \frac{\varphi - \varphi'}{2} \right) + \left( \frac{a}{b} \right)^2}, \quad (2.77)$$

which is consistent with the EFIE used in [20]. With (2.76) an equation is obtained that links the unknown current on the wire to the known boundary conditions. Nevertheless, the drawback of this equation is that the unknown parameter is the argument of a linear operator and cannot be determined directly. As outlined in Section 2.2.1, however, this kind of equation can be solved with the method of moments. The exact procedure is explained in the next section.

---

<sup>6</sup>Note that, mathematically, this operation results in a multiplication with the factor  $b$  on both sides of (2.72).

### 2.4.2 Moment method solution for the electric current distribution

For the numerical evaluation of the EFIE (2.76) the method of moments can be used, see Section 2.2.1. For this, the wire is subdivided into  $N$  equally sized segments on which the pulse basis functions,

$$I_n(\varphi') = \begin{cases} 1, & \text{for } (n-1)\Delta\varphi < \varphi' < n\Delta\varphi, \\ 0, & \text{otherwise,} \end{cases} \quad (2.78)$$

with  $n = 1, 2, \dots, N$  and  $\Delta\varphi = 2\pi/N$ , are defined. The number of testing functions is chosen to be the same as the number of basis functions, i.e.,  $M = N$ . Here, the testing functions are dirac-delta functions, i.e.,

$$w_m(\varphi) = \frac{1}{b}\delta(\varphi - \varphi_m), \quad (2.79)$$

with  $m = 1, 2, \dots, M$  and  $\varphi_m = \frac{(2m-1)\Delta\varphi}{2}$ . The choice of pulse basis functions in combination with dirac testing functions is also known as point-matching method. Applying the MoM with above basis and testing functions to Equation (2.76) yields an equation similar to (2.39), i.e.,

$$b \int_{\varphi} \delta(\varphi - \varphi_m) \mathbf{E}_{\text{inc.}}(\varphi) \cdot \mathbf{u}_{\varphi} d\varphi = \frac{j\eta}{4\pi} \sum_{n=1}^N \alpha_n \int_{\varphi} \delta(\varphi - \varphi_m) \int_{(n-1)\Delta\varphi}^{n\Delta\varphi} K(\varphi - \varphi') d\varphi' d\varphi, \quad (2.80)$$

which can be reduced to

$$\bar{V}_m = \frac{j\eta}{4\pi} \sum_{n=1}^N \alpha_n \int_{(n-1)\Delta\varphi}^{n\Delta\varphi} K(\varphi_m - \varphi') d\varphi', \quad m = 1, 2, \dots, M, \quad (2.81)$$

with  $\bar{V}_m = b E_{\varphi, \text{inc.}}(\varphi_m)$  the normalized tangential component of the incident electric field at  $\varphi = \varphi_m$  and the kernel

$$K(\varphi_m - \varphi') = \left[ kb \cos(\varphi - \varphi') + \frac{1}{kb} \frac{\partial^2}{\partial \varphi^2} \right] \frac{e^{-jkbR_b(\varphi - \varphi')}}{R_b(\varphi - \varphi')} \Big|_{\varphi = \varphi_m}. \quad (2.82)$$

With this, the first line of the MoM-matrix,  $[Z]$ , is now given by

$$Z_{1,n} = \frac{j\eta}{4\pi} \int_{(n-1)\Delta\varphi}^{n\Delta\varphi} K(\varphi_1 - \varphi') d\varphi', \quad n = 1, \dots, N. \quad (2.83)$$

Equation (2.83) represents the tangential electric field in the center of the first loop segment for an uniform 1 A electric current on segment  $n$ . Due to the rotational symmetry of the circular loop, the same tangential electric field will be achieved on a different segment at  $\varphi_m = \varphi_1 + m\Delta\varphi$ , if a 1 A current is present on an accordingly

$m\Delta\varphi$ -shifted location. Therefore, the full MoM-matrix is of Töplitz form and, thus, already given by

$$[Z] = \begin{bmatrix} Z_{1,1} & Z_{1,2} & \cdots & Z_{1,N} \\ Z_{1,2} & Z_{1,1} & \cdots & Z_{1,N-1} \\ \vdots & \vdots & \ddots & \vdots \\ Z_{1,N} & Z_{1,N-1} & \cdots & Z_{1,1} \end{bmatrix}. \quad (2.84)$$

Finally, the amplitudes of the approximate current distribution on the loop can be calculated by

$$[\alpha] = [Z]^{-1}[\bar{V}], \quad (2.85)$$

with the elements  $\bar{V}_m$  of  $[\bar{V}]$  given by

$$\bar{V}_m = \begin{cases} V_{in}/\Delta\varphi & , m = 1 \\ 0 & , m \neq 1 \end{cases} \quad (2.86)$$

for the chosen delta-gap voltage generator as source model.

### 2.4.3 Magnetostatic frill source

With the results from Sections 2.4.1 and 2.4.2 the antenna parameters as described in Section 2.3 could now be calculated. There is, however, a difficulty with the numerical evaluation of the EFIE in combination with the used source model (2.86), i.e., the delta gap voltage generator, which is outlined in this section.

The thin-wire approximation eliminates the source-point singularity of the EFIE by smoothening the right-hand-side of (2.76). In case of a delta-gap voltage generator, however, the left hand side is a dirac-delta function at the source point and is, thus, not smooth at all, which results in numerical instabilities. This problem is well-known and a research subject on its own, see, e.g., [21, 22]. In the outline of this thesis, the problem is largely suppressed by the use of a different feed model that exhibits a similar smoothness as the right-hand-side of (2.76). For this, the magnetostatic frill source from [11] is used<sup>7</sup>, which is a simplified model of a coaxial antenna feed. The feed-model together with its local coordinate system is shown in Figure 2.8 and consists of a single filamentary magnetic current  $\mathbf{M}(\mathbf{r}) = M_0 \mathbf{u}_{\tilde{\varphi}} = -V_{in} \mathbf{u}_{\tilde{\varphi}}$  that encircles the wire at a radius  $\tilde{r}_1$ . The derivation of the electric vector potential for

---

<sup>7</sup>During the implementation of this source model, it turned out that there seems to be a misprint in the cited reference. Therefore, the complete derivation of the used source model is provided in Appendix A.

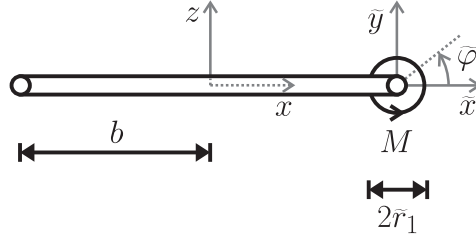


**Figure 2.8.** Topview of the loop antenna with magnetostatic frill source.

such magnetic-current loop in its local coordinates is provided in Appendix A, Section A.1. The result reads

$$F_{\tilde{\varphi}}(\tilde{\mathbf{r}}) = \frac{M_0 R_{m,1}}{2\pi\tilde{r}} \left\{ \left(1 - \frac{\beta_1^2}{2}\right) \mathcal{K}(\beta_1) - \mathcal{E}(\beta_1) \right\}, \quad (2.87)$$

in which the subscript  $\tilde{\varphi}$  denotes the  $\tilde{\varphi}$ -component,

$$R_{m,1} = \sqrt{\tilde{z}^2 + (\tilde{r}_1 + \tilde{r})^2}, \quad (2.88)$$

$$\beta_1 = \frac{\sqrt{4\tilde{r}_1\tilde{r}}}{R_{m,1}}, \quad (2.89)$$

and  $\mathcal{K}(\beta_1)$  and  $\mathcal{E}(\beta_1)$  are the complete elliptical integrals of the first and second kind, respectively. The generated electric field can be calculated by using (2.87) in (2.31). The detailed procedure is shown in Appendix A, Section A.2. The resulting individual field components with respect to its local coordinate system are

$$\mathbf{E}_{\text{inc.}}(\tilde{\mathbf{r}}) \cdot \mathbf{u}_{\tilde{\varphi}} = 0, \quad (2.90)$$

$$\mathbf{E}_{\text{inc.}}(\tilde{\mathbf{r}}) \cdot \mathbf{u}_{\tilde{r}} = \frac{M_0 \tilde{z}}{2\pi\tilde{r}R_{m,1}} \left[ \mathcal{K}(\beta_1) - \frac{\tilde{r}_1^2 + \tilde{r}^2 + \tilde{z}^2}{(\tilde{r}_1 - \tilde{r})^2 + \tilde{z}^2} \mathcal{E}(\beta_1) \right], \quad (2.91)$$

$$\mathbf{E}_{\text{inc.}}(\tilde{\mathbf{r}}) \cdot \mathbf{u}_{\tilde{z}} = \frac{-M_0}{2\pi R_{m,1}} \left[ \mathcal{K}(\beta_1) + \frac{\tilde{r}_1^2 - \tilde{r}^2 - \tilde{z}^2}{(\tilde{r}_1 - \tilde{r})^2 + \tilde{z}^2} \mathcal{E}(\beta_1) \right]. \quad (2.92)$$

Note that the electric field strength is independent of  $\tilde{\varphi}$ . Furthermore, following the recommendation in [11], the radius  $\tilde{r}_1 = \sqrt{3}a$  is chosen here.

In order to fulfill the boundary conditions, the tangential electric field produced by the magnetostatic frill source along the wire has to be determined for the left-hand-side of the integral equation (2.76). For this, Equations (2.91) and (2.92) have to be expressed in terms of the global coordinate system from Figure 2.7, using the relations

$$\tilde{r} = \sqrt{(1 - \cos(\varphi))^2 + \left(\frac{a}{b}\right)^2}, \quad (2.93)$$

$$\tilde{z} = \sin(\varphi). \quad (2.94)$$

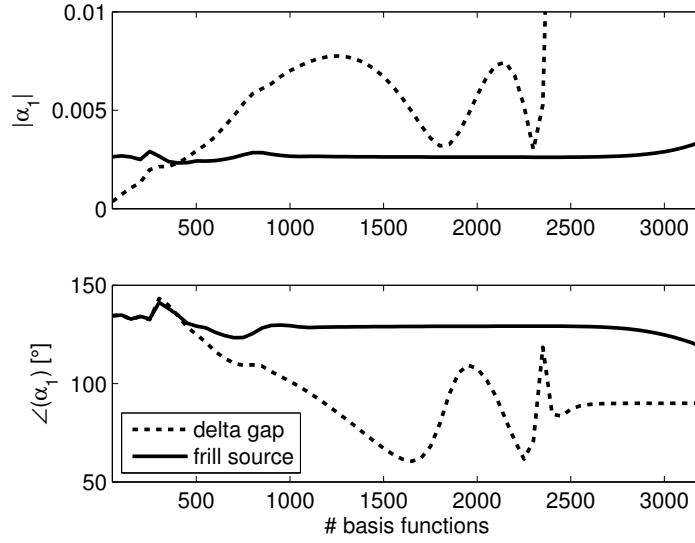


**Figure 2.9.** Computed  $\alpha_1$  at 60 GHz versus the number of used basis functions for  $V_{\text{in}} = 1$  V ( $a = 12.5$   $\mu\text{m}$ ,  $b = 950$   $\mu\text{m}$ ).

Here, the normalization with respect to the loop-radius  $b$ , as used in [20], is already included. The tangential field component can now be determined by computing the inner product of the total electric field strength, given by (2.90) to (2.92), and the tangential unit vector along the wire, which is given by

$$\mathbf{u}_\varphi(\mathbf{r}) = \mathbf{u}_{\tilde{r}} \sin(\varphi) + \mathbf{u}_{\tilde{z}} \cos(\varphi) \Big|_{\tilde{\varphi}=\pi} . \quad (2.95)$$

Therefore, the tangential electric field component is given by

$$\mathbf{E}_{\text{inc.}}(\mathbf{r}) \cdot \mathbf{u}_\varphi(\mathbf{r}) = \mathbf{E}_{\text{inc.}}(\mathbf{r}) \cdot \mathbf{u}_{\tilde{r}} \sin(\varphi) + \mathbf{E}_{\text{inc.}}(\mathbf{r}) \cdot \mathbf{u}_{\tilde{z}} \cos(\varphi) \Big|_{\tilde{\varphi}=\pi} , \quad (2.96)$$

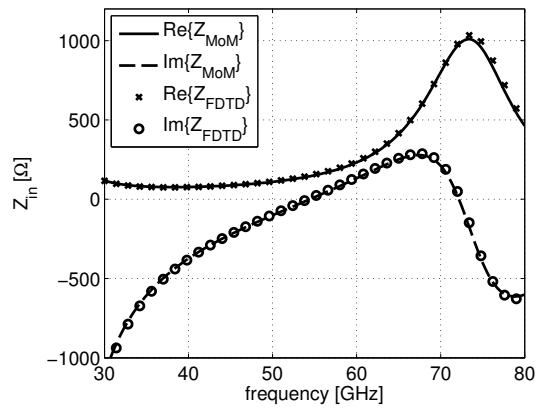
which can now be used in (2.76). Note that, in general, all components of the vector  $[\bar{V}]$  in (2.86) are now non-zero with smoothly decreasing magnitude for an increasing distance away from the source.

Finally, the numerical stability of the solution and the optimal number of basis functions shall be investigated. For this, the electric current amplitude  $\alpha_1$  on the feed segment is computed at 60 GHz for different number of loop-segments/basis-functions and for  $a = 12.5$   $\mu\text{m}$  and  $b = 950$   $\mu\text{m}$ . The result is shown in Figure 2.9. The value  $\alpha_1$  is chosen here since it is of particular importance for the calculation of essential antenna parameters, like the input impedance. As shown in Figure 2.9,  $\alpha_1$  converges to an amplitude of approximately  $2.3 \cdot 10^{-3}$  and a phase of  $129^\circ$  at about  $N = 1000$  and remains stable at this value up to  $N = 2700$ . For larger numbers of basis functions the solution becomes unstable again, which is seen to be a result of the thin-wire approximation. Also provided in Figure 2.9 are the values for  $\alpha_1$  when using the

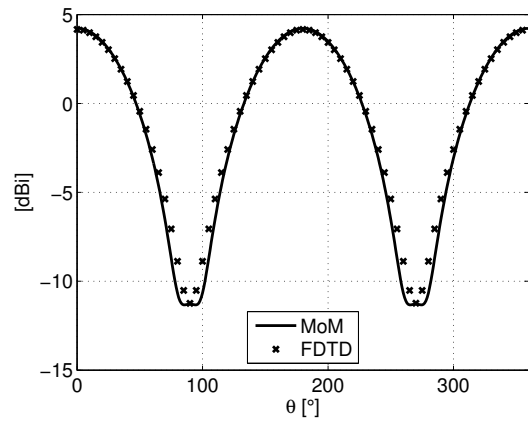
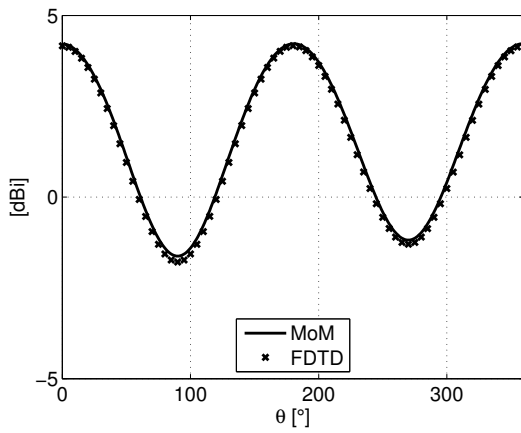
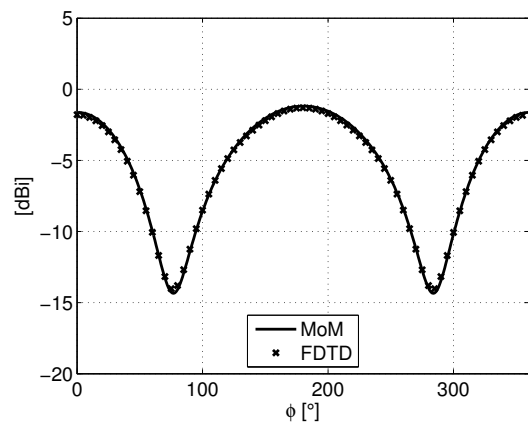
delta-gap voltage generator. From this, it becomes obvious that this source model cannot be used for a reliable prediction of the antenna parameters since it shows no convergence at all.

#### 2.4.4 Comparison with a FDTD solver

In order to prove the validity of the derived antenna model, its solution for a loop radius of  $950\ \mu\text{m}$  and wire thickness of  $25\ \mu\text{m}$  was compared to the solution obtained with a FDTD solver. For this, the MoM model was implemented in Matlab, see [23], and the FDTD solution was obtained with Empire XCcel. Figure 2.10 shows the input impedance and the gain patterns in both principle planes as well as in the loop plane for both models. The gain patterns are plotted in spherical coordinates here, see Figure 2.4. Both computational models agree excellently with respect to each other, although only 501 basis functions were used for the MoM implementation. This value is well below the recommended minimum number of basis functions, see Section 2.4.3. It was found, however, that for a further increase in the amount of basis functions the improvement in the accuracy of the solution is far less significant than the increase in computing time. Hence, 501 basis functions can be finally recommended here as optimal choice for this particular example.



(a) Input impedance

(b) Gain pattern at 60 GHz in E-plane ( $\phi = 90^\circ$ ).(c) Gain pattern at 60 GHz in H-plane ( $\phi = 0^\circ$ ).(d) Gain pattern at 60 GHz in loop-plane ( $\theta = 90^\circ$ ).

**Figure 2.10.** Antenna parameters of a circular loop antenna with  $b = 950 \mu\text{m}$  and  $a = 12.5 \mu\text{m}$  as obtained with the proposed MoM model and a FDTD model, respectively.

# Integrated millimeter-wave antennas: State-of-the-art

---

As a starting point for the integrated mm-wave antenna concepts that were developed in the framework of this thesis, it is meaningful to first give a brief overview of the state-of-the-art. For this, some general requirements of antennas for the 60 GHz band are, firstly, summarized in Section 3.1 since these are common for all concepts. Next, brief overviews of typical state-of-the-art AiP, AoC, and hybrid designs are given in Sections 3.2 to 3.4. The findings of the state-of-the-art overviews then serve as the motivation for the technology choices and antenna concepts that follow in subsequent chapters.

### 3.1 Antenna requirements for 60 GHz communications

It was already pointed out in Chapter 1 that an integrated antenna is preferred at mm-waves in order to keep the interconnect losses as low as possible. Furthermore, since the preferred technology choices for mm-wave front-end ICs are CMOS and BiCMOS with their typical differential amplifier topologies, antennas with a differential feed-structure are favored as well, see [7]. This allows to directly connect the antenna to the amplifier without the need for a balanced-to-unbalanced converter (balun), which would add extra losses to the system.

Furthermore, the antenna should exhibit a high, constant gain at a high radiation efficiency over the entire frequency band, as pointed out in [2]. If this requirement is not met, the overall signal-to-noise ratio (SNR) in the receiver is affected and, as a consequence, the communication distance would be severely compromised and/or the battery lifetime of portable devices unnecessarily shortened. Moreover, since



high gain comes at a cost of a narrow beam-width, the antenna beam should be automatically adjustable in its direction. Therefore, switched-beam or phased arrays are typically suggested, see, for example, [2, 4, 5, 7, 8].

The antenna gain should be high; however, a motivated quantification of the gain requirement is hardly ever stated in the literature. Hence, this issue shall briefly be tackled here based on the Friis transmission equation (2.59), which relates the total received power to the total input power of a radio link in free space. For this, the worst case receiver sensitivity specification from IEEE standard 802.15.3c-2009, see [24], is used as minimum acceptable receiver input power level,  $P_r$ . According to this specification, a power level of at least -46 dBm is the minimum requirement<sup>1</sup>. For the transmitter, the maximum equivalent isotropic radiated power (EIRP), which is the product of transmit power and transmit antenna gain, is in Europe limited to a maximum of 40 dBm, see [3]. Using this value and the worst case receiver sensitivity from above in (2.59), the minimum required receive antenna gain for 60 GHz can be determined to be  $G_r = 2$  dBi for a communication distance of up to  $R = 10$  m. The respective system assumptions for this scenario are summarized as case #1 in Table 3.1. Here, a single transmitter chip like the one published in [25] is assumed that exhibits a maximum output power of  $P_{IC} = 10$  dBm ( $= P_{in}$  in (2.59) for this case). As shown in the table, the resulting transmit antenna gain  $G_t$  has to be 30 dBi in this case in order to achieve the maximum EIRP. Such high gain is difficult to achieve with a single integrated antenna, however, which makes this system approach rather impractical.

Another possibility of achieving a high EIRP is by increasing the transmit power<sup>2</sup>. This could be done, for example, by building an array of antennas whereas every antenna is fed by an individual transmitter chip. By this, the output powers of the ICs are combined "in the air", as described in [4, 7]. Hence, the total transmit power is then as high as  $P_{in} = NP_{IC}$ , with  $N$  the total amount of antenna array elements. Furthermore, this array approach leads to a larger overall antenna gain, with an overall gain increase of approximately the same factor  $N$ . Using this approach and assuming that the single antenna element of the array is a patch antenna, which typically exhibits a gain of  $G_{t,single} = 6$  dBi, and is fed by the same 10 dBm transmitter chip, the total amount of transmit antennas has to be approximately 16, see case #2 in Table 3.1.

In order to reduce the transmit antenna array size, one can use another antenna array of size  $M$  on the receiver side. When choosing  $M = N$  and assuming once again that the single antenna elements exhibit a gain of 6 dBi on both sides, two 6-element

---

<sup>1</sup>This value is stated for a data rate of larger than 3 Gb/s in the Single Carrier Mode with  $\pi/2$  16-QAM modulation.

<sup>2</sup>Note that, besides the EIRP limitation, the maximum output power level might also be limited in some countries and regions.

arrays would easily satisfy the minimum input power requirement for a communication distance of up to  $R = 10$  m, as shown as case #3 in Table 3.1. Note that in this configuration the maximum EIRP does not even have to be fully exploited, such that even larger distances can be reached by this approach.

For the file transfer at a "kiosk in a store" and the wireless interconnect scenario, much shorter communication distances  $R$  are required. For a file transfer application, for example, a maximum distance of 1 m may already be sufficient. For this, a small array could be implemented in the kiosk terminal and a single antenna in the customer's portable device. Using a 4-element patch-antenna array in the kiosk-terminal, the receiver's antenna gain can then be as low as -6 dBi, shown as case #4 in Table 3.1.

Case #5 shows a possible wireless interconnect scenario. Here, only a single antenna is assumed on both sides of the radio link, which is a feasible assumption for a chip-to-chip interconnect, for example. If also for this scenario a 1 m communication distance is assumed, antennas with at least 6 dBi gain are acceptable.

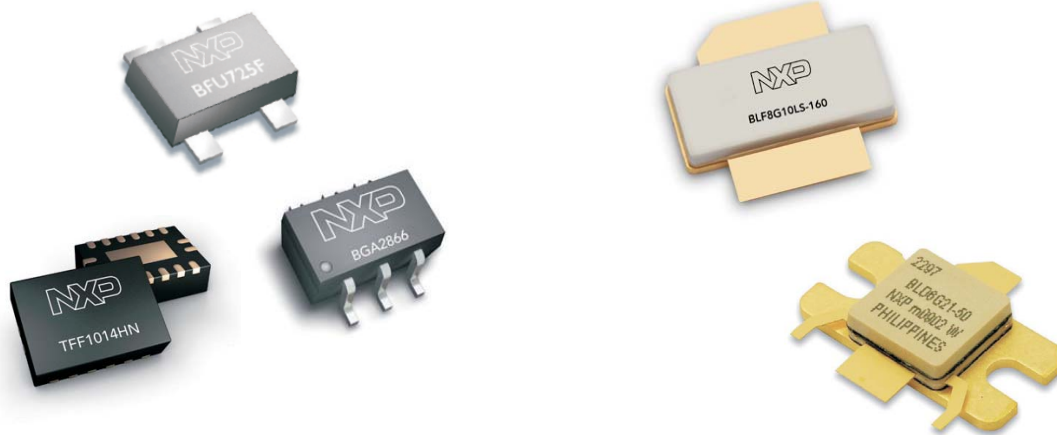
Finally, irrespective of the application scenario, in order to be accepted on the wireless consumer market, the cost of the complete module and, thus, of the antenna should be as low as possible, see [1, 2, 7]. For this, not only the materials and fabrication processes should be low-cost, the solution should also be flexible in order to cover as many application scenarios as possible in order to achieve high production volumes.

Hence, in summary, an integrated mm-wave antenna for the 60 GHz range should exhibit

- a small size and light weight,
- a differential/balanced antenna-feed,
- high radiation efficiency and gain over the entire bandwidth, e.g.,
  - $\geq 6$  dBi for general purpose antennas,
  - $\geq -6$  dBi for file transfers on the customer side,
- beam-forming capabilities,
- low-cost.

**Table 3.1.** Possible antenna system configurations that satisfy the IEEE standard 802.15.3c-2009 ([24]) at 60 GHz using the transmitter chip from [25] with an output power of  $P_{IC} = 10$  dBm.

case #	$G_{t,\text{single}}$ [dBi]	Tx array size ( $N$ )	$G_t$ [dBi]	$P_{\text{in}} = NP_{IC}$ [dBm]	EIRP [dBm]	$R$ [m]	$\left(\frac{\lambda_0}{4\pi R}\right)^2$ [dB]	$G_{r,\text{single}}$ [dBi]	Rx array size ( $M$ )	$G_r$ [dBi]	$P_r$ [dBm]
1	30	1	30	10	40	10	-88	2	1	2	-46
2	6	16	18	22	40	10	-88	2	1	2	-46
3	6	6	13.8	17.8	31.6	10	-88	6	6	13.8	-42.6
4	6	4	12	16	28	1	-68	-6	1	-6	-46
5	6	1	6	10	16	1	-68	6	1	6	-46



(a) Overmolded plastic-packages (OMP-packages).

(b) High-power ceramic-packages.

**Figure 3.1.** Typical high frequency packages from NXP Semiconductors, see [26] (courtesy of NXP).

## 3.2 Antenna-in-Package

### 3.2.1 Definition

An Antenna-in-Package is here defined as an antenna that is integrated in the packaging technology of the IC. Furthermore, the antenna requires a physical interconnect to the on-chip electronics, which can be clearly distinguished from the rest of the antenna structure.

### 3.2.2 Review of typical IC packaging technologies

Before going into detail about state-of-the-art packaging technology concepts for future mm-wave front-end modules, it is meaningful to first briefly review typical IC packaging technologies of already existing high-frequency products. Figure 3.1 shows some typical examples of high-frequency IC packages from NXP Semiconductors, see [26]. The most low-cost type is an overmolded plastic-package (OMP-packages), of which examples are shown in Figure 3.1(a). In its essence, it consists of a metallic lead-frame, on which the IC is placed. In order to connect the on-chip electronics to the lead-frame, standard low-cost wire-bond technology is usually used. For frequencies in the higher microwave range, however, the chip is often also placed up-side-down in order to connect the top-side of the chip directly to the leads of the package. This kind of chip assembly is commonly known as flip-chip technique. Af-

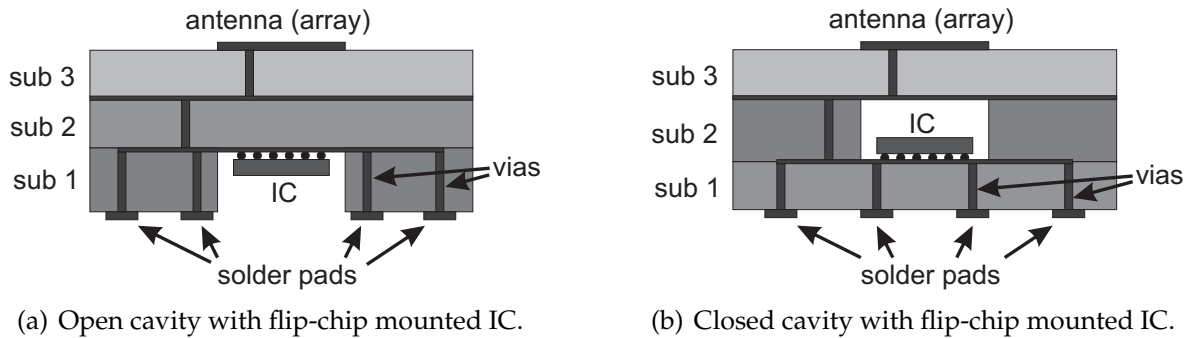


**Figure 3.2.** Conceptual drawings of typical multilayer AiP concepts.

terwards, the chip is then overmolded with a plastic compound such that the chip is protected from external hazards, like moisture, but the metallic leads are still accessible from the outside and can be used to solder the package onto a larger system PCB.

For high power applications, ICs often produce too much heat in order to use plastic as packaging material. Here, ceramic is used instead. Figure 3.1(b) shows two examples of such packages. Compared to plastic, ceramic packaging has the disadvantage of being rather costly and is, therefore, only used if the design specifications cannot be met otherwise.

### 3.2.3 State-of-the-art

#### Low-temperature co-fired ceramic packages

One of the most often reported packaging technologies for AiP designs is known as low-temperature co-fired ceramics (LTCC), see [27]. Typical examples of AiP concepts in this technology are, for example, published in [28, 29, 30]. As explained in [29], LTCC is already a popular packaging technology in the high-frequency industry since it offers low-loss dielectrics, which can be easily stacked to create multiple metal layers for dense routing. Furthermore, open and closed cavities can be created in the multilayer stack, which can be used for integrating the IC here, as shown in Figure 3.2. Hence, using LTCC for the mm-wave range seems a natural choice. And indeed, most reported AiP designs in this technology achieve excellent performances. Some key results of references [28, 29, 30] are summarized in Table 3.2. The stated radiation efficiencies, however, often exclude the insertion loss of the chip-to-package interconnect, such that lower values can be expected in practice. Furthermore, since LTCC is a ceramic packaging technology like the ones shown in Figure 3.1(b), it is often considered as too costly for the consumer electronics market.

### Printed circuit board packages

In order to reduce the costs of a solution according to Figure 3.2, some research groups have proposed to use the same multi-layer approach with less costly high frequency circuit materials, like the RO3000-series and RO4000-series from Rogers Corporation, see [31, 32], or liquid-crystal-polymer substrates, see, for example, [33]. Good examples of such designs can, for instance, be found in [34, 35] and a very recently published AiP design that even uses a multilayer FR4-package, can be found in [36]. An overview of the key figures of all three PCB-based designs are also summarized in Table 3.2. From this, it is evident that these materials exhibit similar electric parameters to LTCC and that AiP designs in those technologies achieve comparable performances. However, a problem with the alignment accuracy of multilayer PCB substrates was presented in [37]. Although this does not appear to be a commonly experienced issue, this potential problem should be considered very seriously since it might result in an insufficient yield in high volume production.

**Table 3.2.** Overview of typical state-of-the-art Antenna-in-Package designs.

ref.	package technology	size [mm <sup>2</sup> ]	feed topology	interconnect technology	impedance bandwidth [GHz]	$\epsilon_r$	$\tan(\delta)$	$\eta_{\text{rad}}$ [%]	gain [dBi]	cost (relative)
[28]	LTCC	100	single-ended	wire-bond	6 @ 60 GHz	5.9	0.002	94	9.5	medium
[29]	LTCC	-	single-ended	flip-chip	-	3.9	0.006	-	8	high
[30]	LTCC	4.84	single-ended	flip-chip	9 @ 60 GHz	5.8	0.004	-	6	high
[34]	PCB	-	differential	flip-chip	10 @ 60 GHz	-	-	-	8	low
[35]	PCB	16	differential	flip-chip	9 @ 60 GHz	3.28-3.74	0.0018-0.0044	80	8	low
[36]	PCB	54	single-ended	-	9 @ 60 GHz	3.54-3.59	0.012	76	4.1	low

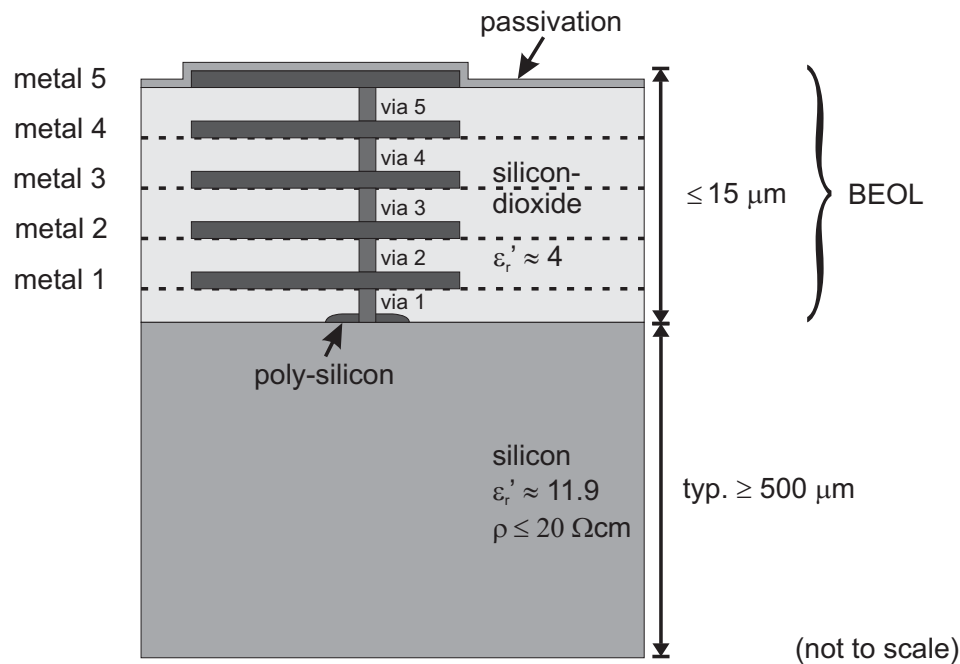


Figure 3.3. Sketched cross-section of a typical silicon IC.

## 3.3 Antenna-on-Chip

### 3.3.1 Definition

Throughout this thesis, an Antenna-on-Chip is defined as an antenna that is integrated in the back-end of an IC, i.e., using a monolithic on-chip metalization process.

### 3.3.2 Review of typical silicon IC technologies

In order to understand above definition of an AoC, it is necessary to know some basics about typical silicon IC processes<sup>3</sup>. Therefore, a sketched cross-section of such an IC including typical material parameters is provided in Figure 3.3. At the bottom it shows the core material of every CMOS and BiCMOS technology, namely the silicon substrate. On the top side of this usually about 750  $\mu\text{m}$  thick (for state-of-the-art high-frequency wafer sizes) silicon bulk, the active components are created by locally adding dopants into the silicon lattice. In the following process step, a stack of silicon-dioxide layers is added on top of the active components. After each of those layers, metal can be deposited in order to create traces for horizontal interconnects.

<sup>3</sup>Note that more specific details on individual (Bi-)CMOS processes are often provided in their, usually confidential, design manuals.



Moreover, vertical interconnects (vias) that connect these metal layers can be implemented, as also indicated in Figure 3.3. Finally, the last metal layer ("metal 5" in the figure) is covered by a thin passivation layer that protects the top metal traces from external hazards, such as moisture. The complete stack of silicon-dioxide, metal, and passivation layer is usually not more than  $10\ \mu\text{m}$  to  $15\ \mu\text{m}$  thick. Since it is created in a "back-end-of-line (BEOL) process", this stack is often generally referred to as BEOL or simply as back-end of the IC. Finally, as a standard post-processing step, the silicon substrate can be ground down in order to reduce its thickness. A typical minimum silicon thickness after grinding is  $200\ \mu\text{m}$ .

For high-frequency applications, passive components, like inductors, are often implemented in the back-end. Since the whole silicon bulk is usually pre-doped, however, it exhibits a low substrate resistivity of typically  $10\ \Omega\text{cm}$  to  $20\ \Omega\text{cm}$ . Thus, the losses in on-chip inductors are typically quite high, see also Section 2.1.2 on the relation between resistivity and loss tangent. Regardless of this drawback, pre-doping is necessary in order to prevent problems with active device parasitics.

### 3.3.3 State-of-the-art

As outlined in the previous section, it is common in high frequency IC designs to integrate passive components, like inductors, in the back-end. Hence, for frequencies at which the wavelength is comparable to the size of a complete silicon chip, it appears natural to also integrate the antenna here. The inherent advantage of this approach is that the antenna can be directly connected to the amplifier without the need for a mm-wave chip-to-off-chip interconnect. On one hand, this can minimize interconnect losses, see [1]. On the other hand, similar as for on-chip inductors, the low electric resistivity of the silicon substrate also introduces significant losses to the antenna. Those dielectric losses even have a more severe impact on on-chip antennas since, in contrast to inductors, their electric fields are not mainly concentrated directly around the antenna but also penetrate deep into the silicon substrate. Hence, the radiation efficiency and, consequently, the gain are significantly affected by this. The on-chip Yagi-antenna in a  $0.18\ \mu\text{m}$  CMOS technology published in [38], for example, only achieved a radiation efficiency of 10 % and a gain of -8 dBi. A suggestion that is often brought up with respect to the lossy silicon substrate, is to shield it from the antenna by implementing a metal plate in the lowest metal layer of the IC's back-end ("metal 1" in Figure 3.3). A popular antenna example that is commonly mentioned in this regard is a patch antenna. As stated in [14], the distance between patch and ground plane should be between  $0.003\ \lambda_0$  and  $0.05\ \lambda_0$  for this antenna type. And although a back-end thickness of  $15\ \mu\text{m}$  is right at the lower edge of this range, a significantly larger distance would be required in order to meet the bandwidth and radiation efficiency demands of the 60 GHz band, as a study on a basic patch

antenna configuration in [39] indicates. An interesting consideration of an on-chip dipole with its resonance at 77 GHz, which is implemented in a 15  $\mu\text{m}$  thick back-end with a ground plane in the lowest metal layer, is presented in [40]. Here, the authors mainly focus on the radiation efficiency of the antenna. Their conclusion is that due to the ohmic loss in the metal traces, the radiation efficiency of this configuration is as low as 5 %. Even at higher frequencies, this approach seems to remain troublesome since a 140 GHz slot antenna design with ground shield only achieved a maximum gain of -2 dBi, see [41]. Finally, the use of frequency selective surfaces, including electromagnetic band-gap (EBG) structures and artificial magnetic conductors (AMC), as proposed by [5], have been reported. Examples of such designs were published in [42] and [43]. The 60 GHz antenna design on a 17.5  $\Omega\text{cm}$  silicon substrate from [42], however, only achieved a radiation efficiency of 19.6 % and a maximum gain as low as -2.1 dBi. The design presented in [43] does not specify any silicon parameters, but the reported maximum gain of -3.7 dBi indicates a similarly low efficiency.

It shall be pointed out here, however, that besides the radiation efficiency issue with this antenna integration technology, all mentioned AoC designs achieved acceptable performances as the key figures in Table 3.3 indicate. Note, however, that the broad impedance bandwidth, for example, might also be caused by significant substrate losses<sup>4</sup>.

Hence, achieving a satisfactory result in terms of bandwidth and radiation efficiency in a standard CMOS or BiCMOS process appears to be a major challenge. However, there are several techniques that can enhance the performance of an on-chip antenna. Since they all require additional processing steps after the usual IC fabrication, those techniques are commonly referred to as post-processing techniques. But although those steps have proven to enhance the performance of on-chip antennas, the semiconductor industry is still reluctant to incorporate them into their standard portfolio. A reason often given for this is the increase in fabrication costs and, therefore, the worries of losing competitiveness on the market. Despite those worries, typical post-processing techniques will be briefly summarized in the following, in order to present all currently available, most important options here. For comparison, the key parameters of all following antenna designs are also provided in Table 3.3.

---

<sup>4</sup>Just like for other resonant circuits, the impedance bandwidth of a resonant antenna is proportional to the inverse of its quality factor.

**Table 3.3.** Overview of typical state-of-the-art Antenna-on-Chip designs.

ref.	$\rho$ [ $\Omega\text{cm}$ ]	silicon thickness [ $\mu\text{m}$ ]	post-proc. technology	size [ $\text{mm}^2$ ]	feed topology	impedance bandwidth [GHz]	$\eta_{\text{rad}}$ [%]	gain [dBi]	cost (relative)
[38]	-	-	none	1.045	differential	10 @ 60 GHz	10	-8	low
[41]	12.5	275	none	0.72	single-ended	5 @ 140 GHz	-	-2	low
[42]	17.5	300	none	1.222	differential	-	19.6	-2.1	low
[43]	-	-	none	3.24	single-ended	71 @ 70 GHz	-	-3.7	low
[44]	-	250	superstrate	0.702	single-ended	10 @ 95 GHz	44-62	0 - 2	medium
[45]	13.5	300	resonator	2.09	single-ended	3 @ 34.5 GHz	59	1.06	medium
[40]	-	100	lense	-	differential	-	-	2	medium
[46]	20	250	lense	-	differential	100 @ 220 GHz	50	17.8	medium
[47]	11-70	300-400	micromach.	12.96-20.2	both	-	-	1 - 1.5	high
[48]	-	-	MEMS	-	single-ended	12 @ 60 GHz	25	-6.75	high
[49]	10	-	proton implantation	0.83	single-ended	7 @ 46.5	-	6.4	high

### Superstrates, resonators, and lenses

One possible method to improve the off-chip radiation of an antenna is to add an additional dielectric on top of the IC's back-end. Possible options for this are a simple superstrate, a resonator, and a lense. A 90 GHz design using a superstrate, for example, achieved a radiation efficiency of 44-62 %, see [44]. At nearly a third of that frequency, a 35 GHz slot antenna design with metal shield in the lowest metal layer of the back-end and dielectric resonator on top of the slot achieved an efficiency of 59 %, see [45]. On-chip antennas including lenses were, for example, presented in [40, 46]. In both cases the lense was attached at the bottom of the chip. Hence, the electromagnetic wave first has to penetrate the low resistive BiCMOS substrates. Therefore, the 77 GHz antenna design from [40] only achieved a maximum gain of 2 dBi, which is rather low for a lense antenna. The design presented in [46], however, achieved 17.8 dBi at 180 GHz with a stated radiation efficiency of 50 %.

### Micromachining

Since the presence of lossy silicon is the core problem of the low radiation efficiencies of on-chip antennas, a typically used post-processing method is to locally remove the silicon substrate around the antenna. This technique is generally known as micromachining. One of the earlier works in this direction was published by Öjefors et al. in [47]. According to this reference, a 30 GHz on-chip full-loop antenna achieved a gain of 1.5 dBi. Unfortunately, an estimation of the radiation efficiency is not given, but in comparison to the above mentioned 60 GHz results without any post-processing, this gain indicates a rather good efficiency.

### MEMS

Micro-electro-mechanical-systems (MEMS) are an up-to-date research topic on its own in the microwave and mm-wave communities. Also for on-chip antennas this technology offers promising possibilities. The authors of [48], for example, present a MEMS-based on-chip monopole antenna that stands perpendicularly on top of the IC. For this, the residual stress in a polymer based MEMS-process is used to create warping in the polymer during curing, resulting in the desired upright orientation of the monopole. Such an antenna configuration allows the implementation of a metal plate in the back-end without sacrificing bandwidth or radiation efficiency. Unfortunately, no simulated radiation efficiency or gain is given in the reference and no gain pattern measurements are shown. From a transmission measurement between two of those antennas, the authors estimated the efficiency to be 25 %. This value seems rather low for this structure, however, which might be a result of the low signal-

to-noise-ratio of the transmission measurement, which is presented in the reference. Moreover, destructive interference with reflected waves from, for example, the probe station may have affected the measurement and caused this low result. Hence, in general, better efficiencies may be expected from such an antenna structure.

### **Proton implantation**

Owing to the fact that the low radiation efficiency of on-chip antennas is mainly due to the pre-doped and, thus, low resistive silicon substrate, one might seek for a method to increase the resistivity in the vicinity of the antenna. One technique that can be used to achieve this is known as proton implantation. Already in 2003 the authors of [49] showed that by locally increasing the resistivity from  $10 \Omega\text{cm}$  to  $10^6 \Omega\text{cm}$ , a gain of 4.2 dBi could be achieved for a 40 GHz printed monopole antenna, which indicates an excellent efficiency. Also the achieved bandwidth of about 15 % would be sufficient for operation in the 60 GHz band.

## **3.4 Hybrid integrated mm-wave antenna**

### **3.4.1 Definition**

An antenna that is integrated in the same package with the front-end IC, but is neither implemented in the packaging technology nor in the back-end of the chip, shall here be referred to as hybrid integrated mm-wave antenna concept, or in short simply as hybrid concept.

### **3.4.2 State-of-the-art**

Besides the AiP and AoC concept, several designs were published in recent years that cannot be uniquely assigned to one of the two categories since the antenna is neither integrated in the back-end of the IC nor in the IC packaging technology. One of the first of those designs was published in [50]. Here, a dipole antenna on a fused silica substrate was mounted half on-chip and half off-chip, such that the antenna could be directly connected to the on-chip electronics, see Figure 3.4(a). The bandwidth of this antenna concept covers the full 60 GHz band and the reported gain is 6 dBi to 8 dBi at a radiation efficiency of larger than 90 %, see Table 3.4. However, the fabrication process appears to be rather complex. A slightly different antenna concept was published three years later in [51]. Here, a patch antenna in standard PCB technology was directly connected to the back-end of the IC by a flip-chip technique, see Figure 3.4(b). By mounting a small PCB onto the chip rather than mounting the

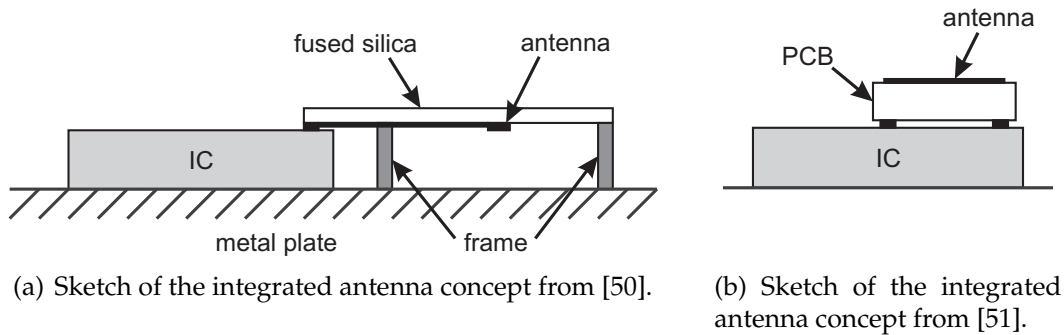


**Figure 3.4.** Examples of hybrid integrated mm-wave antenna concepts.

chip up-side-down onto a PCB, low-cost plastic packaging and bond-wire chip-to-package interconnects could still be used. In the reference, the maximum achieved radiation efficiency including flip-chip interconnect is given as 60 % to 72 %, which results in a gain of 2 dBi to 3.5 dBi. Finally, even generic bond-wires can be used as antennas as shown in references [52, 53], which was even patented, see [54]. While in [52] the bond-wires are used as short monopoles (wire length of  $0.144 \lambda_0$ ) and only achieve a radiation efficiency of 15 % to 30 %, the authors of [53] use half-circular bond-wires for building a Yagi-Uda array with a simulated efficiency of 74.6 % to 90 % and a maximum gain of 6 dBi to 8 dBi. Also here, all key figures are provided in Table 3.4. From this, it can be concluded that hybrid integrated mm-wave antenna concepts seem to be an attractive alternative to pure AiP or AoC concepts.

**Table 3.4.** Overview of typical state-of-the-art hybrid integrated antenna designs.

ref.	technology complexity	size [mm <sup>2</sup> ]	feed topology	impedance bandwidth [GHz]	$\eta_{\text{rad}}$ [%]	gain [dBi]	cost (relative)
[50]	high	12.6	differential	9 @ 60 GHz	90	6 - 8	high
[51]	low	-	single-ended	9 @ 60 GHz	60-72	2 - 3.5	low
[52]	very low	0.0036	single-ended	9 @ 60 GHz	15-30	-4 - 0.4	very low
[53]	very low	-	single-ended	3 @ 40 GHz	51-84	6 - 8	very low

## 3.5 Discussion

From the state-of-the-art overview in this chapter one can conclude that all three integration approaches can be used to design antennas that match the specifications of the 60 GHz band. The AoC approach, however, falls behind the AiP and hybrid approach in terms of radiation efficiency and gain. AiP designs, on the other hand, may not be able to compete with the AoC and hybrid approach in terms of cost due to their normally rather complex multi-layer packaging structure. Moreover, AiP concepts require an additional chip-to-off-chip interconnect that requires extra design effort and introduces additional losses to the system. Therefore, the hybrid solution seems, at first glance, the best solution here. However, for frequencies beyond 60 GHz the structure size and fabrication accuracy of typical hybrid but also AiP technologies might be insufficient. This problem does not exist for the AoC approach, which was already very successfully tested in the terahertz band, see, for example, [10]. Therefore, AoCs should not be completely excluded here yet. Finally, a striking advantage of the AiP approach is its design flexibility and the fact that printed antenna structures can be used, which have been widely studied and successfully implemented in the last decades.

Hence, instead of focusing on a single integration approach, all three options were investigated in the outline of this thesis. For this, competitive antenna concepts for each integration approach were developed. Those concepts are based on basic antenna types in order to focus the consideration on the antenna performance with respect to the integration technology rather than the antenna topology. The three individual concepts for single antenna elements are presented in the three following chapters, where special emphasize is placed on the radiation efficiency. The problem of achieving sufficiently high gain values and beam-steering are then tackled in Chapter 7, which deals with considerations for antenna arrays.





# Antenna-in-Package concept<sup>1</sup>

---

## 4.1 Technology choice

In order to further investigate the AiP approach, an integrated mm-wave antenna concept was developed based on the results of the literature study in Section 3.2. The goal was to achieve a low-cost antenna solution that can be fabricated with standard technologies and materials while being competitive with state-of-the-art AiP solutions. In order to meet the cost constraints of the consumer market, it was decided to base the concept on PCB technology. For this, RO4003C was chosen as substrate material due its low permittivity,  $\epsilon_r = 3.55$ , and low loss tangent,  $\tan(\delta) = 0.0027$ , which are specified up to 40 GHz and 10 GHz, respectively, see [32]. Furthermore, in order to minimize the fabrication costs and prevent possible tolerance problems of multilayer structures as reported in [37], see Section 3.2, a single-substrate design was targeted. With respect to the antenna type, a printed dipole was chosen since it exhibits a differential feed structure and can easily be implemented on a single substrate. However, due to the expected small feature size of the antenna, its bandwidth should be sufficiently large to compensate typical process variations that may alter, for example, the dipole length.

The following section describes the general AiP concept that was developed based on above considerations. A detailed analysis of the antenna design and the simulation results of a prototype are then presented in Section 4.2.2. Descriptions of the used measurement setups are given in Section 4.3, followed by the measurement results in Section 4.4. A short summary and conclusions with respect to state-of-the-art are then presented in Section 4.5.

---

<sup>1</sup>The results presented in this chapter were published in [55].

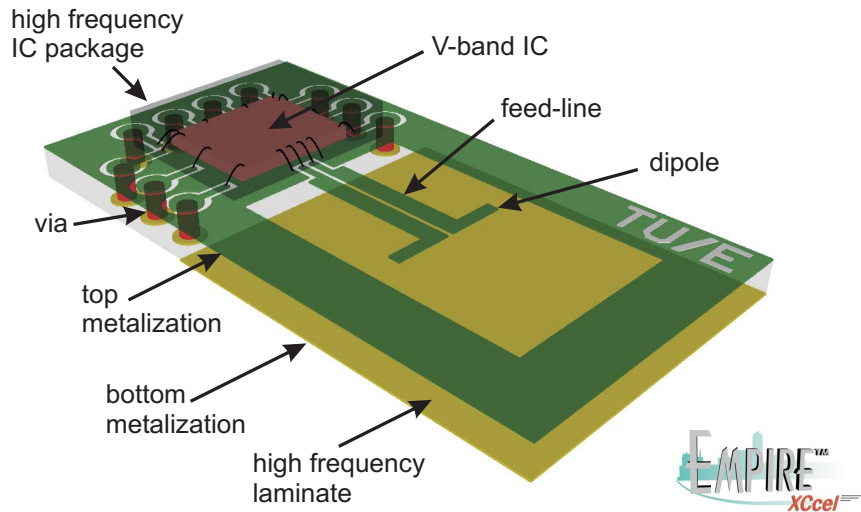


**Figure 4.1.** Conceptual drawing of the proposed mm-wave AiP design.

## 4.2 Design

### 4.2.1 General module concept

The general concept of the proposed AiP is depicted in Figure 4.1. It shows a printed dipole antenna on a single-layer high frequency PCB that is directly connected to an active front-end IC. The interconnect can be implemented as bond-wire transmission line, as reported in [56], or in flip-chip technology. The basic building blocks of the active front-end are an amplifier, a mixer, and a local-oscillator (LO) including phase-locked-loop (PLL). The DC-supply, clock signal for LO synchronization, and the intermediate frequency (IF) path are connected to the PCB in standard technology, i.e., using regular wire-bonds or flip-chip. In order to connect the module to a larger system-PCB that contains the power management, the clock generator, and the IF components of the wireless system, vias route to the bottom side of the PCB. Here, due to the significantly lower frequencies of the IF band and the clock signal, the physical connection to the system-PCB can be achieved using standard soldering technology. Finally, the front-end IC and, if present, the bond-wires have to be protected from external hazards such as moisture and physical impact. For this, they can be overmolded just like the high-frequency OMP-packages shown in Figure 3.1(a). A possible plastic packaging technology that allows the antenna to be free of any mold-compound is, for example, the cavity molding technology from Sencio BV, see [57].

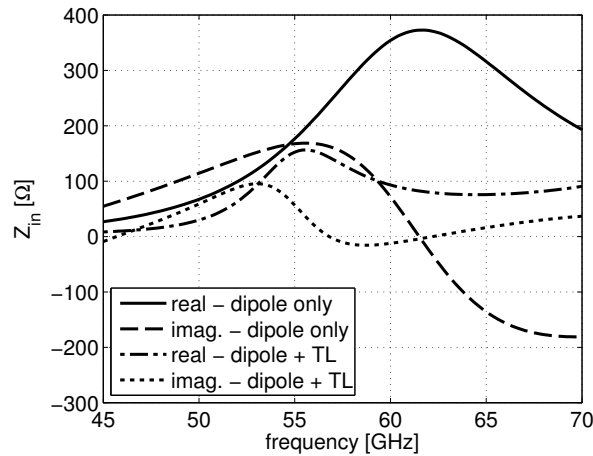


**Figure 4.2.** Simulated input impedance of a 60 GHz printed dipole on an infinite, grounded RO4003C substrate with a thickness of 0.508 mm (“dipole only”) and the same dipole with a 2.3 mm coupled microstrip feed-line with optimized characteristic impedance (“dipole + TL”).

#### 4.2.2 Antenna design

The antenna design is based on the observation that the input impedance of a printed dipole on top of a relatively thick grounded substrate exhibits a wide-band non-zero real part as depicted in Figure 4.2. It shows the simulation results of a dipole with an arm length of 0.92 mm on a 0.508 mm thick RO4003C substrate, i.e., with the cut-off frequency of the  $TE_1$ -mode at 92.5 GHz, see (2.34) and [32]. For the simulation, Empire XCcel was used. Besides the direct radiation from the dipole, the reason for the broad-band non-zero real part is seen to be a significant coupling of electromagnetic energy into an unguided TE-mode that is steadily radiated while propagating away from the dipole. This phenomenon is also described in [12, 15] and can generally be referred to as a leaky wave contribution. In order to match this dipole to a fixed reference impedance over a broad frequency range, a coupled microstrip line can be used as indicated in Figure 4.1. By adjusting its length and differential characteristic impedance, the input impedance of the dipole can be closely matched to 100  $\Omega$  in the entire 60 GHz band, see Figure 4.2. At a certain distance away from the dipole the leaky wave contribution has decayed sufficiently such that also the top side of the substrate can be metalized here without significantly disturbing the radiation mechanisms. Furthermore, the PCB can be truncated here and one arrives at the antenna design shown in Figure 4.1.

Figure 4.3 shows a photograph of a manufactured prototype of this antenna design together with its design parameters. Here, the metalized top-side of the RO4003C laminate also serves as ground plane and heat-sink for the front-end IC. To assure

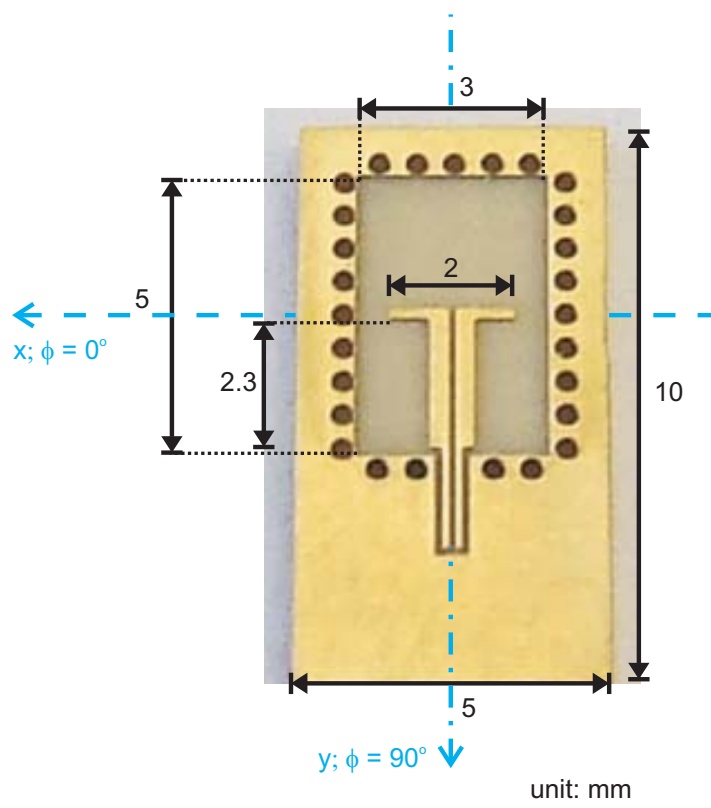
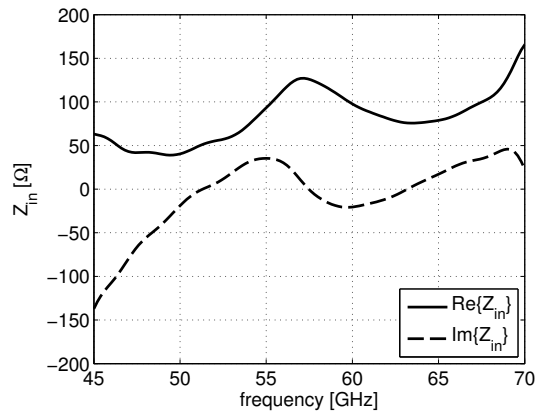
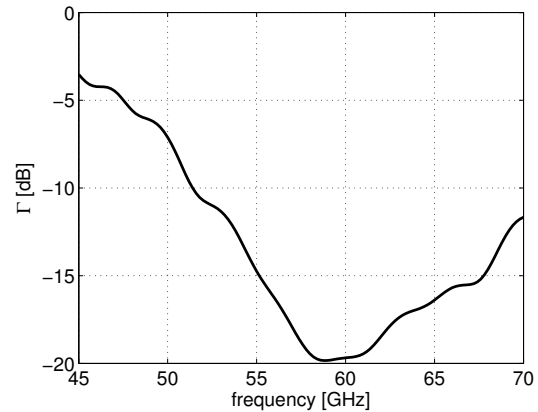


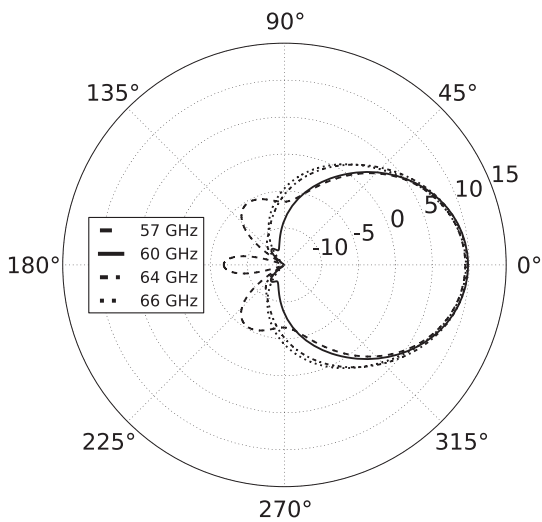
**Figure 4.3.** Photograph of a fabricated antenna prototype.



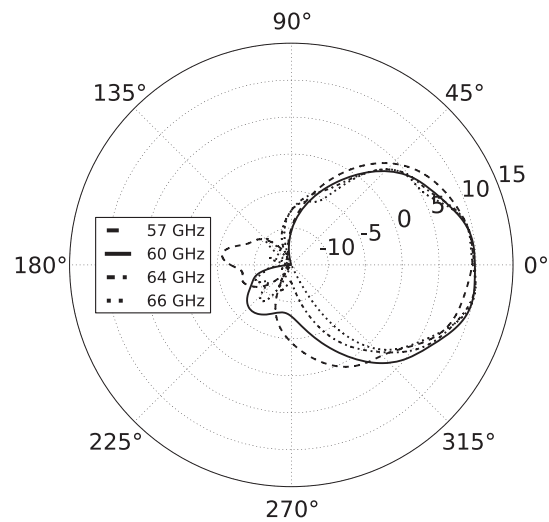
(a) Simulated input impedance of the prototype.



(b) Simulated input reflection coefficient of the prototype ( $Z_0 = 100 \Omega$ ).



(c) Gain pattern in E-plane.



(d) Gain pattern in H-plane.

**Figure 4.4.** Simulated antenna parameters of the AiP prototype shown in Figure 4.3.

that no parallel plate modes will be excited, via-fences connect the upper and lower metal plate around the dipole. Furthermore, the coupled microstrip lines are extended with a transmission line that allows the landing of a mm-wave measurement probe with a pitch of  $200 \mu\text{m}$ . Further details about the probes are given further below in Section 4.3. The line length is chosen such that it exhibits a phase shift of  $180^\circ$  at 60 GHz. By this, the input impedance around 60 GHz is not significantly changed while the possibility of coupling between antenna and probe-tip is reduced due to the increased distance between them.

The simulation results of the input impedance, input reflection coefficient, and the gain pattern in the principal planes for this prototype are shown in Figure 4.4. It clearly shows a similar behavior in the 60 GHz band as the design without top-

metalization (cp. Figures 4.4(a) and 4.2). The obtained -10 dB bandwidth of this antenna (with 60 GHz as reference frequency) exceeds 30 %. This alone, however, does not prove the usability of the antenna for applications in the 60 GHz band. For this, the radiation pattern should maintain a similar shape and gain throughout the frequency band, see Section 3.1. From Figures 4.4(c) and 4.4(d), which show the gain patterns of the antenna at four characteristic frequencies, it can be observed that the basic pattern is indeed similar and the maximum gain ranges from 9.63 dBi at 57 GHz to 10.14 dBi at 66 GHz. Finally, the simulation results predict a radiation efficiency of 93 % throughout the 60 GHz-band. As already mentioned in Chapter 3, however, the chip-to-antenna interconnect has to be taken into account as well for a fair comparison with the designs from Chapters 5 and 6. Here, the interconnect option from Infineon Technologies, published in [58], is used to estimate the resulting overall radiation efficiency by

$$\eta_{(\text{rad,AiP})} \approx |S_{21}|^2 \eta_{(\text{rad,ant.})}, \quad (4.1)$$

where the two-port S-parameter  $|S_{21}| = 0.928$  (= -0.65 dB) is the stated best-case transmission value in the reference and  $\eta_{(\text{rad,ant.})}$  is the efficiency as mentioned above. Using (4.1), the overall radiation efficiency of the AiP design described in this chapter can be estimated to about 80 %.

### 4.3 Measurement setups

State-of-the-art commercial electromagnetic modeling tools exhibit a high degree of accuracy. However, the underlying computational methods only approximate the electromagnetic relations inside a given structure and the obtained results are, therefore, not exact. Furthermore, the computation is always based on a simplified model of the exact physical constitution since the complexity of, for example, "real-world" materials is virtually impossible to accommodate in a practical amount of bits and bytes. And although an extremely high degree of detail has proven not to be necessary for many electromagnetic engineering problems in modern wireless communications for the consumer market, the outcome of modeling tools still has to be, and will always have to be, verified by measurements. The main reason for this strict necessity is the need to verify whether the model was set up correctly and covers a sufficient level of details in order to include all characteristics of the structure under investigation.

Since often the constitutive parameters of the used materials are not exactly known at mm-wave frequencies, verification by measurements is of particular importance for the antenna designs described throughout this thesis. More specifically, the input impedance and far-field characteristics, represented by its gain, polarization, and ra-

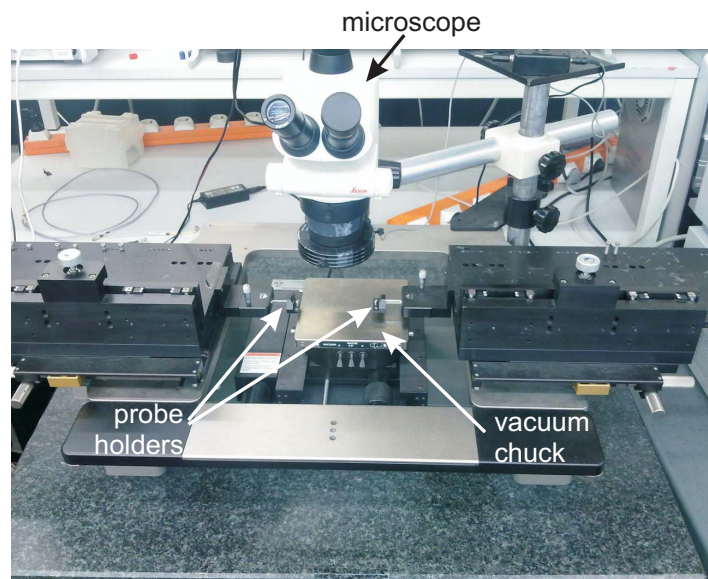


**Figure 4.5.** Photograph of a model 9000 probe station from Cascade Microtech, Inc., see [59].

diation pattern, are of interest. The radiation efficiency, for example, a key parameter for the consideration of integrated mm-wave antennas as pointed out in Section 2.3.2, can be derived from those parameters. Therefore, high performance measurement setups for determining impedance and far-field quantities are fundamental. The respective setups that were used for the characterization of the antennas presented throughout this thesis are described in this section.

### 4.3.1 Input impedance

For determining the input impedance of an integrated mm-wave antenna, a generic wafer-prober can be used, like the Model 9000 probe station from Cascade Microtech, Inc., shown in Figure 4.5. It consists of a metallic chuck, on which the antenna-under-test (AUT) can be placed. A built-in vacuum fixation avoids any movement of the AUT such that a mm-wave measurement probe can easily be landed using the adjustable probe holders and the microscope that are also shown in the figure. The measurement probe itself connects the antenna via a coaxial cable to an Agilent PNA E8361A vector network analyzer (VNA), see [60], as depicted in the sketched measurement setup provided in Figure 4.6. Various probe types with different pin configurations on the antenna side are commercially available. For the characterization of the antennas presented in this thesis, the Picoprobe Models 67A in ground-signal-ground (GSG), ground-signal (GS), and signal-ground (SG) configuration were used, see [61]. Their basic pin structure is illustrated in Figure 4.7. For each of those probes



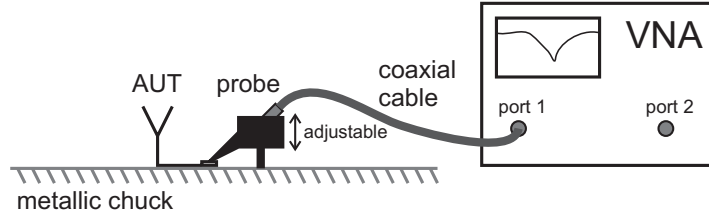


**Figure 4.6.** Sketch of the input-impedance measurement-setup.

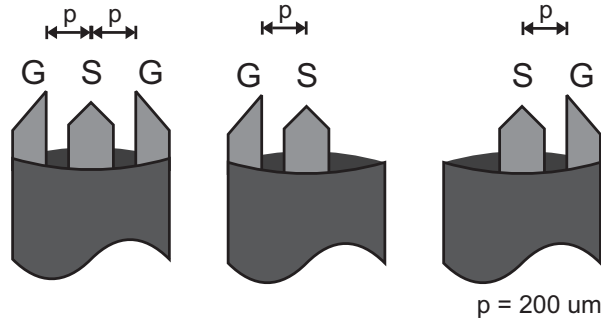


**Figure 4.7.** Illustration of probe tips in ground-signal-ground, ground-signal, and signal-ground configuration, respectively.

a calibration substrate is available such that the input reflection coefficient,  $\Gamma_{in}$ , of the AUT can be directly measured as seen from the probe tip's position. If the reference point is desired to be at a different location inside the AUT structure, for example, if the feed-line should be excluded from the measurements, additional de-embedding structures are required, see, for example, [62]. For the validation of the simulation results presented throughout this thesis, however, the feed-lines were included in the simulation setup rather than de-embedded from the measurements. By this approach, the impact of measurement uncertainties is reduced to a minimum since the accuracy only depends on a single measurement. Finally, the input impedance of the antenna can be determined by the following relation:

$$Z_{in} = \frac{1 + \Gamma_{in}}{1 - \Gamma_{in}} Z_0, \quad (4.2)$$

where  $Z_0$  is the reference impedance of the measurement setup, i.e.,  $50 \Omega$  for single-ended measurements.

### 4.3.2 Radiation pattern

Unlike the input impedance of the AUT, its radiation pattern cannot be accurately measured on a standard wafer prober. This has to do with the fact that the radia-

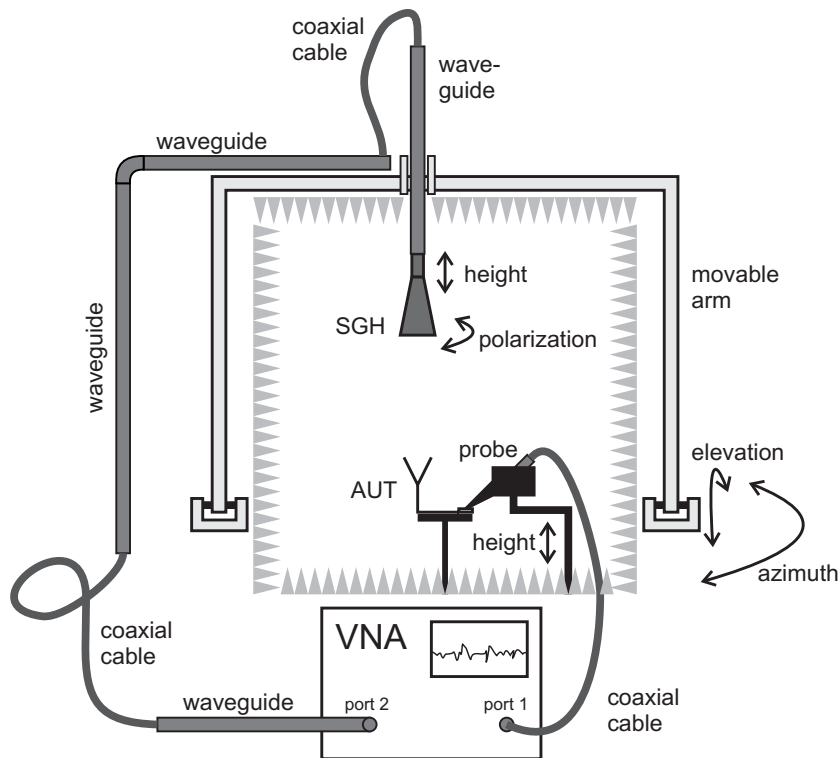
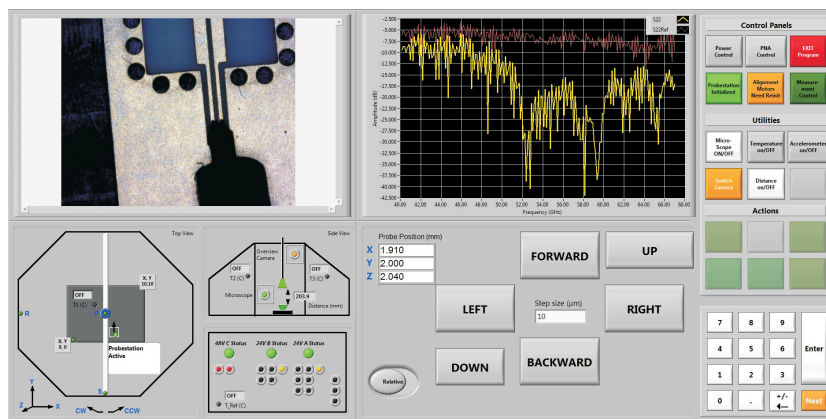


**Figure 4.8.** Schematic drawing of the radiation pattern measurement setup.

tion pattern is measured in the far-field of the antenna where the measured signal strength is generally lower than the one for impedance measurements. Therefore, reflections from nearby objects, even though they might be in the far-field of the AUT, can cause a significant interference with the line-of-sight signal. In order to minimize those undesired room reflections, the radiation pattern is usually measured in an anechoic chamber. A schematic drawing of the measurement setup, used for the radiation pattern measurements of the antennas presented in Chapters 4 and 6, is provided in Figure 4.8. It shows the AUT on a plastic chuck inside a fully closed anechoic chamber. Also here, a vacuum fixture keeps the antenna in position and a Picoprobe Model 67A connects the AUT via a coaxial cable to the Agilent PNA E8361A. Opposite the AUT, a standard gain horn (SGH) is mounted at the end of a rectangular waveguide. This waveguide is fed through a gap in the outside wall of the anechoic chamber and is attached to a movable arm that allows to change the elevation and azimuth angle of the SGH with respect to the AUT. The gain horn itself can be adjusted in height and, by means of rotation, its polarization can be aligned with the expected co-polarization or cross-polarization of the AUT. Finally, a network of coaxial cables and rectangular waveguides connects the SGH from the center of the arm to the second port of the VNA. By this, the relative radiation pattern of the co- and cross-polarization of the AUT can be measured by means of a transmission mea-



(a) Photograph of the mm-wave anechoic chamber (chamber opened to show inside).



(b) Screenshot of the control panel in "probe-landing mode".

**Figure 4.9.** Anechoic chamber for radiation pattern measurements.

surement from port one to port two, or vice versa. In order to determine the gain of the AUT, it can be replaced by a reference antenna with known gain. Afterwards, the gain in dBi can be estimated by

$$G_{\text{AUT,dBi}} = S_{21,\text{AUT,dB}} - S_{21,\text{ref.,dB}} + G_{\text{ref.,dBi}} - S_{21,\text{probe,dB}} - 10 \log_{10}(1 - |S_{11,\text{AUT}}|^2), \quad (4.3)$$

with  $S_{21,\text{AUT,dBi}}$  and  $S_{21,\text{ref.,dB}}$  the transmission measurements of the AUT and known reference antenna, respectively,  $G_{\text{ref.,dBi}}$  the gain of the reference antenna,  $-S_{21,\text{probe,dB}}$  the insertion loss of the measurement probe and  $10 \log_{10}(1 - |S_{11,\text{AUT}}|^2)$  the relative accepted power by the AUT.

A photograph of the measurement setup is provided in Figure 4.9(a). It shows the opened anechoic chamber. The AUT, probe, and SGH are especially highlighted. Furthermore, a control panel with touch screen is shown on the right hand side. From here, the position of the movable arm as well as the height and orientation of SGH can be adjusted. Also the VNA and probe landing is controlled using this interface. For the latter, a camera can be mounted on top of the AUT. The video signal is then displayed in a window in the control panel as shown on the top left in Figure 4.9(b). In order to detect whether the probe has landed, the real-time measured input reflection coefficient of the AUT (port one in Figure 4.8) is shown in a window next to the camera image. As soon as the probe is properly landed, this signal will drastically change. By this, a well controlled and highly repeatable characterization of the AUT can be assured.

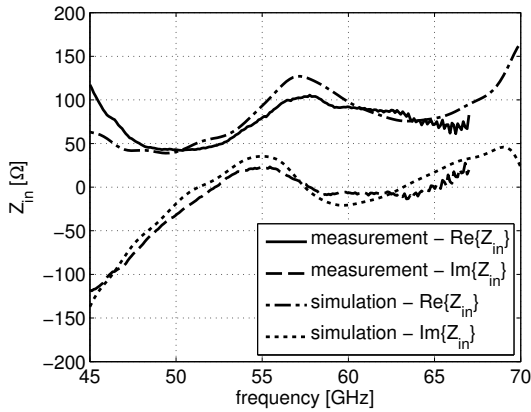
## 4.4 Measurement results

Several samples of the AiP design shown in Figure 4.3 were manufactured and measured using the setups described in Section 4.3. A comparison between measured and simulated input impedance and input reflection coefficient of a randomly picked sample is depicted in Figures 4.10(a) and 4.10(b), respectively. The measurement was carried out using a single-ended Picoprobe Model 67A-GS-200-DP in a GS configuration. By landing the GS-probe on the signal lines, the antenna is excited in the desired differential mode<sup>2</sup>. From Figures 4.10(a) and 4.10(b) a good agreement between simulation and measurement can be concluded.

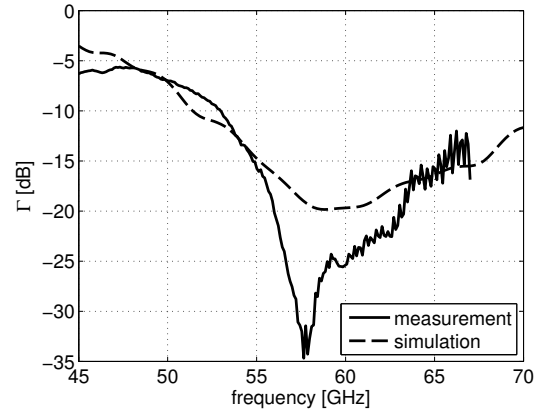
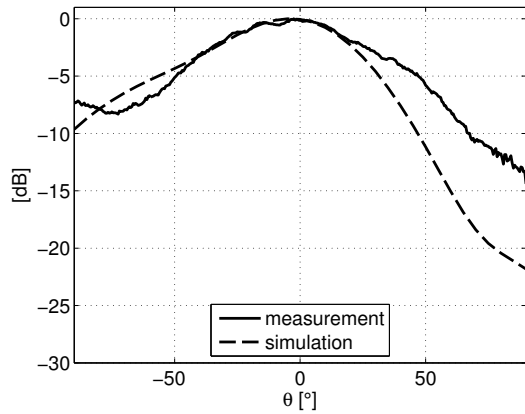
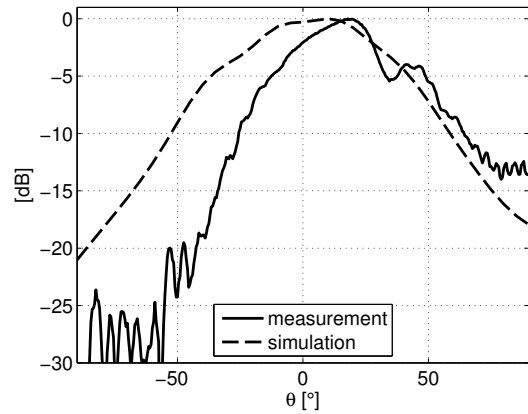
A comparison between the simulated and measured normalized radiation pattern at 60 GHz is provided for both principal planes in Figures 4.10(c) and 4.10(d). For

---

<sup>2</sup>It was verified by a simulation with Empire XCcel that the probe-tip itself does not radiate when terminated in a matched load, i.e., no (significant) cable-currents are present.

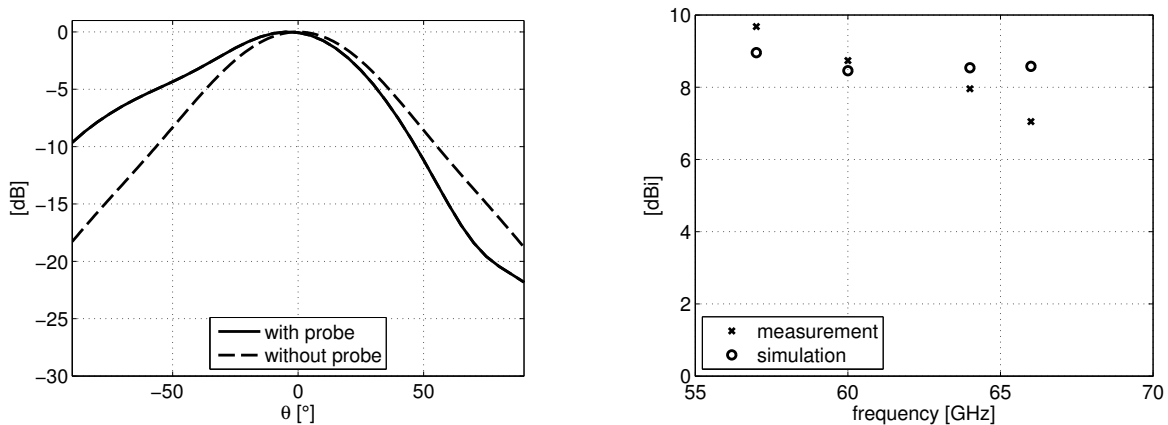


(a) Input impedance.

(b) Input reflection coefficient ( $Z_0 = 100 \Omega$ ).(c) Normalized gain pattern for the copolarization component at  $\phi = 0^\circ$  ( $E_\theta$ , normalized to maximum value; probe model included in simulation setup).(d) Normalized gain pattern for the copolarization component at  $\phi = 90^\circ$  ( $E_\phi$ , normalized to maximum value; probe model included in simulation setup).

**Figure 4.10.** Comparison between measured and simulated antenna parameters of the AiP prototype from Figure 4.3.

the simulations, a simplified model of the probe-tip that could not be covered with absorbers was added to the model in Empire XCell. This was necessary since even reflections at the probe-tip significantly affect the overall radiation pattern, as can be observed from Figure 4.11(a), which shows the normalized gain patterns for the case with and without probe model in the  $\phi = 0^\circ$  plane at 60 GHz. However, slight deviations between measurement and simulation remain, see Figures 4.10(c) and 4.10(d). This is seen to be also caused by the presence of the probe since, although the probe was largely covered with absorbers, reflections and refractions at its body cannot be entirely avoided. Moreover, for measurements in the  $\phi = 90^\circ$  plane, the probe blocks the line-of-sight for a substantial angular range, which explains the measured low gain values for negative angles  $\theta$  in Figure 4.10(d). Given these circumstances, the



(a) Simulated normalized gain patterns of the AiP-prototype with and without probe model.

(b) Measured versus simulated gain in broadside direction ( $\theta = 0^\circ$ ).

**Figure 4.11.** Influence of the probe-tip on the radiation pattern of the AiP prototype and its resulting gain in broadside direction.

simulation results agree well with the measurements. For completeness, the radiation patterns at 57 GHz, 64 GHz, and 66 GHz are provided in Figure B.1 in Appendix B, which show similarly good agreement.

In order to estimate whether the simulated efficiencies of the AiP prototype are reasonable, its broadside gain ( $\theta = 0^\circ$ ) was determined with the method described in the previous section. A comparison between those measurements and the values obtained from the simulations including the probe model are provided in Figure 4.11(b). The measured gain values deviate between 0.28 dB at 60 GHz and 1.53 dB at 66 GHz from the simulated values. In view of the accuracy between simulated and measured radiation patterns, see Figures 4.10(c) and 4.10(d), this agreement is considered to be acceptable.

Hence, above summarized results of the experiments provide sufficient evidence that the used Empire-model is a valid representation of the prototype and includes all its major characteristics.

Finally, in order to obtain a first glance at the yield of this antenna design in standard PCB technology, six different samples from the manufactured batch were randomly chosen and their input reflection coefficients were measured. Figure 4.12 summarizes the results. All six samples show a very similar behavior that is considered to be acceptable for consumer market applications. This first glance does not replace a thorough yield investigation however since the measurement of six samples from the same batch is hardly enough to derive statistical quantities from it.

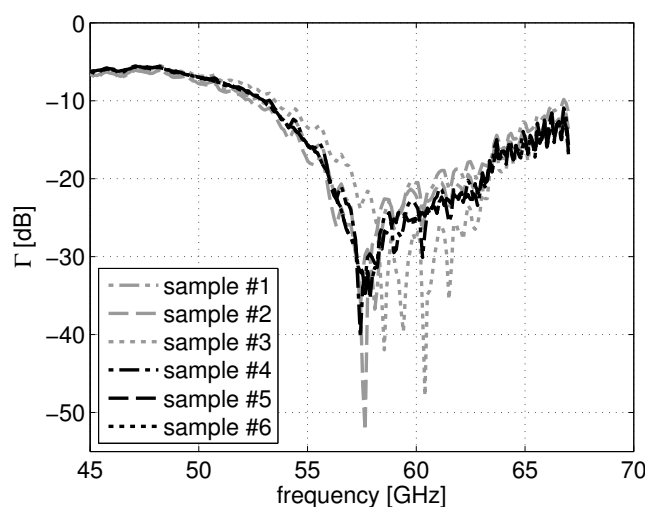


**Figure 4.12.** Input reflection coefficients of six randomly chosen antenna samples ( $Z_0 = 100 \Omega$ ).

## 4.5 Summary and conclusions

In this chapter, a AiP concept based on PCB technology is presented. The simulation results, obtained with Empire XCell and verified by measurements, are summarized in Table 4.1. It can be concluded that the proposed concept can compete with state-of-the-art AiP concepts in terms of size, radiation efficiency, and gain, see also Table 3.2. The impedance bandwidth of over 30 %, which can easily compensate typical variations in modern PCB processes, is even outstanding. Moreover, the single substrate-layer approach is seen to be superior to multi-layer approaches in terms of yield in high volume production. The higher yield together with the anyway less costly single-layer fabrication process give this approach also a possible advantage in terms of costs. On the contrary, a drawback of this solution is seen to be the antenna size in combination with the IC placement next to the antenna, which results in less design flexibility for antenna arrays. Some ideas in this direction are therefore presented in Chapter 7.

Regarding the suitability of this AiP concept for the three major application areas stated in Chapter 1, this antenna is seen to be most adequate for HD video streaming, wireless Gigabit Ethernet, and a "kiosk in a store" type of file transfer applications. The reasons for this conclusion lie in the antenna's relatively large size, high radiation efficiency, and associated high gain. Especially the relatively large devices for the HD video streaming and wireless Gigabit Ethernet applications, like laptops and televisions, provide sufficient space to implement this antenna concept as an array that fulfills the gain requirements for communication of up to 10 m, see Table 3.1. For the same reasons, the antenna is seen to be a suitable choice for the terminal side of

**Table 4.1.** Key figures of the proposed AiP concept according to Table 3.2.

package technology	PCB
size [mm <sup>2</sup> ]	15
feed topology	differential
interconnect tech.	bond-wire/flip-chip
impedance bandwidth [GHz] ( $\Gamma_{in} \leq -10$ dB)	> 18.5 @ 60 GHz
$\epsilon_r$	3.55 (@ 40 GHz)
$\tan(\delta)$	0.0027 (@ 10 GHz)
$\eta_{rad}$ [%]	93 (excl. interconnect) 80 (incl. interconnect)
gain [dBi]	9.63 - 10.14
cost (relative)	low

a "kiosk in a store" scenario, see also Table 3.1 and the argumentation in Section 3.1.

Finally, it shall be pointed here that the radiation efficiency of the antenna could not be confirmed directly. Here, the broadside gain measurement was used as an indication for the validity of the simulation result. Hence, in order to measure the efficiency in future experiments, it is recommended to extend the radiation pattern setup from Section 4.3 to include full hemispherical scan capabilities. By this, the total radiated power can be determined, such that the radiation efficiency can be calculated directly using Equation (2.50).





## Antenna-on-Chip concept<sup>1</sup>

---

### 5.1 Technology choice

Based on the results of the literature study in Section 3.3, an AoC concept was developed in standard IC fabrication technology. For this, NXP's BiCMOS process Qubic4X was chosen as integration technology due to its relatively high substrate resistivity of about  $20 \Omega\text{cm}$ , see [64]. Qubic4X features an approximately  $10 \mu\text{m}$  thick back-end with five metal layers, see also Figure 3.3. Moreover, NXP grinds down their wafers to a minimum silicon thickness of  $200 \mu\text{m}$  as a standard processing step. Similar to the micromachining post-processing technique described in Section 3.3, substrate thinning is used here to increase the radiation efficiency of the on-chip antenna design. In contrast to micromachining, however, the used grinding process is a standard technique in the semiconductor world and does not significantly increase the fabrication costs. With respect to the antenna type, an on-chip dipole structure was chosen since, just like for the AiP design from the preceding chapter, a basic differential antenna topology is desired, see Section 3.1, that can be implemented in the electrically thin back-end of the IC.

From the results of the literature study in Section 3.3, the radiation efficiency was identified as the major bottle-neck for AoC designs. Therefore, the substrate loss mechanism of an on-chip dipole antenna was extensively investigated in the outline of this study. The results are summarized in the following section. Based on those findings, a basic AoC concept was developed that exhibits a significantly higher radiation efficiency as compared to similar state-of-the-art designs. This concept is described in Section 5.2.2, where also simulation results of a prototype are presented.

---

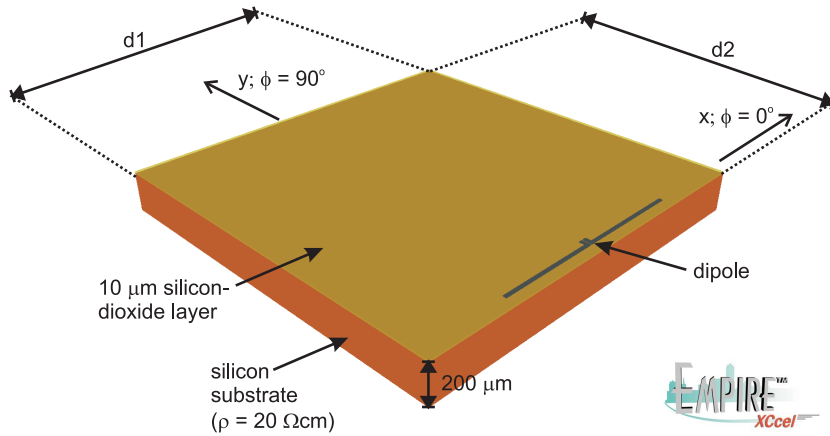
<sup>1</sup>The results of this chapter were published in [56] and [63].

Section 5.3 then presents a general packaging concept for the AoC design, which was also used for the radiation pattern measurements of the AoC prototype. A summary of all measurement results is given in Section 5.4. As a further prove of feasibility and as an application example of on-chip antennas at 60 GHz, a complete radar including antennas was integrated in a single Qubic4Xi chip in a research project together with Omnicaradar, see [65]. Some initial measurement results of this demonstrator are given in Section 5.5. Finally, conclusions and a comparison to state-of-the-art AoC designs are presented in Section 5.6.

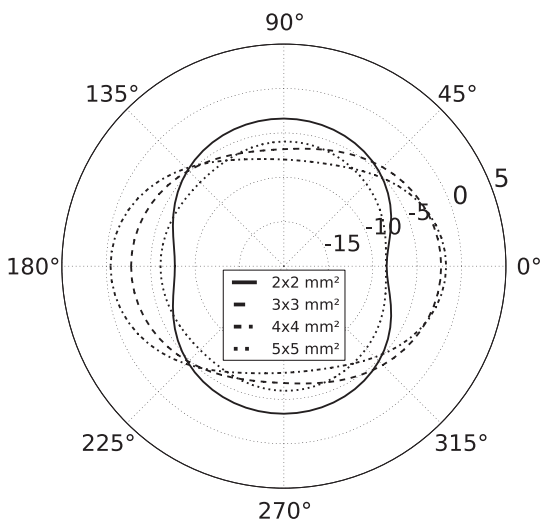
## 5.2 Design

### 5.2.1 Mode suppression in the silicon substrate

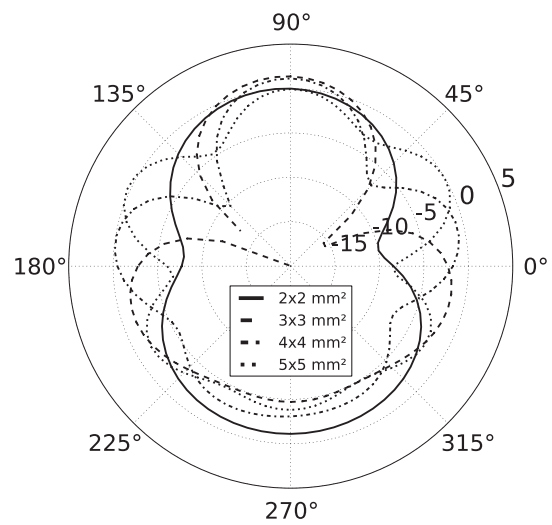
In general, any dielectric substrate can guide electromagnetic energy, as introduced in Section 2.1.4. The cut-off frequencies of the individual modes can be calculated from Equation (2.33). From this, the 0<sup>th</sup> order TE and TM mode can be determined to have a 0 Hz cut-off frequency and, consequently, can always get excited. The amount of energy that is launched in those modes by an antenna depends on the specific antenna type, its location and orientation with respect to the substrate, but also on the dielectric contrast between the substrate and the surrounding medium, usually air. The larger the permittivity of the substrate material, the more energy is confined in it. Since the real part of the dielectric constant of silicon,  $\epsilon'_r = 11.9$ , is rather large in comparison with typical microwave materials, like RO4003 with  $\epsilon'_r = 3.55$ , this topic requires special attention for a AoC design. This holds in particular for the doped silicon of typical (Bi-)CMOS processes since a significant portion of that confined electromagnetic energy will simply get dissipated into heat here. Furthermore, since silicon chips are of finite size, the excited substrate waves get partly reflected and partly radiated at the chip's edges. The radiated part superimposes with the waves that are directly radiated from the antenna and, hence, strongly affects the antenna's radiation pattern. Therefore, the exact overall pattern depends to a large extent on the dimensions of the chip. Figure 5.1 illustrates this relation. It shows the simulated gain patterns at 60 GHz of an integrated dipole antenna on BiCMOS chips of different dimensions  $d_1 \times d_2$ , see Figure 5.1(a). In order to reduce the amount of lossy silicon around the dipoles, they were placed at a distance of 50  $\mu\text{m}$  from the edge of the silicon substrate, which has a thickness of 200  $\mu\text{m}$  and an electric resistivity of 20  $\Omega\text{cm}$ . Also shown in the figure are the simulated radiation efficiencies for each chip size. Since, generally, in a larger chip more energy is dissipated in the silicon substrate before it gets radiated from the chip's edge, a larger chip achieves a lower efficiency.



(a) Considered antenna integration scenario for analyzing the chip size impact on the radiation characteristics.



(b) Gain pattern at 60 GHz for  $\phi = 0^\circ$ .



(c) Gain pattern at 60 GHz for  $\phi = 90^\circ$ .

$2 \times 2 \text{ mm}^2$	$\eta_{\text{rad}} = 51.52 \%$	$4 \times 4 \text{ mm}^2$	$\eta_{\text{rad}} = 38.73 \%$
$3 \times 3 \text{ mm}^2$	$\eta_{\text{rad}} = 40.74 \%$	$5 \times 5 \text{ mm}^2$	$\eta_{\text{rad}} = 36.41 \%$

**Figure 5.1.** Considered antenna integration scenario and its simulated gain patterns for different chip sizes.

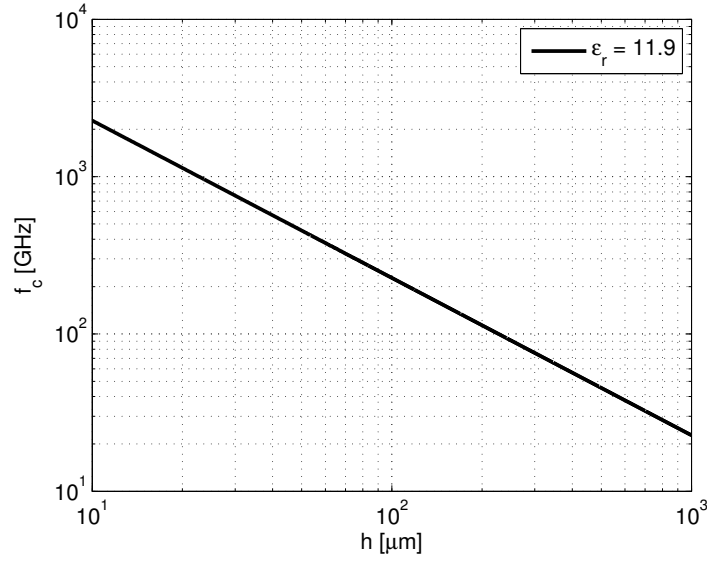
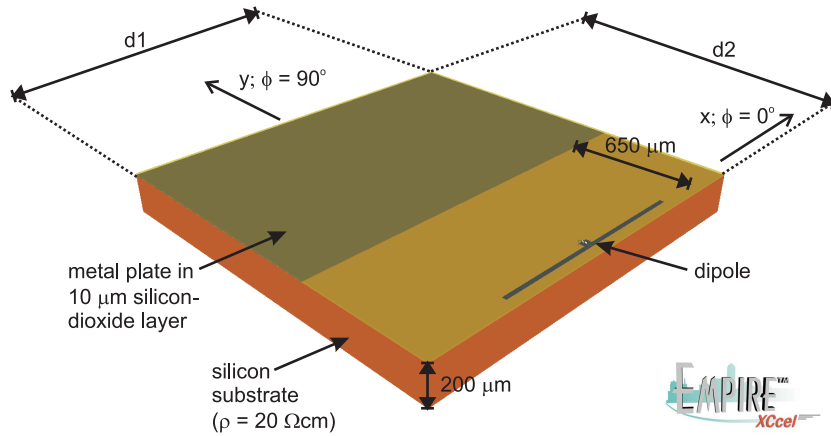


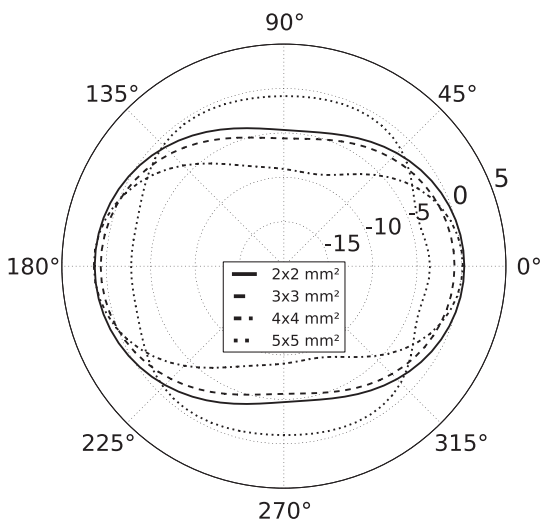
**Figure 5.2.** Cut-off frequency,  $f_c$ , versus the thickness of a silicon substrate,  $h$ , according to Equation (2.34).

In order to enhance the radiation properties of the on-chip dipole, a metal plate on top of the silicon can be implemented. By this simple measure, the substrate can be considered as a grounded dielectric slab, also known as surface waveguide, with corresponding surface-waveguide modes, see Section 2.1.4. The cut-off frequencies of its modes can be obtained from Equation (2.34). From this, the lowest-order TM-mode (TM<sub>0</sub>-mode) can be determined to exhibit its cut-off frequency at 0 Hz, i.e., it can still always get excited. The lowest-order TE-mode (TE<sub>1</sub>-mode), however, exhibits a non-zero cut-off frequency. Hence, for frequencies below cut-off, all guided TE-modes are suppressed. For a 60 GHz antenna design, for example, the thickness of the silicon substrate needs to be below 350  $\mu\text{m}$  in order to avoid the propagation of TE-modes up to 66 GHz, as shown in Figure 5.2.

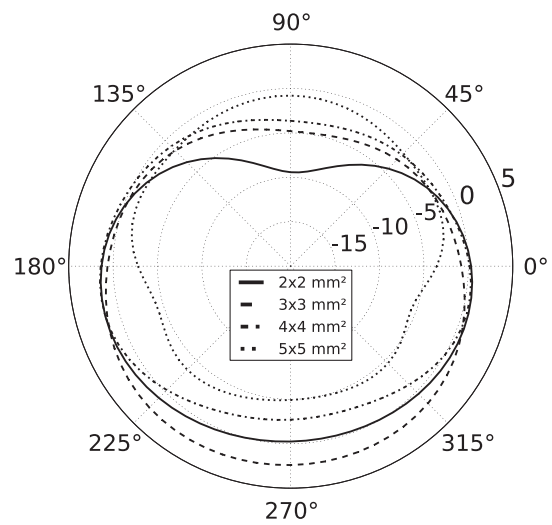
Figure 5.3 shows the radiation patterns and efficiencies of the on-chip dipole antennas from Figure 5.1 when a rectangular metal plate is implemented at a distance of 650  $\mu\text{m}$  from the dipole, see Figure 5.3(a). By this, the plate also acts as a reflector with a length  $d_1$  while suppressing the TE-modes behind the reflecting edge. Therefore, the design can be understood as a rudimentary on-chip Yagi-antenna, see [66]. Comparing the results presented in Figure 5.3 with the ones from Figure 5.1, it is evident that the simulated radiation efficiencies are significantly improved. The radiation pattern still changes with varying chip size, however, but the sensitivity of its shape to the chip's dimension is reduced. The remaining chip size dependence might be caused by the TM<sub>0</sub>-mode or the varying reflector length  $d_1$ .



(a) Considered antenna integration scenario with metal plate for TE-mode suppression.



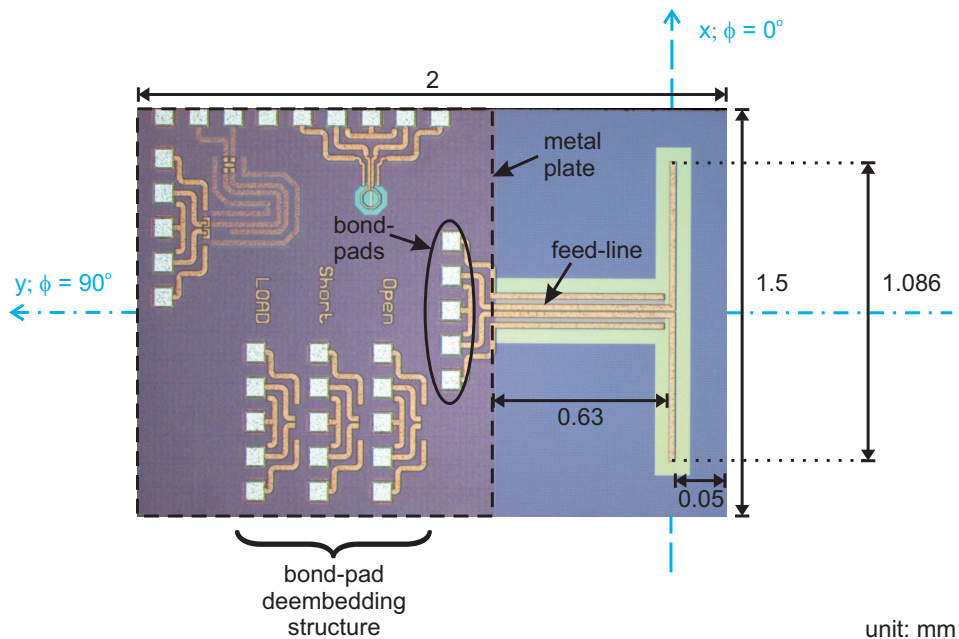
(b) Gain pattern at 60 GHz for  $\phi = 0^\circ$ .



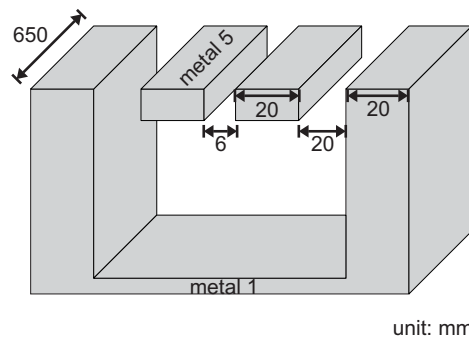
(c) Gain pattern at 60 GHz for  $\phi = 90^\circ$ .

$2 \times 2 \text{ mm}^2$	$\eta_{\text{rad}} = 66.67 \%$	$4 \times 4 \text{ mm}^2$	$\eta_{\text{rad}} = 60.09 \%$
$3 \times 3 \text{ mm}^2$	$\eta_{\text{rad}} = 66.32 \%$	$5 \times 5 \text{ mm}^2$	$\eta_{\text{rad}} = 53.66 \%$

**Figure 5.3.** Improved radiation characteristics of the dipoles from Figure 5.1 by implementing a metal plate in the lowest layer of the IC's back-end.



(a) Photograph of fabricated AoC prototype.



(b) Feed-line details

**Figure 5.4.** Final design parameters of the AoC prototype.

## 5.2.2 Antenna design

The metal-covered-substrate approach from Section 5.2.1 was used to design an on-chip dipole antenna for the 60 GHz band using NXP's BiCMOS process Qubic4X. A photograph of a fabricated prototype is shown in Figure 5.4(a). Since an on-chip antenna does not necessarily require any packaging of the IC, a conceptual design was made for an unpackaged chip here. By this, the antenna performance solely depends on the IC technology parameters and, therefore, package-independent conclusions can be drawn. Furthermore, since the on-chip implementation allows a direct matching of antenna and amplifier, the reference impedance for the AoC was chosen to  $Z_0 = 35 \Omega$ , which is based on the amplifier design from [67]. Moreover,

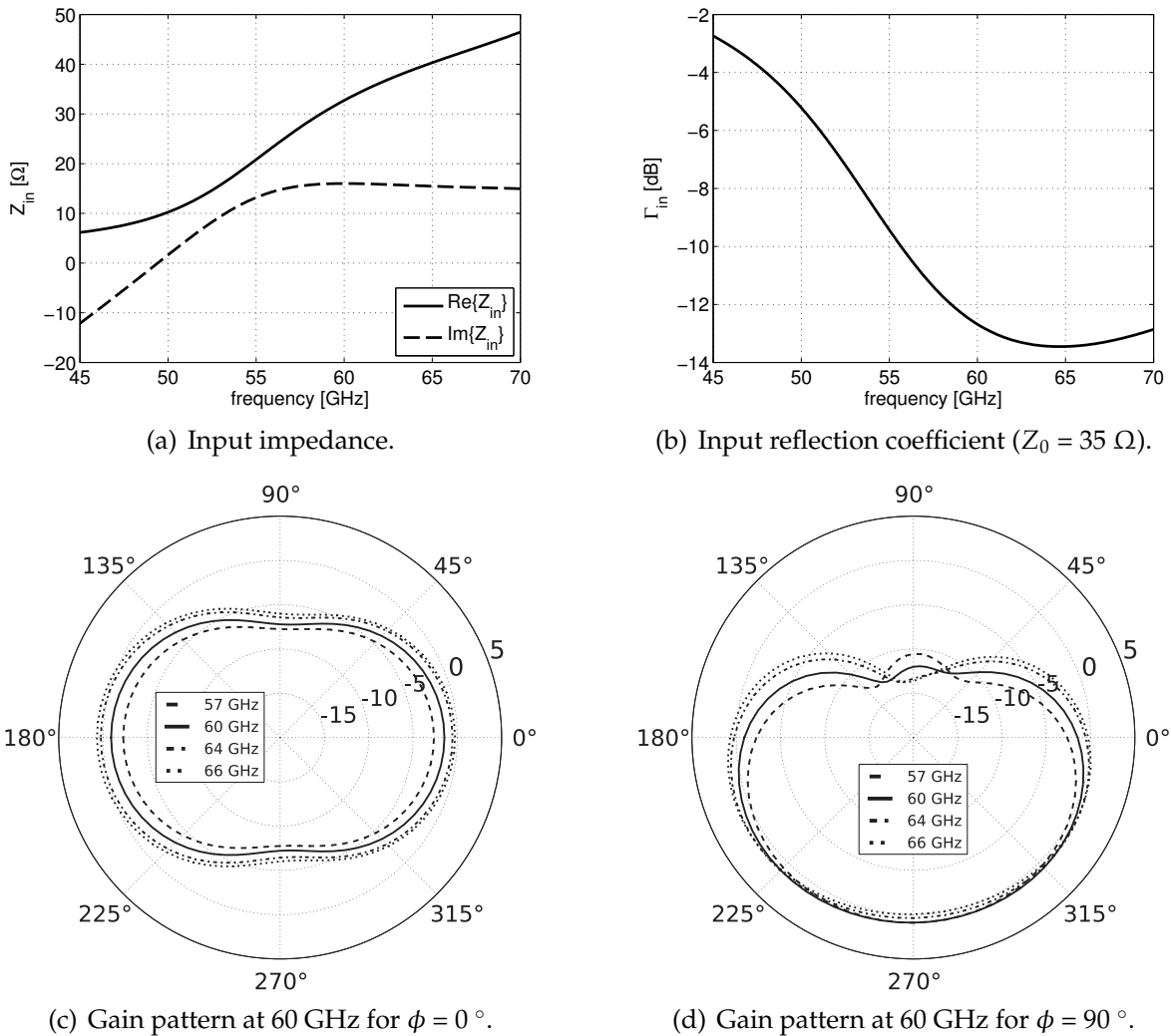


**Figure 5.5.** Simulated antenna parameters of the AoC prototype from Figure 5.4(a).

the metal plate for substrate mode suppression is implemented in the lowest layer of the IC's back-end. Hence, the on-chip interconnects for the front-end electronics can be implemented on top of the metal plate, whereas cut-outs will then be required for accessing the transistors as well as for on-chip inductors. The shown feed-line that connects the dipole to the amplifier is based on those published in [68] with a U-shaped ground plane. A detailed drawing with its dimensions is provided in Figure 5.4(b). Its characteristic impedance is optimized in order to match the input impedance of the dipole to the specified reference impedance.

The simulated antenna parameters of this prototype, obtained with Empire XCell, are summarized in Figure 5.5. The predicted input impedance, shown in Figure 5.5(a), is well matched to the specified reference of 35  $\Omega$ , see Figure 5.5(b). The gain patterns for  $\phi = 0^\circ$  and  $\phi = 90^\circ$  are provided in Figures 5.5(c) and 5.5(d), respec-



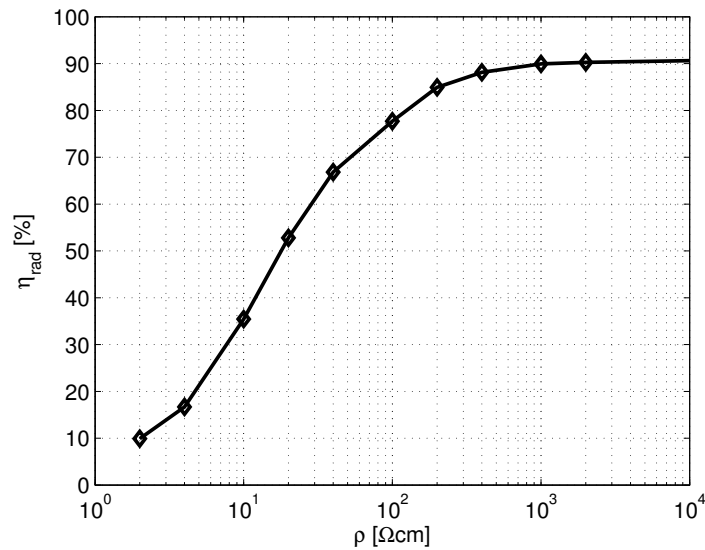


**Figure 5.6.** Simulated radiation efficiency at 60 GHz of the AoC design with respect to its substrate resistivity.

tively. The maximum gain of this design lies between 0.96 dBi at 57 GHz and 1.47 dBi at 66 GHz. These values are rather low for a dipole-based antenna, especially since the on-chip metal plate reflects some of the radiated power and, thus, increases the directivity of the overall structure. Since antenna gain and directivity are directly related by the radiation efficiency of the antenna, see Equation (2.54), this already indicates the expected lower efficiency of the on-chip antenna with respect to the AiP design. And indeed, the simulated values for the AoC range from only 45 % to 60 % throughout the 60 GHz-band.

The simulation results of this prototype show a significant improvement of this AoC design in standard technologies with respect to similar state-of-the-art designs, see Table 3.3. However, the radiation efficiency does not match the value of the AiP design from Chapter 4, which is mainly related to the low resistivity of the silicon substrate. Therefore, the question might be raised what substrate resistivity value would be required in order to achieve a similar efficiency as the AiP design from the previous chapter. Figure 5.6 shows the relation between the silicon's resistivity and the radiation efficiency of the prototype from Figure 5.4(a) at 60 GHz. It shows a general  $1/(1 + \tan(\delta))$  relation between the efficiency and the resistivity, with  $\tan(\delta)$  as defined in (2.18). Especially for large substrate resistivity values, however, the ohmic losses in the back-end metalization result in a convergence of the efficiency towards 90 %. For very low substrate resistivities, the silicon substrate approaches the behavior of a conductor. Thus, the radiation efficiency converges towards the value of a dipole over a metal plate below the back-end. Moreover, from Figure 5.6 it is evident that a substrate resistivity of at least 100  $\Omega\text{cm}$  is required to achieve a comparable

radiation efficiency of this AoC design to the AiP concept from Chapter 4.

### 5.3 Basic package concept

The AoC concept from the preceding section does not use any packaging in order to draw package independent conclusions for antennas in standard IC technologies. Such an antenna concept is conceivable, for example, for complete systems on a single chip. However, in a general scenario the mm-wave ICs are mounted on a larger system PCB where they also have to be interconnected to off-chip components. Therefore, a package concept for the AoC design from Section 5.2.2 was developed for this general case, which is presented in this section.

When the AoC concept with thinned silicon substrate from Section 5.2.2 is directly placed on a larger system PCB, the antenna's near-field will be influenced and, thus, its input impedance will change. In an extreme case, the antenna could be so seriously mismatched with respect to the on-chip amplifier that most of the impinging power will get reflected at its interface. Hence, in order to achieve a robust AoC performance that is independent of the choice of the system PCB's material and thickness, a package has to be designed that shields the antenna from the system PCB. In general, the whole package has to be taken into consideration already in the antenna design process since, just like the system PCB, the package also influences the near-field of the antenna. The package presented in this section, however, was designed to adjust the input impedance of the AoC from the preceding section towards the reference impedance of the measurement equipment, i.e.,  $100 \Omega$ , see Section 4.3.

The proposed basic package concept is shown in Figure 5.7. It consists of a RO3003 substrate with a relative dielectric constant of  $\epsilon'_r = 3$  and loss tangent of  $\tan(\delta) = 0.0013$ , which are specified up to 40 GHz and 10 GHz, respectively, see [31]. The bottom side of the substrate is entirely metalized in order to shield the antenna from the system PCB and to achieve upward radiation. The top-side is also metalized, whereas a sufficiently large area is left open around the dipole. Since the input/output signals of the chip are at IF or even baseband level, the chip can be easily connected to the top-side of the package by generic wire-bond technology. The signals are then routed to the bottom-side of the substrate using vias, where the interconnect to a system PCB can be accomplished in generic soldering technology, see also Section 4.2. The thickness of the RO3003 substrate was chosen to 0.5 mm in order to obtain an acceptable input impedance of the antenna with respect to the measurement equipment, i.e.,  $100 \Omega$  for differential measurements. By this, the input impedance and input reflection coefficient as shown in Figures 5.8(a) and 5.8(b) are achieved. The input match with respect to the differential system impedance of  $100 \Omega$  is better than -10 dB around 59 GHz and better than -6 dB throughout the

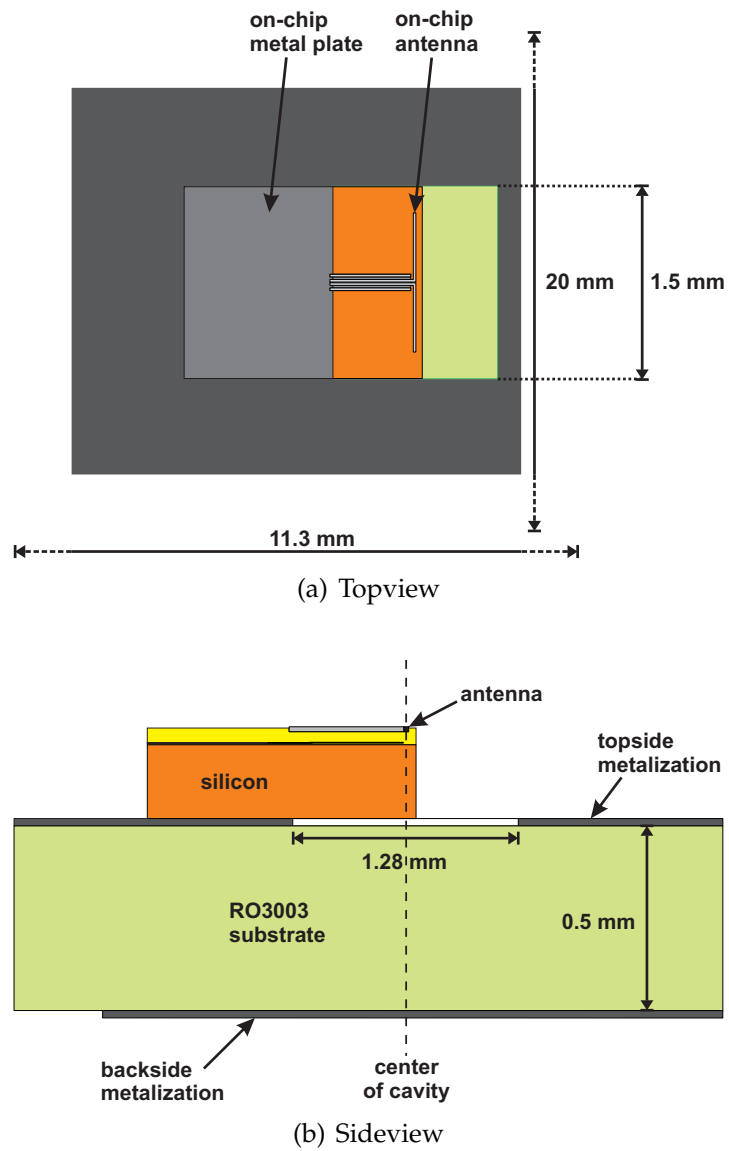
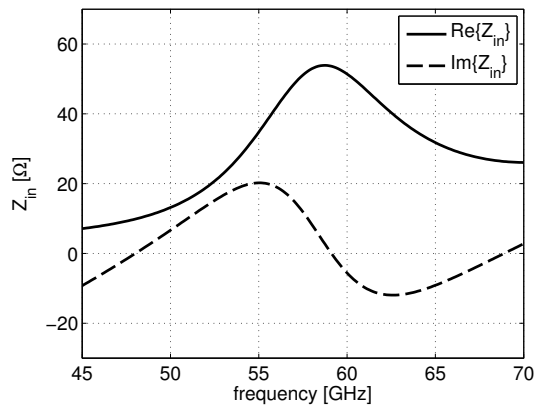
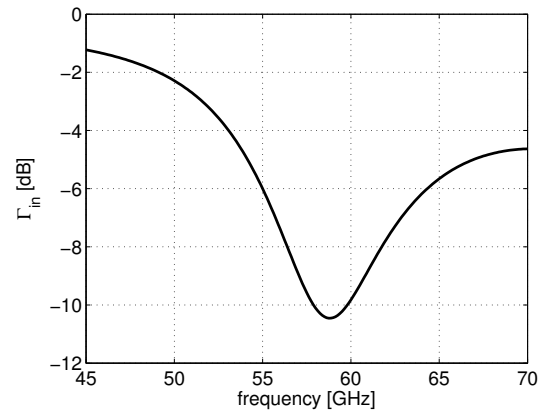


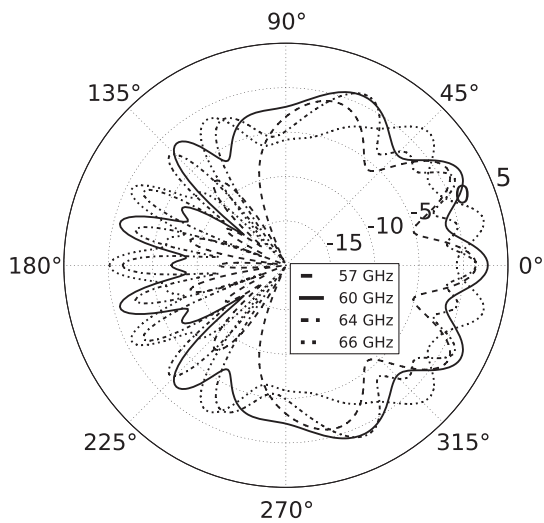
Figure 5.7. Conceptual drawing of the proposed package.



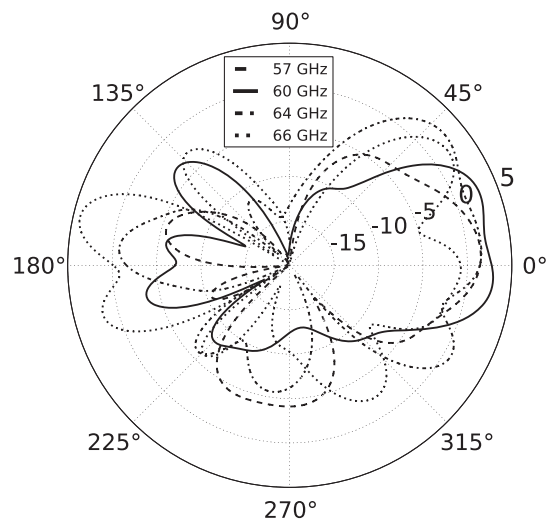
(a) Input impedance



(b) Input reflection coefficient ( $Z_0 = 100 \Omega$ ).



(c) Gain pattern at 60 GHz for  $\phi = 0^\circ$ .



(d) Gain pattern at 60 GHz for  $\phi = 90^\circ$ .

**Figure 5.8.** Antenna parameters of the AoC design from Section 5.2.2 when mounted on the PCB shown in Figure 5.7.

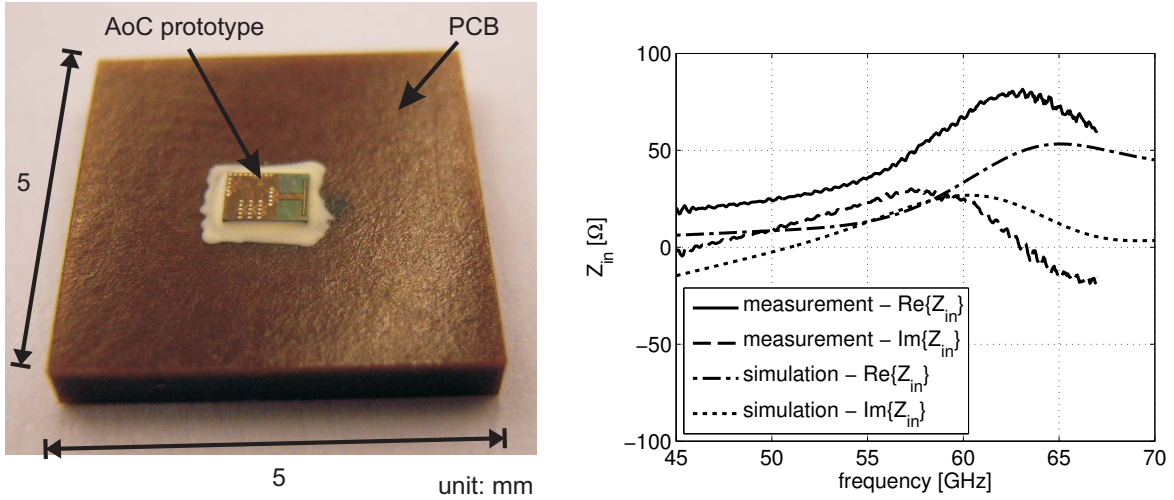
whole 60 GHz band. The predicted gain patterns of this structure for  $\phi = 0^\circ$  and  $\phi = 90^\circ$  are provided in Figures 5.8(c) and 5.8(d), respectively. Due to the electrically large size of the RO3003 substrate, the pattern exhibits large gain variations in the  $\phi = 0^\circ$  plane. Those ripples are a result of diffraction. The energy radiated towards to the edges of the PCB gets diffracted there and superimposes with the direct radiation from the on-chip antenna. Depending on the observation angle, the superimposed components can be in phase, resulting in a gain-peak for this angle, or they can be in opposite phase, resulting in a gain-dip. The same diffraction mechanism is also the cause of noticeable back-lobes in the gain pattern. Note that both effects, strong gain ripples and a large back-side radiation, are normally undesired for an antenna design. Therefore, EBG structures like the one presented in [69] may be used to suppress those effects or a significantly smaller package has to be chosen to avoid this problem. For a first prototype, however, a low package design complexity was desired and its size was determined by handling considerations for production and measurement purposes, such that those effects were accepted here. Finally, the radiation efficiency of the AoC inside the measurement package was computed to range from 36 % at 57 GHz to 57 % at 66 GHz, from which it can be concluded that the package does not severely deteriorate the AoC performance.

## 5.4 Measurement results

For the verification of the simulation results from Section 5.2.2, a prototype was measured using the input impedance measurement setup that is described in Section 4.3. The obtained results are presented in Section 5.4.1. The radiation pattern was then measured with the radiation pattern measurement setup published in [70]. For this, the chips were mounted on a package prototype from Section 5.3, whose design was extended to allow the probe to land at a sufficient distance from the chip. A detailed description of this package extension as well as the obtained measurement results are provided in Section 5.4.2.

### 5.4.1 Input impedance

In order to determine the input impedance of the AoC prototype, some ICs were glued in the center of PCBs as shown in Figure 5.9(a). The PCBs had a thickness of 1.6 mm and their permittivity was approximated to  $\epsilon'_r = 4.4$ . After calibration, the measurements were then performed by landing a differential GSSG-probe with a pin pitch of 200  $\mu\text{m}$  directly on the bond-pads of the antenna, shown in Figure 5.4(a). The GSSG-probe essentially consists of a GS-probe and a SG-probe, see Figure 4.7 in Section 4.3, that are mounted together on the same body such that the signal pins



(a) Photograph of a AoC prototype on PCB support. (b) Input impedance of the prototype shown in (a).

**Figure 5.9.** Photograph and input impedance of a AoC prototype, which was glued on a PCB for direct on-chip probing.

exhibit the desired pitch of  $200 \mu\text{m}$ . In order to achieve a differential excitation of the antenna, the individual probes were then connected to a magic-Tee, i.e., a balun, which was used to split the unbalanced signal from the VNA into two signals with equal amplitude but  $180^\circ$  phase difference with respect to each other. For deembedding, three exact copies of the bond-pads with short, open, and load termination, respectively, were measured. Those pad structures are also shown in the photograph of the prototype, i.e., Figure 5.4(a). Their measured input reflection coefficients are related to the input reflection coefficients of the termination according to

$$\Gamma_{\text{meas.,short}} = S_{11,\text{pads}} + \frac{S_{12,\text{pads}} S_{21,\text{pads}} \Gamma_{\text{short}}}{1 - S_{22,\text{pads}} \Gamma_{\text{short}}}, \quad (5.1)$$

$$\Gamma_{\text{meas.,open}} = S_{11,\text{pads}} + \frac{S_{12,\text{pads}} S_{21,\text{pads}} \Gamma_{\text{open}}}{1 - S_{22,\text{pads}} \Gamma_{\text{open}}}, \quad (5.2)$$

$$\Gamma_{\text{meas.,load}} = S_{11,\text{pads}} + \frac{S_{12,\text{pads}} S_{21,\text{pads}} \Gamma_{\text{load}}}{1 - S_{22,\text{pads}} \Gamma_{\text{load}}}, \quad (5.3)$$

where the left-hand-side are the measured quantities. The right-hand-side consists of the reflection coefficients of the short, open, and load termination, i.e.,  $\Gamma_{\text{short}} = -1$ ,  $\Gamma_{\text{open}} = 1$ , and  $\Gamma_{\text{load}} = 0$ , respectively, and the two-port S-parameters of the bond-pads. From the three linearly independent Equations (5.1) to (5.3), the parameters  $S_{11,\text{pads}}$ ,  $S_{22,\text{pads}}$ , as well as the product  $S_{12,\text{pads}} S_{21,\text{pads}}$  can be determined. The input reflection

coefficient  $\Gamma_{\text{AUT}}$  of the on-chip antenna is then given by

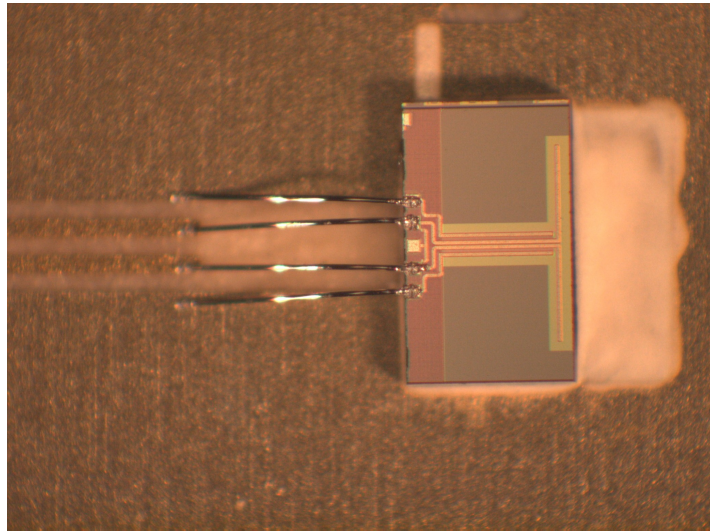
$$\Gamma_{\text{AUT}} = \frac{\Gamma_{\text{AUT+pads}} - S_{11,\text{pads}}}{S_{22,\text{pads}}(\Gamma_{\text{meas}} - S_{11,\text{pads}}) + (S_{12,\text{pads}}S_{21,\text{pads}})}, \quad (5.4)$$

with  $\Gamma_{\text{AUT+pads}}$  the measured input reflection coefficient of the prototype, i.e., including the bond-pads. The input impedance of the antenna can now be calculated with the aid of (4.2), see Section 4.3.

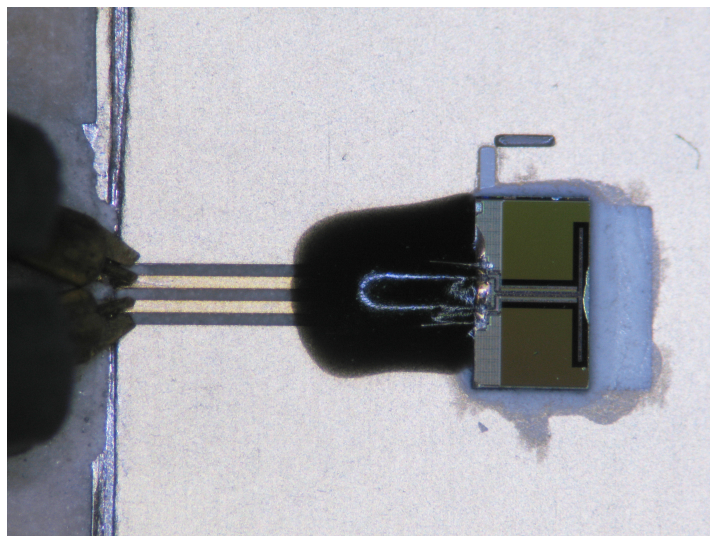
A comparison of the impedance obtained by this method with the results obtained with Empire XCel is provided in Figure 5.9(b). From this, a frequency offset of about 3 GHz for the imaginary part and a magnitude offset of about 28  $\Omega$  (peak-to-peak) for the real part becomes evident. There are several possible reasons for this deviation with respect to the measurement setup. First of all, the chips were glued by hand, such that they might not have been perfectly centered on the PCBs. Moreover, the glue was neglected in the simulation and the permittivity of the PCBs, assumed to be  $\epsilon'_r = 4.4$ , was not exactly known at 60 GHz. Furthermore, perfect short, open, and load terminations were assumed in Equations (5.1) to (5.3) for deembedding the probe-pads. For the short, however, a parasitic inductance is likely while the open may exhibit a parasitic capacitance. Hence, those approximations are expected to affect the accuracy of the measurement. Finally, due to the close proximity of antenna and probe-tip, the possibility of mutual coupling between antenna and probe cannot be excluded. In view of all those factors, the shown agreement between simulation and measurement can be considered as acceptable here.

### 5.4.2 Radiation pattern

For the radiation pattern measurements of the AoC prototype, a chip was mounted on a package prototype as described in Section 5.3. In order to reduce the impact of the probe on the measurement results, the on-chip probe pads were connected to an off-chip transmission line using standard wire-bond technology, see Figure 5.10(a). By this, the probe could be landed at a sufficient distance away from the radiating element. As described in [6], however, a bond-wire is commonly considered to be a non-negligible inductance at mm-wave frequencies that significantly adds to the overall impedance. Here, instead of adding the bond-wires as parasitic elements, an alternative approach of creating a differential bond-wire transmission line was considered. For this, the chip had to be cut directly at the bond-pads that are connected to the antenna. Figure 5.10(a) shows the truncated chip with the bond-wires in GSSG configuration. In order to protect the wires from external hazards, they were overmolded as shown in Figure 5.10(b). Moreover, in order to connect the chip to the PCB without significantly altering the input impedance of the overall structure, the bond-wire transmission line length was chosen to be 1.44 mm, which corresponds



(a) Before adding glob-top.

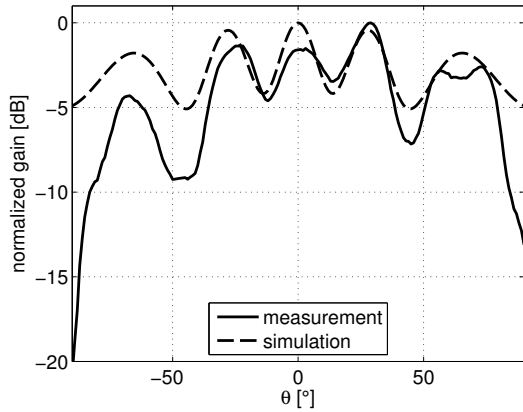


(b) With glob-top over bond-wires.

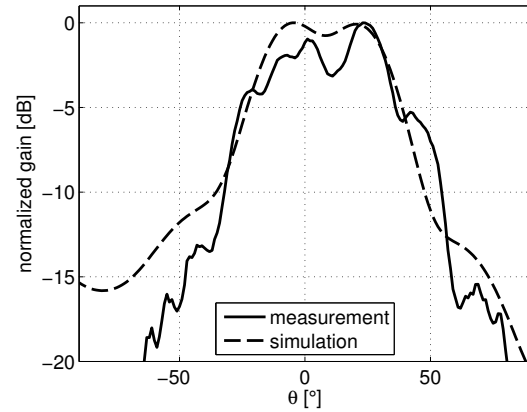
**Figure 5.10.** Photograph of the AoC prototype when mounted on the package prototype.

to half a guided wavelength at 60 GHz for the approximated relative permittivity  $\epsilon'_r = 3$  of the molding compound. On the PCB level, the bond-wires are connected to a differential coplanar waveguide (CPW). Its dimensions were chosen to allow the landing of a GSSG measurement-probe with a pin-pitch of  $200\ \mu\text{m}$ . Hence, the spacing between each conductor was  $100\ \mu\text{m}$  with a signal line width of also  $100\ \mu\text{m}$ . The characteristic impedance of this differential CPW is  $130\ \Omega$  and, therefore, its length was also designed to be half a guided wavelength at 60 GHz, i.e.,  $1.81\ \text{mm}$ , in order to transform the on-chip input impedance to the probe-tip with as little disturbance

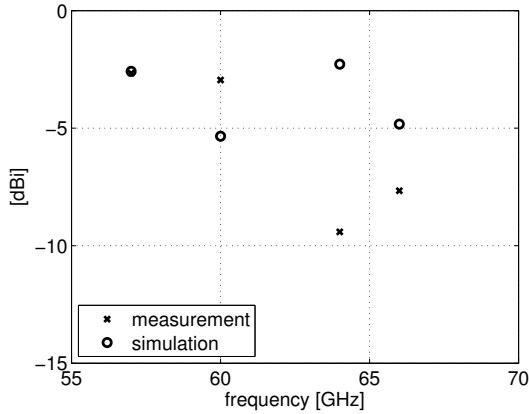




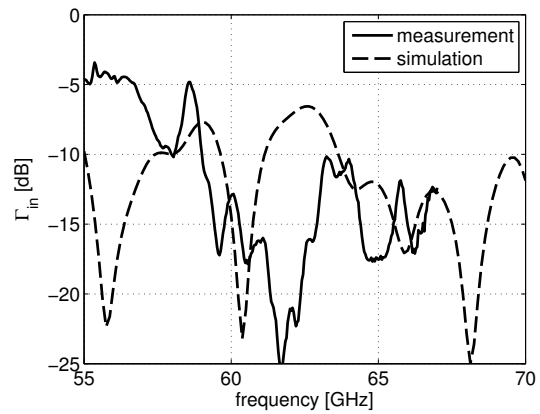
(a) Normalized gain pattern for the copolarization component at  $\phi = 0^\circ$  ( $E_\theta$ , normalized to maximum value).



(b) Normalized gain pattern for the copolarization component at  $\phi = 90^\circ$  ( $E_\phi$ , normalized to maximum value).



(c) Measured versus simulated gain in broadside direction ( $\theta = 0^\circ$ ).



(d) Input reflection coefficient ( $Z_0 = 50 \Omega$ ).

**Figure 5.11.** Comparison between measured and simulated antenna parameters of the AoC prototype mounted on the package as shown in Figure 5.10(b).

as possible.

Figures 5.11(a) and 5.11(b) show a comparison between the simulated and measured normalized gain patterns at 60 GHz of this prototype for both its principal planes. The simulated patterns agree well with the measurements, which were performed with the setup described in [70]. The deviations can be explained by the same reasons as described in Section 4.4, which are mainly related to the presence of the mm-wave probe. The patterns for 57 GHz, 64 GHz, and 66 GHz are again provided in Appendix B for completeness, see Figure B.2. Finally, the broadside gain of the antenna was measured using the setup from Section 4.3 in combination with a GS-probe. Figure 5.11(c) provides those results in comparison with the gain values obtained from a simulation with Empire XCell. For the simulation, the same simplified probe model

was included that was also used for the gain determination of the AiP prototype. The simulated values deviate between 0.1 dB at 57 GHz and 7.1 dB at 64 GHz, which is significantly larger than the results of the AiP concept. Since the simulated input reflection coefficient also deviates from the measurements, see Figure 5.11(d), the reason for this is seen to be an additional loss mechanism in the measurement package that is not accounted for in the simulation setup. The soft RO3003 substrate, for example, turned out to be disadvantageous for wire-bonding, such that only one sample could be successfully fabricated. The deviations between simulated and measured gain might, therefore, be a result of a defective electrical connection between the bond-wires and the transmission line on the PCB. Further causes for a deviation between simulation and measurement are the negligence of the glue under the IC in the simulation and the not exactly known and therefore approximated shape of the bond-wires and the glob-top encapsulation.

Due to the acceptable agreement between simulated and measured input impedance presented in Section 5.4.1 as well as the normalized gain patterns, the Empire-model can still be concluded to be a good representation of the antenna. Similar to the AiP concept presented in Chapter 4, however, the accurate verification of the radiation efficiency remains an open task for future work.

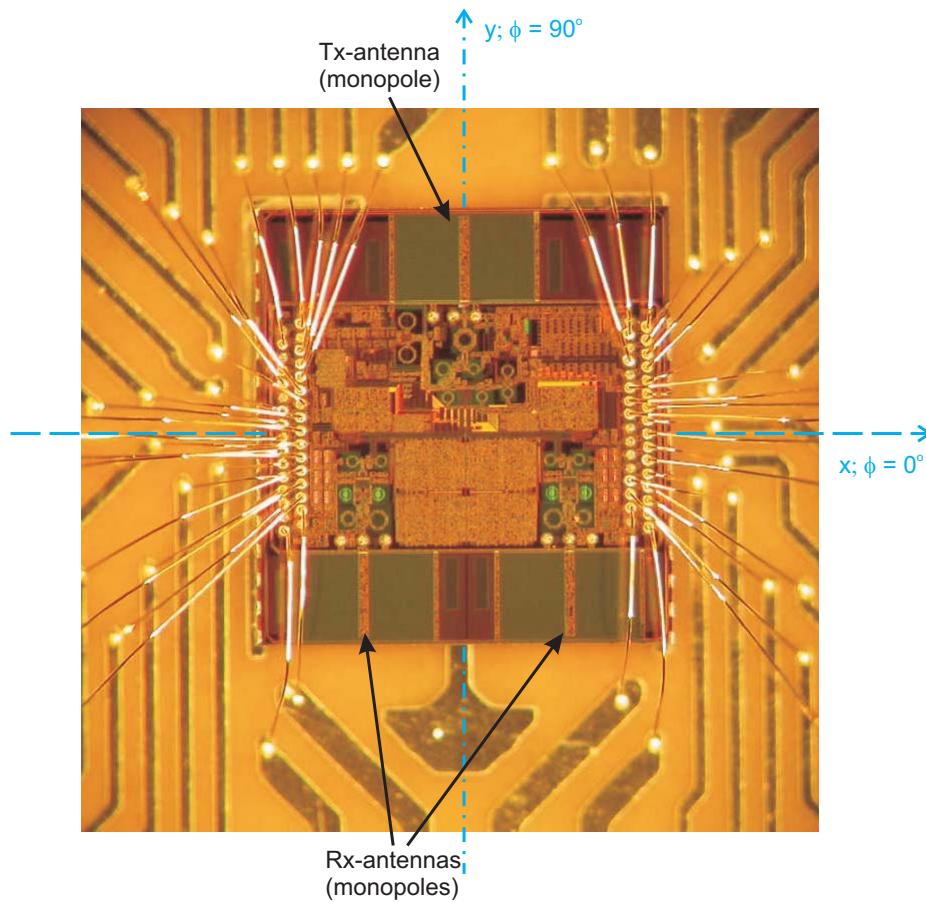
## 5.5 Application example: Single-chip radar module

As a final prove of feasibility and as an application example for on-chip antennas in standard BiCMOS technology, a complete 60 GHz radar system was implemented in a single 200  $\mu\text{m}$  thick Qubic4Xi-chip<sup>2</sup>. This section briefly summarizes the initial results from this experiment.

The single-chip radar module is based on the frequency-modulated continuous-wave (FMCW) radar chip from Omnicor, which was modified to also include the antennas. Thanks to the use of on-chip antennas, the chip's radar input and output signals are reduced to the analog or digital baseband level, depending on the programmed settings, see [65]. A photograph of a fabricated chip prototype is shown in Figure 5.12(a). It consists of a transmitter and two independent receivers. Here, rather than using dipole antennas, monopoles were chosen as antenna types since they require significantly less on-chip real-estate. The monopoles were designed to exhibit their first resonance at 60 GHz. Using the inherent AoC advantage, the antennas are directly connected to the amplifiers, with the on-chip electronics acting as ground plane for the monopoles. Furthermore, in order to minimize the disturbance

---

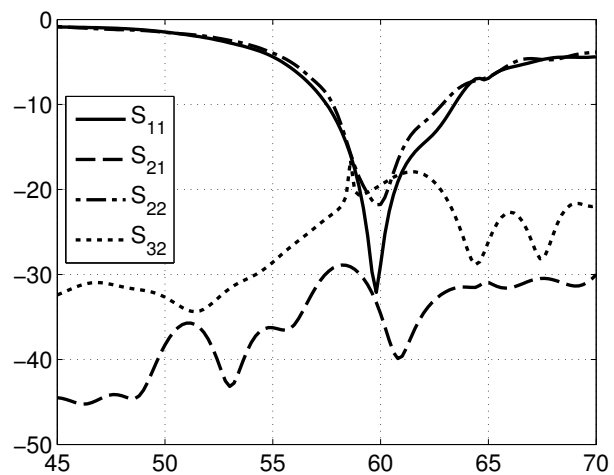
<sup>2</sup>Just like Qubic4X, the silicon substrate of the Qubic4Xi process also exhibits an electric resistivity of 20  $\Omega\text{cm}$ . Moreover, the back-ends of both processes are mainly identical.



(a) Radar-chip (topview) with the transmit antenna (top) and the two receive antennas (bottom).



(b) Packaged chips from the top side (top right) and bottom side (bottom left).



(c) Simulated S-parameters ( $Z_0 = 50 \Omega$ ) of the monopole antennas in the single-chip radar modules (port 1: Tx; port 2&3: Rx).

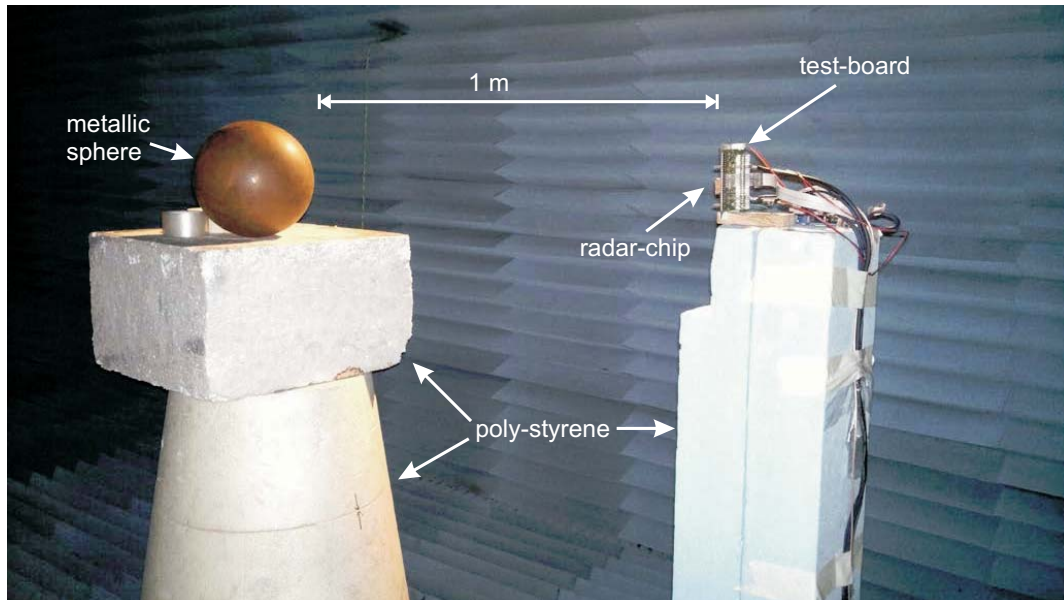
**Figure 5.12.** Photographs of the single-chip-radar module (courtesy of Omniradar).

of the antenna's near-field, a sufficiently large area was left un-metalized to both sides of the antenna. Finally, the chip packaging was done according to the approach presented in Section 5.3. Due to the problems with wire-bonding on RO3003, however, the substrate was substituted for RO4003. The chip was then electrically connected to the top-side of the substrate by bond-wires, also shown in Figure 5.12(a). On the PCB-level, a dense network of transmission lines routes the signals further to the edge of the package where vias connect them to pads on its bottom side, such that the module can be soldered to a larger system PCB. The area around the monopoles on the top side of the RO4003 substrate was, again, left un-metalized. As a last step, the whole single-chip radar module was overmolded with a plastic compound, resulting in the packaged modules shown in Figure 5.12(b). The magnitude of the resulting simulated S-parameters of the on-chip antennas are provided in Figure 5.12(c), showing an input match of better than -10 dB to the reference impedance of  $Z_0 = 50 \Omega$  between 57.5 GHz and 63 GHz. The coupling between the antennas is smaller than -15 dB. The simulated radiation efficiencies range from 30 % at 57 GHz to 43 % at 66 GHz for the receive antennas and from 31 % at 57 GHz to 47 % at 66 GHz for the transmit antenna. Hence, although a process was used that is nearly identical to the one used for the packaged AoC prototype described in Section 5.3, the radiation efficiencies are slightly lower for this radar module. The reasons for this are seen to be the overmolded plastic compound as well as the different antenna topology, which cannot be placed as close to the chip's edge as the dipole from Section 5.3.

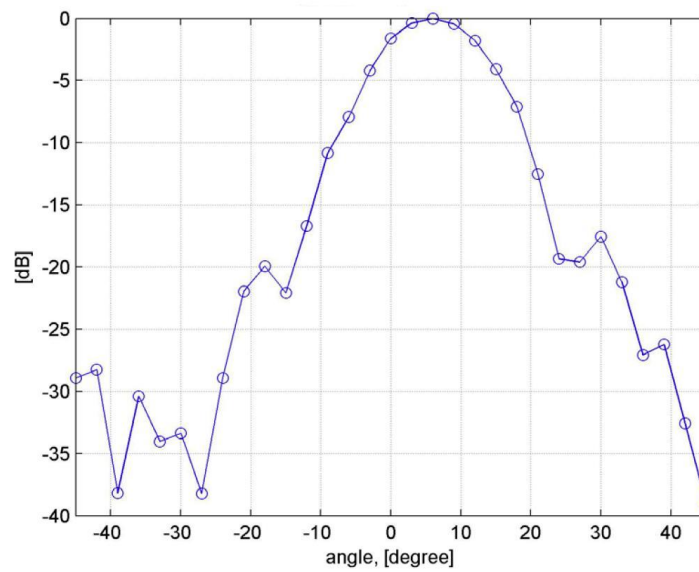
For initial test purposes, a single-chip radar-module, shown in Figure 5.12(b), was mounted on a test-board together with the peripheral electronics for programming and data signal processing<sup>3</sup>. The system was then set up in an anechoic chamber and calibrated with a corner reflector with a radar-cross-section (RCS) of  $1 \text{ m}^2$ , which was positioned at a distance of 1 m from the radar module. For this, only one receiver was used and the FMCW bandwidth was set to 4.9 GHz with approximately 59.5 GHz as center frequency. The corner reflector was then replaced by a metallic sphere with a radius of 13 cm. This setup is shown in Figure 5.13(a). With this configuration, the RCS value of the sphere was determined to be approximately -13 dBsm, which is given in decibels with respect to a  $1 \text{ m}^2$  target. This value is in line with the theoretical cross section of the electrically large metallic sphere, which is  $(\pi 13^2) \text{ cm}^2$  corresponding to -12.75 dBsm. Finally, since the signal strength and, thus, the maximum reliable detection distance strongly depend on the antenna gain in the direction of the target, the effective radar pattern was measured for the  $\phi = 0^\circ$  plane (see Figure 5.12(a)). The normalized result is shown in Figure 5.13(b), which shows the average receive signal strength over the whole FMCW bandwidth. From this, it is evident that the

---

<sup>3</sup>Note that also a metal structure was mounted on the top-side of the module that focuses the antenna beams towards the broadside direction.



(a) Radar test-setup inside anechoic chamber.



(b) Measured effective radar pattern of the radar-chip, obtained with the setup shown in (a), for  $\phi = 0^\circ$  (normalized to maximum value).

**Figure 5.13.** Radar test-setup and initial results of the single-chip-radar module (courtesy of Omnicardar).

**Table 5.1.** Key figures of proposed AoC concept according to Table 3.3.

$\rho$ [ $\Omega\text{cm}$ ]	20
silicon thickness [ $\mu\text{m}$ ]	200
post-proc. technology	none
size [ $\text{mm}^2$ ]	1.02 (Section 5.2.2)
	< 0.5 (Section 5.5)
feed topology	differential (Section 5.2.2)
	single-ended (Section 5.5)
impedance bandwidth [GHz]	> 14 @ 60 GHz (Section 5.2.2)
( $\Gamma_{\text{in}} \leq -10$ dB)	5.5 @ 60 GHz (Section 5.5)
$\eta_{\text{rad}}$ [%]	45 - 60 (Section 5.2.2)
	30 - 47 (Section 5.5)
gain [dBi]	0.96 - 1.47 (Section 5.2.2)
cost (relative)	low

maximum effective radar gain is achieved for an angle of about  $6^\circ$ , which is seen to be the result of the receive antenna offset in the x-direction, see Figure 5.12(a).

In conclusion, these initial measurement results indicate that the single-chip radar module with on-chip antennas is working excellently. Since only standard and low-cost materials and processes were used for the fabrication, this module is applicable for mass-employment in, for example, short-range industrial applications. Therefore, Omniradar is now further investigating this antenna technology for implementation in some of their future products.

## 5.6 Summary and conclusions

In this chapter, a AoC concept in standard IC technology is proposed as well as an application example presented. The simulation results of the prototypes were largely confirmed by experiments and are summarized in Table 5.1. In comparison with the state-of-the-art, see Table 3.3, it can be concluded that this approach achieves an excellent performance with respect to other AoC designs without post-processing technologies. Compared to reference designs in which post-processing techniques were applied, the proposed approach achieves comparable results. However, since only standard processes were used for the concept presented in this chapter, it is seen to exhibit a clear cost advantage.

The results of the dipole antenna from Section 5.2.2 are for an unpackaged chip. A packaged solution with this antenna type will most likely have a smaller bandwidth and lower efficiency. The -10 dB bandwidth of the packaged on-chip monopole an-

tenna presented in Section 5.5, for example, does not fulfill the European bandwidth requirement of 9 GHz. Moreover, its single-ended feed topology does not meet the specifications stated in Section 3.1. However, due to its low on-chip real-estate requirement, this antenna type still remains an attractive possibility. This conclusion is, for example, supported by the successful demonstration of the single-chip radar module, which is presented in Section 5.5.

In view of the three major application areas stated in Chapter 1, this integration concept is seen to be most suitable for the file transfer scenario. Here, the small size of an AoC solution allows a dense integration in hand-held devices while its gain of  $\geq 0.96$  dBi is sufficiently large, see Table 3.1.

## Hybrid concept<sup>1</sup>

---

### 6.1 Technology choice

After developing integrated antenna concepts for the AiP and AoC approach, which are presented in Chapters 4 and 5, respectively, an antenna concept for the hybrid approach was developed based on the findings from the literature study in Section 3.4. Here, wire-bond technology was chosen as integration platform due to its very low-cost nature, its wide-spread availability in the semiconductor industry, and its expected high radiation efficiency. For this technology, no additional processing steps are required since bond-wires are used for most IC products anyway. Moreover, even small IC design houses often own or have access to wire-bonding facilities, which makes this technology not only an ideal choice for high-volume products, but also for first prototypes and low-volume test-series. Finally, state-of-the-art wire-bonders offer a high degree of freedom with respect to the wire-shape and bond-heads for various wire-diameters are available that can either bond aluminum, gold, or even copper wires. However, so far mostly single-ended antennas were presented in this technology. Although this is seen as a disadvantage for 60 GHz communications as mentioned in Section 3.1, the vast amount of benefits of this technology permits to accept this draw-back. Therefore, for the following hybrid integrated antenna concept, a single-ended circular half-loop antenna was chosen as basic antenna type. For the wire material gold was chosen with a diameter of 25  $\mu\text{m}$  since this is common standard for most high frequency IC products.

The following section presents a general concept of a mm-wave front-end module with the proposed integrated antenna in hybrid technology. Since this concept is

---

<sup>1</sup>The results presented in this chapter were published in [71], [72], and [73].



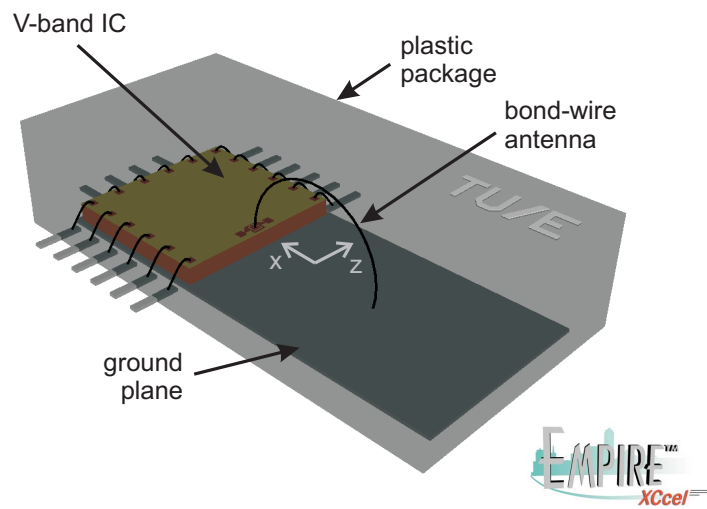


**Figure 6.1.** Conceptual drawing of the mm-wave front-end module with BWA.

also of interest for small IC design houses, a dedicated, computationally efficient modeling tool is also presented here that supplements typical IC design tools and can be integrated in the design flow process. Section 6.3 then summarizes the results of a fabricated prototype, where special emphasis is placed on the construction of a semi-circular bond-wire. Furthermore, the time-efficient antenna model from Section 6.2 is used to conduct a unified yield analysis for this antenna concept in the entire mm-wave band, which is given in Section 6.4. Finally, the chapter ends with a short summary and conclusions with respect to state-of-the-art hybrid integrated mm-wave antenna concepts.

## 6.2 Design and modeling approach

### 6.2.1 General module concept

A general concept of a mm-wave front-end module with the proposed hybrid integrated antenna concept is depicted in Figure 6.1. It shows a V-band IC inside a high frequency plastic package. The heat sink below the IC is extended on one side and serves as ground plane for a semi-circular bond-wire-antenna (BWA). The antenna originates on the chip and ends on the ground plane. The basic building blocks on the IC are an amplifier, a mixer, and a LO including PLL. The DC-supply, clock signal for LO synchronization, and the IF-path are connected to the leads of the package using bond-wires.

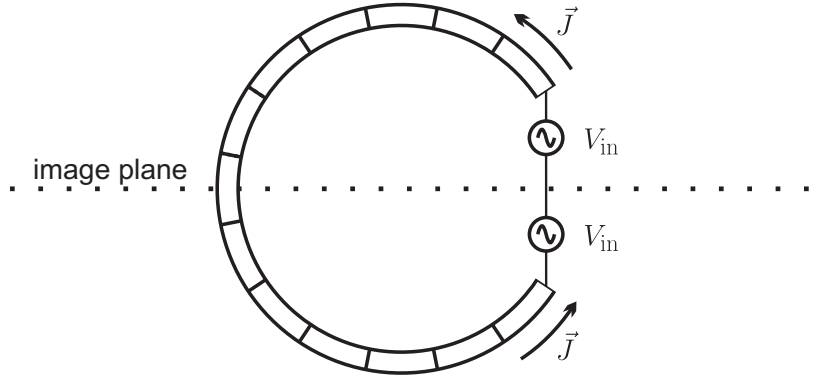


Figure 6.2. Basic model of the BWA from Figure 6.1.

### 6.2.2 Antenna design and modeling approach

The BWA shown in Figure 6.1 is a semi-circular loop antenna. For a sufficiently large ground plane, image theory can be applied to replace the ground plane by the image of the bond-wire. Consequently, the BWA can be modeled as a circular loop antenna as shown in Figure 6.2. Here, the effect of the plastic package is excluded such that the surrounding environment can be assumed to be air only. Like for the AoC design from Chapter 5, package independent conclusions can then be drawn by this investigation approach<sup>2</sup>. Therefore, the computationally efficient loop antenna model from Section 2.4 can now be employed to determine the antenna parameters of the full loop. Afterwards, the antenna parameters of the BWA can be determined from the full-loop antenna data as explained below.

#### Input impedance

In general, the input impedance of the semi-circular BWA,  $Z_{\text{in,BWA}}$ , is related to the input impedance of the circular full-loop antenna,  $Z_{\text{in,loop}}$ , according to

$$Z_{\text{in,BWA}} = \frac{1}{2} Z_{\text{in,loop}}. \quad (6.1)$$

This relation can be explained by the doubling of the driving voltage due to its image, as illustrated in Figure 6.2. In the model from Section 2.4, this has to be accounted for by using  $\mathbf{M}(\mathbf{r}) = 2M_0 \mathbf{u}_{\tilde{\varphi}} = -2V_{\text{in}} \mathbf{u}_{\tilde{\varphi}}$  in the magnetostatic frill source model, see Section 2.4.3.

Moreover, since the BWA in Figure 6.1 originates from a GSG bond-pad configuration on the IC, its effect on the input impedance of the antenna has to be included in

<sup>2</sup>For some packages, e.g., the hollow plastic packages from [74], this modeling approach might even already be sufficient.

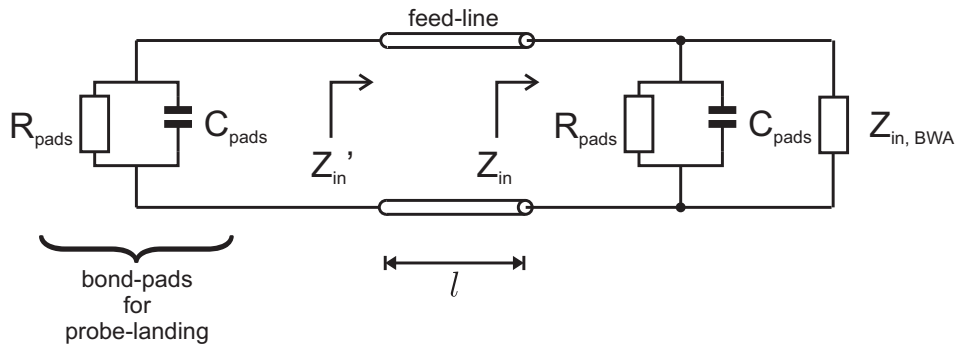


**Figure 6.3.** Equivalent circuit model of the BWA prototype (including feed-line and bond-pads for probe landing).

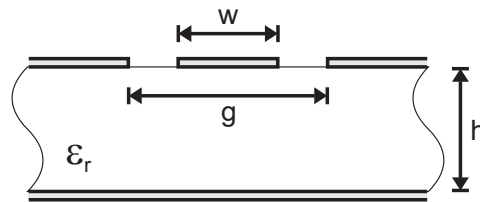


**Figure 6.4.** Illustration of the feed-line parameters.

the model as well. The impedance of the bond-pads can be well approximated by a lossy capacitance, which is connected in parallel to the BWA as shown in Figure 6.3. The capacitance value,  $C_{\text{pads}}$ , and its associated loss resistance,  $R_{\text{pads}}$ , are often provided in the design manual of the IC technology. If they are not given, they will have to be determined for the correct characterization of the on-chip electronics anyway since bond-pads are typically used as landing area for measurement probes, see also Chapter 5. For the BWA design that is presented in this thesis, the capacitance and resistance values were determined by simulating the impedance of the bond-pad structure on top of a  $200 \mu\text{m}$  thick silicon substrate with a resistivity of  $20 \Omega\text{cm}$  using Empire XCell. Figure 6.5 shows a comparison between this result and the lossy capacitance model for  $C_{\text{pads}} = 30 \text{ fF}$  and  $R_{\text{pads}} = 300 \Omega$ . From this, the lossy capacitance model can be concluded to agree sufficiently well, such that it can be used as a good approximation here.

Furthermore, for the targeted prototype, a  $1.4 \text{ mm}$  long CPW with bottom ground plane was designed as on-chip feed-line for the BWA, see Figure 6.4. It is also shown in the circuit model representation in Figure 6.3. At its end, another GSG bond-pad structure was connected in order to land a measurement probe here. In the model, the feed-line can be accounted for by the transmission line impedance

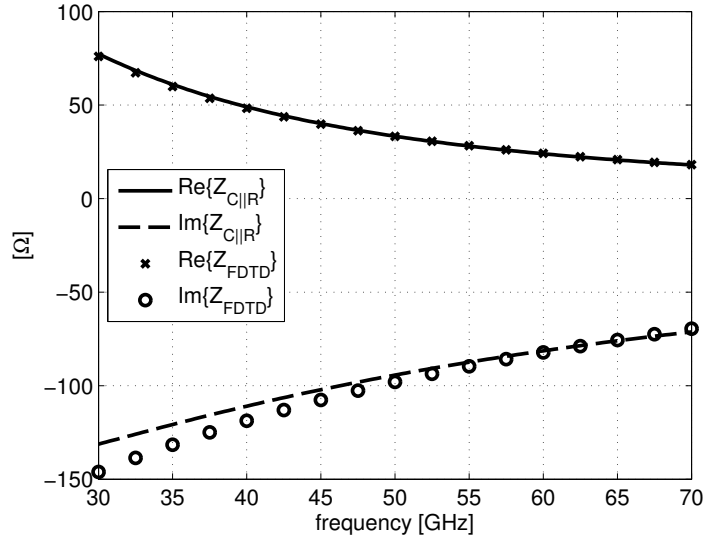


**Figure 6.5.** Comparison between the lossy capacitance model, subscript  $C_{||R}$ , and the simulation results of the bond-pad structure from Empire, subscript  $FDTD$ .

equation,

$$Z'_{in} = Z_0 \frac{Z_{in} + Z_0 \tanh(\gamma l)}{Z_0 + Z_{in} \tanh(\gamma l)}, \quad (6.2)$$

with  $Z_0$  the characteristic impedance of the CPW,  $Z_{in}$  the combined impedance of half-loop BWA and bond-pad parasitics,  $\gamma = \alpha + j\beta$  the propagation constant of the CPW mode with the attenuation constant  $\alpha$  and the phase term  $\beta$ , and  $l$  the length of the feed-line ([13]). Neglecting transmission line losses, i.e.,  $\alpha = 0$ , the propagation constant reduces to  $\gamma = j\beta = j\omega\sqrt{\epsilon_{r,eff}}\sqrt{\epsilon_0\mu_0}$ . Finally,  $Z_0$  and  $\epsilon_{r,eff}$  can be calculated with the following approximate formulas from [75]:

$$Z_0 = \frac{60\pi}{\sqrt{\epsilon_{r,eff}}} \frac{1}{\frac{\mathcal{K}(\tilde{\kappa})}{\mathcal{K}(\tilde{\kappa}')} + \frac{\mathcal{K}(\tilde{\kappa}_1)}{\mathcal{K}(\tilde{\kappa}'_1)}}, \quad (6.3)$$

$$\epsilon_{r,eff} = \frac{1 + \epsilon'_r \frac{\mathcal{K}(\tilde{\kappa}')}{\mathcal{K}(\tilde{\kappa})} \frac{\mathcal{K}(\tilde{\kappa}_1)}{\mathcal{K}(\tilde{\kappa}'_1)}}{1 + \frac{\mathcal{K}(\tilde{\kappa}')}{\mathcal{K}(\tilde{\kappa})} \frac{\mathcal{K}(\tilde{\kappa}_1)}{\mathcal{K}(\tilde{\kappa}'_1)}}, \quad (6.4)$$

where  $\mathcal{K}(\tilde{\kappa})$  is again the complete elliptical integral of the first kind,  $\epsilon'_r$  the relative

permittivity of the back-end dielectric, and

$$\tilde{\kappa} = w/g, \quad (6.5)$$

$$\tilde{\kappa}' = \sqrt{1 - \tilde{\kappa}^2}, \quad (6.6)$$

$$\tilde{\kappa}_1 = \frac{\tanh\left(\frac{\pi w}{4h}\right)}{\tanh\left(\frac{\pi g}{4h}\right)}, \quad (6.7)$$

$$\tilde{\kappa}'_1 = \sqrt{1 - \tilde{\kappa}_1^2}, \quad (6.8)$$

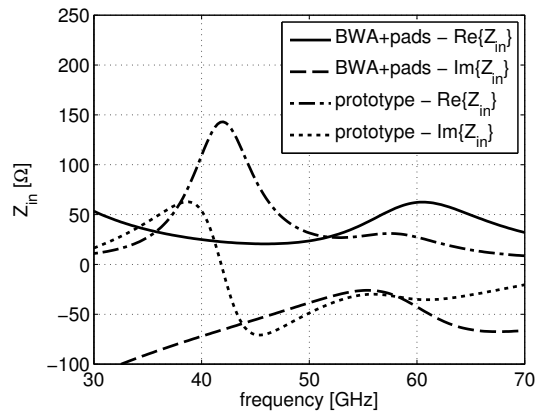
in which  $w = 18 \mu\text{m}$  is the signal line width,  $g = 48 \mu\text{m}$  is the distance between the ground conductors, and  $h \approx 10 \mu\text{m}$  is the thickness of the the back-end dielectric.

Using this modeling approach and assuming  $b = 0.933 \text{ mm}$  for the loop radius, the input impedance as shown in Figure 6.6(a) is predicted. The figure also shows impedance of the BWA without the feed-line and bond-pads for probe-landing. Note that the BWA is not matched to a specific reference impedance, like  $50 \Omega$ , here since the direct on-chip feed-point allows for direct matching schemes to the amplifier. Hence, rather than matching the antenna to a hypothetical reference impedance, special emphasize is paid here to the validity and accuracy of the modeling approach. Matching the antenna to a specific on-chip amplifier can then be done by a hybrid approach, i.e., using this antenna model and a circuit level simulator for the amplifier.

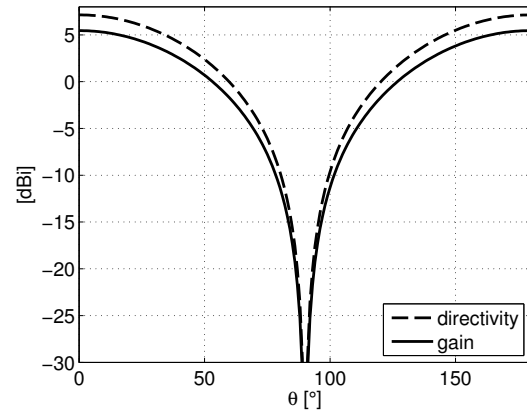
### Radiation Properties

For an infinite ground plane underneath the semi-circular BWA, the shape of its radiation pattern in the upper hemisphere is identical to the radiation pattern of the loop antenna from Section 2.4, see Figures 6.6(b), 6.6(c), and 6.6(d). For the lower hemisphere, the radiated fields are zero, however, since the ground plane reflects all electromagnetic energy. This, in turn, also results in a 3 dB larger directivity in the upper hemisphere as compared to the full-loop antenna, which results in a maximum directivity of 7.1 dBi. In the computational model, the 3 dB directivity increase can be traced back to the mirrored magnetostatic frill source. Due to this doubling of the magnetic current's amplitude, the generated electric current distribution on the lossless wire is twice as high as for the full-loop antenna from Section 2.4. This, consequently, results in the shown 3 dB larger directivity. In order to calculate the gain of the BWA, the directivity has to be multiplied by the radiation efficiency, see Equation (2.54). The radiation efficiency can be estimated by Equation (2.50), i.e.,

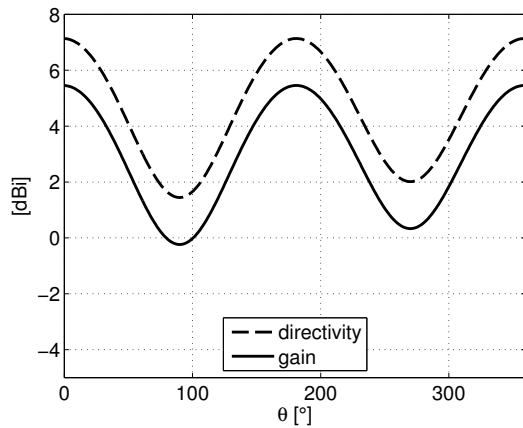
$$\eta_{\text{rad}} = \frac{\text{Re}\{Z_{\text{in,BWA}}^{-1}\}}{\text{Re}\{Z_{\text{in,BWA}}^{-1}\} + R_{\text{pads}}^{-1}}, \quad (6.9)$$



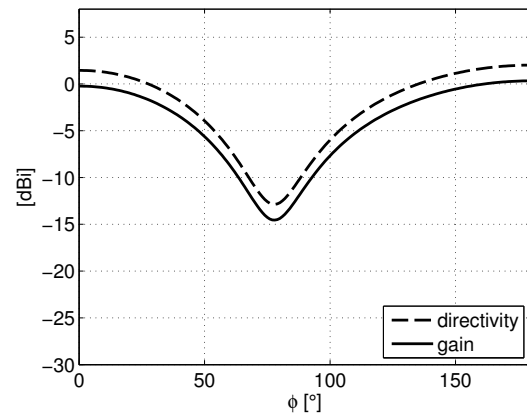
(a) Input impedance of the BWA with on-chip bond-pads and of the designed prototype, i.e., including feed-line.



(b) Gain pattern at 60 GHz in E-plane ( $\phi = 90^\circ$ ).



(c) Gain pattern at 60 GHz in H-plane ( $\phi = 0^\circ$ ).



(d) Gain pattern at 60 GHz in loop-plane ( $\theta = 90^\circ$ ).

**Figure 6.6.** Antenna parameters of the BWA prototype from Figure 6.1 (w/o plastic package) with  $b = 933 \mu\text{m}$  and  $a = 25 \mu\text{m}$  as obtained with the proposed model.

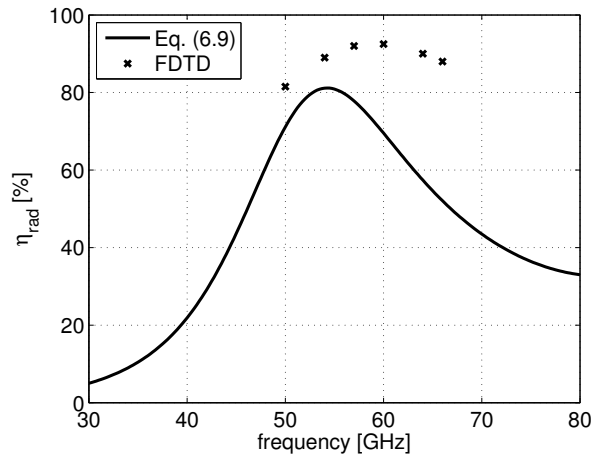


**Figure 6.7.** Radiation efficiency for the BWA prototype shown in Figure 6.1 as predicted by Equation (6.9) in comparison with the result obtained with Empire XCcel.

with  $Z_{\text{in,BWA}}$  and  $R_{\text{pads}}$  as defined in Figure 6.3. The resulting radiation efficiency, calculated with (6.9), in comparison with the results obtained with Empire XCcel for the prototype is provided in Figure 6.7. It shows a significant discrepancy between both solutions, which is seen to be the result of the simplified bond-pad model. A possible contribution of the bond-pads to the overall radiation mechanism is not incorporated, for example. However, from the radiation efficiency approximation (6.9), the radiation efficiency in the 60 GHz band can be obtained to range from 52 % at 66 GHz to 78 % at 57 GHz. The maximum radiation efficiency of 81 % for this loop radius is achieved at 54 GHz, indicating that the loop radius should be shorter in order to shift the maximum value in the 60 GHz band. Moreover, using (6.9), the predicted maximum gain at 60 GHz for the BWA is 5.5 dBi as also shown in Figures 6.6(b), 6.6(c), and 6.6(d).

## 6.3 Fabrication and measurement results

### 6.3.1 Bond-wire shape

In Section 6.2 an efficient modeling approach for the semi-circular BWA from Figure 6.1 is presented. In practice, however, a semi-circular shape is not commonly used, such that the wire-bonder parameters for this shape are not known beforehand. Hence, the right settings have to be determined from an experiment. For this, in cooperation with IMST GmbH, several wires with different bonder settings were fabricated on 500  $\mu\text{m}$  thick RO4003 substrates, see [32]. One of the prototypes is shown in Figure 6.8. In all cases, one end of the bond-wire was connected to a

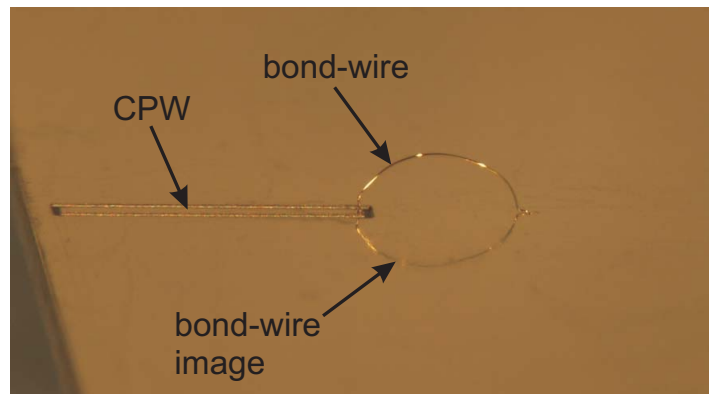


**Figure 6.8.** Photograph of a fabricated semi-circular bond-wire on a large ground plane.

3.6 mm long CPW while the other end was connected to a large ground plane. Note that also the (optical) image of the wire is clearly visible in Figure 6.8. Since it was not possible to visually inspect the exact shape of the fabricated wires, input impedance measurements of all prototypes were performed with the setup described in Section 4.3. The measurement results were compared with the simulation results for this prototype using the modeling approach from Section 6.2.2. Since no bond-pads exist in the prototype shown in Figure 6.8, the bond-pads were removed from the model here. The feed-line parameters were adjusted to match the values of the fabricated PCB-prototype, whereas a CPW length of 3.4 mm instead of 3.6 mm was chosen to account for the effectively shorter distance between the BWA input and the probe-tip. The measurement result of the best matching sample is provided in Figure 6.9. The effective loop radius was found to be  $800 \mu\text{m}$  to achieve this good agreement<sup>3</sup>, which is in line with the distance between the two bond-points. Hence, the achieved shape can be concluded to sufficiently approximate that of a semi-circle such that the bonder settings for this shape can be used to build an on-chip prototype.

### 6.3.2 Prototype

The wire-bond settings found in the experiment from Section 6.3.1 were used to build a prototype of the proposed hybrid integrated mm-wave antenna. A photograph of one of the samples is provided in Figure 6.10. Again, the input impedances of the prototypes were measured with the setup described in Section 4.3. A comparison between the measurement result of one of the samples and the prediction of the model from Section 6.2.2 is provided in Fig. 6.11(a) and shows very good agreement. For

<sup>3</sup>Note that also here the losses in the CPW were omitted.



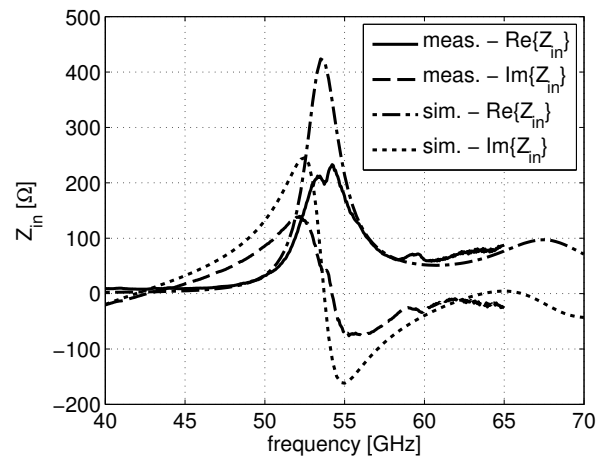


**Figure 6.9.** Comparison of the input impedances between the measurement of the BWA from Figure 6.8 ("meas.") and the model described in Section 6.2.2 ("sim.").

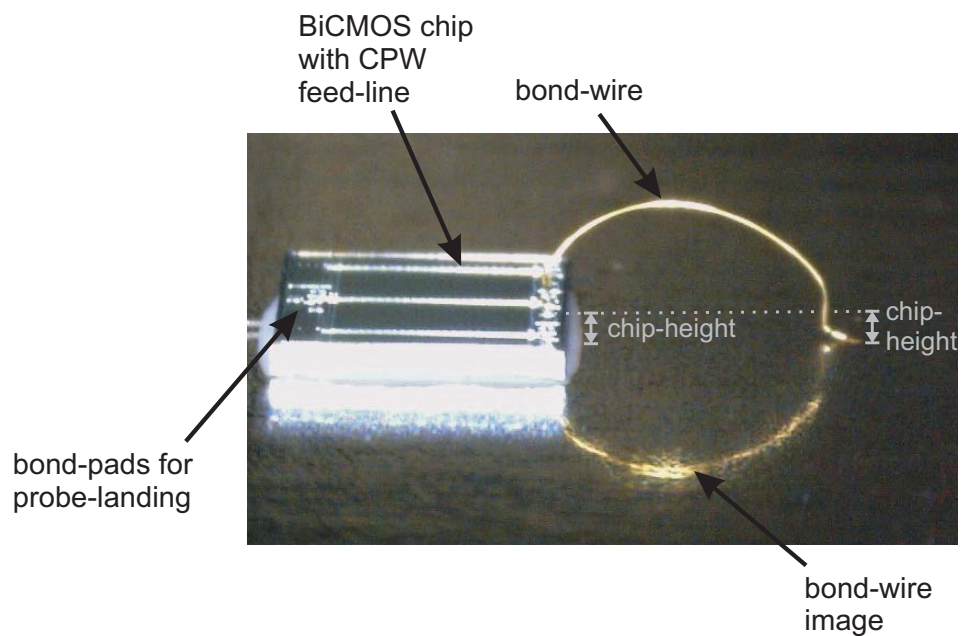
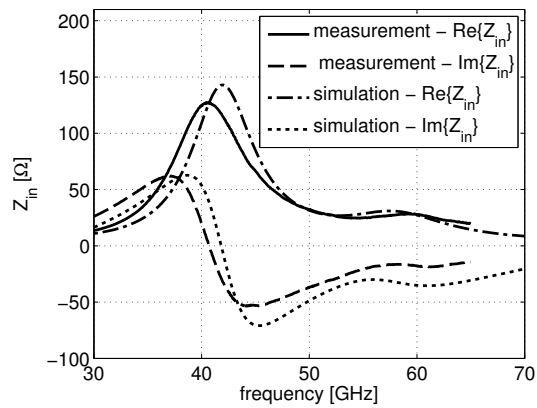
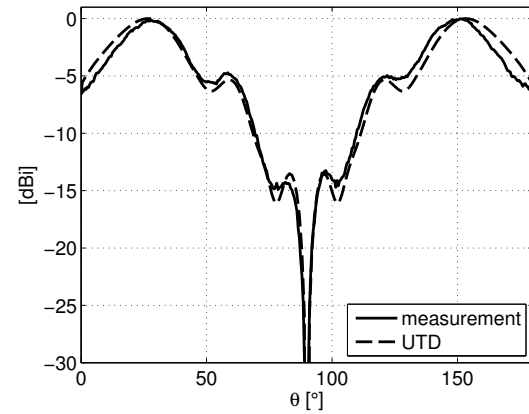


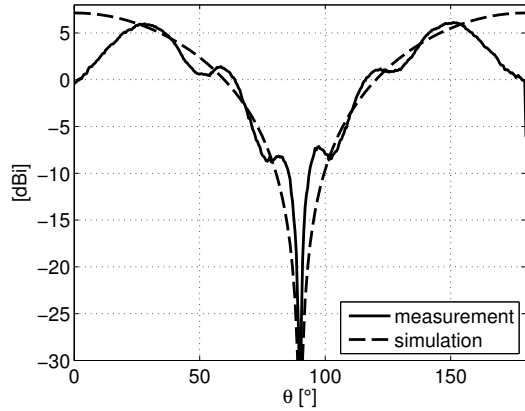
**Figure 6.10.** Photograph of a fabricated prototype.



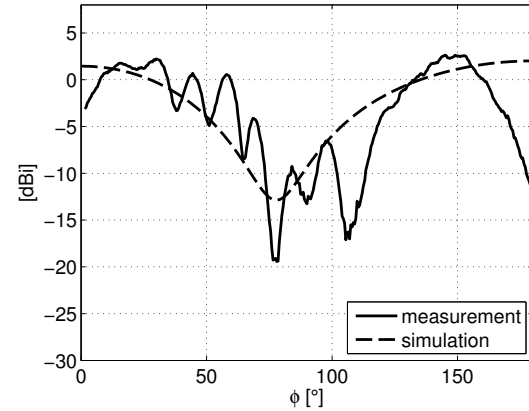
(a) Comparison between the measured input impedances of the BWA from Figure 6.10 and the proposed model



(b) Simulated normalized gain pattern of the BWA at 60 GHz and  $\phi = 0^\circ$  when incorporating the diffraction terms by the UTD.



(c) Normalized gain pattern for the co-polarization component at  $\phi = 90^\circ$  ( $E_\theta$ , normalized to maximum value).



(d) Normalized gain pattern for the co-polarization component at  $\theta = 90^\circ$  ( $E_\phi$ , normalized to maximum value).

**Figure 6.11.** Comparison between measured gain pattern and simulated directivity of the prototype from Figure 6.8.

the simulation model, the loop-radius was enlarged to include the elongated bond-wire of approximately twice the chip height, which results in a loop circumference increase of four times the chip height. The remaining deviation between model and measurement can be partially explained by the simplifications that were made for the model, i.e., perfectly semi-circular wire-shape, simplified bond-pad model, loss-less metals, etc. Furthermore, unavoidable imperfections during the measurements, for example, the presence of the probe close to the antenna, are seen to be another cause for the deviation.

Furthermore, Figures 6.11(c) and 6.11(d) provide a comparison between the measured gain pattern of the BWA at 60 GHz and the simulated directivity of the respective co-polarization component in both its principal planes. Note that the gain calculation was directly done during the radiation pattern measurement with the setup described in Section 4.3 here, such that the results in the figures are not normalized. Furthermore, the measurement was performed with a sample as shown in Figure 6.8 since the GSG-probe could not be adequately landed on the version with chip<sup>4</sup>. Since the radiation pattern of both versions are expected to be very similar, however, this measurement can still be used to verify the BWA-model. Moreover, by this approach the gain and, therefore, the efficiency of an antenna in bond-wire technology can be determined independent of the IC technology. The respective measurements for 57 GHz, 64 GHz, and 66 GHz can be found in Figure B.3 in Appendix B. In all cases, the measured gain pattern follows the basic trend of the directivity pattern and exhibits a similar magnitude. Therefore, the efficiency of this antenna can be concluded to be very high, i.e., at least in the range of the AiP concept. Note, however, that also during this measurement the presence of the probe caused perturbations in the pattern, which is particularly noticeable in the  $\theta = 90^\circ$  plane. Furthermore, the finite size of the ground plane underneath the BWA has an impact on the radiation pattern since a part of the radiated energy gets diffracted at its edges and corners. In order to include this effect in the proposed model, the uniform geometrical theory of diffraction (UTD) was used, see [72]. Figure 6.11(b) shows the computed normalized gain pattern of the BWA, where the UTD was used to include diffraction due to the finiteness of the ground plane. Also shown in the figure is the corresponding measurement result, which agrees excellently with the UTD solution.

Finally, from the results presented in this section, it can be concluded that the model from Section 6.2 can be used for further investigations on the suitability of wire-bond technology for the implementation of mm-wave antennas.

---

<sup>4</sup>With a further improvement of the setup that allows the probe-tips to be leveled by tilting the probe, this problem can be solved.

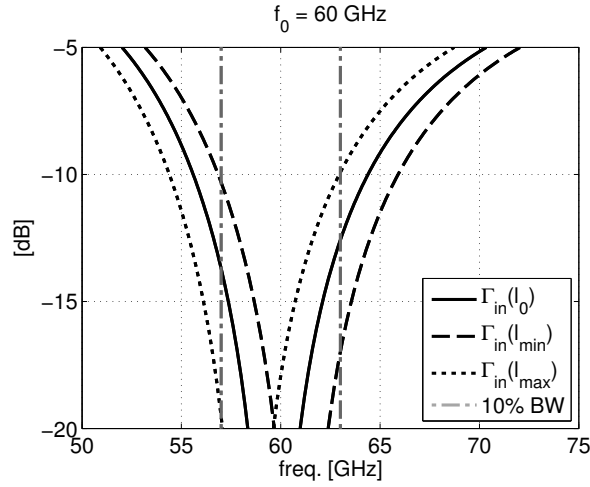


**Figure 6.12.** Simulated input reflection coefficients of a circular BWA with nominal wire-length  $l_0 = 2.733$  mm, i.e.,  $f_0 = 60$  GHz,  $l_{\min} = 2.668$  mm, and  $l_{\max} = 2.793$  mm, respectively.

## 6.4 Yield analysis

### 6.4.1 Analysis

A concern that is often stated with respect to antennas in wire-bond technology is a low yield due to an insufficient reproducibility of the wire-length, which is a result of, for example, bond-head positioning tolerances. Hence, it has to be investigated to what extent this concern is justified. For this, the time-efficient modeling approach from Section 6.2 is used to explore the impact of typical wire-length tolerances on the matching condition of the antenna throughout the mm-wave band. For this purpose, BWAs with different resonant frequencies,  $f_0$ , are designed that operate within the mm-wave band. The specification for those antennas is defined as to exhibit an input reflection coefficient,  $\Gamma_{\text{in}}$ , that stays below -10 dB with respect to a  $75 \Omega$  amplifier in a 10 % bandwidth around the center frequency  $f_0$ . For each nominal resonant frequency, the wire-length is then varied in order to determine for which minimum and maximum value, respectively, the specification is still fulfilled. As an example, Figure 6.12 shows the input reflection coefficients of a BWA with  $f_0 = 60$  GHz for its nominal wire-length,  $l_0$ , minimum wire-length,  $l_{\min}$ , and maximum wire-length,  $l_{\max}$ . The yield of the antenna with respect to the -10 dB bandwidth specification can now be determined by calculating the likelihood that the wire-length stays within the two boundary values  $l_{\min}$  and  $l_{\max}$ . Figure 6.13 illustrates the relation between the probability density function (PDF) of the bond-wire-length and the yield of the antenna. Here, it is assumed that the wire-length variation can be represented by

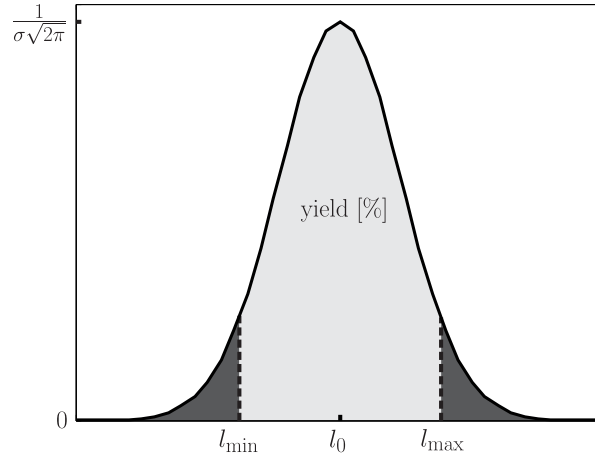


**Figure 6.13.** Assumed PDF of the bond-wire-length, with  $l_0$  the nominal (mean) value and  $l_{\min}, l_{\max}$  the minimum and maximum length that satisfy the -10 dB bandwidth specification.

the Gaussian distribution with mean value  $\bar{\mu} = l_0$  and a bonder-specific standard deviation  $\sigma$ . Hence, the yield  $\Psi$  can be calculated by

$$\begin{aligned} \Psi &= \mathcal{G}(l_{\max}|l_0, \sigma) - \mathcal{G}(l_{\min}|l_0, \sigma) \\ &= \frac{1}{\sigma\sqrt{2\pi}} \left[ \int_{-\infty}^{l_{\max}} e^{-\frac{(l-l_0)^2}{2\sigma^2}} dl - \int_{-\infty}^{l_{\min}} e^{-\frac{(l-l_0)^2}{2\sigma^2}} dl \right], \end{aligned} \quad (6.10)$$

with  $\mathcal{G}(\Lambda|\bar{\mu}, \sigma)$  the result of the cumulative distribution function (CDF) of the Gaussian PDF for the length value  $\Lambda$ . Table 6.1 summarizes the yield values of the 60 GHz example along with the results for designs with other resonant frequencies. The consideration was done for two different standard deviations, i.e., a realistic value of state-of-the-art bonders,  $3\sigma_1 = 25 \mu\text{m}$ , and a more pessimistic value,  $3\sigma_2 = 50 \mu\text{m}$ , respectively.

#### 6.4.2 Result discussion

Analyzing Table 6.1 it may be concluded that high volume wire-bond technology with  $3\sigma = 25 \mu\text{m}$  can be expected to achieve a sufficiently high yield, i.e., larger than 99.99 %, for designs of nearly up to 250 GHz. It decreases below 99 % at about 270 GHz, after which it drops below 75 % at 300 GHz. Dependent on the specific bandwidth requirements of a desired application, however, wire-bond technology might still be a suitable choice for antennas above 270 GHz. For a standard deviation of  $3\sigma = 50 \mu\text{m}$  a yield of more than 99 % can be expected for almost up to 200 GHz.

Since the circular loop-antenna's directivity is rather insensitive to small lengths variations, see [14], those effects were excluded from this consideration. For applications

**Table 6.1.** Summary of expected yield values for semi-circular BWAs in the mm-wave band ( $Z_0 = 75 \Omega$ ).

$f_0$ [GHz]	$l_0$ [mm]	$l_{\min}$ [mm]	$l_{\max}$ [mm]	yield [%] ( $3\sigma_1 = 25 \mu\text{m}$ )	yield [%] ( $3\sigma_2 = 50 \mu\text{m}$ )
30	5.498	5.438	5.557	$\geq 99.99$	99.97
60	2.733	2.668	2.793	$\geq 99.99$	99.97
100	1.665	1.605	1.725	$\geq 99.99$	99.97
150	1.131	1.086	1.186	$\geq 99.99$	99.61
200	0.864	0.824	0.909	$\geq 99.99$	98.83
250	0.707	0.677	0.740	99.98	94.02
270	0.654	0.634	0.681	99.12	83.23
300	0.594	0.587	0.609	76.36	47.87

in the unlicensed 60 GHz band, for example, slight directivity fluctuations are not expected to result in any yield reduction since the exact radiation pattern will mainly be influenced by the package of the final product, for example a mobile phone, anyway.

Finally, it should be mentioned that this consideration solely focuses on a circular BWA with the impedance matching requirement of -10 dB in a 10 % bandwidth around  $f_0$  and with respect to a  $75 \Omega$  reference impedance. For a different wire shape, bandwidth requirement, and reference impedance the yield values might differ. Hence, a universal upper frequency limit for the usage of BWAs cannot be given here. The results, however, clearly indicate that, in general, wire-bond technology can be expected to achieve sufficient yield for high volume mm-wave antenna production.

## 6.5 Summary and conclusions

In this chapter, a hybrid integrated mm-wave antenna concept in generic wire-bond technology is presented. A prototype was designed with the aid of a dedicated, computationally efficient modeling approach, which could be successfully verified by measurements. A summary of the simulation results, obtained with this model, is provided in Table 6.2. In comparison with the state-of-the-art, see Table 3.4, it can be concluded that this approach achieves comparable key figures to the design published in [53]. Due to its low on-chip real-estate requirement as well as low-cost and wide-spread fabrication technology, this technology is seen to be a very attractive alternative to state-of-the-art AiP and AoC concepts. Moreover, as also shown in this chapter, the yield in high volume production can be expected to be comparable with other concepts. However, the low design flexibility may not permit the use of this

**Table 6.2.** Key figures of proposed hybrid concept according to Table 3.4.

technology complexity	very low
size [mm <sup>2</sup> ]	0.0064 (on-chip real-estate)
feed topology	single-ended
impedance bandwidth [GHz] ( $\Gamma_{in} \leq -10$ dB)	not specified
$\eta_{rad}$ [%]	52 - 78 (model from Section 6.2.2) 88 - 92 (Empire XCcel)
gain [dBi]	approx. 7.1
cost (relative)	very low

technology for some applications. Moreover, the effect of packaging on the antenna performance still has to be investigated in the future.

Finally, this integration technology can be recommended for wireless interconnect applications, see Chapter 1. Here, especially for wireless chip-to-chip or PCB-to-PCB connections, the extremely low-cost nature of the wire-bond technology permits a vast amount of these antennas inside a single consumer product. Furthermore, the BWA achieves its gain maximum along the ground plane, which is for wireless chip-to-chip links often the line-of-sight direction to the other communication nodes. Moreover, its estimated gain meets the requirements stated in Table 3.1 for this scenario, i.e., case #6.

# Antenna array considerations<sup>1</sup>

---

Antenna arrays are of particular interest in the mm-wave band since they offer high antenna gain, which is, for example, necessary for communicating over the maximum targeted distance of 10 m at 60 GHz, see Chapter 3. For this, arrays with a fixed amplitude and phase distribution are often considered in the literature. Especially for mobile applications, however, the antenna array must exhibit the capability to align its narrow beam in the direction of the strongest signal. Otherwise, the full capacity and/or communication distance of the system can hardly ever be exploited. Hence, an antenna array with beam-steering capability is imperative, see [2, 4, 5, 7, 8]. Such a solution for linear and circular polarization based on the AiP concept from Chapter 4 is presented in the following section. Furthermore, a method for improving the axial ratio over the whole scan range of circularly polarized arrays is proposed in Section 7.2. Finally, an extension of the computational model for the BWA from Chapter 6 is introduced in Section 7.3 and conclusions regarding antenna arrays in the mm-wave range are drawn in Section 7.4.

## 7.1 Modular array concept

With respect to beam-steerable antenna arrays, the authors of [7] propose to integrate all array electronics in one single chip in order to minimize the total required chip area as well as the differentiation between antenna branch properties. A complete 60 GHz receiver module with integrated antenna array that uses this kind of approach was published in [35]. Such a solution, however, is not very flexible since the number of antenna elements and their arrangement is fixed. As a result, the range of

---

<sup>1</sup>The results presented in this chapter were published in [76], [77], and [78].



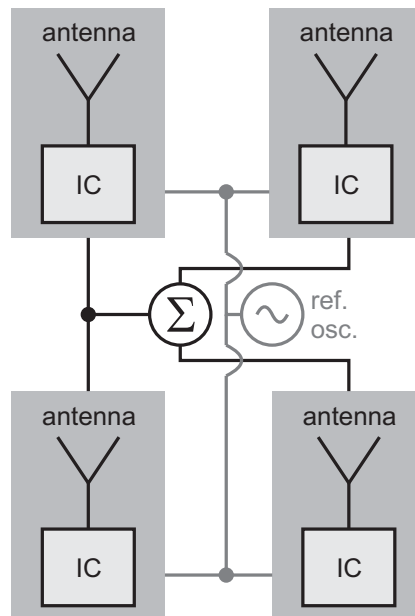


**Figure 7.1.** Conceptual drawing of the modular array approach.

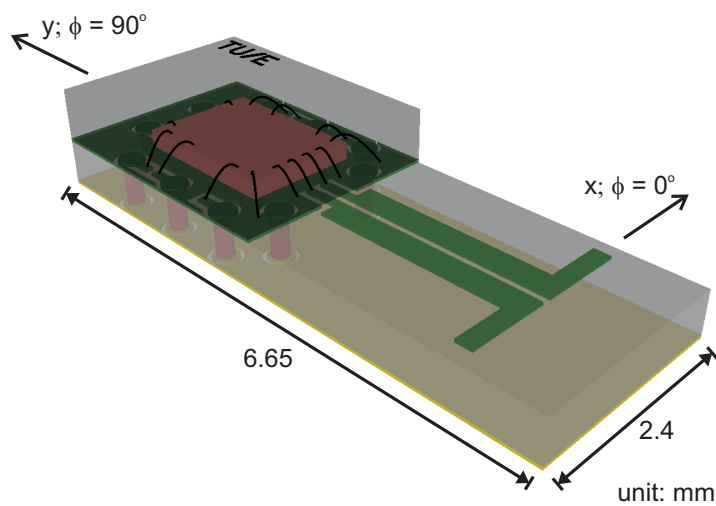


**Figure 7.2.** Conceptual drawing of the AiP design for use in a modular array.

suitable applications is limited, which ultimately results in high costs for the module due to low production volumes. In order to achieve a high flexibility that can target a larger application range and, therefore, lower the costs by increasing the production volume, a modular array concept is proposed here. A conceptual drawing of this approach is provided in Figure 7.1. It consists of mm-wave front-end modules like the ones presented in Chapters 4 to 6. The desired overall array size and antenna element arrangement is then composed out of several such modules. As shown in Figure 7.1, a low-frequency reference oscillator for phase synchronization can be supplied to the modules from an external source using a distribution network. On-chip phase shifters and variable gain amplifiers can then be used to apply the desired amplitude and phase distribution to each individual antenna element. As for the reference oscillator signal, the data signal can be distributed to the modules in IF, base-band, or even digital domain.

### 7.1.1 Linearly polarized array

As a first example for the modular array concept, a variation of the AiP design from Chapter 4 is used as basic array element. The considered module is shown in Figure 7.2. Its antenna dimensions are identical to the ones from Chapter 4. The PCB had to be truncated, however, in order to be able to arrange the modules in the typical  $\lambda_0/2$  element spacing for rectangular arrays. As a result of this size reduction, the antenna gain now ranges from 7 dBi to 7.5 dBi, which is 2.5 dBi lower than the achieved gain for the design from Chapter 4. However, its input impedance, resulting input reflection coefficient, and gain pattern are still well within the acceptable range for generic applications in the 60 GHz band, see Figure 7.3.

A linearly polarized array can now be built by arranging several modules of this type as shown in Figure 7.4, which shows a  $2 \times 2$  array with a spacing of  $\lambda_0/2$  between the printed dipoles. As can be observed from Figure 7.5, the antennas are still well matched in this configuration. Furthermore, the mutual coupling to neighboring elements is -15 dB or lower, which is considered acceptable for this example. If all modules are now transmitting simultaneously with the same amplitude and phase, a combined gain of 11.4 dBi at 57 GHz to 12.7 dBi at 66 GHz is achieved. The resulting overall gain pattern for this scenario is provided in Figure 7.6 along with the input impedance and input reflection coefficient of a single element for this scenario.

Finally, if a time delay is applied to modules #1 and #3, the main beam can be steered in the  $\phi = 0^\circ$  plane. Figure 7.7 shows the gain pattern for the scan angle  $\theta_0 = -15^\circ$  along with the resulting input reflection coefficient for each antenna element. From this, it can be observed that the input reflection coefficient for modules #1 and #3 exceed -10 dB for frequencies larger than 64 GHz, but remain below -8.5 dB such that

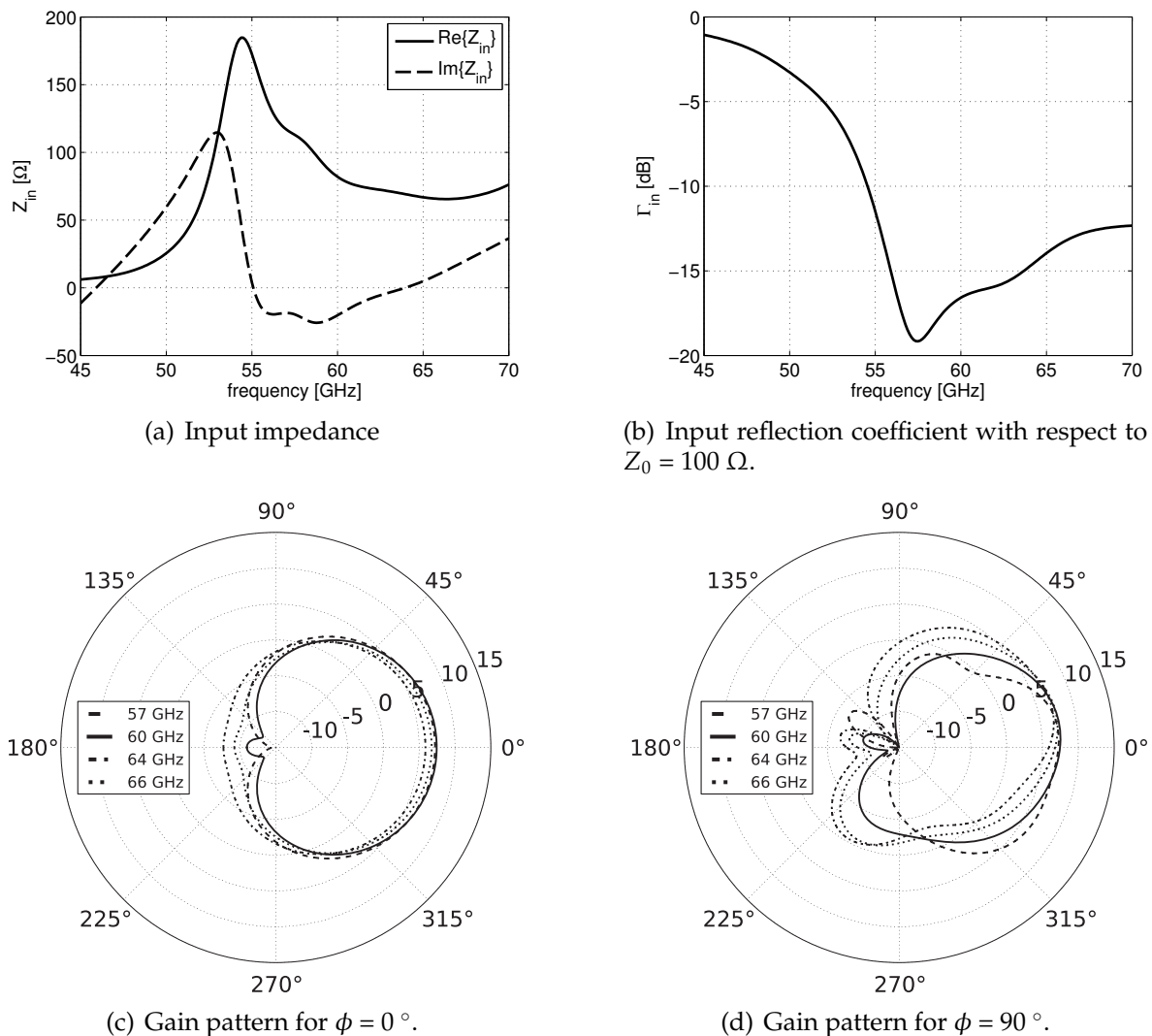


**Figure 7.3.** Simulated antenna parameters of the antenna shown in Figure 7.2.

this can be considered as still acceptable here. Furthermore, the maximum achieved gain values range from 11.4 dBi at 66 GHz to 12.2 dBi at 60 GHz here. Similarly, the main beam can be steered in the  $\phi = 90^\circ$  plane by applying a time delay to modules #1 and #2. Figure 7.8 shows the gain pattern and input reflection coefficients for a  $-15^\circ$  scan angle in this plane with a maximum achieved gain between 11.5 dBi at 57 GHz and 12.3 dBi at 66 GHz. Hence, by this method, a linearly polarized phased array can be constructed that achieves a gain of at least 11 dBi over a scan range of  $\pm 15^\circ$ .

For achieving higher gain values, a larger array can be built in the same manner by simply using more integrated mm-wave modules. Here, the particular module choice in this example exhibits a limitation in this respect. Its size does namely not

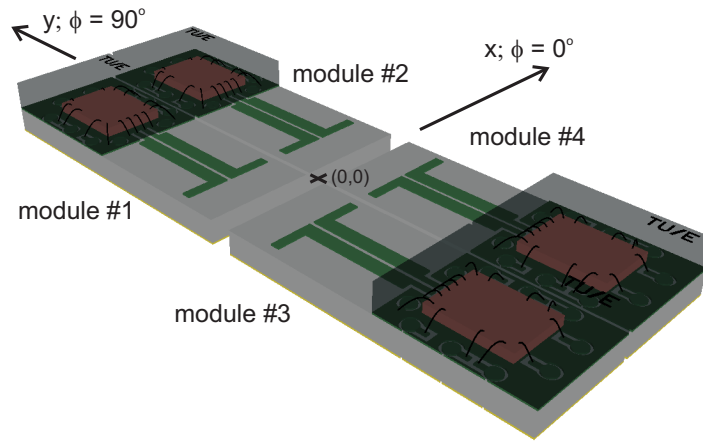


**Figure 7.4.**  $2 \times 2$  linearly polarized antenna array consisting of integrated mm-wave front-end modules as shown in Figure 7.2.

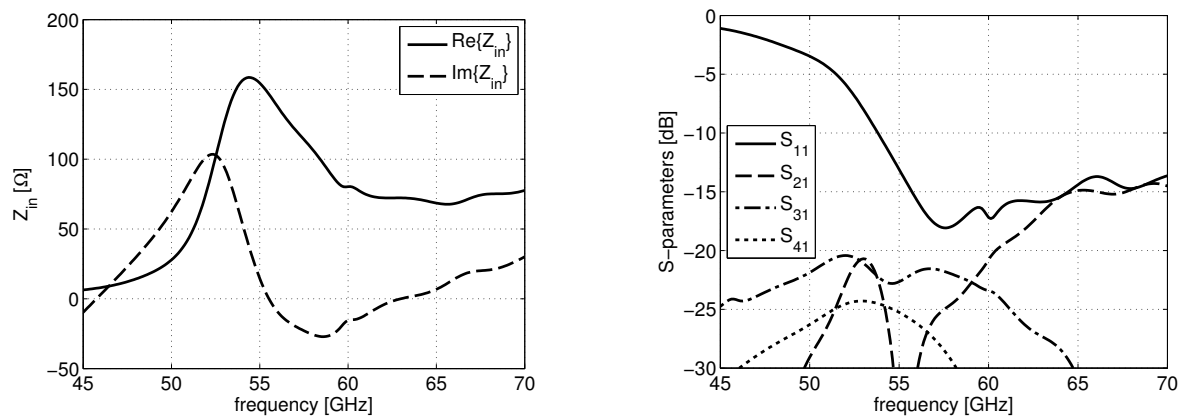
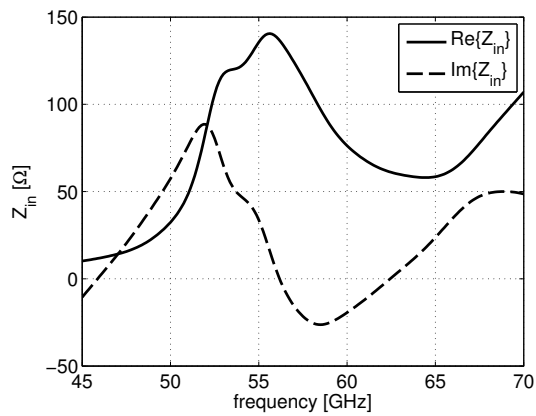
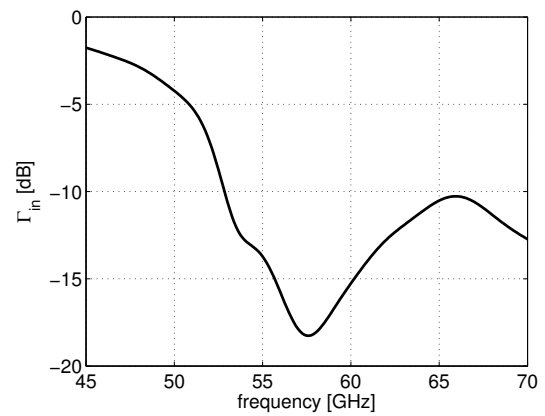


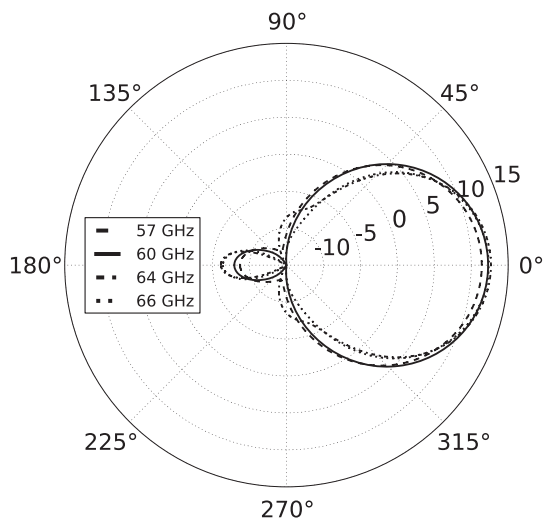
**Figure 7.5.** Input impedance and S-parameters of the antenna array from Figure 7.4.



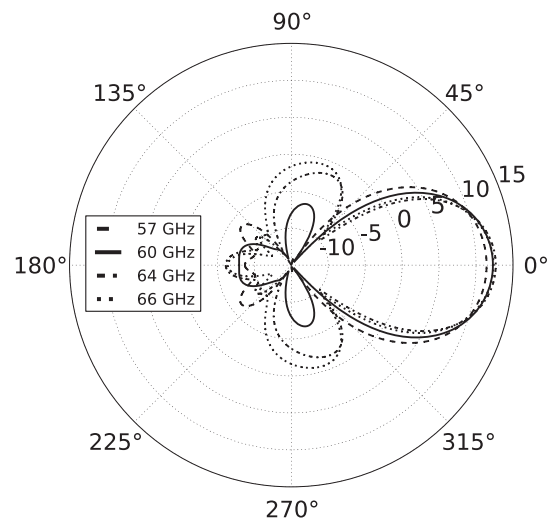
(a) Input impedance



(b) Input reflection coefficient with respect to  $Z_0 = 100 \Omega$ .



(c) Gain pattern at  $\phi = 0^\circ$  of the antenna array from Figure for a scan angle  $\theta_0 = 0^\circ$ .



(d) Gain pattern at  $\phi = 90^\circ$  of the antenna array from Figure for a scan angle  $\theta_0 = 0^\circ$ .

**Figure 7.6.** Antenna parameters for the antenna array from Figure 7.4 for simultaneous excitation of all four elements with the same amplitude and phase.

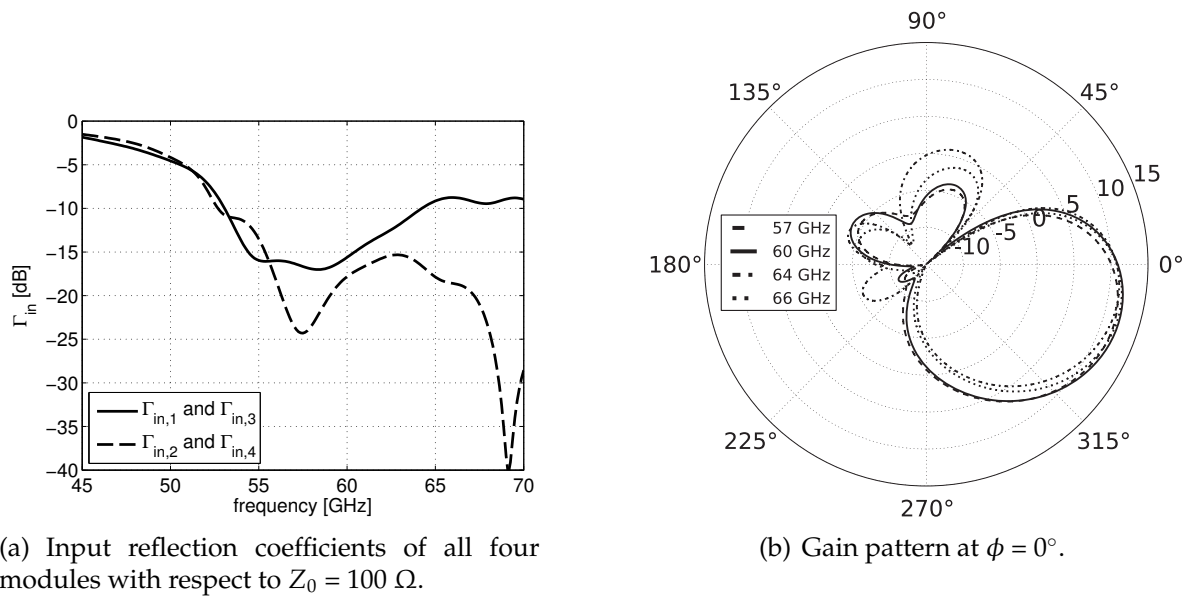


**Figure 7.7.** Antenna parameters for the antenna array from Figure 7.4 for a scan angle of  $-15^\circ$  in the  $\phi = 0^\circ$  plane.

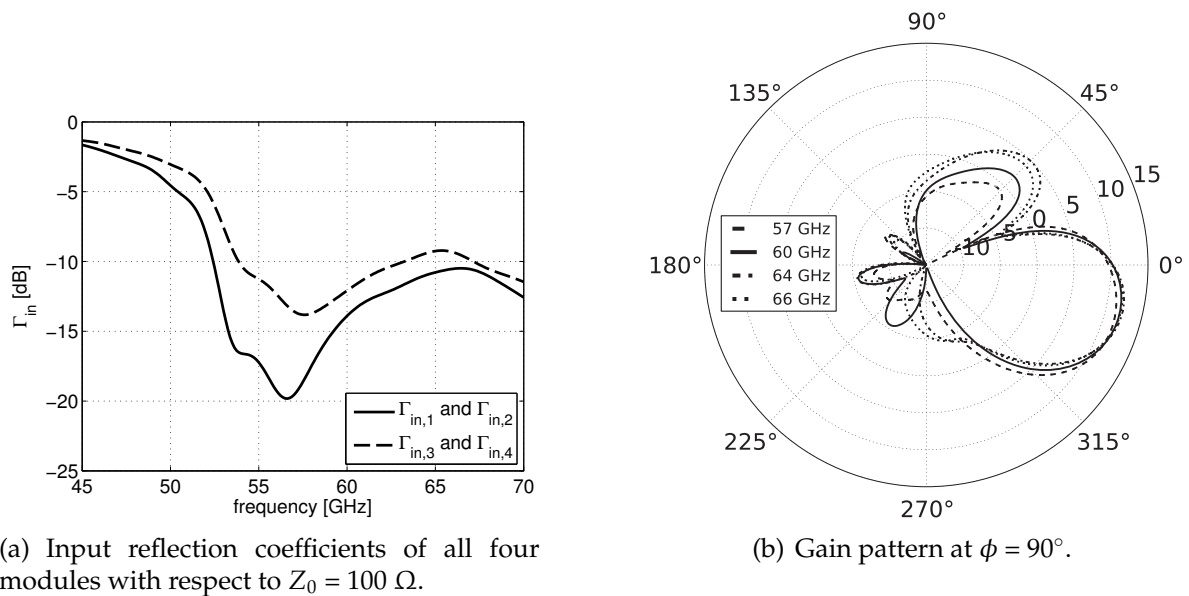


**Figure 7.8.** Antenna parameters for the antenna array from Figure 7.4 for a scan angle of  $-15^\circ$  in the  $\phi = 90^\circ$  plane.

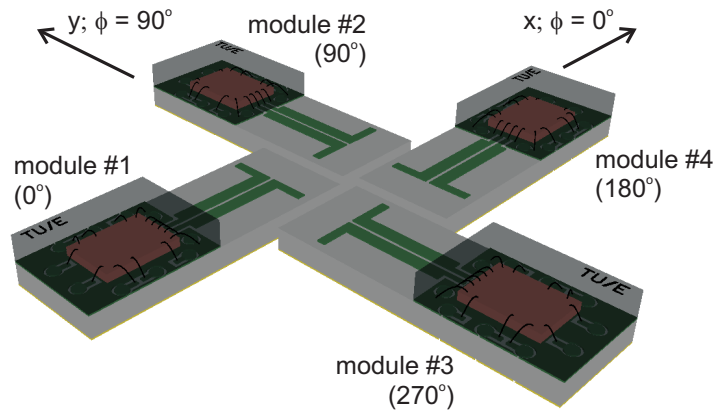
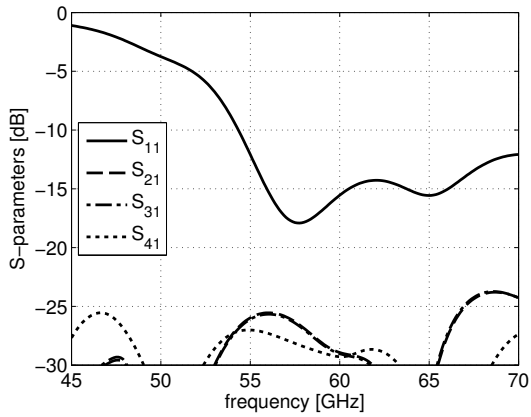


**Figure 7.9.**  $2 \times 2$  antenna array that achieves circular polarization.

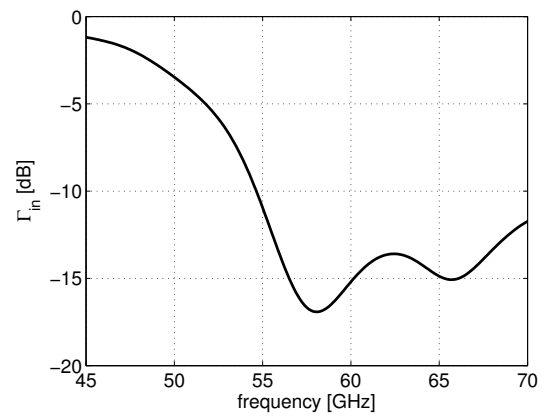
permit a  $\lambda_0/2$  spacing in  $y$ -direction, see Figure 7.2. However, a  $2 \times N$ -array can easily be constructed, with  $N$  being any number of elements in  $x$ -direction. By this, a high gain fan-beam can be generated that exhibits, for example, a large coverage in elevation while being steerable in azimuth, or vice versa.

### 7.1.2 Circularly polarized array

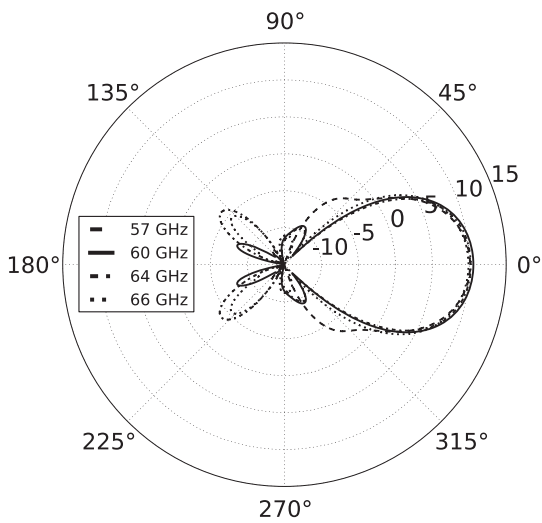
As another example, the flexibility of the modular array approach is used to construct a circularly polarized array with the same modules. Especially for handheld devices, circular polarization can significantly increase the robustness of a wireless communication link due to the line-of-sight nature of the communication channel at 60 GHz. Otherwise, linearly polarized solutions may require an accurate polarization alignment, which is not very practical to implement for portable applications. An elegant way to create circular polarization with linearly polarized elements in an array environment is by using the sequential rotation technique as introduced by John Huang in 1986 [79]. Figure 7.9 shows the basic antenna arrangement for this method. Here, circularly polarized radiation is achieved by applying proper phase shifts to sequentially rotated linearly polarized antenna elements, as also illustrated in the figure. Using this configuration for a transmitting array, a right-hand circular polarization is achieved. The S-parameters of the sequentially rotated integrated antennas for an antenna spacing of  $\lambda_0/2$  and their input reflection coefficients for simultaneous excitation with the same amplitude for each antenna element are shown in Figures 7.10(a) and 7.10(b), respectively. The overall gain pattern for the  $\phi = 0^\circ$  and  $\phi = 90^\circ$  planes are provided in Figure 7.10(c). The achieved maximum gain was computed to range from 9.9 dBi to 10.6 dBi with a 3 dB beam-width of  $42^\circ$  at 60 GHz, i.e., the gain outside the  $\pm 21^\circ$  range is at least 3 dB lower than the maximum gain. Furthermore, the axial ratio, defined in Equation (2.55), at 60 GHz of



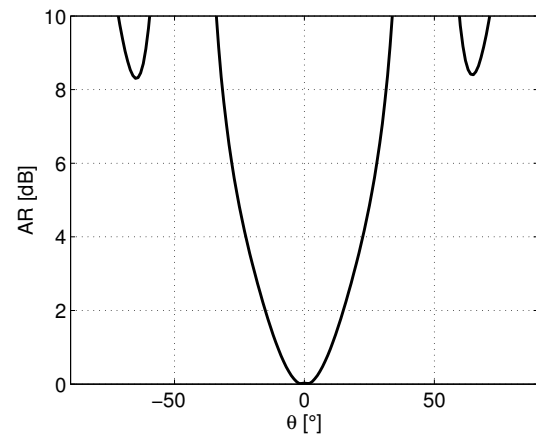
(a) S-parameters ( $Z_0 = 100 \Omega$ )



(b) Input reflection coefficient with respect to  $Z_0 = 100 \Omega$ .



(c) Gain pattern at 60 GHz for the  $\phi = 0^\circ$  and  $\phi = 90^\circ$  planes when steering the beam towards  $\theta_0 = 0^\circ$ .



(d) Axial ratio at 60 GHz for the  $\phi = 0^\circ$  and  $\phi = 90^\circ$  planes.

**Figure 7.10.** S-parameters of the antenna array shown in Figure 7.9 and its antenna parameters for simultaneous excitation of all four elements with the same amplitude and a phase-delay distribution as shown in the figure.



this circularly polarized antenna array in the  $\phi = 0^\circ$  and  $\phi = 90^\circ$  planes is shown in Figure 7.10(d). It shows that for  $\theta = 0^\circ$  practically perfect circular polarization is achieved. The AR exceeds 3 dB for angles beyond  $\pm 19^\circ$  and, hence, nearly the full 3 dB beam-width exhibits an acceptable degree of circular polarization. When the beam is steered away from the broad-side direction ( $\theta_0 \neq 0^\circ$ ), however, the axial ratio at the desired scan angle degrades, as can be seen from Figure 7.11. It shows the gain pattern in the  $\phi = 0^\circ$  plane (Figure 7.11(b)) when the beam is steered towards  $\theta_0 = -15^\circ$ . All elements are still well matched (Figure 7.11(a)) and a maximum gain of 9.2 dBi to 9.9 dBi is achieved. The simulated axial ratio at the scan angle, however, is already degraded to 1 dB, see Figure 7.11(c), which is basically a result of the unequal gain patterns of the single mm-wave module in its  $\phi = 0^\circ$  and  $\phi = 90^\circ$  planes. Hence, for even larger scan angles, this degradation can be expected to increase. A method to improve the axial ratio over a wide scan range is presented in [76] and is summarized in the following section.

## 7.2 Axial ratio enhancement for modular array concept

As shown in the previous section, the sequential rotation technique results in a degradation of the axial ratio when applying beam-steering. The main reason for this is the fact the gain pattern of each individual element is not the same in its  $\phi = \phi_0$  and  $\phi = \phi_0 \pm 90^\circ$  planes. Therefore, in this section a method to compensate this effect is proposed, which was also published in [76].

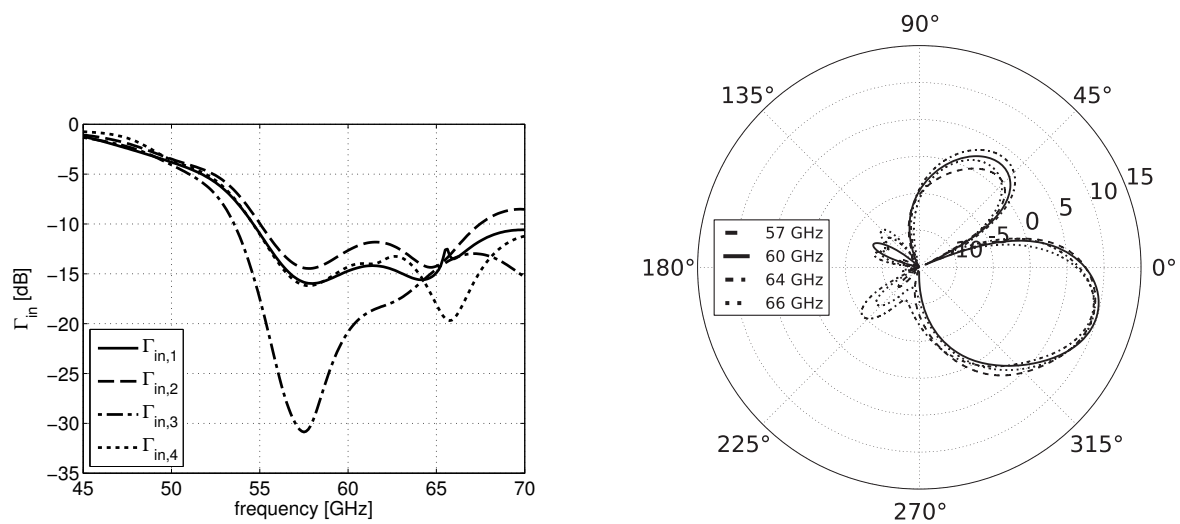
### 7.2.1 Sequential rotation technique for beam-steering

The basic idea to compensate the axial ratio degradation for beam-steering, is to pre-measure or simulate the element patterns of each array element for both the co- and cross polarization. For the  $\phi = 0^\circ$  plane, for example, the following general expressions hold in the antenna's far-field:

$$E_\theta^{\text{tot}} = a_1 E_\theta^{1,\text{co}}(\theta) + a_3 E_\theta^{3,\text{co}}(\theta) + a_2 E_\theta^{2,\text{X}}(\theta) + a_4 E_\theta^{4,\text{X}}(\theta), \quad (7.1)$$

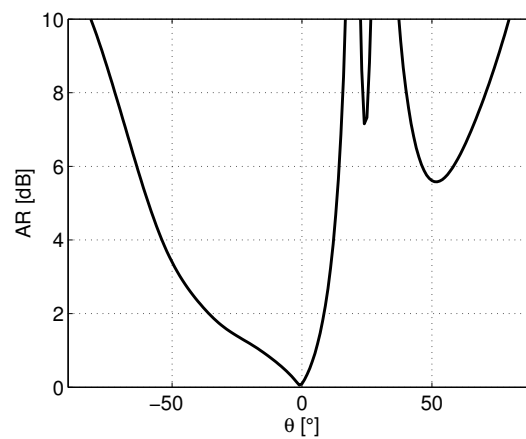
$$E_\phi^{\text{tot}} = a_1 E_\phi^{1,\text{X}}(\theta) + a_3 E_\phi^{3,\text{X}}(\theta) + a_2 E_\phi^{2,\text{co}}(\theta) + a_4 E_\phi^{4,\text{co}}(\theta), \quad (7.2)$$

where  $E_\theta^{\text{tot}}$  and  $E_\phi^{\text{tot}}$  represent the  $\theta$ - and  $\phi$ -component of the total electric field,  $E_\theta^{1,\text{co}}$  is the co-polarized component due to antenna element 1, and  $E_\theta^{2,\text{X}}$  is the cross-polarized component due to element 2. A similar explanation holds for the other field components. Note that it is assumed here that the required phase related to beam steering is already included in the various field components. Furthermore,  $a_i$  (with  $i = 1, 2, 3, 4$ ) represents the complex excitation of element  $i$ , excluding the phase associated with



(a) Input reflection coefficient with respect to  $Z_0 = 100 \Omega$ .

(b) Gain pattern at  $\phi = 0^\circ$ .



(c) Axial ratio at 60 GHz for the  $\phi = 0^\circ$  plane.

**Figure 7.11.** Antenna parameters of the antenna array shown in Figure 7.9 for a scan angle of  $-15^\circ$  in the  $\phi = 0^\circ$  plane.

beam-steering. For sequentially rotated antennas,  $a_3 = -a_1$  and  $a_4 = -a_2$  is typically chosen. Therefore, (7.1) and (7.2) can be simplified to

$$\begin{aligned} E_{\theta}^{\text{tot}}(\theta) &= a_1(E_{\theta}^{1,\text{co}}(\theta) - E_{\theta}^{3,\text{co}}(\theta)) + a_2(E_{\theta}^{2,\text{X}}(\theta) - E_{\theta}^{4,\text{X}}(\theta)), \\ &= a_1 E_{\theta}^{1-3,\text{co}}(\theta) + a_2 E_{\theta}^{2-4,\text{X}}(\theta), \end{aligned} \quad (7.3)$$

$$\begin{aligned} E_{\phi}^{\text{tot}}(\theta) &= a_1(E_{\phi}^{1,\text{X}}(\theta) - E_{\phi}^{3,\text{X}}(\theta)) + a_2(E_{\phi}^{2,\text{co}}(\theta) - E_{\phi}^{4,\text{co}}(\theta)), \\ &= a_1 E_{\phi}^{1-3,\text{X}}(\theta) + a_2 E_{\phi}^{2-4,\text{co}}(\theta), \end{aligned} \quad (7.4)$$

where the short-hand notation  $E_{\theta}^{1-3,\text{co}}(\theta)$  is used for  $(E_{\theta}^{1,\text{co}}(\theta) - E_{\theta}^{3,\text{co}}(\theta))$ . The correction procedure is now based on solving the far-field components (7.3) and (7.4) for optimal circular polarization at the required scan angle  $\theta_0$ . This is done by solving the following set of linear equations:

$$E_{\theta}^{\text{tot}}(\theta_0) = a_1 E_{\theta}^{1-3,\text{co}}(\theta_0) + a_2 E_{\theta}^{2-4,\text{X}}(\theta_0) = 1, \quad (7.5)$$

$$E_{\phi}^{\text{tot}}(\theta_0) = a_1 E_{\phi}^{1-3,\text{X}}(\theta_0) + a_2 E_{\phi}^{2-4,\text{co}}(\theta_0) = j, \quad (7.6)$$

in which the total field components have been normalized. Solving this set of linear equations results in

$$a_2(\theta_0) = \frac{jE_{\theta}^{1-3,\text{co}}(\theta_0) - E_{\phi}^{2-4,\text{X}}(\theta_0)}{E_{\phi}^{2-4,\text{co}}(\theta_0)E_{\theta}^{1-3,\text{co}}(\theta_0) - E_{\phi}^{1-3,\text{X}}(\theta_0)E_{\theta}^{2-4,\text{X}}(\theta_0)}, \quad (7.7)$$

$$a_1(\theta_0) = \frac{1 - a_2(\theta_0)E_{\theta}^{2-4,\text{X}}(\theta_0)}{E_{\theta}^{1-3,\text{co}}(\theta_0)}, \quad (7.8)$$

which are the optimal complex excitation coefficients for obtaining perfect circular polarization at the scan angle  $\theta_0$ . If a larger array has to be compensated, the same calibration can be performed on a  $2 \times 2$  sub-array level, using (7.7) and (7.8) for each of the sub-arrays.

## 7.2.2 Experiment

### Array design

In order to test this method, a  $2 \times 2$  array of sequentially rotated dipoles was designed. Figure 7.12 shows a photograph of the prototype. The dipole design is, again, based on the antenna from Chapter 4. Here, however, it was printed on a RO3003 substrate (thickness 0.5 mm) for this experiment, see [31]. For obtaining the radiation pattern of a single element, one dipole was fed by a GSSG-probe via a differential line. All other dipoles were matched via resistors into  $100 \Omega$  (specified up to 20 GHz). Together with the long feed-lines of seven guided wavelengths and their

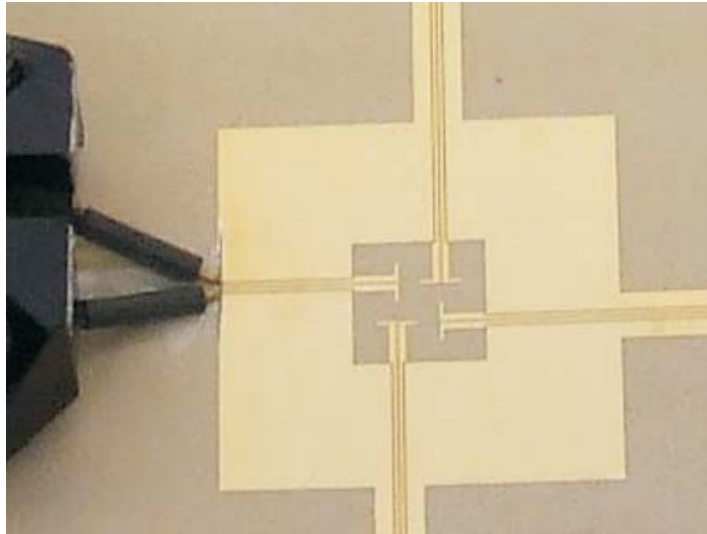


**Figure 7.12.** Photograph of the fabricated  $2 \times 2$  array consisting of sequentially rotated dipoles.

associated loss, these elements can be considered as sufficiently matched. The mm-wave antenna setup as described in [70] was then used to measure the normalized gain pattern of the single element. The effect of the environment (e.g., the probe-station) was reduced by employing time-gating. The measured gain patterns of the single element in its  $\phi = 0^\circ$  and  $\phi = 90^\circ$  planes are shown in Figure 7.13. Note that the gain pattern for angles smaller than  $-40^\circ$  in the  $\phi = 90^\circ$  plane is deteriorated due to the probe that blocks the line-of-sight between AUT and the reference antenna.

## Results

The measured axial ratio of the  $2 \times 2$  array with and without calibration is shown in Figure 7.14 for the case of scanning towards  $\theta_0 = 25^\circ$ . From this, it is apparent that the AR is noticeably improved by applying the proposed calibration scheme and is below 3 dB over a wide range around the scan angle. The required dynamic range of the correction factors is within a  $\pm 3$  dB range in this example. The frequency dependence of the calibration factors was also investigated. It was found that the AR is deteriorated with 2 dB for a frequency offset of 1 GHz as compared to the calibration frequency. This corresponds to a bandwidth of approximately 3.2%. An initial study on amplitude and phase quantization effects was published in [77].

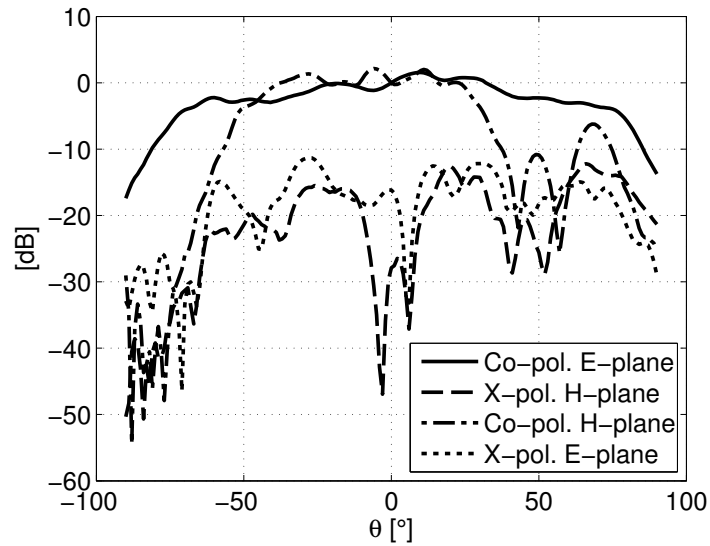


**Figure 7.13.** Measured normalized gain patterns at 60 GHz of the array prototype shown in Figure 7.12 (normalized with respect to  $\theta = 0^\circ$ ).

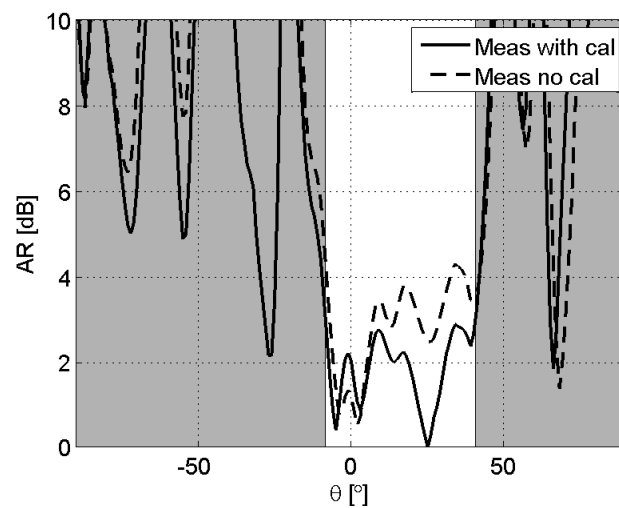


**Figure 7.14.** Axial ratio with and without the proposed calibration scheme of the antenna array from Figure 7.12 at 60 GHz and for a scan angle of  $25^\circ$  (the angular range in which the ratio is smaller than 3 dB is highlighted).

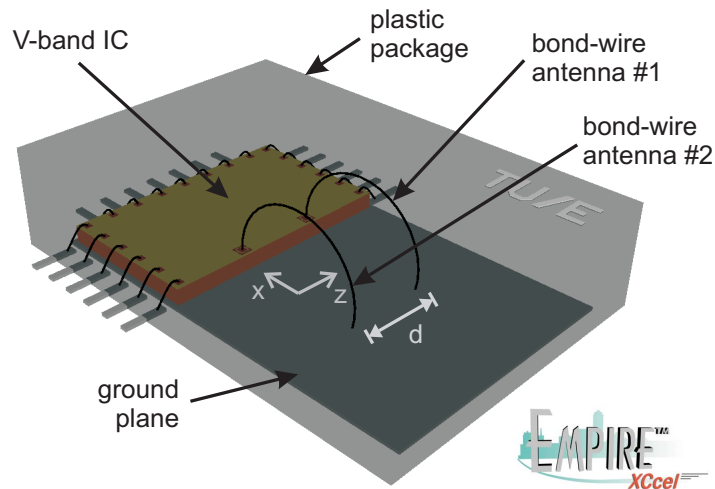


**Figure 7.15.** Conceptual drawing of the mm-wave front-end module with two integrated BWAs.

## 7.3 Mutual coupling between bond-wire-antennas

The modular array concept and the sequential rotation technique, which were presented in Section 7.1 and 7.2, can be applied to the AiP concept from Chapter 4 and to the AoC concept from Chapter 5. For the hybrid concept from Chapter 6, this method is not as easily applicable since the antenna exhibits a gain minimum in the broadside direction of the ground plane. However, this antenna type might still be of interest for a multi-antenna system. As an example, Figure 7.15 shows a mm-wave front-end module with two integrated BWAs that are separated by a distance  $d$ . Such a configuration could, for example, be used to achieve a larger maximum gain, as proposed by the authors of [53], to exploit advantages due to antenna diversity, or simply to integrate transmitter and receiver on the same IC. In any case, the two BWAs will influence each other's radiation pattern and input impedance due to mutual coupling. Therefore, the model from Section 6.2.2 is extended here, in order to determine the changed current distribution on the wires for such a configuration.

### 7.3.1 Model extension

Due to the presence of a second antenna, the boundary condition (2.60) on each wire-loop<sup>2</sup> is now given by

$$\mathbf{n} \times [\mathbf{E}_{\text{scat.}}(\mathbf{r}) + \mathbf{E}_{\text{inc.}}(\mathbf{r}) + \mathbf{E}_{\text{coupl.}}(\mathbf{r})] = 0 \Big|_{\mathbf{r} \in S}, \quad (7.9)$$

<sup>2</sup>Note that the ground plane is again replaced by the image of the wires in the model.

where  $\mathbf{E}_{\text{coupl.}}(\mathbf{r})$  was added to the equation to also account for the incident electric field on the wire that originates from the other antenna. In analogy to the derivation of the EFIE for a single loop, see Section 2.4.1, and assuming that both antennas are identical, i.e., they have the same loop-radius and wire thickness, Equation (7.9) can be formulated for BWA #1, see Figure 7.15, as

$$b \mathbf{E}_{\text{inc.}}(\varphi) \cdot \mathbf{u}_\varphi = \frac{j\eta}{4\pi} \int_{\varphi'} K_a(\varphi - \varphi') I_1(\varphi') d\varphi' + \frac{j\eta}{4\pi} \int_{\varphi'} K_d(\varphi - \varphi') I_2(\varphi') d\varphi', \quad (7.10)$$

with

$$K_a(\varphi - \varphi') = \left[ kb \cos(\varphi - \varphi') + \frac{1}{kb} \frac{\partial^2}{\partial \varphi^2} \right] \frac{e^{-jkbR_{b,a}(\varphi - \varphi')}}{R_{b,a}(\varphi - \varphi')}, \quad (7.11)$$

$$K_d(\varphi - \varphi') = \left[ kb \cos(\varphi - \varphi') + \frac{1}{kb} \frac{\partial^2}{\partial \varphi^2} \right] \frac{e^{-jkbR_{b,d}(\varphi - \varphi')}}{R_{b,d}(\varphi - \varphi')}, \quad (7.12)$$

in which  $R_{b,a}(\varphi - \varphi')$  is identical to  $R_b(\varphi - \varphi')$  as defined in Equation (2.77) and

$$R_{b,d}(\varphi - \varphi') = \sqrt{4 \sin^2 \left( \frac{\varphi - \varphi'}{2} \right) + \left( \frac{d}{b} \right)^2}. \quad (7.13)$$

In (7.10), the first integral on the right hand side describes the tangential electric field in an observation point on BWA #1 that originates from the current distribution  $I_1(\varphi')$  on *the same antenna*. This term is identical to the one used for the single loop BWA from Chapter 4. The second integral in (7.10) describes the additional tangential electric field that originates from the current distribution  $I_2(\varphi')$  on *the other antenna*, i.e., BWA #2. Hence, this term represents the coupling mechanism. Since both loops are assumed to be identical, the EFIE for the second loop is the same as (7.10), whereas the current distributions  $I_1(\varphi')$  and  $I_2(\varphi')$  have to be interchanged.

The EFIE (7.10) and the corresponding EFIE of BWA #2 can be evaluated in the same way as described in Section 2.4.2. The resulting MoM-matrix has the following form:

$$[\tilde{\mathbf{Z}}] = \begin{bmatrix} [Z^{(1)}] & [Z^{(2)}] \\ [Z^{(2)}] & [Z^{(1)}] \end{bmatrix}, \quad (7.14)$$

with  $[Z^{(1)}]$  the MoM-matrix of the first integral in (7.10), which is identical to the matrix  $[Z]$  for the single BWA, and  $[Z^{(2)}]$  the MoM-matrix of the second integral in (7.10), which can be evaluated in the same manner as shown in Section 2.4.2. The amplitudes of the approximate current distribution  $[\alpha^{(1)}]$  and  $[\alpha^{(2)}]$  on BWA #1 and

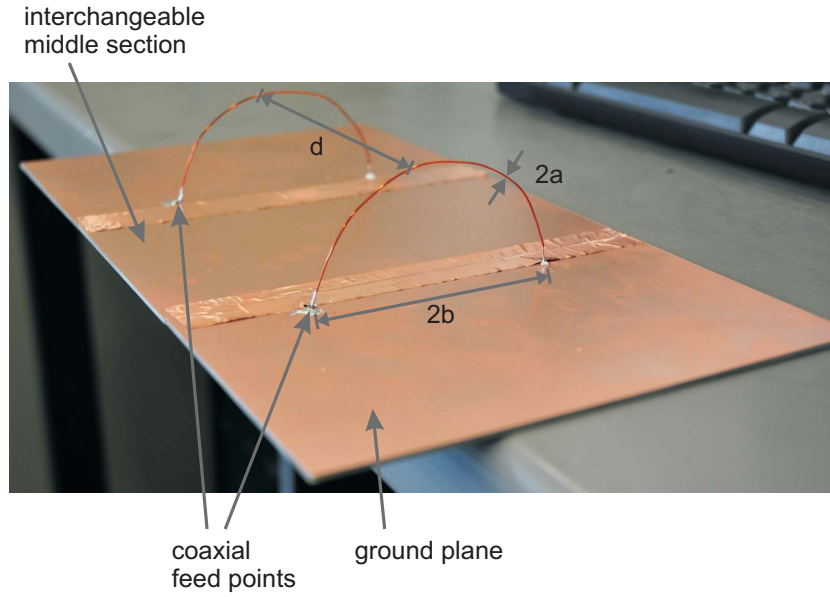


**Figure 7.16.** Photograph of the scaled prototype.

#2, respectively, are then given by

$$\begin{aligned} [\tilde{\alpha}] &= [\tilde{Z}]^{-1} [\tilde{V}], \\ \begin{bmatrix} [\alpha^{(1)}] \\ [\alpha^{(2)}] \end{bmatrix} &= \begin{bmatrix} [Z^{(1)}] & [Z^{(2)}] \\ [Z^{(2)}] & [Z^{(1)}] \end{bmatrix}^{-1} \begin{bmatrix} [\bar{V}^{(1)}] \\ [\bar{V}^{(2)}] \end{bmatrix}, \end{aligned} \quad (7.15)$$

with  $[\bar{V}^{(1)}]$  and  $[\bar{V}^{(2)}]$  the excitation vectors due to the (magnetostatic frill) sources at BWA #1 and #2, respectively.

### 7.3.2 Verification

In order to verify the model from the preceding section, the prototype shown in Figure 7.16 was built. It consists of two copper wires with a wire-diameter of  $2a = 0.6$  mm. The wires were bent to exhibit a semi-circular shape with an approximate radius of  $b = 4$  cm and were soldered onto a large copper ground-plane. One end of each antenna was attached to a coaxial connector, such that a VNA can be connected here. Moreover, an interchangeable middle section in the ground plane allows the two antennas to be located at various distances  $d$ . For the measurements, the interfaces between the individual ground-planes were covered with adhesive copper-tape in order to achieve electrical continuity here. Figure 7.17 shows a comparison between the magnitudes of measured S-parameters of this prototype and



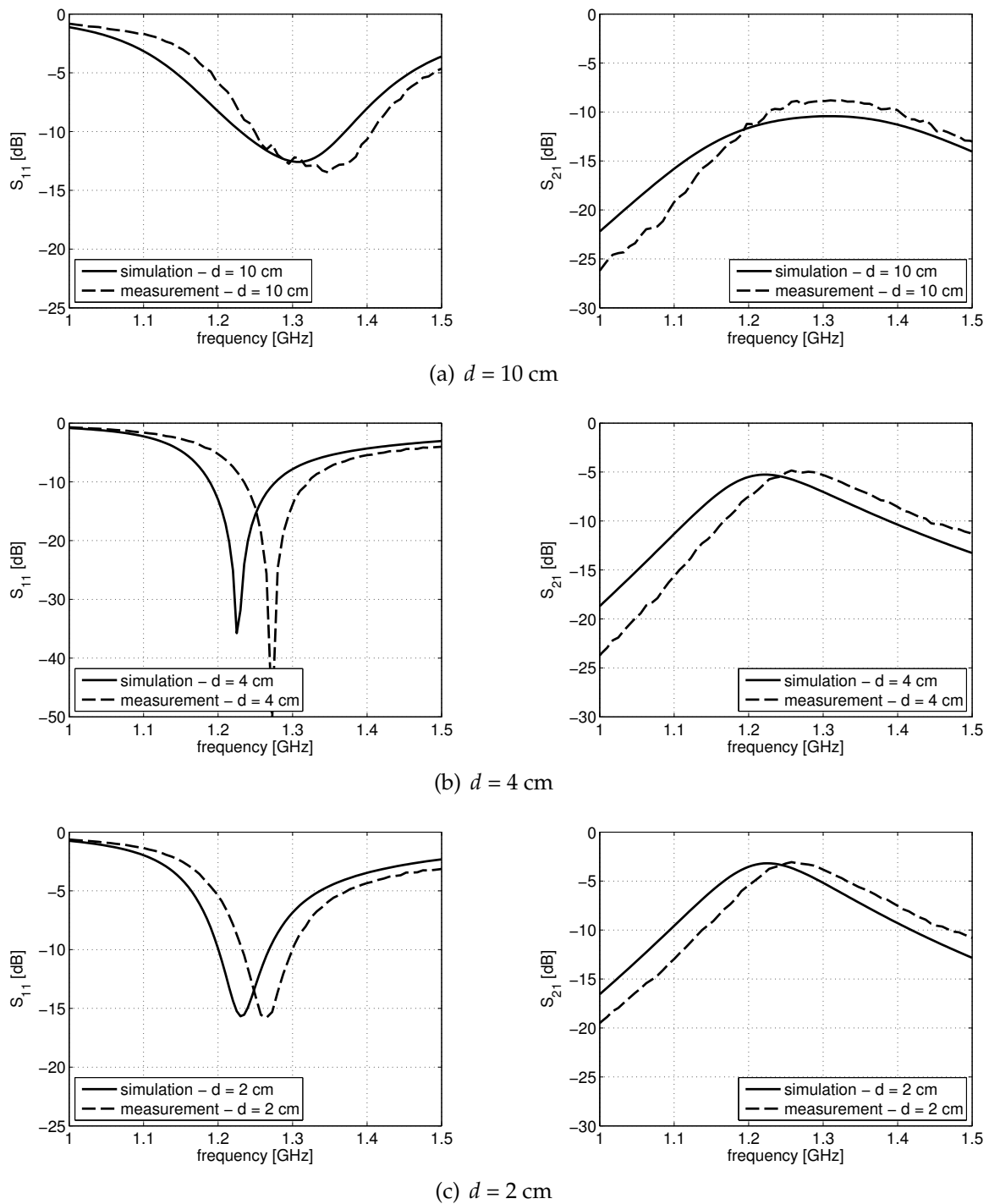


**Figure 7.17.** Magnitude of S-parameters with respect to the reference impedance  $Z_0 = 50 \Omega$  for different distances  $d$ , obtained with the model described in Section 7.3.1, in comparison with the measurement results of the scaled prototype from Figure 7.16.

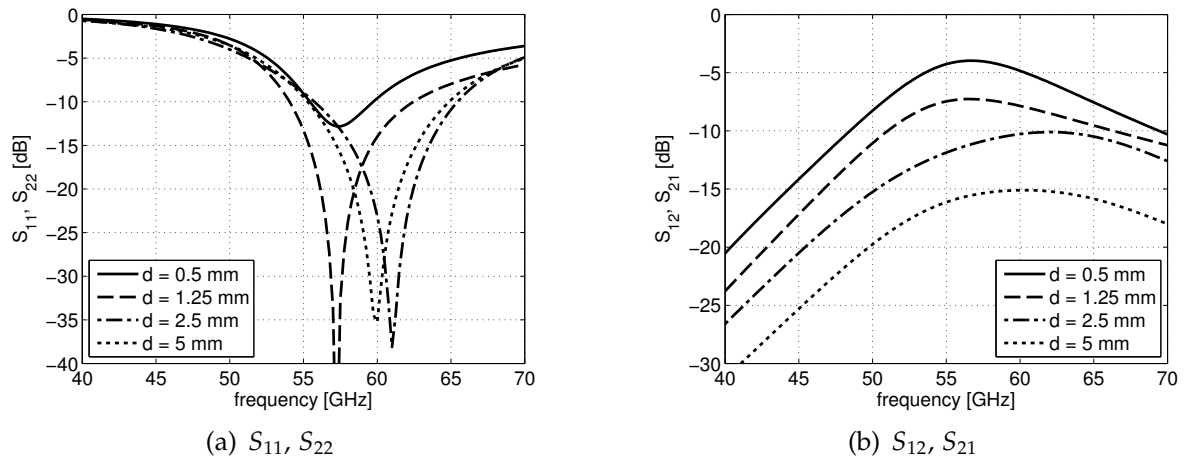


**Figure 7.18.** Simulated magnitude of the S-parameters for the BWA configuration from Figure 7.15, with  $2a = 25 \mu\text{m}$  and  $b = 870 \mu\text{m}$ , for different distances  $d$  ( $Z_0 = 75 \Omega$ ).

the results obtained with the model from the preceding section. A comparison between the measured and simulated phase terms for the shown cases is provided in Appendix C. Since the cables that were used for the measurements were not phase-stable, however, those plots are provided for completeness rather than for verification purposes here. From the results shown in Figure 7.17, it can be concluded that, besides a frequency offset of  $< 50$  MHz, the results agree excellently. Since the frequency offset is seen to be mainly caused by manufacturing tolerances, the model can be concluded to be successfully verified.

### 7.3.3 60 GHz example

As shown in Section 7.3.2, the model from Section 7.3.1 can be used to predict the mutual coupling between semi-circular loop-antennas over a large ground-plane. Since the BWA configuration shown in Figure 7.15 can essentially be modeled as such a configuration, see also Chapter 4, this model can also be used to predict the coupling for this scenario throughout the mm-wave band. As an example, the magnitude of the S-parameters ( $Z_0 = 75 \Omega$ ) as well as the Z-parameters for two BWAs with a wire-diameter  $2a = 25 \mu\text{m}$  and a loop-radius  $b = 870 \mu\text{m}$  are provided in Figure 7.18 and 7.19, respectively.

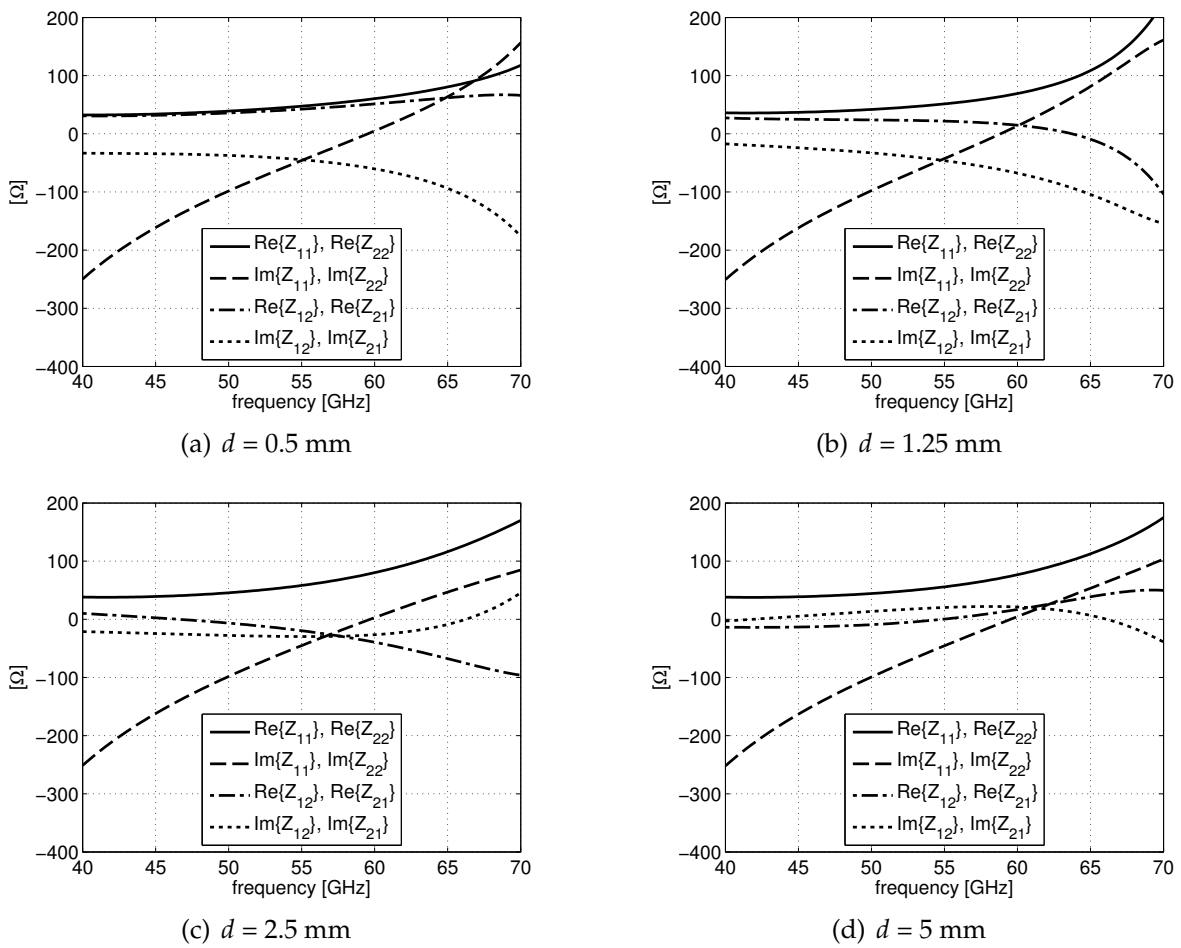


**Figure 7.19.** Simulated Z-parameters of the BWA configuration from Figure 7.15, with  $2a = 25 \mu\text{m}$  and  $b = 870 \mu\text{m}$ , for different distances  $d$ .

## 7.4 Conclusions

In this chapter, a modular, scalable antenna array concept is proposed that exhibits beam-steering capabilities and a high design flexibility. In particular, possible array configurations for achieving linear and circular polarization were demonstrated and tested by means of numerical simulations. Since the axial ratio for the proposed circularly polarized antenna array degrades for beams that are steered off broad-side, however, a method was proposed that can compensate this effect. Finally, an extension of the BWA model from Section 6.2.2 was introduced that can be used to predict the mutual coupling between parallel oriented BWAs. Especially a successful fabrication and test of a modular array prototype at mm-waves as well as the verification of the predicted BWA coupling shown in Figures 7.18 and 7.19 remain an open task for future research.



# Conclusions and recommendations

---

## 8.1 Conclusions

The goal of this thesis is to answer the question which of the three antenna integration technologies, i.e., AiP, AoC, or hybrid approach, is ultimately the best choice for wireless consumer applications in the mm-wave band. For this, integration concepts for each approach were developed based on state-of-the-art solutions. The proposed concepts are individually presented in Chapters 4, 5, and 6, respectively. For each concept, prototypes were manufactured and measured in order to verify their producibility and simulated performance. Each of those concepts was concluded to be feasible and highly competitive to respective state-of-the-art solutions. While detailed conclusions for each integration concept are given in the individual chapters, their simulated performances are used in this last chapter to come to a final conclusion, which is presented in the following section. Furthermore, conclusions with respect to integrated mm-wave antenna modeling and measurements are presented in Sections 8.1.2 and 8.1.3, respectively.

### 8.1.1 Technology choice

Table 8.1 provides the key figures of the individual antenna concepts with respect to the 60 GHz antenna requirements from Chapter 3. From this overview, it becomes evident that the AiP and hybrid approach achieve the best radiation efficiency and one might, therefore, regard them as better suited than the AoC approach. When comparing those two solutions with each other, the hybrid, consisting only of a bondwire, is expected to have a cost advantage over the AiP since standard packaging can be used here. Moreover, the yield analysis presented in Section 6.4 indicates that

**Table 8.1.** Overview of the integrated mm-wave antenna concepts from Chapters 4 to 6 with respect to the 60 GHz key requirements stated in Section 3.1.

concept	size [mm <sup>2</sup> ]	feed topology	$\eta_{\text{rad}}$ [%]	gain [dBi]	cost (relative)
AiP	15	differential	80 (incl. interconnect)	9.63 - 10.14	medium - high
AoC	1.02	differential	45 - 60	0.96 - 1.47	medium - high
AoC	< 0.5	single-ended	30 - 47	-	medium
Hybrid	2.56 <sup>(a)</sup>	single-ended	52 - 92 (model-dependent)	5.5 - 7.1	low

<sup>(a)</sup>The in-package antenna size was estimated as the square of the loop-diameter here, i.e.,  $(2b)^2$ .

BWAs are suitable for nearly the entire mm-wave band. And since typical PCB processes do not exhibit a similar fabrication accuracy like wire-bonders, AiPs are not expected to match the high yield performance of the hybrid at the upper end of the mm-wave spectrum. On the contrary, the BWA exhibits a single-ended feed topology and its design flexibility is limited to the choice of the wire thickness, length, and shape. Therefore, especially at the lower and upper end of the spectrum, in-package and on-chip antennas, respectively, might come into play again since they offer a much higher design flexibility. Hence, a single low-cost integration technology that is superior throughout the entire frequency band does not seem to emerge from this consideration. Therefore, rather than trying to find the best compromise of the three solutions, one should rather make use of the existing technology diversity and choose an approach that fits best to the given specifications of a target application. For this, a general guideline with respect to the operating frequency is provided in Figure 8.1, which is based on above considerations with respect to performance and producibility of the individual antenna concepts. It shows that the AiP approach is then considered to be the generally best suited technology for the lower frequency range. At the upper end of the mm-wave spectrum, the AoC approach is seen to be superior, which is also in line with the successful use of on-chip antennas in the terahertz band, see, for example, [10]. The hybrid approach can then be understood as a bridge-technology that comes into play when both other approaches turn out to be insufficient.

The general recommendation from Figure 8.1 is a nice starting point for choosing a suitable antenna technology. However, it does not state any general corner frequencies at which one approach becomes superior to the others. For this, specific requirements for the antenna would be necessary. Due to the vast amount of possible applications throughout the mm-wave band, such definite transition points cannot be given here. Furthermore, at a single frequency band with different application

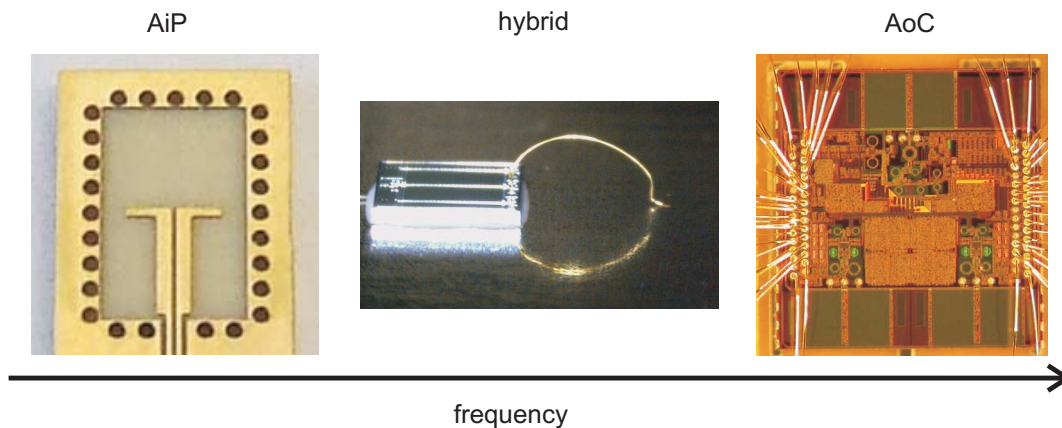


**Figure 8.1.** General recommendation for antenna integration technologies in the mm-wave band.

**Table 8.2.** Proposed technology choices for the three major application areas in the 60 GHz band, see Chapter 1.

concept	application area
AiP	HD video streaming and wireless Gigabit Ethernet, file transfer (terminal side)
AoC	file transfer (hand-held side)
Hybrid	wireless interconnects

scenarios, even all three integration approaches may be a valid choice. As an example for this, Table 8.2 shows the antenna concepts from Chapters 4 to 6 versus their recommended application scenario for the 60 GHz band from Chapter 1<sup>1</sup>. It clearly shows a preference of a certain technology for a specific application. Note, however, that this does not mean that the other concepts are not feasible at all for those applications.

Hence, as a final conclusion it can be stated that there is no single antenna integration technology that meets the requirements of the consumer electronics market in the entire mm-wave band. For the 60 GHz band in particular, however, it is advised here to focus on the AiP approach since it offers the highest design freedom, excellent antenna performances, and a potentially high yield.

<sup>1</sup>Detailed explanations why an antenna concept is particularly suited for the shown application area are provided in the conclusions-sections of the respective antenna chapters.



### 8.1.2 Antenna modeling

For the investigation of the integrated mm-wave antenna concepts as well as the design of their prototypes, extensive use of modeling tools was made. For this, mostly the commercial tool Empire XCcel was used. Thanks to its FDTD-based approach that can handle computationally large structures very efficiently, it has proven to be excellently suited for such complex antenna systems. This statement is, for example, supported by the high degree of agreement between the simulation and measurement results.

Moreover, for the hybrid integrated mm-wave antenna concept from Chapter 6, a dedicated, computationally efficient model was developed that is particularly suited for statistical analyses. Furthermore, in order to compute the radiation pattern of an antenna on a finite ground-plane, it was shown that the UTD can be used to incorporate the effect of diffraction at its edges and corners. For the prediction of mutual coupling in a multi-antenna system, the modeling tool was extended to incorporate the effect of a second antenna. In all cases, the results of the proposed model were successfully verified by Empire XCcel or measurements. Therefore, this tool is seen to be very useful as a low-cost supplement for IC design tools in IC or system design houses that do not have access to commercial full-wave EM simulation software.

### 8.1.3 Millimeter-wave measurements

In the outline of this thesis, several prototypes were fabricated and measured in order to validate their producibility and simulated performance. For the measurement of the input impedance in particular, good agreements were achieved by the use of a regular probe-station in combination with robust mm-wave probes, which were landed at a sufficient distance away from the antennas. For this, the feed-lines of the antennas had to be extended. In order to reduce the impact of measurement uncertainties, those feed-lines were included in the simulation setup as well rather than de-embedded from the measurements.

With respect to the radiation pattern measurements, good agreements were achieved by, again, including all necessary details of the antenna prototype also in the simulation setup. In some cases, even the probe-tip had to be included. Moreover, a dedicated setup, which is described in detail in Section 4.3, allowed the anechoic measurement of normalized gain patterns of the AUTs. Here, special emphasis was placed on the repeatability of the placement and probing of the AUT. Based on this setup, a straightforward method to determine the antenna gain was proposed as well.

Finally, it was demonstrated in Section 4.4 that the differential antenna from Chapter 4 can be characterized by a (single-ended) GS-probe without causing spurious

radiation from the probe-tip or significant common-mode excitation.

## 8.2 Recommendations

### 8.2.1 Technology choice

In the outline of this thesis, the electric properties of the used materials were taken from the respective datasheets of the material suppliers. However, those values are usually not confirmed at 60 GHz. Therefore, they need to be properly characterized in order to achieve a better prediction of the antenna concepts. Moreover, the properties of typical packaging materials, like molding compounds, have to be determined as well. With this knowledge, suitable packaging concepts for the AoC and hybrid approach can then be developed.

Another open task for the future is to determine the yield of the proposed integrated antenna concepts. Although the input reflection coefficients of some AiP samples were already measured and indicated a potentially high yield of this antenna design, it does not prove the feasibility of this concept for high volume production yet. For the AoC concept, the variations in the actual IC process may be very small, but in combination with the die packaging the yield might be affected as well. Lastly, although a first yield analysis of the BWA was conducted, a thorough investigation of tolerances in the wire's shape and the effect of packing have to be included as well.

The literature study for the AoC concept in Section 3.3 has shown that excellent on-chip antennas can be fabricated when suitable post-processing steps are applied. Therefore, the semiconductor industry is strongly encouraged here to investigate to what extent such post-processing steps would be feasible to implement in their standard processing portfolio. Such an investigation is seen to be particularly valuable since also other on-chip passive devices, like inductors, could greatly benefit from such processes.

Finally, the feasibility of the modular antenna array concept, presented in Section 7.1, needs to be proven. For this, complete mm-wave front-end modules including antennas need to be built. Those modules should then be used to construct several different array configurations and sizes. For this, a suitable clock distribution network has to be designed and the data signals from each individual front-end module need to be combined as well. The latter could, for example, be done in the digital domain.

### 8.2.2 Antenna modeling

With respect to the proposed BWA modeling approach, a thorough investigation of the bond-pad model is advised since this is seen to be the cause of the deviation between the radiation efficiency obtained with Empire XCcel and the model.

Furthermore, a mm-wave prototype of the mutual coupling experiment, presented in Section 7.3, should be fabricated. The measurement results of this experiment can then be used to gain further insights in the validity and boundaries of the proposed modeling approach.

Lastly, the BWA-model from Chapter 4 and Section 7.3 is limited to semi-circular wire-shapes. In order to increase the flexibility of the model and, thus, to provide the antenna designer with more freedom, the model should be extended to arbitrary wire shapes.

### 8.2.3 Millimeter-wave measurements

The conclusions, drawn in Section 8.1.1, are based on the findings and conclusions of the previous chapters. Here, a strong emphasis is placed on the simulation results, which were mostly verified by measurements of fabricated prototypes. The simulated radiation efficiency of the antenna concept could not be verified directly, however. In order to be able to perform direct efficiency measurements, it is recommended here to extend the radiation pattern measurement setup, described in Section 4.3, to include complete hemispherical scans. By this, the total radiated power of an antenna can be determined. Furthermore, the input power that is accepted by the AUT has to be known for this, such that Equation (2.50) can be applied directly. This input power can, for example, be measured with a power meter or by a measurement of a reference antenna with known efficiency. For this, a standard gain horn could be used, for which the radiation efficiency may be assumed to be 100 %. The resulting accuracy of this assumption remains to be shown, however.

Furthermore, the radiation pattern of the on-chip BWA could not be measured since the probe could not be adequately landed on the on-chip bond-pads. Therefore, the radiation pattern measurement setup needs to be extended to allow the probe to be tilted around its longitudinal axis.

Finally, as mentioned in Section 8.1.3, it was demonstrated that a differential antenna can be characterized by a (single-ended) GS-probe. Using such a probe appears to be easier since no balun is required. However, it remains to be investigated whether this probe can be used for any differential antenna type or, if not, under what conditions this method is a legitimate choice.

## Derivation of the magnetostatic frill source model

---

### A.1 The electric vector potential

The electric vector potential due to an arbitrary magnetic current distribution  $\mathbf{M}(\mathbf{r}')$  is given by Equation (2.30). For a magnetostatic current loop

$$\mathbf{M}(\mathbf{r}') = M_0 \mathbf{u}_{\varphi'} = \text{const.} \quad (\text{A.1})$$

that is concentric with the  $z$ -axis with radius  $r_1$  and lying in the  $xy$ -plane ( $z = 0$ ), (2.30) simplifies to

$$\mathbf{F}(\mathbf{r}) = \frac{M_0}{4\pi} \int_0^{2\pi} \frac{\cos(\varphi - \varphi') \mathbf{u}_\varphi + \sin(\varphi - \varphi') \mathbf{u}_r}{\sqrt{r^2 + r_1^2 - 2rr_1 \cos(\varphi - \varphi') + z^2}} r_1 d\varphi'. \quad (\text{A.2})$$

The  $r$ -component of the vector potential

$$F_r(\mathbf{r}) = \frac{M_0}{4\pi} \int_0^{2\pi} \frac{r_1 \sin(\varphi - \varphi')}{\sqrt{r^2 + r_1^2 - 2rr_1 \cos(\varphi - \varphi') + z^2}} d\varphi', \quad (\text{A.3})$$

$$= \frac{M_0}{4\pi} \left[ -\frac{1}{r} \sqrt{r^2 + r_1^2 - 2rr_1 \cos(\varphi - \varphi') + z^2} \right]_0^{2\pi}, \quad (\text{A.4})$$

$$= 0, \quad (\text{A.5})$$

vanishes such that one is left with the  $\varphi$ -component

$$F_\varphi(\mathbf{r}) = \frac{M_0}{4\pi} \int_0^{2\pi} \frac{r_1 \cos(\varphi - \varphi')}{\sqrt{r^2 + r_1^2 - 2rr_1 \cos(\varphi - \varphi') + z^2}} d\varphi', \quad (\text{A.6})$$

which is not as straightforward to solve. However, since the magnetic current is constant, the field radiated by the loop is not a function of  $\varphi$  and, thus, any observation angle can be chosen [14]. Here,  $\varphi = \pi$  is chosen, which results in

$$F_\varphi(\mathbf{r}) = \frac{M_0}{4\pi r} \int_0^{2\pi} \frac{rr_1 \cos(\pi - \varphi')}{\sqrt{r^2 + r_1^2 - 2rr_1 \cos(\pi - \varphi') + z^2}} d\varphi', \quad (\text{A.7})$$

where the integrand was also multiplied by the factor  $r/r = 1$ . Furthermore, the integration range can be halved according to

$$F_\varphi(\mathbf{r}) = \frac{M_0}{4\pi r} \int_0^\pi \frac{2rr_1 - 2rr_1[1 + \cos(\varphi')]}{\sqrt{r^2 + r_1^2 - 2rr_1 + 2rr_1[1 + \cos(\varphi')] + z^2}} d\varphi'. \quad (\text{A.8})$$

Here, the term  $2rr_1 - 2rr_1 = 0$  was added to the numerator and inside the square-root in the denominator. Now, the following substitution:

$$\varphi' = 2\psi', \quad (\text{A.9})$$

$$d\varphi' = 2d\psi', \quad (\text{A.10})$$

can be applied, which leads to

$$F_\varphi(\mathbf{r}) = 2 \frac{M_0}{4\pi r} \int_0^{\pi/2} \frac{2rr_1 - 4rr_1 \cos^2(\psi')}{\sqrt{r^2 + r_1^2 - 2rr_1 + 4rr_1 \cos^2(\psi') + z^2}} d\psi', \quad (\text{A.11})$$

$$= \frac{M_0}{2\pi r} \int_0^{\pi/2} \frac{2rr_1 - 4rr_1[1 - \sin^2(\psi')]}{\sqrt{r^2 + r_1^2 - 2rr_1 + 4rr_1[1 - \sin^2(\psi')] + z^2}} d\psi', \quad (\text{A.12})$$

$$= \frac{M_0}{2\pi r} \int_0^{\pi/2} \frac{-2rr_1 + 4rr_1 \sin^2(\psi')}{\sqrt{r^2 + r_1^2 + 2rr_1 - 4rr_1 \sin^2(\psi') + z^2}} d\psi', \quad (\text{A.13})$$

$$= \frac{M_0}{2\pi r} \int_0^{\pi/2} \frac{-2rr_1 + 4rr_1 \sin^2(\psi')}{\sqrt{(r + r_1)^2 + z^2 - 4rr_1 \sin^2(\psi')}} d\psi'. \quad (\text{A.14})$$

Now define

$$R_{m,1} = \sqrt{(r + r_1)^2 + z^2} \quad (\text{A.15})$$

$$\beta_1 = \frac{\sqrt{4rr_1}}{R_{m,1}} \quad (\text{A.16})$$

to write

$$F_\varphi(\mathbf{r}) = \frac{M_0}{2\pi r} \int_0^{\pi/2} \frac{-R_{m,1}^2 \beta_1^2 / 2 + R_{m,1}^2 \beta_1^2 \sin^2(\psi')}{\sqrt{R_{m,1}^2 - R_{m,1}^2 \beta_1^2 \sin^2(\psi')}} d\psi', \quad (\text{A.17})$$

$$= \frac{M_0 R_{m,1}}{2\pi r} \int_0^{\pi/2} \frac{-\beta_1^2 / 2 + \beta_1^2 \sin^2(\psi')}{\sqrt{1 - \beta_1^2 \sin^2(\psi')}} d\psi', \quad (\text{A.18})$$

$$= \frac{M_0 R_{m,1}}{2\pi r} \int_0^{\pi/2} \frac{1 - \beta_1^2 / 2 - (1 - \beta_1^2 \sin^2(\psi'))}{\sqrt{1 - \beta_1^2 \sin^2(\psi')}} d\psi', \quad (\text{A.19})$$

$$= \frac{M_0 R_{m,1}}{2\pi r} \int_0^{\pi/2} \frac{1 - \beta_1^2 / 2}{\sqrt{1 - \beta_1^2 \sin^2(\psi')}} - \sqrt{1 - \beta_1^2 \sin^2(\psi')} d\psi', \quad (\text{A.20})$$

$$= \frac{M_0 R_{m,1}}{2\pi r} \left[ \left(1 - \frac{\beta_1^2}{2}\right) \mathcal{K}(\beta_1) - \mathcal{E}(\beta_1) \right], \quad (\text{A.21})$$

with  $\mathcal{K}(\beta_1)$  and  $\mathcal{E}(\beta_1)$  the complete elliptical integral of the first and second kind, respectively, which is consistent with Equation (7) in [11] beside an additional factor of  $1/2\pi$ .

## A.2 Generated electric fields

The electric fields that are generated by the magnetostatic frill source can now be calculated by using (A.21) in (2.31), which yields

$$\begin{aligned} \mathbf{E}(\mathbf{r}) &= -\nabla \times \mathbf{F}(\mathbf{r}) = \frac{\partial F_\varphi(\mathbf{r})}{\partial z} \mathbf{u}_r - \frac{1}{r} \frac{\partial (r F_\varphi(\mathbf{r}))}{\partial r} \mathbf{u}_z, \\ &= \frac{\partial F_\varphi(\mathbf{r})}{\partial z} \mathbf{u}_r - \frac{1}{r} F_\varphi(\mathbf{r}) \mathbf{u}_z - \frac{\partial F_\varphi(\mathbf{r})}{\partial r} \mathbf{u}_z. \end{aligned} \quad (\text{A.22})$$

In order to evaluate (A.22), the following derivatives are required:

$$\begin{aligned} \frac{\partial F_\varphi(\mathbf{r})}{\partial z} &= \frac{M_0}{2\pi r} \left\{ \left[ \left(1 - \frac{\beta_1^2}{2}\right) \mathcal{K}(\beta_1) - \mathcal{E}(\beta_1) \right] \frac{\partial R_{m,1}}{\partial z} + \right. \\ &\quad \left. R_{m,1} \left[ \frac{\partial \mathcal{K}(\beta_1)}{\partial z} - \mathcal{K}(\beta_1) \frac{\partial \beta_1^2 / 2}{\partial z} - \frac{\beta_1^2}{2} \frac{\partial \mathcal{K}(\beta_1)}{\partial z} - \frac{\partial \mathcal{E}(\beta_1)}{\partial z} \right] \right\}, \end{aligned} \quad (\text{A.23})$$

$$\begin{aligned} \frac{\partial F_\varphi(\mathbf{r})}{\partial r} &= \frac{M_0}{2\pi} \left\{ \left[ \left(1 - \frac{\beta_1^2}{2}\right) \mathcal{K}(\beta_1) - \mathcal{E}(\beta_1) \right] \frac{\partial}{\partial r} \left( \frac{R_{m,1}}{r} \right) + \right. \\ &\quad \left. \frac{R_{m,1}}{r} \left[ \frac{\partial \mathcal{K}(\beta_1)}{\partial r} - \mathcal{K}(\beta_1) \frac{\partial \beta_1^2 / 2}{\partial r} - \frac{\beta_1^2}{2} \frac{\partial \mathcal{K}(\beta_1)}{\partial r} - \frac{\partial \mathcal{E}(\beta_1)}{\partial r} \right] \right\}. \end{aligned} \quad (\text{A.24})$$

For re-writing Equation (A.23), the following set of derivatives is needed:

$$\frac{\partial R_{m,1}}{\partial z} = \frac{z}{R_{m,1}}, \quad (\text{A.25})$$

$$\frac{\partial \beta_1}{\partial z} = \frac{-z\beta_1}{R_{m,1}^2}, \quad (\text{A.26})$$

$$\frac{\partial \mathcal{K}(\beta_1)}{\partial z} = \frac{\partial \mathcal{K}(\beta_1)}{\partial \beta_1} \frac{\partial \beta_1}{\partial z} = \frac{\mathcal{E}(\beta_1) - (1 - \beta_1^2)\mathcal{K}(\beta_1)}{1 - \beta_1^2} \frac{-z}{R_{m,1}^2}, \quad (\text{A.27})$$

$$\frac{\partial \mathcal{E}(\beta_1)}{\partial z} = \frac{\partial \mathcal{E}(\beta_1)}{\partial \beta_1} \frac{\partial \beta_1}{\partial z} = (\mathcal{E}(\beta_1) - \mathcal{K}(\beta_1)) \frac{-z}{R_{m,1}^2}. \quad (\text{A.28})$$

where the derivatives of the complete elliptic integrals from reference [80] have been used<sup>1</sup>. Similarly, Equation (A.24) contains

$$\frac{\partial}{\partial r} \left( \frac{R_{m,1}}{r} \right) = \frac{r(r + r_1) - R_{m,1}^2}{R_{m,1}r^2}, \quad (\text{A.29})$$

$$\frac{\partial \beta_1}{\partial r} = \frac{2r_1 - \beta_1^2(r + r_1)}{\beta_1 R_{m,1}^2}, \quad (\text{A.30})$$

$$\frac{\partial \mathcal{K}(\beta_1)}{\partial r} = \frac{\partial \mathcal{K}(\beta_1)}{\partial \beta_1} \frac{\partial \beta_1}{\partial r} = \frac{\mathcal{E}(\beta_1) - (1 - \beta_1^2)\mathcal{K}(\beta_1)}{(1 - \beta_1^2)\beta_1} \frac{2r_1 - \beta_1^2(r + r_1)}{\beta_1 R_{m,1}^2}, \quad (\text{A.31})$$

$$\frac{\partial \mathcal{E}(\beta_1)}{\partial r} = \frac{\partial \mathcal{E}(\beta_1)}{\partial \beta_1} \frac{\partial \beta_1}{\partial r} = \frac{\mathcal{E}(\beta_1) - \mathcal{K}(\beta_1)}{\beta_1} \frac{2r_1 - \beta_1^2(r + r_1)}{\beta_1 R_{m,1}^2}. \quad (\text{A.32})$$

Now, by simply inserting Equations (A.25) to (A.28) in (A.23), one obtains

$$\begin{aligned} \frac{\partial F_\varphi(\mathbf{r})}{\partial z} &= \frac{M_0}{2\pi r} \left\{ \left[ \left( 1 - \frac{\beta_1^2}{2} \right) \mathcal{K}(\beta_1) - \mathcal{E}(\beta_1) \right] \frac{z}{R_{m,1}} + \right. \\ &R_{m,1} \left[ \frac{\mathcal{E}(\beta_1) - (1 - \beta_1^2)\mathcal{K}(\beta_1)}{1 - \beta_1^2} \frac{-z}{R_{m,1}^2} - \mathcal{K}(\beta_1)\beta_1 \frac{-z\beta_1}{R_{m,1}^2} - \right. \\ &\left. \left. \frac{\beta_1^2}{2} \frac{\mathcal{E}(\beta_1) - (1 - \beta_1^2)\mathcal{K}(\beta_1)}{1 - \beta_1^2} \frac{-z}{R_{m,1}^2} - (\mathcal{E}(\beta_1) - \mathcal{K}(\beta_1)) \frac{-z}{R_{m,1}^2} \right] \right\} \quad (\text{A.33}) \end{aligned}$$

$$\begin{aligned} &= \frac{M_0 z}{2\pi r R_{m,1}} \left\{ \mathcal{K}(\beta_1) - \frac{\beta_1^2}{2} \mathcal{K}(\beta_1) - \mathcal{E}(\beta_1) - \frac{\mathcal{E}(\beta_1)}{1 - \beta_1^2} + \mathcal{K}(\beta_1) + \right. \\ &\left. \beta_1^2 \mathcal{K}(\beta_1) + \frac{\beta_1^2}{2} \frac{\mathcal{E}(\beta_1)}{1 - \beta_1^2} - \frac{\beta_1^2}{2} \mathcal{K}(\beta_1) + \mathcal{E}(\beta_1) - \mathcal{K}(\beta_1) \right\}, \quad (\text{A.34}) \end{aligned}$$

$$= \frac{M_0 z}{2\pi r R_{m,1}} \left\{ \mathcal{K}(\beta_1) - \frac{2 - \beta_1^2}{2(1 - \beta_1^2)} \mathcal{E}(\beta_1) \right\}, \quad (\text{A.35})$$

<sup>1</sup>Note that  $z = \beta_1^2$  is used in the reference and needs to be re-substituted. Furthermore, the results have then to be multiplied by the factor  $\partial z / \partial \beta_1 = 2\beta_1$  in order to account for the different derivation parameter.

$$\frac{\partial F_\varphi(\mathbf{r})}{\partial z} = \frac{M_0 z}{2\pi r R_{m,1}} \left\{ \mathcal{K}(\beta_1) - \frac{r^2 + r_1^2 + z^2}{(r - r_1)^2 + z^2} \mathcal{E}(\beta_1) \right\}. \quad (\text{A.36})$$

Inserting Equations (A.29) to (A.32) in (A.24) yields

$$\begin{aligned} \frac{\partial F_\varphi(\mathbf{r})}{\partial r} &= \frac{M_0}{2\pi} \left\{ \left[ \left( 1 - \frac{\beta_1^2}{2} \right) \mathcal{K}(\beta_1) - \mathcal{E}(\beta_1) \right] \frac{r(r + r_1) - R_{m,1}^2}{R_{m,1} r^2} + \right. \\ &\quad \frac{R_{m,1}}{r} \left[ \frac{\mathcal{E}(\beta_1) - (1 - \beta_1^2) \mathcal{K}(\beta_1)}{(1 - \beta_1^2) \beta_1} \frac{2r_1 - \beta_1^2(r + r_1)}{\beta_1 R_{m,1}^2} - \right. \\ &\quad \left. \left. \mathcal{K}(\beta_1) \beta_1 \frac{2r_1 - \beta_1^2(r + r_1)}{\beta_1 R_{m,1}^2} - \right. \right. \\ &\quad \left. \left. \frac{\beta_1^2 \mathcal{E}(\beta_1) - (1 - \beta_1^2) \mathcal{K}(\beta_1)}{2(1 - \beta_1^2) \beta_1} \frac{2r_1 - \beta_1^2(r + r_1)}{\beta_1 R_{m,1}^2} - \right. \right. \\ &\quad \left. \left. \frac{\mathcal{E}(\beta_1) - \mathcal{K}(\beta_1)}{\beta_1} \frac{2r_1 - \beta_1^2(r + r_1)}{\beta_1 R_{m,1}^2} \right] \right\}, \quad (\text{A.37}) \end{aligned}$$

$$\begin{aligned} &= \frac{M_0}{2\pi R_{m,1}} \left\{ \left[ \mathcal{K}(\beta_1) - \frac{\beta_1^2}{2} \mathcal{K}(\beta_1) - \mathcal{E}(\beta_1) \right] \left[ \frac{r + r_1}{r} - \frac{R_{m,1}^2}{r^2} \right] + \right. \\ &\quad \left[ \frac{\mathcal{E}(\beta_1)}{r(1 - \beta_1^2) \beta_1^2} - \frac{\mathcal{K}(\beta_1)}{r \beta_1^2} \right] [2r_1 - \beta_1^2(r + r_1)] - \\ &\quad \frac{\mathcal{K}(\beta_1)}{r} (2r_1 - \beta_1^2(r + r_1)) - \\ &\quad \left[ \frac{\mathcal{E}(\beta_1)}{2r(1 - \beta_1^2)} - \frac{\mathcal{K}(\beta_1)}{2r} \right] [2r_1 - \beta_1^2(r + r_1)] - \\ &\quad \left. \left[ \frac{\mathcal{E}(\beta_1)}{r \beta_1^2} - \frac{\mathcal{K}(\beta_1)}{r \beta_1^2} \right] [2r_1 - \beta_1^2(r + r_1)] \right\}, \quad (\text{A.38}) \end{aligned}$$

$$\begin{aligned} &= \frac{M_0}{2\pi R_{m,1}} \left\{ \mathcal{K}(\beta_1) \left[ \frac{r + r_1}{r} - \frac{R_{m,1}^2}{r^2} - \frac{\beta_1^2}{2} \frac{r + r_1}{r} + \frac{\beta_1^2}{2} \frac{R_{m,1}^2}{r^2} - \frac{2r_1}{r \beta_1^2} + \right. \right. \\ &\quad \left. \frac{r + r_1}{r} - \frac{2r_1}{r} + \frac{\beta_1^2(r + r_1)}{r} + \frac{r_1}{r} - \frac{\beta_1^2(r + r_1)}{2r} + \frac{2r_1}{r \beta_1^2} - \frac{r + r_1}{r} \right] + \\ &\quad \mathcal{E}(\beta_1) \left[ -\frac{r + r_1}{r} + \frac{R_{m,1}^2}{r^2} + \frac{2r_1}{r(1 - \beta_1^2) \beta_1^2} - \frac{r + r_1}{r(1 - \beta_1^2)} - \frac{r_1}{r(1 - \beta_1^2)} + \right. \\ &\quad \left. \frac{\beta_1^2(r + r_1)}{2r(1 - \beta_1^2)} - \frac{2r_1}{r \beta_1^2} + \frac{r + r_1}{r} \right] \right\}, \quad (\text{A.39}) \end{aligned}$$

$$\begin{aligned} &= \frac{M_0}{2\pi R_{m,1}} \left\{ \mathcal{K}(\beta_1) \left[ 1 - \left( 1 - \frac{\beta_1^2}{2} \right) \frac{R_{m,1}^2}{r^2} \right] + \right. \\ &\quad \left. \mathcal{E}(\beta_1) \left[ \frac{R_{m,1}^2}{r^2} + \frac{-2r + r \beta_1^2 + r_1 \beta_1^2}{2r(1 - \beta_1^2)} \right] \right\}, \quad (\text{A.40}) \end{aligned}$$



$$\begin{aligned} \frac{\partial F_\varphi(\mathbf{r})}{\partial r} &= \frac{M_0}{2\pi R_{m,1}} \left\{ \mathcal{K}(\beta_1) \left[ 1 - \left( 1 - \frac{\beta_1^2}{2} \right) \frac{R_{m,1}^2}{r^2} \right] + \right. \\ &\quad \left. \mathcal{E}(\beta_1) \left[ \frac{R_{m,1}^2}{r^2} + \frac{r_1^2 - r^2 - z^2}{(r - r_1)^2 + z^2} \right] \right\}. \end{aligned} \quad (\text{A.41})$$

Finally, the electric fields are then given by

$$E_r(\mathbf{r}) = \mathbf{E}(\mathbf{r}) \cdot \mathbf{u}_r = \frac{\partial F_\varphi(\mathbf{r})}{\partial z}, \quad (\text{A.42})$$

$$= \frac{M_0 z}{2\pi r R_{m,1}} \left\{ \mathcal{K}(\beta_1) - \frac{r^2 + r_1^2 + z^2}{(r - r_1)^2 + z^2} \mathcal{E}(\beta_1) \right\}, \quad (\text{A.43})$$

and

$$E_z(\mathbf{r}) = \mathbf{E}(\mathbf{r}) \cdot \mathbf{u}_z = -\frac{1}{r} F_\varphi(\mathbf{r}) \mathbf{u}_z - \frac{\partial F_\varphi(\mathbf{r})}{\partial r} \quad (\text{A.44})$$

$$\begin{aligned} &= -\frac{M_0}{2\pi R_{m,1}} \left[ \left( 1 - \frac{\beta_1^2}{2} \right) \frac{R_{m,1}^2}{r^2} \mathcal{K}(\beta_1) - \frac{R_{m,1}^2}{r^2} \mathcal{E}(\beta_1) \right] - \\ &\quad \frac{M_0}{2\pi R_{m,1}} \left\{ \mathcal{K}(\beta_1) \left[ 1 - \left( 1 - \frac{\beta_1^2}{2} \right) \frac{R_{m,1}^2}{r^2} \right] + \right. \\ &\quad \left. \mathcal{E}(\beta_1) \left[ \frac{R_{m,1}^2}{r^2} + \frac{r_1^2 - r^2 - z^2}{(r - r_1)^2 + z^2} \right] \right\}, \end{aligned} \quad (\text{A.45})$$

$$= -\frac{M_0}{2\pi R_{m,1}} \left\{ \mathcal{K}(\beta_1) + \frac{r_1^2 - r^2 - z^2}{(r - r_1)^2 + z^2} \mathcal{E}(\beta_1) \right\}. \quad (\text{A.46})$$

Comparing (A.43) to Equation (8a) and (A.46) to Equation (8b) in [11] shows that there is a discrepancy of a factor of (-1/2) in both cases.

## APPENDIX B

# Measured radiation patterns of all antenna concepts at a glance

---

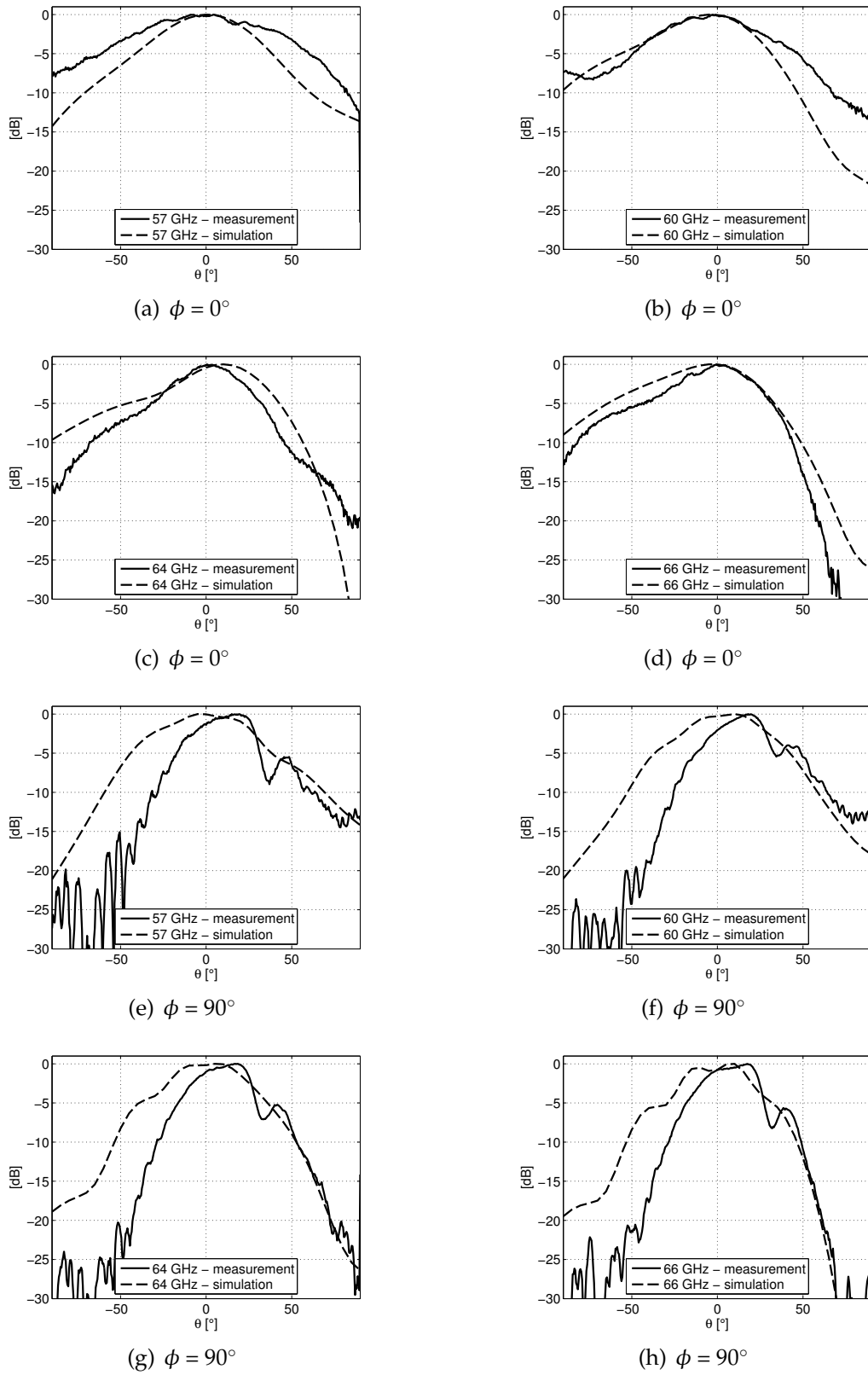


**Figure B.1.** AiP from Chapter 4 (co-polarization).

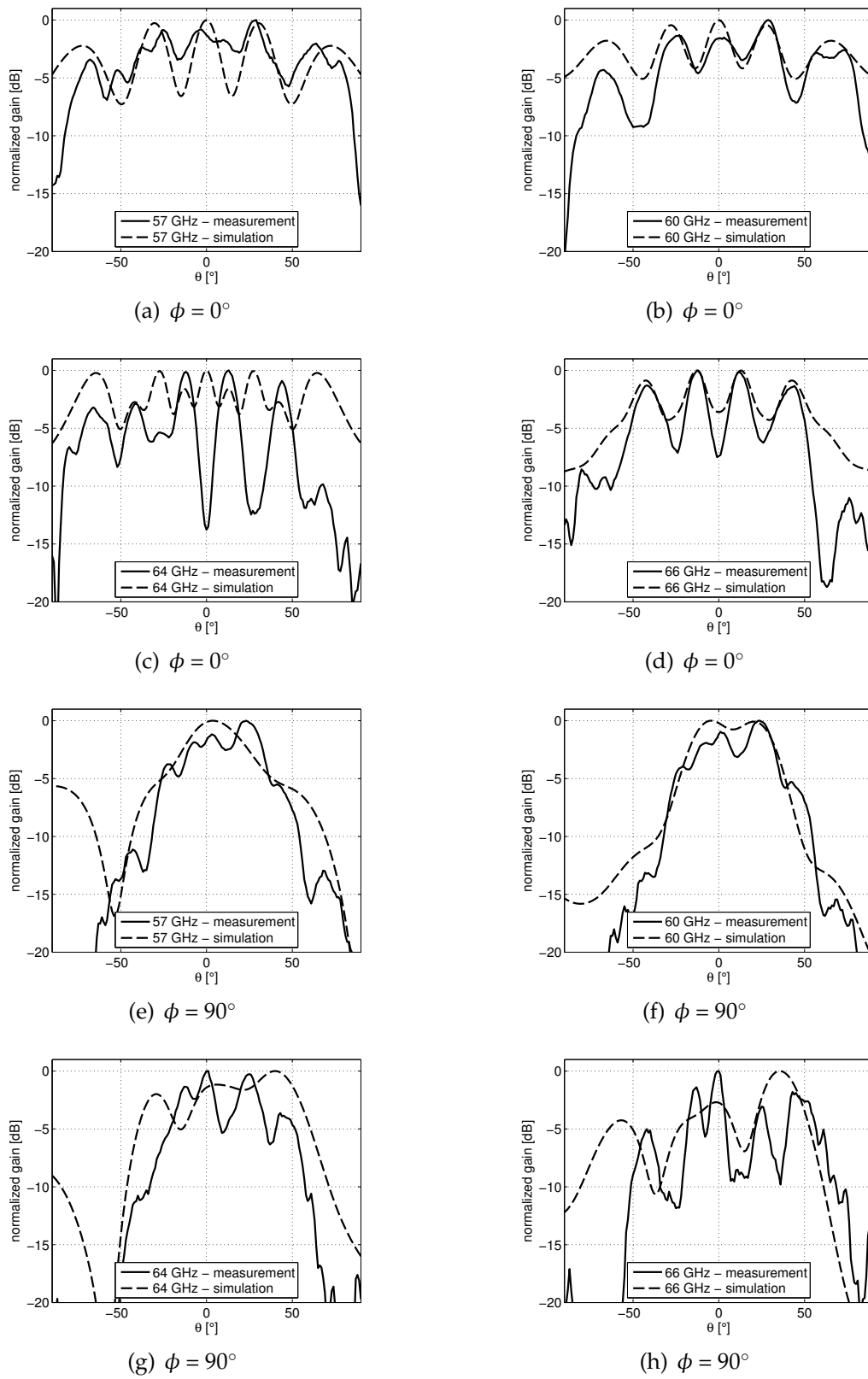


**Figure B.2.** AoC in measurement package from Chapter 5 (co-polarization).

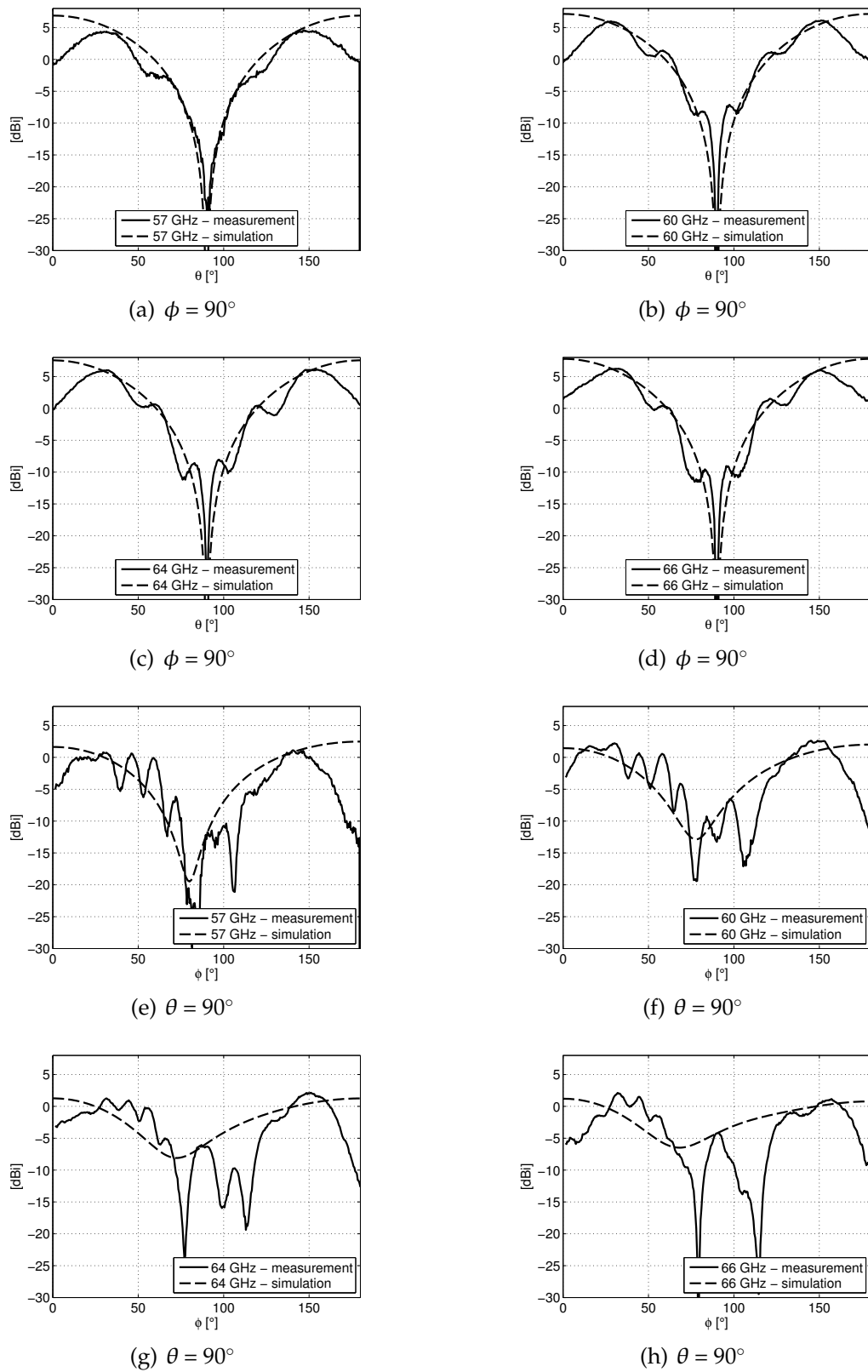
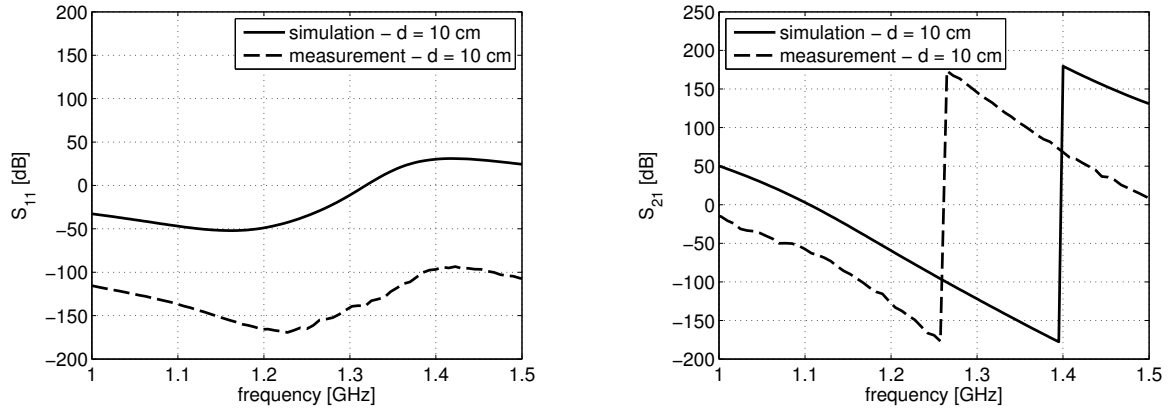


**Figure B.3.** BWA versus simplified model from Chapter 6 (co-polarization).

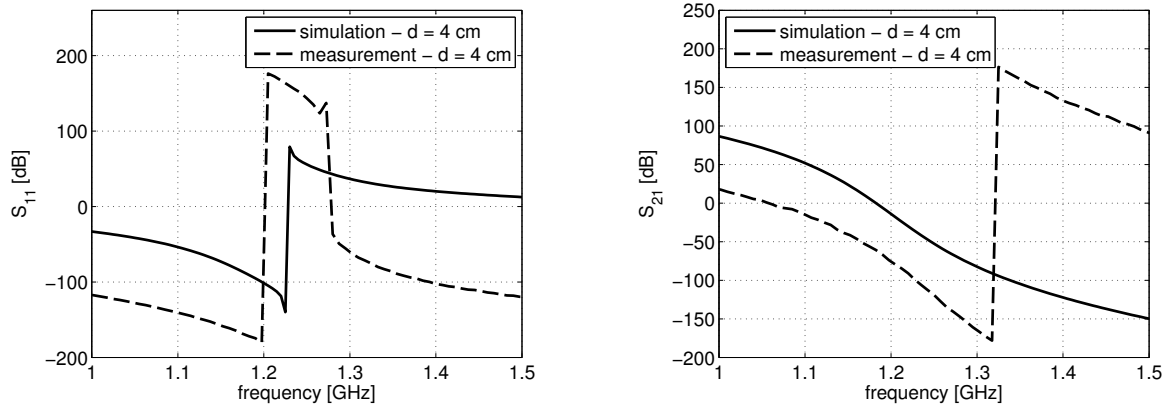
## APPENDIX C

# **Phase angles of the S-parameters shown in Figure 7.17**

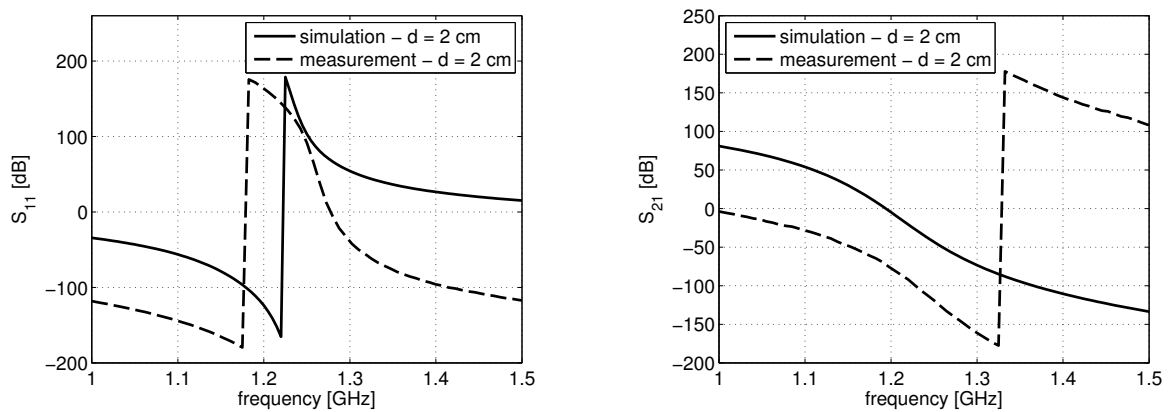
---



(a)  $d = 10$  cm



(b)  $d = 4$  cm



(c)  $d = 2$  cm

**Figure C.1.** Phase angles of the S-parameters shown in Figure 7.17.

# List of publications

---

## Journal publications

- [J1] A. B. Smolders and U. Johannsen, "Axial Ratio Enhancement for Circularly-Polarized Millimeter-Wave Phased-Arrays Using a Sequential Rotation Technique," *IEEE Transactions on Antennas and Propagation*, vol. 59, no. 9, pp. 3465-3469, sept. 2011.
- [J2] U. Johannsen and A. B. Smolders, "On the yield of millimeter-wave bond-wire-antennas in high volume production," *IEEE Transactions on Antennas and Propagation*, 2013, (accepted for publication).

## Conference publications

- [C1] U. Johannsen, A. B. Smolders, R. Mahmoudi, and J. A. G. Akkermans, "Substrate loss reduction in antenna-on-chip design," in *Antennas and Propagation Society International Symposium, 2009. APSURSI 09*. IEEE, 2009, pp. 1-4, (honorable mention at student paper contest).
- [C2] U. Johannsen, A. B. Smolders, and A. C. F. Reniers, "Measurement package for mm-wave Antennas-on-Chip," in *ICECom, 2010 Conference Proceedings*, sept. 2010, pp. 1-4, (invited paper).
- [C3] A. Stark, U. Johannsen, and A. F. Jacob, "In-situ probes for antenna array calibration," *European Microwave Conference (EuMC)*, 2010, 2010, pp. 465-468, (Young Engineer's Prize).
- [C4] U. Johannsen, M. Spirito, and A. B. Smolders, "Contactless measurement method for integrated mm-wave antennas," in *Proceedings of the 5th European Conference on Antennas and Propagation (EUCAP), 2011*, 2011, pp. 797-801.
- [C5] T. Papatheologou, A. B. Smolders, and U. Johannsen, "A hairpin Antenna-in-Package concept for RFID tag applications," *Radio and Wireless Symposium (RWS)*, 2011 IEEE, 2011, pp. 54-57.
- [C6] U. Johannsen and A. B. Smolders, "A Glance at Two Years Antenna-on-Chip Research," *URSI Benelux Forum 2011*, june 2011.
- [C7] A. B. Smolders and U. Johannsen, "The effect of phase and amplitude quantization on the axial ratio quality of mm-wave phased-arrays with sequential rotation," in *2011 IEEE International Symposium on Antennas and Propagation (APSURSI)*, july 2011, pp. 3283-3286.
- [C8] U. Johannsen, A. B. Smolders, A. C. F. Reniers, A. R. V. Dommele, and M. D. Huang, "Integrated antenna concept for millimeter-wave front-end modules in proven technologies," in *6th European Conference on Antennas and Propagation (EUCAP), 2012*, 2012, pp. 2560-2563, (invited paper).



- [C9] U. Johannsen, A. Smolders, J. Leiss, and U. Gollor, "Bond-wires: Readily available integrated millimeter-wave antennas," *European Microwave Conference (EuMC)*, 2012, pp. 197-200, nov. 2012.
- [C10] M. v. t. Westeinde, U. Johannsen, and A. B. Smolders, "Analytical modeling of radiation patterns for a Bond-Wire Antenna," in *IEEE Antennas and Propagation Society International Symposium (APSURSI)*, 2012, july 2012, pp. 1-2.
- [C11] U. Johannsen and A. B. Smolders, "Suitability of Wire-Bond-Technology for mm-Wave Antennas," *URSI Benelux Forum 2012*, sept. 2012.
- [C12] A. B. Smolders, A. C. F. Reniers, U. Johannsen and M.H.A.J. Herben, "Measurement and Calibration Challenges of Microwave and Millimeter-wave Phased-Arrays", in *Proc. of the IEEE International Workshop on Antenna Technology (iWAT)*, Karlsruhe, 2013, pp.354-357, March 2013 (invited paper).
- [C13] R. v. Kemenade, U. Johannsen, and A. B. Smolders, "Efficient Model for Computing the Mutual Coupling Between Millimeter-Wave Antennas in Wire-Bond Technology," in *7th European Conference on Antennas and Propagation (EUCAP)*, 2013, 2013.
- [C14] H. Gao, U. Johannsen, M. K. Matters-Kammerer, D. Milosevic, A. B. Smolders, A. van Roermund and P. Baltus, "A 60-GHz Rectenna for Monolithic Wireless Sensor Tags", in *Proceedings of the IEEE International Symposium on Circuits and Systems (ISCAS)*, may 2013.
- [C15] H. Gao, M. K. Matters-Kammerer, P. Harpe, D. Milosevic, U. Johannsen, A. van Roermund, and Peter Baltus, "A 71GHz RF Energy Harvesting Tag with 8% Efficiency for Wireless Temperature Sensors in 65nm CMOS," in *Proceedings of the 2013 IEEE Radio Frequency Integrated Circuits (RFIC) Symposium*, june 2013 (accepted).

# Bibliography

---

- [1] P. Smulders, "Exploiting the 60 GHz band for local wireless multimedia access: prospects and future directions," *IEEE Communications Magazine*, vol. 40, no. 1, pp. 140–147, jan. 2002.
- [2] S. K. Yong and C.-C. Chong, "An Overview of Multigigabit Wireless through Millimeter Wave Technology: Potentials and Technical Challenges," *EURASIP Journal on Wireless Communications and Networking*, vol. Volume 2007 Issue 1, pp. 50–50, 2007.
- [3] "Broadband Radio Access Networks (BRAN); 60 GHz Multi-Gigabit WAS/RLAN Systems; Harmonized EN covering the essential requirements of article 3.2 of the R&TTE Directive," *ETSI EN 302 567 v.1.2.1 (12-01)*, January 2012.
- [4] N. Guo, R. C. Qiu, S. S. Mo, and K. Takahashi, "60-GHz Millimeter-Wave Radio: Principle, Technology, and New Results," *EURASIP Journal on Wireless Communications and Networking*, vol. 2007, no. 1, 2007.
- [5] R. Daniels, J. Murdock, T. Rappaport, and R. Heath, "60 GHz Wireless: Up Close and Personal," *IEEE Microwave Magazine*, vol. 11, no. 7, pp. 44–50, dec. 2010.
- [6] Y. Zhang and D. Liu, "Antenna-on-Chip and Antenna-in-Package Solutions to Highly Integrated Millimeter-Wave Devices for Wireless Communications," *IEEE Transactions on Antennas and Propagation*, vol. 57, no. 10, pp. 2830–2841, Oct. 2009.
- [7] P. Smulders, H. Yang, and I. Akkermans, "On the Design of Low-Cost 60-GHz Radios for Multigigabit-per-Second Transmission over Short Distances [Topics in Radio Communications]," *IEEE Communications Magazine*, vol. 45, no. 12, pp. 44–51, december 2007.
- [8] R. Daniels and R. Heath, "60 GHz wireless communications: emerging requirements and design recommendations," *IEEE Vehicular Technology Magazine*, vol. 2, no. 3, pp. 41–50, sept. 2007.
- [9] K.-K. Huang and D. Wentzloff, "A 60GHz antenna-referenced frequency-locked loop in 0.13 um CMOS for wireless sensor networks," in *2011 IEEE International Solid-State Circuits Conference Digest of Technical Papers (ISSCC)*, feb. 2011, pp. 284–286.
- [10] E. Ojefors, U. Pfeiffer, A. Lisauskas, and H. Roskos, "A 0.65 thz focal-plane array in a quarter-micron cmos process technology," *IEEE Journal of Solid-State Circuits*, vol. 44, no. 7, pp. 1968–1976, july 2009.
- [11] T. Simpson, "The Magnetostatic Frill Source," *IEEE Transactions on Antennas and Propagation*, vol. 59, no. 9, pp. 3313–3317, sept. 2011.
- [12] H.-G. Unger, *Elektromagnetische Theorie für die Hochfrequenztechnik - Teil I: Allgemeine Gesetze und Verfahren, Antennen und Funkübertragung, planare, rechteckige und zylindrische Wellenleiter*, 2nd ed. Dr. Alfred Hüthig Verlag GmbH Heidelberg, 1988.
- [13] D. M. Pozar, *Microwave Engineering*, 3rd ed. New York: John Wiley & Sons, Inc., New York., 2005.

- [14] C. A. Balanis, *Antenna Theory - Analysis and Design*, 3rd ed. John Wiley & Sons, Inc., 2005.
- [15] R. F. Harrington, *Time-Harmonic Electromagnetic Fields*, ser. on Electromagnetic Wave Theory, D. G. Dudley, Ed. IEEE Press, John Wiley & Sons, Inc., 2001.
- [16] —, *Field Computation by Moment Methods*, ser. on Electromagnetic Waves, D. G. Dudley, Ed. IEEE Press, John Wiley & Sons, Inc., 2000.
- [17] A. Taflove and S. C. Hagness, *Computational Electrodynamics: The Finite-Difference Time-Domain Method*, 3rd ed. Artech House Inc., 2005.
- [18] (2012, December) EMPIRE XCcel. IMST GmbH. [Online]. Available: <http://www.empire.de>
- [19] A. Ludwig, "The definition of cross polarization," *Antennas and Propagation, IEEE Transactions on*, vol. 21, no. 1, pp. 116–119, 1973.
- [20] J. E. Storer, "Impedance of Thin Wire Loop Antennas," Craft Laboratory, Harvard University, Cambridge, Massachusetts, Tech. Rep. 212, May 1955.
- [21] M. C. van Beurden, "Integro-differential equations for electromagnetic scattering - Analysis and computation for objects with electric contrast," Ph.D. dissertation, Eindhoven University of Technology, 2003. [Online]. Available: [http://w3.tue.nl/en/services/library/digilib/publications\\_from\\_tue/dissertations/](http://w3.tue.nl/en/services/library/digilib/publications_from_tue/dissertations/)
- [22] M. C. van Beurden and A. G. Tijhuis, "Analysis and Regularization of the Thin-Wire Integral Equation With Reduced Kernel," *IEEE Transactions on Antennas and Propagation*, vol. 55, no. 1, pp. 120–129, jan. 2007.
- [23] (2012, December) Matlab website. MathWorks, Inc. [Online]. Available: [www.mathworks.com/products/matlab/](http://www.mathworks.com/products/matlab/)
- [24] "IEEE Standard for Information technology - Telecommunications and information exchange between systems - Local and metropolitan area networks - Specific requirements. Part 15.3: Wireless Medium Access Control (MAC) and Physical Layer (PHY) Specifications for High Rate Wireless Personal Area Networks (WPANs) Amendment 2: Millimeter-wave-based Alternative Physical Layer Extension," *IEEE Std 802.15.3c-2009 (Amendment to IEEE Std 802.15.3-2003)*, pp. c1–187, December 2009.
- [25] S. Reynolds, B. Floyd, U. Pfeiffer, T. Beukema, J. Grzyb, C. Haymes, B. Gaucher, and M. Soyuer, "A silicon 60-ghz receiver and transmitter chipset for broadband communications," *Solid-State Circuits, IEEE Journal of*, vol. 41, no. 12, pp. 2820–2831, dec. 2006.
- [26] *RF Manual - Application and design manual for High Performance RF products*, 16th ed., NXP Semiconductors, June 2012. [Online]. Available: <http://www.nxp.com>
- [27] (2012, December) LTCC @ IMST. IMST GmbH. [Online]. Available: <http://www.ltcc.de>
- [28] Y. Zhang, M. Sun, K. Chua, L. Wai, and D. Liu, "Antenna-in-Package Design for Wirebond Interconnection to Highly Integrated 60-GHz Radios," *IEEE Transactions on Antennas and Propagation*, vol. 57, no. 10, pp. 2842–2852, Oct. 2009.
- [29] D. G. Kam, D. Liu, A. Natarajan, S. Reynolds, H.-C. Chen, and B. Floyd, "LTCC Packages With Embedded Phased-Array Antennas for 60 GHz Communications," *IEEE Microwave and Wireless Components Letters*, vol. 21, no. 3, pp. 142–144, march 2011.
- [30] W. Hong, A. Goudelev, K. Baek, V. Arkhipenkov, and J. Lee, "24-Element Antenna-in-Package for Stationary 60-GHz Communication Scenarios," *IEEE Antennas and Wireless Propagation Letters*, vol. 10, pp. 738–741, 2011.
- [31] "RO3000 Series Circuit Materials - RO3003, RO3006 and RO3010 High Frequency Laminates," Datasheet, December 2012. [Online]. Available: <http://www.rogerscorp.com>
- [32] "RO4000 Series - High Frequency Circuit Materials," Datasheet, December 2012. [Online]. Available: <http://www.rogerscorp.com>

- [33] "ULTRALAM 3000 Liquid Crystalline Polymer Circuit Material," Datasheet, December 2012. [Online]. Available: <http://www.rogerscorp.com>
- [34] D. G. Kam, D. Liu, A. Natarajan, S. Reynolds, and B. Floyd, "Organic Packages With Embedded Phased-Array Antennas for 60-GHz Wireless Chipsets," *IEEE Transactions on Components, Packaging and Manufacturing Technology*, vol. 1, no. 11, pp. 1806–1814, nov. 2011.
- [35] D. Liu, I. Akkermans, H.-C. Chen, and B. Floyd, "Packages with Integrated 60-GHz Aperture-Coupled Patch Antennas," *IEEE Transactions on Antennas and Propagation*, vol. PP, no. 99, p. 1, 2011.
- [36] W. Hong, K. Baek, and A. Goudelev, "Multilayer Antenna Package for IEEE 802.11ad employing Ultra-low Cost FR4," *IEEE Transactions on Antennas and Propagation*, vol. PP, no. 99, p. 1, 2012.
- [37] M. I. Kazim, M. H. A. J. Herben, and M. D. Huang, "Half truncated icosahedral passive electromagnetic deflector for the 60 GHz band," in *2010 Proceedings of the Fourth European Conference on Antennas and Propagation (EuCAP)*, april 2010, pp. 1–5.
- [38] S.-S. Hsu, K.-C. Wei, C.-Y. Hsu, and H. Ru-Chuang, "A 60-GHz Millimeter-Wave CPW-Fed Yagi Antenna Fabricated by Using 0.18- $\mu\text{m}$  CMOS Technology," *IEEE Electron Device Letters*, vol. 29, no. 6, pp. 625–627, june 2008.
- [39] A. B. Smolders, "Microstrip Phased-Array Antennas: A Finite-Array Approach," Ph.D. dissertation, Eindhoven University of Technology, 1994. [Online]. Available: [http://w3.tue.nl/en/services/library/digilib/publications\\_from\\_tue/dissertations/](http://w3.tue.nl/en/services/library/digilib/publications_from_tue/dissertations/)
- [40] A. Babakhani, X. Guan, A. Komijani, A. Natarajan, and A. Hajimiri, "A 77-GHz Phased-Array Transceiver With On-Chip Antennas in Silicon: Receiver and Antennas," *IEEE Journal of Solid-State Circuits*, vol. 41, no. 12, pp. 2795–2806, dec. 2006.
- [41] S. Pan and F. Capolino, "Design of a CMOS On-Chip Slot Antenna With Extremely Flat Cavity at 140 GHz," *IEEE Antennas and Wireless Propagation Letters*, vol. 10, pp. 827–830, 2011.
- [42] K. Kang, F. Lin, D.-D. Pham, J. Brinkhoff, C.-H. Heng, Y. X. Guo, and X. Yuan, "A 60-GHz OOK Receiver With an On-Chip Antenna in 90 nm CMOS," *IEEE Journal of Solid-State Circuits*, vol. 45, no. 9, pp. 1720–1731, sept. 2010.
- [43] X.-Y. Bao, Y.-X. Guo, and Y.-Z. Xiong, "60-GHz AMC-Based Circularly Polarized On-Chip Antenna Using Standard 0.18- $\mu\text{m}$  CMOS Technology," *IEEE Transactions on Antennas and Propagation*, vol. 60, no. 5, pp. 2234–2241, may 2012.
- [44] Y.-C. Ou and G. Rebeiz, "On-Chip Slot-Ring and High-Gain Horn Antennas for Millimeter-Wave Wafer-Scale Silicon Systems," *IEEE Transactions on Microwave Theory and Techniques*, vol. 59, no. 8, pp. 1963–1972, aug. 2011.
- [45] M.-R. Nezhad-Ahmadi, M. Fakharzadeh, B. Biglarbegian, and S. Safavi-Naeini, "High-Efficiency On-Chip Dielectric Resonator Antenna for mm-Wave Transceivers," *IEEE Transactions on Antennas and Propagation*, vol. 58, no. 10, pp. 3388–3392, oct. 2010.
- [46] M. Neshat, D. Hailu, M. Nezhad-Ahmadi, G. Rafi, and S. Safavi-Naeini, "Gain Measurement of Embedded On-Chip Antennas in mmW/THz Range," *IEEE Transactions on Antennas and Propagation*, vol. 60, no. 5, pp. 2544–2549, may 2012.
- [47] E. Ojefors, H. Kratz, K. Grenier, R. Plana, and A. Rydberg, "Micromachined Loop Antennas on Low Resistivity Silicon Substrates," *IEEE Transactions on Antennas and Propagation*, vol. 54, no. 12, pp. 3593–3601, dec. 2006.
- [48] A. Mahanfar, S.-W. Lee, A. Parameswaran, and R. Vaughan, "Self-Assembled Monopole Antennas With Arbitrary Shapes and Tilt Angles for System-on-Chip and System-in-Package Applications," *IEEE Transactions on Antennas and Propagation*, vol. 58, no. 9, pp. 3020–3028, sept. 2010.

- [49] K. Chan, A. Chin, Y. Lin, C. Chang, C. Zhu, M. Li, D. Kwong, S. McAlister, D. Duh, and W. Lin, "Integrated antennas on Si with over 100 GHz performance, fabricated using an optimized proton implantation process," *IEEE Microwave and Wireless Components Letters*, vol. 13, no. 11, pp. 487–489, nov. 2003.
- [50] U. Pfeiffer, J. Grzyb, D. Liu, B. Gaucher, T. Beukema, B. Floyd, and S. Reynolds, "A chip-scale packaging technology for 60-GHz wireless chipsets," *IEEE Transactions on Microwave Theory and Techniques*, vol. 54, no. 8, pp. 3387–3397, aug. 2006.
- [51] G. Felic and S. Skafidas, "Flip-Chip Interconnection Effects on 60-GHz Microstrip Antenna Performance," *IEEE Antennas and Wireless Propagation Letters*, vol. 8, pp. 283–286, 2009.
- [52] H.-T. Wu *et al.*, "Bond Wire Antenna/Feed for Operation Near 60 GHz," *IEEE Transactions on Microwave Theory and Techniques*, vol. 57, no. 12, pp. 2966–2972, dec. 2009.
- [53] R. Willmot *et al.*, "A Yagi-Uda Array of High Efficiency Wire-Bond Antennas for On-Chip Radio Applications," *IEEE Transactions on Microwave Theory and Techniques*, no. 12, pp. 3315–3321, 2009.
- [54] B. P. Gaucher, D. Liu, U. R. R. Pfeiffer, and T. M. Zwick, "Apparatus and methods for constructing antennas using wire bonds as radiating elements," U.S. Patent 7,295,161, Nov. 13, 2007.
- [55] U. Johannsen, A. B. Smolders, A. C. F. Reniers, A. R. V. Dommele, and M. D. Huang, "Integrated antenna concept for millimeter-wave front-end modules in proven technologies," in *6th European Conference on Antennas and Propagation (EUCAP), 2012*, 2012, pp. 2560–2563, (invited paper).
- [56] U. Johannsen, A. B. Smolders, and A. C. F. Reniers, "Measurement package for mm-wave Antennas-on-Chip," in *ICECom, 2010 Conference Proceedings*, sept. 2010, pp. 1–4, (invited paper).
- [57] (2012, December) Sencio - functional packaging center. Sencio BV. [Online]. Available: <http://www.sencio.nl/technologies/item/cavity-molding>
- [58] K. Pressel, G. Beer, T. Meyer, M. Wojnowski, M. Fink, G. Ofner, and B. Roe andmer, "Embedded wafer level ball grid array (eWLB) technology for system integration," in *IEEE CPMT Symposium Japan, 2010*, aug. 2010, pp. 1–4.
- [59] (2012, December) Cascade Microtech website. Casacde Microtech, Inc. [Online]. Available: <http://www.cmicro.com/>
- [60] "Agilent PNA Microwave Network Analyzers," Datasheet, December 2012, (discontinued model). [Online]. Available: <http://www.agilent.com>
- [61] (2012, December) Picoprobe website. GGB Industries, Inc. [Online]. Available: <http://www.picoprobe.com>
- [62] B. Yang, A. Yarovoy, O. Shoykhetbrod, and D. Nuessler, "Experimental verification of Ka band LTCC antenna," in *European Microwave Conference (EuMC), 2010*, 2010, pp. 779–782.
- [63] U. Johannsen, A. B. Smolders, R. Mahmoudi, and J. A. G. Akkermans, "Substrate loss reduction in antenna-on-chip design," in *Antennas and Propagation Society International Symposium, 2009. APSURSI '09. IEEE*, 2009, pp. 1–4, (honorable mention at student paper contest).
- [64] P. Deixler, A. Rodriguez, W. De Boer, H. Sun, R. Colclaser, D. Bower, N. Bell, A. Yao, R. Brock, Y. Bouttement, G. Hurkx, L. Tiemeijer, J. Paasschens, H. Huizing, D. Hartskeerl, P. Agrarwal, P. Magnee, E. Aksen, and J. Slotboom, "QUBiC4X: An  $f_T/f_{max} = 130/140$ GHz SiGe:C-BiCMOS manufacturing technology with elite passives for emerging microwave applications," *Bipolar/BiCMOS Circuits and Technology, 2004. Proceedings of the 2004 Meeting*, pp. 233–236, sept. 2004.
- [65] (2012, December) Omniradar website. Omniradar. [Online]. Available: <http://www.omniradar.eu/>
- [66] Y. Zhang, M. Sun, and L. Guo, "On-chip antennas for 60-GHz radios in silicon technology," *IEEE Transactions on Electron Devices*, vol. 52, no. 7, pp. 1664–1668, July 2005.

- [67] E. Janssen, R. Mahmoudi, E. v. d. Heijden, P. Sakian, A. d. Graauw, R. Pijper, and A. v. Roermund, "Fully balanced 60 GHz LNA with 37% bandwidth, 3.8 dB NF, 10 dB gain and constant group delay over 6 GHz bandwidth," in *Proceedings of 10th Topical Meeting on Silicon Monolithic Integrated Circuits in RF Systems (SIRF 2010)*, January 2010, pp. 124–127.
- [68] W. van Noort, C. Detcheverry, A. Rodriguez, and R. Pijper, "On-chip mm-Wave passives," *IEEE Bipolar/BiCMOS Circuits and Technology Meeting, 2007. BCTM '07.*, pp. 168–171, 30 2007-oct. 2 2007.
- [69] N. Llombart, A. Neto, G. Gerini, and P. De Maagt, "Planar circularly symmetric EBG structures for reducing surface waves in printed antennas," *IEEE Transactions on Antennas and Propagation*, vol. 53, no. 10, pp. 3210–3218, 2005.
- [70] J. Akkermans, R. van Dijk, and M. Herben, "Millimeter-wave antenna measurement," in *Proceedings of the 2007 European Microwave Conference (EuMC 2007)*, October 2007.
- [71] U. Johannsen, A. Smolders, J. Leiss, and U. Gollor, "Bond-wires: Readily available integrated millimeter-wave antennas," *European Microwave Conference (EuMC), 2012*, pp. 197–200, nov. 2012.
- [72] M. v. t. Westeinde, U. Johannsen, and A. B. Smolders, "Analytical modeling of radiation patterns for a Bond-Wire Antenna," in *IEEE Antennas and Propagation Society International Symposium (AP-SURSI), 2012*, July 2012, pp. 1–2.
- [73] U. Johannsen and A. B. Smolders, "On the yield of millimeter-wave bond-wire-antennas in high volume production," *IEEE Transactions on Antennas and Propagation*, 2013, (accepted for publication).
- [74] G. Steenbruggen and P. Dijkstra, "Air cavity package for flip-chip," U.S. Patent US8 153 480, 2012.
- [75] B. C. Wadell, *Transmission Line Design Handbook*. Artech House, Inc., 1991.
- [76] A. B. Smolders and U. Johannsen, "Axial Ratio Enhancement for Circularly-Polarized Millimeter-Wave Phased-Arrays Using a Sequential Rotation Technique," *IEEE Transactions on Antennas and Propagation*, vol. 59, no. 9, pp. 3465–3469, sept. 2011.
- [77] —, "The effect of phase and amplitude quantization on the axial ratio quality of mm-wave phased-arrays with sequential rotation," in *2011 IEEE International Symposium on Antennas and Propagation (APSURSI)*, July 2011, pp. 3283–3286.
- [78] R. v. Kemenade, U. Johannsen, and A. Smolders, "Efficient Model for Computing the Mutual Coupling Between Millimeter-Wave Antennas in Wire-Bond Technology," in *7th European Conference on Antennas and Propagation (EUCAP), 2013*, 2013.
- [79] J. Huang, "A technique for an array to generate circular polarization with linearly polarized elements," *IEEE Transactions on Antennas and Propagation*, vol. 34, no. 9, pp. 1113–1124, sep 1986.
- [80] (2012, December) Wolfram Functions Site. Wolfram Research, Inc. [Online]. Available: <http://functions.wolfram.com/EllipticIntegrals/EllipticK/introductions/CompleteEllipticIntegrals/ShowAll.html>



# Acknowledgements

---

That's it! Four years of work compressed into a paperback. Work that I would not have done without Thomas Bluhm, who had probably no idea what he initiated when he sent me on an internship to Shanghai (thanks, Thomas!). Work that was inspired by discussions with and supported by various individuals. This last chapter is, therefore, devoted to those many people.

In particular, I would like to thank my first promotor, or Doktorvater ("doctoral-father") as he is called in German, Bart Smolders. By providing me with lots of space to be creative, to struggle, but also to grow, he has raised me to become an independent researcher. Moreover, he always willingly supported my fondness for organizational tasks and my career ambitions. For example, he recommended me for the task as project proposal coordinator for a European project, which I perceived as a high amount of trust.

Furthermore, I wish to thank my second promotor, Giampiero Gerini, as well as the other members of my Ph.D. committee, i.e., Peter Baltus, Patrice Gamand, Alexander Yarovoy, and Arne Jacob for the fruitful discussions and their valuable input during various stages of my Ph.D. student period.

Especially during the writing phase of my thesis, Martijn van Beurden was of great help. The structure of this thesis, for example, is a result of a series of discussions with him. Besides this, he supported me by patiently answering questions regarding electromagnetic theory and modeling, for which I am also very grateful. Here, thanks are also due to Bas de Hon for his valuable input on various topics, such as the FDTD method. Furthermore, thanks to Vito Lancellotti for sharing his knowledge about elliptic integrals. For sharing his experience with his own thesis and providing me with his Latex template, I would like to thank Rob Mestrom. Furthermore, I am grateful to Floris van der Wilt for his critical review of the loop-antenna section.

Although not being directly involved with my daily supervision, Anton Tjihuis supported me not only in his general role as head of the Electromagnetics group, but also encouraged and trusted me with chairing the European Microwave Week Stu-



dent Challenge, for which I am very grateful. Special thanks to Suzanne Kuijlaars for all these many "small" things she did in the past four years. Likewise, thanks are also due to Margot van den Heuvel for her support during the Par4CR project.

Thanks to my, also former, office-mates Rob Mestrom, Jean-Pierre Vaessen, Mojtaba (Abolghasem) Zamanifekri, and Sissy (Theodosia) Papatheologou for the always pleasant atmosphere in our office. To all my colleagues from the TU/e as well as the partners within the PANAMA and Par4CR project I am grateful for their enthusiasm, critical questions, and their valuable support. Here, special thanks are due to Rainier van Dommele and Ad Reniers for their support during measurements and for building the mm-wave anechoic chamber, to Niels Kramer and Marcel Geurts from NXP Semiconductors for organizing the fabrication of the IC prototypes, to the team of NXP's pilot line in Nijmegen for realizing my packaging ideas, and to the entire staff of IMST GmbH for the fabrication and measurements of the BWA prototypes as well as for the lovely time I had there during my exchange period. Furthermore, thanks to Paul van Zeijl, Hans Brouwer, Timofey Savelyev, and Jacques Rompen from Omniradar for their great interest in my work, the opportunity to explore the AoC approach in a real application scenario, and the performance of the radar measurements.

I often had more ideas than time in the past four years, but was lucky enough to find motivated students to work out some of them. For their valuable contributions, I would like to thank Maaïke van 't Westeinde, Rick van Kemenade, Juanito (Juan Enrique) Lopez Carcelen, Henk Jan Keizer, Bedilu Adela, Hao Wang, and Chen Ye.

A greater achievement than any thesis or professional success, is having friends and finding new ones. And I have had and have found many of them during my time at the TU/e. Therefore, I will not attempt to address everybody individually here since this would easily fill another book. Instead, I would simply wish to thank you all for being there and being yourself! Thank you for inviting me to your weddings, to your birthdays or other parties. Special thanks to Anđelko Katalenić with whom I escaped from the space-box park and who dared to share an apartment with me.

Sharing my life with me for over two years now is Miss (Danielle) Webb. *Miss Webb, a paragraph is not enough to describe what you mean to me. I love you! You are my world! And, ironically, a lousy old post-card from Büsum wraps it all up: "Ich möchte mit dir alt werden, es hat aber keine Eile!"*

I am grateful to my big brother, Thomas, who understood the world seemingly so easily when we were children, which inspired me to try and understand it too.

Last, but certainly not least, I wish to thank my parents: *Mama und Papa, dieses Buch ist für euch! Für eure fantastische Unterstützung seit jetzt schon fast dreißig Jahren, für die ich so unsagbar dankbar bin!*

# Curriculum Vitae

---

Ulf Johannsen was born on January 11th, 1984, in Flensburg, Germany. He enrolled in electrical engineering at the Technische Universität Hamburg-Harburg (TUHH) in Hamburg, Germany, in 2003 and obtained his Dipl.-Ing. degree in 2009. During this period he also worked part-time at the DLR\_School\_Lab, a student laboratory of the German Aerospace Center (DLR) at the TUHH, and then changed to NXP Semiconductors in Hamburg where he assisted the Application Support team by designing and testing analog circuits. As part of his study, he completed two internships at NXP Semiconductors in Shanghai, China, and Nijmegen, the Netherlands, respectively. He was furthermore in the organization committee of the first IEEE Germany Student Conference in 2009. In the same year he started at the Electromagnetics group of the Technische Universiteit Eindhoven (TU/e), Eindhoven, the Netherlands, as Ph.D.-student. His main research focus is concentrated on technologies for millimeter-wave antenna integration. Throughout his research he has been collaborating with several international and national companies, research institutes, and universities and completed an exchange project with IMST GmbH in Kamp-Lintfort, Germany. He was the organizer of bi-monthly EM colloquia as well as the chair-person of the organization committee of the fifth European Microwave Week Student Challenge in Amsterdam in 2012.

Ulf Johannsen is a member of the VDE and a Student Member of the IEEE Antennas & Propagation Society. He is furthermore a reviewer for peer-reviewed IEEE journals.